

# Reinforced Supramolecular Networks of End Functionalized Polymers for Tailored Thermomechanical Property Profiles

Présentée le 5 juin 2023

Faculté des sciences et techniques de l'ingénieur  
Laboratoire des matériaux organiques et macromoléculaires  
Programme doctoral en science et génie des matériaux

pour l'obtention du grade de Docteur ès Sciences

par

## Yevhen HRYSHUNIN

Acceptée sur proposition du jury

Prof. A. Mortensen, président du jury  
Prof. H. Frauenrath, directeur de thèse  
Dr V. Bourg, rapporteuse  
Prof. L. Bouteiller, rapporteur  
Prof. F. Stellacci, rapporteur



## **Acknowledgments**

This PhD journey has been a long and winding road, filled with numerous discoveries, surprises, disappointments, and invaluable lessons. I would like to express my heartfelt gratitude to everyone who accompanied me on this path.

First and foremost, I extend my sincere appreciation to Prof. Holger Frauenrath for our many fruitful discussions. Working with him over the years has been an enlightening experience, and I have gained a wealth of knowledge and insights through our collaboration.

I would also like to acknowledge the expertise and guidance of Dr. Cristopher Plummer and Dr. Shuichi Haraguchi in my research. Their support has been instrumental in shaping my work. Furthermore, I am deeply grateful to all the members of LMOM, including Michael, Matthieu, Sophia, Lucile, Daniel, Enzo, Reuben, Clement, Alex, Giorgia, Nicolas, Bilal, Julian, Oguz, Piotr, Armande, Shawn, and Sylvie. The time we spent together has been truly memorable, and I appreciate all the wonderful experiences we shared.

I would also like to express my gratitude to my mom and dad for their unwavering support throughout these years. Their love and encouragement have been invaluable to my success. To my chosen family and friends, including Oleg and his family, John, Rachel, Kaycie, Vitor, Michael, Katy, Rene, Viera, Michi, Marcel, Tom, Wessel, Eva, Alexis, Renato, Armand, Shuichi, Jenny, Rieke, Megan, and the NearBirds team, I am incredibly thankful. You all hold a special place in my little world, and I feel blessed to have each and every one of you. You are fantastic beasts!

Thank you all from the bottom of my heart.

## Abstract

One promising class of materials for a circular plastic economy is bio-sourced and biodegradable aliphatic polyesters that can undergo chemical recycling to monomer via ring-closing depolymerization. However, they are often limited in their application due to inherent brittleness and low heat resistance, or due to processing difficulties, such as slow crystallization rate and poor melt strength. The supramolecular modification of polymers with end groups capable of hydrogen-bonding is a promising approach to increase toughness and melt properties. However, this approach is limited to polymers of low molecular weight that are insufficient for robust entanglement, resulting in materials that show brittle failure at low strains.

In this thesis, we show that the simultaneous improvement of mechanical properties, melt behavior, and crystallization rate of high molecular weight aliphatic polyesters is achieved when one blends a polymer end-modified with a ditopic, self-complementary self-assembling units based on three-fold hydrogen bonding and a low molecular weight additive based on the same supramolecular motif.

In the first chapter, we demonstrate that blending of a poly( $\epsilon$ -caprolactone) (PCL) modified with acetyl-L-alanyl-L-alanyl amide end groups ( $\text{PCL}_{80}(\text{Ala}_2\text{Ac})_2$ ) with 2-octyldodecyl acetyl-L-alanyl-L-alanyl (**A**) as a corresponding low molecular weight additive results in the formation of nanofibrillar aggregates. Covalent attachment of the polymer chains to the nanofibrillar network results in rubber-like behavior at temperatures above the PCL melting temperature and strain-hardening behavior at high strains. We utilize the newly obtained melt behavior for film melt stretching, which facilitates polymer orientation and leads to a shift from classical spherulitic morphology to shish-kebab structures, which in turn enables tailoring of the mechanical properties at room temperature.

In the second chapter, we make use of the previously observed melt behavior of  $\text{PCL}_{80}(\text{Ala}_2\text{Ac})_2/\mathbf{A}$  blends to prepare oriented filaments by melt stretching. The obtained filaments exhibit a shish-kebab morphology and significantly increased Young's modulus, yield strength, and ultimate strength.

In the third chapter, we demonstrate that blending a poly(L-lactic acid) (PLLA) modified with acetyl-L-alanyl-L-alanyl amide end groups ( $\text{PLLA}_{60}(\text{Ala}_2\text{Ac})_2$ ) with the additive **A** and low molecular weight additive results in a significant increase in the additive dispersion and leads to a one-order-of-magnitude decrease in crystallization half-time of the PLLA matrix.

In the fourth chapter, we modify PLLA with *N,N'*-diisopentyl 1,3,5-benzenetricarboxamide (BTA) end groups and prepare blends with the corresponding low molecular weight *N,N',N''*-triisopentyl BTA (**B5**). Co-assembly of the polymer end groups and **B5** additive yields a network of compliant, polymer-tethered nanofibrils aligned at a periodic spacing of. 10 – 12 nm. The obtained nanofibrillar network allows a much higher dispersion of the **B5** additive and a concomitant increase in the nucleation efficiency by three orders of magnitude compared to pristine PLLA. Additionally, a new rubber-like regime is established above PLLA melting transition, which results in an order of magnitude increase in PLA melt strength at large strains.

KEYWORDS | additives, nanofibrils, phase separation, poly( $\epsilon$ -caprolactone), poly(lactic acid), semicrystalline, supramolecular, reinforcement, telechelic

## Résumé

Une classe de matériaux prometteuse pour une économie circulaire du plastique sont les polyesters aliphatiques biosourcés et biodégradables pouvant être recyclés en monomères par dépolymérisation par fermeture de cycle. Leurs applications sont pourtant souvent limitées par leur fragilité, leur faible résistance thermique ou de mauvaises caractéristiques de mise en œuvre, telles qu'une faible vitesse de cristallisation ou une faible résistance à l'état fondu. L'utilisation de matériaux supramoléculaires liés par des liaisons hydrogène est une approche intéressante pour remédier à ces inconvénients. Cependant, cette approche est limitée aux polymères de faibles poids moléculaire qui sont insuffisamment enchevêtrés, conduisant à une rupture fragile à de faibles déformations.

Dans cette thèse, nous montrons qu'une amélioration des propriétés mécaniques, du comportement à l'état fondu, et de la vitesse de cristallisation, peut être obtenue dans des polyesters aliphatiques de haut poids moléculaire en mélangeant un polymère modifié aux extrémités avec une unité ditopique, auto-complémentaire et auto-associative, formant de triples liaisons hydrogène, avec un additif de faible poids moléculaire basé sur le même motif supramoléculaire.

Premièrement, nous démontrons que le mélange de poly( $\epsilon$ -caprolactone) modifié avec l'amide d'acétyl-L-alanyl-L-alanyl (**PCL<sub>80</sub>(Ala<sub>2</sub>Ac)<sub>2</sub>**), avec l'additif 2-octyldodécyl acétyl-L-alanyl-L-alanyl (**A**), conduit à la formation d'agrégats nanofibrillaires étendus. L'attachement des chaînes de polymère aux nanofibrilles entraîne un comportement caoutchouteux à l'état fondu et un écrouissage aux déformations élevées. Nous exploitons ce comportement lors de l'étirage de films à chaud, où il facilite l'orientation du polymère et provoque le passage d'une morphologie sphérolitique à une structure de type "shish-kebab", ce qui permet d'ajuster les propriétés mécaniques à température ambiante.

Deuxièmement, ce comportement caoutchouteux est utilisé pour préparer des filaments orientés par filage à chaud du mélange **PCL<sub>80</sub>(Ala<sub>2</sub>Ac)<sub>2</sub>/A** (5 % en poids). Les filaments obtenus présentent également une morphologie de type shish-kebab, ainsi qu'une augmentation importante du module de Young, du seuil de cisaillement, et de la contrainte à la rupture.

Troisièmement, nous démontrons que les mélanges d'acide poly(lactique) (PLA) modifié aux extrémités avec **Ala<sub>2</sub>Ac**, avec l'additif **A** présentent une augmentation importante de la dispersion de l'additif, ce qui conduit à une diminution d'un ordre de grandeur du demi-temps de cristallisation du PLA.

Quatrièmement, nous modifions les extrémités du PLA avec du N,N'-diisopentyl BTA et le mélangeons avec le N,N',N''-triisopentyl BTA (**B5**). Le co-assemblage des groupes terminaux du polymère et le **B5** produit un réseau nanofibrillaire souple, attaché au polymère, et composé d'empilements simples de BTA avec un espacement latéral de 10 – 12 nm. Ce réseau nanofibrillaire implique une dispersion très élevée du **B5** et une augmentation du taux de nucléation du PLA de trois ordres de grandeur. De plus, un nouveau régime caoutchouteux s'établit au-dessus du point de fusion du PLA en raison de l'attachement du polymère aux nanofibrilles, entraînant une augmentation d'un ordre de grandeur de la résistance à l'état fondu du PLA aux grandes déformations.

MOTS CLÉS | additifs, nanofibrilles, séparation de phase, poly( $\epsilon$ -caprolactone), acide polylactique, semicristallin, supramoléculaire, renforcement, téléchélique.

## Table of Contents

<b>Abstract</b>	<b>2</b>
<b>Resume</b>	<b>4</b>
<b>Table of Contents</b>	<b>6</b>
<b>List of Abbreviations</b>	<b>8</b>
<b>1. Introduction</b>	<b>11</b>
<b>1.1 Plastic Waste, Recycling, and Sustainable Solutions</b>	<b>11</b>
1.1.1 Plastics Production	11
1.1.2 Plastics Recycling	12
<b>1.2 PLA and PCL as Examples of Aliphatic Sustainable Polyester Materials</b>	<b>15</b>
1.2.1 Polylactide	15
1.2.2 Poly( $\epsilon$ -caprolactone)	21
1.2.3 Properties of Aliphatic Polyesters	22
1.2.4 Effects of Molecular Weight and Chain Architecture	23
<b>1.3 Polymer Mixtures</b>	<b>25</b>
1.3.1 Phase Behavior of Polymer Mixtures	25
1.3.2 Polymer-Polymer Blends	27
1.3.4 Nucleating Agents	28
<b>1.3 Supramolecular Materials</b>	<b>31</b>
1.4.1 Monotopic Hydrogen-Bonded Supramolecular Motifs	32
1.4.2 Ditopic Hydrogen-Bonded Supramolecular Motifs	34
1.4.3 Molecular Weight Dependence of Polymer End Group Assembly	39
1.4.5 Supramolecular Fillers	40
1.4.6 Limitations of Supramolecular Modification for Sustainable Plastics	40
<b>1.4 Scope and Outline of This Thesis</b>	<b>41</b>
<b>2. Supramolecular Modification for High Performance Sustainable Polyesters</b>	<b>44</b>
2.1 Introduction	46
2.2 Results and Discussion	49
2.3 Conclusions	79
<b>3. Supramolecular Modification for Poly(<math>\epsilon</math>-caprolactone) Filaments</b>	<b>80</b>
<b>3.1 Introduction</b>	<b>82</b>
<b>3.2 Results and Discussion</b>	<b>83</b>
3.2.1 Structural and Mechanical Analysis of Melt-Stretched Fibers	83
3.2.2 Characterization, and Mechanical Analysis of Cold-Stretched Fibers	88
<b>3.3 Conclusions</b>	<b>90</b>
<b>4. Supramolecular Modification of PLA for Improved Nucleation</b>	<b>92</b>
<b>4.1 Introduction</b>	<b>94</b>
<b>4.2 Results and Discussion</b>	<b>97</b>
4.2.1 Materials Design and Synthesis	97
4.2.2 Morphology and Thermal Properties of PDLLA-A/A and PDLLA/A blends	98
4.2.3 Thermal Properties of PLLA-A/A and PLLA/A blends	103
<b>4.3 Conclusions</b>	<b>105</b>
<b>5. Supramolecular Modification of PLA for Improved Nucleation and Melt Strength</b>	<b>108</b>
<b>5.1 Introduction</b>	<b>108</b>
<b>5.2 Results and Discussion</b>	<b>111</b>
5.2.1 Materials Design and Synthesis	111
5.2.2 Morphology and Thermal Properties of PDLLA-B5/B5	112



5.2.3 Morphology and Thermal Properties of PLLA-B5/B5	118
5.2.3 Melt Properties of the Blends	122
<b>5.3 Conclusions</b>	<b>124</b>
<b>6. Conclusions and Outlook</b>	<b>126</b>
<b>7. Experimental</b>	<b>130</b>
<b>8. References</b>	<b>145</b>
<b>9. Appendix</b>	<b>159</b>
<b>10. Curriculum Vitae</b>	<b>178</b>

## List of Abbreviations

Å	angstrom
<b>A8</b>	acetyl-L-alanyl-L-alanine (2-ethylhexyl) amide
<b>A18</b>	acetyl-L-alanyl-L-alanine (2-octadecyl) amide
AFM	atomic force microscopy
Ala <sub>2</sub> Ac / AcAla <sub>2</sub>	acetyl-L-alanyl-L-alanyl amide
<b>B5</b>	<i>N,N,N</i> -Tri(3-methylbutyl) benzene-1,3,5-tricarboxamide
BTA	benzene-1,3,5-tricarboxamide
CDCl <sub>3</sub>	deuterated chloroform (NMR)
$\chi$	Flory-Huggins parameter
d	doublet (NMR)
Đ	dispersity index (GPC)
DCM	dichloromethane
$\delta$	chemical shift (NMR)
DIPEA	<i>N,N</i> -diisopropylethylamine
DMSO	dimethyl sulfoxide
DSC	differential scanning calorimetry
<i>E</i>	Young's modulus / elastic modulus
$\epsilon$	strain at break
FT-IR	Fourier transform infrared spectroscopy
<i>G'</i>	Storage modulus (rheology)
<i>G''</i>	Loss modulus (rheology)
GPC	gel permeation chromatography
HRMS	high resolution mass spectrometry
Hz	hertz
<i>J</i>	coupling constant (NMR)
LDPE	low density polyethylene
LiOH	lithium hydroxide
LLDPE	linear low density polyethylene
m	multiplet (NMR)
[M] <sup>+</sup>	molecular peak (mass spectrometry)
m/z	mass-to-charge ratio (mass spectrometry)

MeOH	methanol
$M_n$	number-average molecular weight (GPC)
mol	mole
$M_w$	weight-average molecular weight (GPC)
NA	nanoscopic additive, ill-defined aggregates
NaOH	sodium hydroxide
NF	nanofibril
NMR	nuclear magnetic resonance
OM	optical microscopy
Pa	Pascal
PCL	poly( $\epsilon$ -caprolactone)
<b>PCL(Ala<sub>2</sub>Ac)</b>	poly( $\epsilon$ -caprolactone) functionalized with Ala <sub>2</sub> Ac end-groups
PDMS	polydimethylsiloxane
PE	polyethylene
PET	polyethylene terephthalate
$\phi$	volume fraction
PLA	polylactide
PDLLA	pol(DL-lactide)
PLLA	pol(L, L -lactide)
PDLA	pol(D, D -lactide)
<b>PDLLA-A</b>	pol(DL-lactide) modified with <b>Ala<sub>2</sub>Ac</b> end-groups
<b>PLLA-A</b>	pol(L,L-lactide) modified with <b>Ala<sub>2</sub>Ac</b> end-groups
<b>PLLA-B5</b>	pol(L, L -lactide) modified with <b>B5</b> end-groups
<b>PDLLA-B5</b>	pol(DL-lactide) modified with <b>B5</b> end-groups
PP	polypropylene
PyBOP	benzotriazol-1-yloxytripyrrolidinophosphonium hexafluorophosphate
q	quartet (NMR)
$R_f$	retention factor
rt	room temperature
s	singlet (NMR)
$\sigma$	strength
SEM	scanning electron microscopy

$\sigma_{\max}$	ultimate strength
$\sigma_y$	yield strength
$T$	Temperature
$t$	time
$t$	triplet (NMR)
$\tan \delta$	loss tangent factor
$T_c$	crystallization temperature
$T_d$	dissociation temperature (additives)
$T_{ds}$	dissociation temperature, dilute solution (additives)
$T_g$	glass transition temperature
TGA	thermogravimetric analysis
$\theta$	scattering angle (X-ray diffraction)
THF	tetrahydrofuran
$T_m$	melting temperature
$T_{ns}$	nanostructure dissociation temperature (additives)
$T_{rh}$	rheological crossover temperatures ( $G' = G''$ )
UHMWPE	ultra high molecular weight polyethylene
UPy	ureidopyrimidinone
$W$	tensile energy at break
wt%	weight percent
XRD	X-ray diffraction

# **Introduction**



# 1. Introduction

## 1.1 Plastic Waste, Recycling, and Sustainable Solutions

### 1.1.1 Plastics Production

Although the mass production of plastics started only in the 1950s, it has rapidly become a critical sector of the global economy, significantly transforming many aspects of our lives and society. Plastics are now an essential component of everyday items such as food packaging, disposable medical equipment, and electronics. The global production of plastics has surged from 2 million tons in 1950 to 460 million tons in 2021, and a total of 10 billion tons was produced between 1950 and 2021.<sup>1-3</sup> Plastics are expected to reach 15 billion tons by 2035 accounting for 20% of global petroleum consumption and 15% of the annual carbon budget as defined by the Paris Climate agreement.<sup>3,4</sup>

With the surge of plastics production and as a result of poor global waste management, 79% of the total of plastics produced as of 2015 is accumulated in landfills and has leaked into the natural environment, while only around 9% of plastic is recycled and 12% incinerated.<sup>1</sup> Perhaps the most prominent showcase of the plastic waste crisis is the *Great Pacific Garbage Patch*,<sup>5</sup> an island of mostly plastic debris that continues to rapidly grow and has meanwhile reached 1.6 million km<sup>2</sup>, almost three times the surface area of Ukraine. Half-lives of plastics in the environment are very long and strongly depend on various conditions, such as temperature, microbial loading, UV-irradiation, size and shape of plastics which further complicates the understanding of plastics degradation byproducts, rates, and pathways in the natural environment.<sup>6,7</sup> For example, although polylactic acid bottle (PLA) degrade 20 times faster than high-density polyethylene bottle (HDPE) on land, the two polymers have similar degradation half-lives in the marine environment which is estimated to be around 58 years.<sup>6</sup> In addition, there is an associated problem of plastic microparticles polluting the entire planet. These particles are now even found in plankton in the Arctic Ocean and have contaminated the entire food chain. The consequences of this pollution for environmental and human health are currently unknown.<sup>8</sup> Therefore, the plastic waste crisis is one of the most pressing issues that mankind needs to address. In fact, plastics production and pollution have been suggested as potential markers for the start of a new geological era dominated by human activity, the *Anthropocene*.<sup>9</sup> Similar to how fossils indicate when different life-forms emerged, preserved plastics may once serve as a geological record of humanity's ascent to global dominance.

### 1.1.2 *Plastics Recycling*

In an effort to address the plastic waste crisis, the US Environmental Protection Agency (EPA) has devised a four-level strategy. The first level involves waste reduction, which includes reuse. The second level is recycling, including composting. The third level is combustion with energy recovery, and the fourth level is disposal through landfill. Plastics recycling according to the second and third level of that strategy can be categorized into four main types: closed-loop recycling (primary recycling), mechanical recycling (secondary recycling), chemical recycling (tertiary recycling), and thermal recycling by incineration with energy recovery (quaternary recycling).<sup>10</sup>

1. Primary (closed-loop) recycling involves reprocessing a plastic to produce a product that is used for the same purpose as the original plastic. This method is only applicable to near-pristine waste, such as process scrap or post-consumer materials of known origin. The production of plastic bottles from blends of recycled PET (rPET) and virgin PET is an excellent example of primary recycling. However, only 2% of plastics are currently recovered for primary recycling.<sup>11</sup> Additionally, most reclaimed post-consumer waste (PCW) is too contaminated for primary recycling and has to be addressed differently.
2. Secondary (mechanical) recycling involves using the material for purposes other than the ones it was originally manufactured for. This type of recycling includes cleaning, shredding, melting, and remolding of the polymer, which is often blended with virgin plastic of the same type to produce a material with suitable properties for manufacturing. The products resulting from secondary recycling are usually of lower value, which is why this type of recycling is often referred to as 'downgrading' or 'down-cycling'.<sup>11</sup>
3. Tertiary (chemical) recycling of plastics involves using a chemical reaction to recover plastic components. For instance, the catalytic thermolysis of polyolefins is used to produce waxes, oils, lubricants, and fuels. Chemical recycling to monomer (CRM), in particular, is a desirable method because it can selectively convert plastics into their own starting materials by complete depolymerization, which results in no loss of properties in the reproduced polymers. However, polymerization of most commonly used polymers is so exergonic that CRM of most polymers requires high energy inputs, making the process less favorable than mechanical recycling.<sup>12,13</sup>

4. Thermal recycling aims to recover energy in the form of heat from plastics. However, in addition to the environmental impact of greenhouse gases and pollutants generated, the energy produced by incinerating plastics is significantly less than the energy saved through recycling.<sup>11</sup>

Large PCW mechanical recycling streams only exist, and only in some countries, for PE, PP, and (only *bottle-grade*) PET. Chemical recycling to monomer of PWC is currently impossible due to the high energy inputs required for depolymerization reaction of typical commodity polymers. Recycling of plastic packaging materials is further complicated by prevalence of complex, multi-material, and multi-layer assemblies that consist of different types of polymers. These assemblies require efficient and precise separation technologies to effectively convert heterogeneous plastic waste into high-quality feedstocks.<sup>11</sup> As a result, only 14% of plastic is recycled and 14% incinerated, the remainder is accumulated in landfill or leaks into the environment.<sup>14</sup> Addressing the complex issue of plastics waste requires a multifaceted approach, as there is no single best strategy.

One promising solution is the use of chemical recycling to monomer (CRM). CRM is not a viable option for commonly used commodity polymers like PE, PP, or PS, which are extensively employed in packaging, due to their highly exergonic polymerizations.<sup>12,15</sup> On the other hand, heterocyclic monomers that can undergo ring-opening polymerization (ROP) offer better opportunities for CRM because the enthalpy and entropy of polymerization are much smaller, and there is a clear and selective depolymerization pathway by ring-closing depolymerization (RCD).<sup>12,16</sup> Seven-membered to eleven-membered rings, as well as five-membered and six-membered rings with structural characteristics that increase polymerization enthalpy, are appealing options due to the energetic considerations involved.<sup>12</sup> In addition to CRM, other aspects of an ideal polymer recycling system include the use of bio-sourced and/or biodegradable materials which can complement efforts towards a circular plastics economy. Bio-sourced plastics, especially those derived from renewable feedstock of second or third generation, have a favorable life cycle assessment (LCA) as they help to save fossil fuel resources and reduce carbon footprint.<sup>17</sup> Biodegradability, while not a universal solution, is important in providing additional end-of-life options such as composting and in mitigating problems associated with the inevitable polymer leakage into the environment.<sup>18</sup> Min et al. have ranked polymers for their tendency to undergo biodegradation, decreasing in the order of polyesters > polyamides > polyolefins.<sup>19</sup> Looking at it from this perspective, biodegradable polyesters produced through the ring-opening polymerization (ROP) of monomers sourced from renewable resources are a promising class of materials for a circular plastics



economy. For example, the exclusive production of the  $\epsilon$ -caprolactone monomer can be achieved by RCD from poly( $\epsilon$ -caprolactone) (PCL).<sup>12,20</sup> Another promising example is polylactide, also known as polylactic acid (PLA), although it is susceptible to elimination to yield acrylic acid, it can be hydrolyzed to lactic acid and resubmitted to the step-growth process to obtain PLA oligomers that are subsequently selectively depolymerized to obtain lactides, the heterocyclic monomers to produce PLA by ROP (see below).<sup>12</sup>

## 1.2 PLA and PCL as Examples of Aliphatic Sustainable Polyester Materials

### 1.2.1 Polylactide

Among aliphatic polyesters, PLA is one of the most promising bio-sourced and biodegradable polymers for replacing some of the commodity plastics. The synthesis was first described by Carothers *et al.*<sup>21</sup> in 1932, followed by a patent from DuPont in 1954.<sup>22</sup> Since then, the production of PLA has continuously risen, reaching 0.3 million tons in 2019, which represents 24% of the global production capacity of biodegradable polymers.<sup>23</sup> PLA is produced from lactic acid, mainly obtained through but not limited to the fermentation of starch derived from sugarcane and corn. Due to the chirality of the  $\alpha$  carbon, L- and D-isomers of lactic acid exist and can be produced by bacteria; however, the L-isomer is more predominantly produced.<sup>24,25</sup> Polymerization of the L- and D-isomers results in the formation of stereoregular poly-L-lactic acid (PLLA) and poly-D-lactic acid (PDLA), respectively, and atactic poly-DL-lactic acid (PDLLA) in the case of a racemic mixture of the isomers. However, high molecular weight PLA ( $M_n > 60'000$ ),<sup>26</sup> which has significant industrial value, cannot be obtained by the direct polycondensation of lactic acid due to the incomplete condensation reaction that yields only PLA oligomers, as described by Carothers. There are three main pathways to obtain high molecular weight PLA: (i) chain coupling of the oligomers obtained by the direct polycondensation of lactic acid; (ii) polycondensation of lactic acid coupled with continuous removal of water by azeotropic distillation; and (iii) ring-opening polymerization of lactides obtained from the depolymerization of PLA oligomers obtained from lactic acid.<sup>10</sup> An analysis of the carbon footprint of each step in PLA production (Figure 1) showed that due to the CO<sub>2</sub> uptake by plants from the atmosphere, the gross greenhouse gas emission of PLA is 0.62 kg of CO<sub>2</sub> per kilogram of polymer, as reported by NatureWorks and confirmed by Boren *et al.*<sup>27</sup>

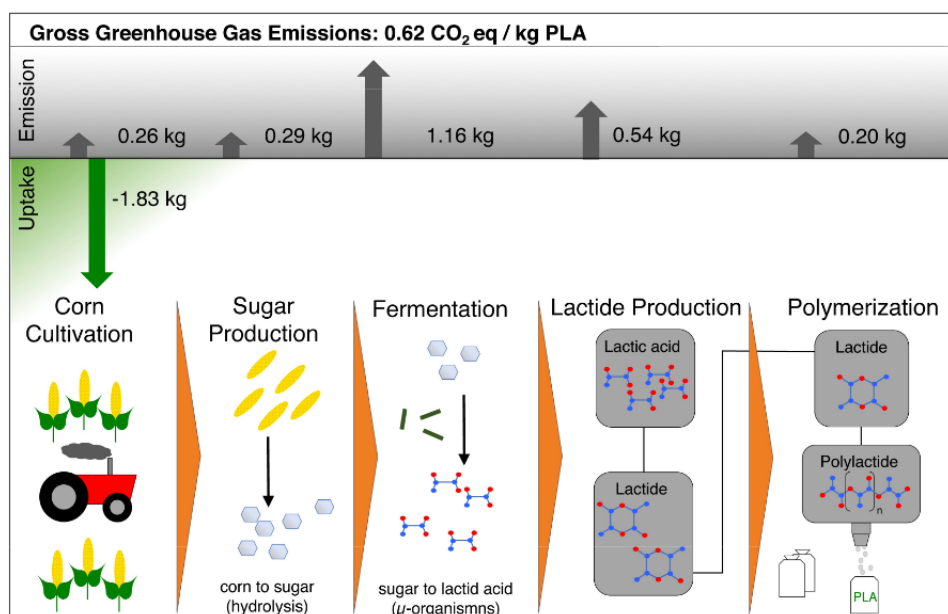


**Figure 1.** Carbon footprint for each step of PLA production. Reproduced with permission from reference 24.

There are several scenarios for the end-of-life of PLA, including reuse, chemical or mechanical recycling, composting, landfill, and incineration. The most interesting option is chemical recycling to monomer, during which PLA can be hydrolyzed to lactic acid and then used for the production of new PLA.<sup>6,28</sup> However, since plastic leakage into the environment is inevitable, it is equally advantageous that PLA can degrade through hydrolysis (Figure 2), thermal-oxidative, or photo-oxidative mechanisms in the natural environment.<sup>10</sup> Thermal degradation of PLA can also occur, but only at temperatures much higher than those found in the natural environment ( $> 200\text{ }^{\circ}\text{C}$ ).<sup>29</sup> Slow hydrolysis at temperatures  $> 30\text{ }^{\circ}\text{C}$  initially takes place in amorphous regions within the polymer and can be accelerated by acidic or basic media.<sup>10</sup> However, hydrolysis reactions are unlikely to occur in marine environments where the temperature rarely reaches  $30\text{ }^{\circ}\text{C}$ . Instead, a photo-oxidative mechanism takes place due to the absorption of UV irradiation by the carbonyl group.<sup>6,30</sup> Depending on the chirality of the repeating unit, stereoregular poly-L-lactic acid (PLLA), poly-D-lactic acid (PDLA), and atactic poly-DL-lactic acid (PDLLA) exist. While the latter is amorphous ( $T_g = 60\text{ }^{\circ}\text{C}$ ), the stereoregular variant is a semicrystalline polymer capable of crystallization in four different forms termed  $\alpha$ ,  $\delta$  (or  $\alpha'$ ),  $\beta$ , and  $\gamma$  modifications. The most common  $\alpha$  modification can be obtained from the crystallization from the melt or solution and has a melting temperature of  $T_m(\alpha) = 180\text{ }^{\circ}\text{C}$ . It features an orthorhombic unit cell ( $a = 10.68\text{ \AA}$ ,  $b = 6.17\text{ \AA}$ , and  $c = 28.86\text{ \AA}$ ), in which the polymer assumes a 10/3 helical chain conformation (Table 1).

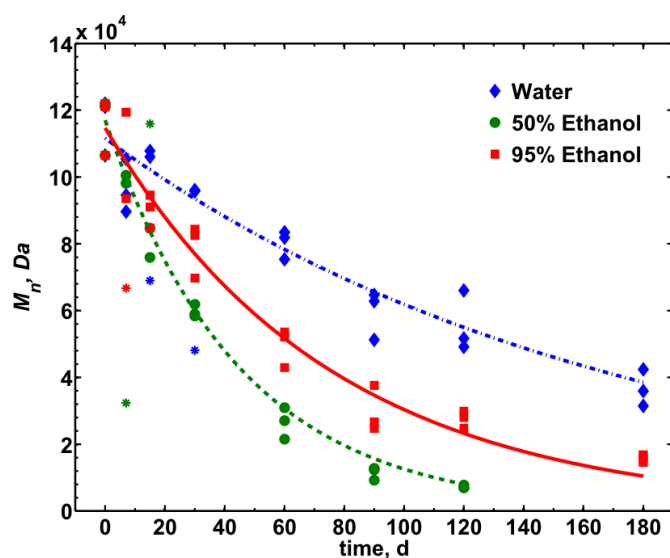


**Figure 2.** Degradation of PLA in aqueous solutions. Number-average molecular weight  $M_n$  as a function of time during hydrolytic degradation of PLA film immersed in water (blue), 50% ethanol (green) and 95% ethanol at 40 °C. Reproduced with permission from reference 31.

The  $\delta$  modification is obtained during rapid cooling or on cold-crystallization of quenched specimens between 100 °C and 120 °C, and was initially believed to be a disordered modification of  $\alpha$  form, hence it was historically called  $\alpha'$ . Although the  $\delta$  modification includes two conformationally disordered 10/3 helices and has an orthorhombic unit cell ( $a = 10.80 \text{ \AA}$ ,  $b = 6.20 \text{ \AA}$ , and  $c = 28.80 \text{ \AA}$ ), Wasanasuk and Tashiro<sup>32</sup> showed that positions and relative intensities of the observed Bragg reflections were different from those observed in the  $\alpha$  form, which suggests it to be an independent crystalline form. Eling *et al.*<sup>33</sup> first reported PLA in the  $\beta$  form in 1982, which was obtained by stretching PLA  $\alpha$  crystals at high temperatures. The  $\beta$  modification has a  $T_m(\beta) = 175 \text{ °C}$  and is characterized by an orthorhombic unit cell in which the polymer adopts a 3/1 helical conformation.<sup>34</sup> It was reported that PLLA fibers crystallized in the frustrated  $\beta$ -form might possess higher impact toughness due to facilitated chain motion of the polymer chains compared with the usual  $\alpha$  form.<sup>35-37</sup> However, research on the mechanical properties of the  $\beta$  modification of PLA is scarce. The  $\gamma$  modification is even less studied and was obtained by B. Lotz *et al.* in 2000 by epitaxial growth on a hexamethylbenzene substrate.<sup>38</sup>

Stereopurity can significantly impact the melting temperature and crystallinity of the resulting crystalline structure. For instance, a 1% increase in D-isomer content in PLLA results in approximately a 5 °C reduction in the melting temperature.<sup>39,40</sup> Additionally, as the amount of D-isomer increases, crystallinity decreases substantially, such that at 10-12 mol%, the material becomes practically amorphous.<sup>39</sup> Nevertheless, due to incomplete chain disentanglement during crystallization, 100%

crystallinity cannot be reached even with stereopure PLA, and amorphous regions exist between crystalline domains. The unperturbed crystallization of PLLA and PDLA hence results in lamellar domains, which radiate from the points of crystal nucleation to form spherulites, whose size may vary significantly depending on the cooling conditions. Additionally, there is evidence for a rigid amorphous fraction (RAF) or mesophase constituted by chain segments whose mobility is limited by their proximity to the crystalline domains (Figure 3a). It was hypothesized that the low RAF in PLLA compared with PET, and the consequent lack of stress transfer from the amorphous to crystalline domains, are among the reasons for the brittle behavior of semicrystalline PLLA materials (Figure 3b).<sup>41-43</sup>

**Table 2** Unit cell parameters of PLA crystals. Reproduced with permission from reference 44.

Crystal Form	Crystal System	Cell Parameters					
		a / nm	b / nm	c / nm	$\alpha / ^\circ$	$\beta / ^\circ$	$\gamma / ^\circ$
$\alpha$	Orthorombic	1.05	0.61	2.88	90	90	90
$\alpha$	Pseudo-Orthorombic	1.07	0.645	2.78	90	90	90
$\beta$	Orthorombic	1.031	1.821	0.90	90	90	90
$\beta$	Trigonal	1.052	1.052	0.88	90	90	90
$\gamma$	Orthorombic	0.995	0.625	0.88	90	90	90
scPLLA	Triclinic	0.916	0.916	0.87	109	109	110
scPLLA	Triclinic	1.498	1.498	0.87	90	90	120

PLA obtained via standard processing conditions possesses the stiffness and tensile strength of PET but a comparably low elongation at break, which significantly decreases toughness and limits widespread application (Table 2). Recently, Wang *et al.* indicated that there should be a high enough entanglement density for amorphous PLA to be ductile and that brittle failure was caused by rapid physical aging (Figures 4a,b).<sup>42</sup> Since melt stretching of PLA is difficult due to its inherently low melt strength, the authors prepared quenched amorphous PLLA (aPLLA) and performed film stretching immediately above  $T_g$ , i.e., below the onset temperature for cold crystallization. The obtained materials showed ductile behavior even after ageing for long times, which was attributed to mechanical rejuvenation effect that facilitated segmental motion and afforded materials yielding. Other recent studies showed that facilitated segmental motion can also be achieved by chain rearrangement from *gt* conformers of the C(O)-O-C bonds in the polymer backbone to higher energy *gg* conformers during the stretching of the materials, resulting in an elongation at break of about 200%.<sup>44-46</sup> Additionally, the alignment of PLA chains during orientation led to facilitated crystallization during stretching, so that PLLA exhibited 30% crystallinity at 100% elongation, which considerably improved the heat resistance of the obtained material (Figure 4c).<sup>44,47</sup>

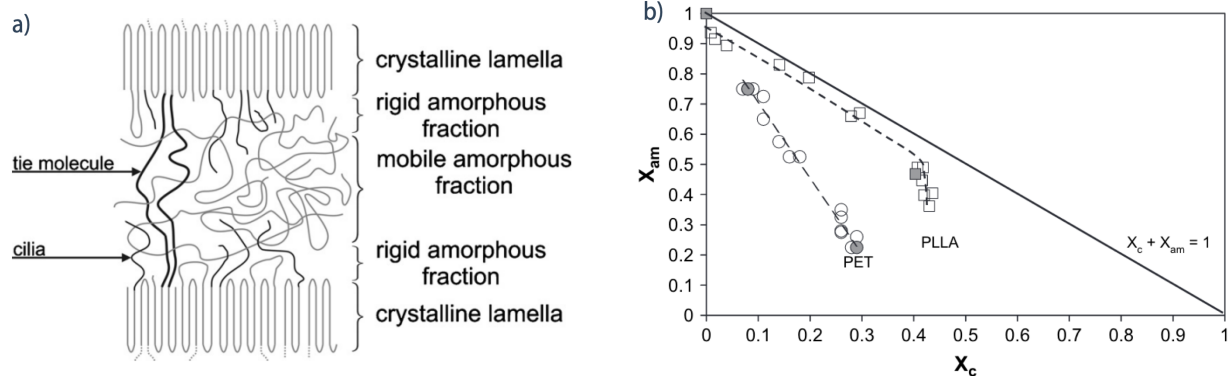


**Figure 3.** Schematic structures of crystalline domains, as well as mobile amorphous and rigid amorphous fractions in semicrystalline polymers. *a)* Complex phase structure of semicrystalline polymers, and *b)* plot of the mobile amorphous fraction vs. crystallinity for PET and PLA, demonstrating deviations from a linear dependence and suggesting the presence of the RAF as a third phase. Reproduced with permission from reference 41 and 44.

**Table 1.** Properties of PLLA, PS, and PET. Reproduced with permission from reference 49.

	PLLA	PS	PET
density, kg/m <sup>3</sup>	1.26	1.05	1.40
tensile strength (MPa)	59	45	57
elastic modulus (GPa)	3.8	3.2	2.8 – 4.1
elongation at break	4 – 7	3	300
notched izod (J/m)	26	21	59
heat deflection (°C)	55	75	67

Obtaining PLLA materials with a sufficiently high degree of crystallinity to retain a good heat resistance above the glass transition is challenging due to the low crystallization rate of the homopolymer at the high cooling rates imposed by industrial processing. Adding a nucleating agent that lowers the surface energy penalty during the formation of a polymer nucleus can significantly accelerate polymer crystallization. For example, the melting temperature,  $T_m$ , of PLLA can be tuned between 120 °C and the thermodynamic melting point of around 200 °C depending on the D-lactide content, molecular weight, and crystallization conditions.<sup>39,40,50,51</sup> Blending 0.1 wt% of high-melting-point PLLA (hPLLA,  $T_m = 187$  °C) with a standard commercial PLLA grade (e.g., NatureWorks LLC, trade name 4032D,  $T_m = 169$  °C) led to an increase in crystallization temperature of the latter from 105 to 141 °C, which was attributed to self-nucleation effect.<sup>40</sup>

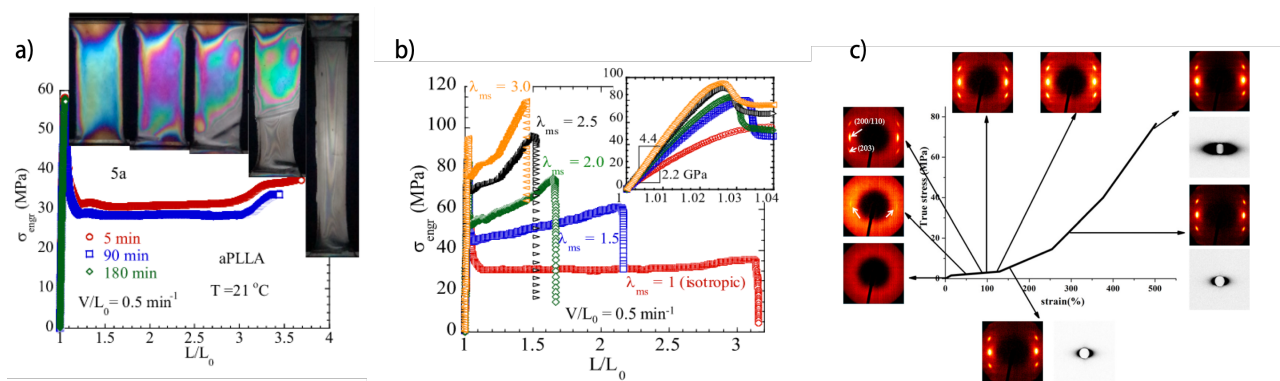


**Figure 4.** Mechanical properties of PLA materials. *a)* Engineering stress vs. draw ratio for quenched amorphous aPLLA after varying amounts of storage time that results in different degrees of physical aging. *b)* Engineering stress vs. draw ratio,  $\lambda_{ms}$ , from uniaxial drawing of melt-stretched aPLLA at room temperature; the inset shows that the Young's modulus increases markedly increased with  $\lambda_{ms}$ , from 2.2 GPa for the isotropic aPLLA to 4.4 at  $\lambda_{ms} = 3$ . *c)* The true stress-strain curve and 2D-WAXS and SAXS patterns collected at different applied strains during uniaxial tensile deformation of amorphous PLA; the deformation direction was vertical (strain rate:  $0.2 \text{ s}^{-1}$ ). Reproduced and adapted with permission from references 42 and 50.

The formation of PLA stereocomplexes (scPLA) between two pure stereoisomers PLLA and PDLA was first observed by Ikada *et al.*<sup>52</sup> in 1987 and reported to result in a  $T_m = 230 \text{ }^\circ\text{C}$  for a 1:1 blend, which is about  $50 \text{ }^\circ\text{C}$  higher than the  $T_m$  of the homopolymers (Figure 5).<sup>53,54</sup> The influence of the molecular weight, blending ratio, and stereopurity on the formation and properties of the stereocomplexes are well-documented.<sup>55-57</sup> For example, a material obtained by mixing PLLA with 0.5 wt% PDLA has a  $T_m = 215 \text{ }^\circ\text{C}$ , and a crystallization temperature increased to  $T_c = 130 \text{ }^\circ\text{C}$  by providing nucleating sites.<sup>56</sup> Additionally, scPLA crystallites act as physical crosslinks in the polymer melt and thus strongly increase melt strength.<sup>58-60</sup> However, the preparation of scPLA materials by melt mixing is not possible due to the required processing temperatures above  $230 \text{ }^\circ\text{C}$ , which already induces significant depolymerization. Specimens of scPLA therefore have to be processed from solution, which limits their industrial applicability.<sup>61,62</sup> Moreover, while there are efforts to develop more efficient and sustainable processes for the production of D,D-lactide, its availability has so far remained limited. This presents a challenge for the widespread industrial application of scPLA-based materials.<sup>63</sup>

In summary, the various advantages of PLA, such as its scalable production from renewable resources, its suitability for chemical recycling, its biodegradability in case of leakage to the natural environment, its glass transition above room temperature and high melting temperature, as well as high stiffness and strength, make it one of the most promising sustainable polymers to replace petroleum-based plastics. Moreover, the versatility in controlling the ratio of stereoisomers, molecular weight, and end-group functionalization allows for fine control of crystallinity, melting temperature, and crystal morphology.

However, its shortcomings such as its low toughness and difficulties in processing caused by the low crystallization rate and comparably poor melt strength must be addressed to broaden the application spectrum of PLA-based materials.

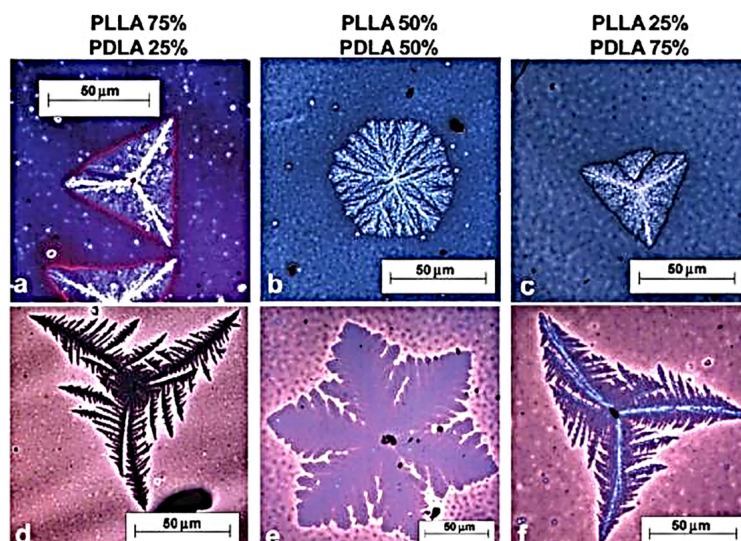


**Figure 5.** Optical microscopy micrographs of the PLLA and PDLA stereocomplex crystals at various concentrations obtained at 200 °C. Reproduced with permission from reference 54.

### 1.2.2 Poly( $\epsilon$ -caprolactone)

PCL is prepared by the ring opening polymerization (ROP) of the cyclic monomer  $\epsilon$ -caprolactone and was studied as early as the 1930s.<sup>64</sup> Recently, a wide range of catalysts for the ROP of  $\epsilon$ -caprolactone has been reviewed.<sup>65</sup> Catalysts such as stannous octoate are used to catalyze the polymerization, and low molecular weight alcohols can be used to control the molecular weight of the polymer.<sup>66</sup> Although  $\epsilon$ -caprolactone is currently derived from petroleum, it can be obtained from renewable biological resources. For example,  $\epsilon$ -caprolactone has been obtained by the catalytic reduction of 1,6-hexanediol derived from bio-sourced 5-hydroxymethylfurfural.<sup>67</sup> Another method involves synthesizing 4-methyl caprolactone from biomass, such as lignin, which requires more steps and leads to the formation of methylated poly( $\epsilon$ -caprolactone).<sup>68</sup>

The degradation of PCL can take anywhere from several months to several years, depending on factors such as the molecular weight, degree of crystallinity, and the specific conditions of degradation.<sup>69,70</sup> In nature, many microbes are capable of fully biodegrading PCL. PCL degradation is accelerated by the carboxylic acids that are released during hydrolysis,<sup>71</sup> as well as by enzymes,<sup>72</sup> which can catalyze the process and result in faster decomposition. The ring-closing depolymerization (RCD) of PCL has been

reported in 1976, and it has been shown to exhibit a high level of selectivity for the  $\epsilon$ -caprolactone monomer.<sup>12,73</sup> When bulk PCL containing residual Zn polymerization catalyst is subjected to temperatures of 250-300 °C, it primarily produces  $\epsilon$ -caprolactone, with only a small amount of cyclic oligomers present.<sup>74</sup>

PCL is a semicrystalline aliphatic polyester with a degree of crystallinity of up to 69%. The polymer crystallizes in an orthorhombic unit cell with lattice constants of  $a = 7.496 \text{ \AA}$ ,  $b = 4.974 \text{ \AA}$ , and  $c = 17.297 \text{ \AA}$ , with  $c$  parallel to the chain axis.<sup>75</sup> PCL is a biocompatible and FDA approved polymer<sup>76</sup> and thus is widely applied in biomedical applications such as scaffolds in tissue engineering, implants and sutures and in long-term drug delivery.<sup>77-79</sup> Due to its glass transition temperature of  $T_g = -60 \text{ °C}$  and a melting temperature of  $T_m = 60 \text{ °C}$ , PCL has comparatively poor thermal stability, which severely limits its applications. PCL is known to be a highly ductile material with an elongation at break of up to 1000%, a Young's modulus of approximately 200 MPa, and a yield strength and ultimate strength of 15 MPa and 40 MPa, respectively.<sup>65,80</sup> However, the mechanical properties of PCL can be drastically altered, for instance by melt and room temperature drawing in the case of PCL fibers. Recently, Selli *et al.* showed that PCL fibers can achieve yield and ultimate strengths of 300 MPa and 450 MPa, respectively, with a concomitant decrease in elongation at break to 70%.<sup>77,81</sup>

In summary, despite the many advantages of PCL, such as its high ductility, its suitability for chemical recycling to the monomer, its biodegradability and biocompatibility, it is not broadly used in engineering or commodity applications, such as packaging, mostly due its insufficient thermal stability and its poor processability because of its very low melt strength.

### 1.2.3 Properties of Aliphatic Polyesters

Multiple polymer structural features such as crystallinity, polymorphism, chain orientation and phase separation behavior can be significantly impacted during processing via processing parameters, such as cooling rates, temperature gradients, shear velocities, or extensional strain rates. A prominent example is polyethylene (PE), whose microstructure can be varied from spherulitic to shish-kebab to fully extended-chain structures without changing its chemical composition and chain architecture, using processes such as gas-assisted foaming, extrusion co-extension, fiber spinning or gel spinning. These different microstructures result in materials with up to four orders of magnitude differences in Young's



modulus, from  $E = 0.05$  GPa to over 200 GPa. Having such a wide range of properties allows one to use the different PE grades in a broad variety of applications.<sup>82</sup>

By contrast, the advanced processing of aliphatic polyesters like polyhydroxyalkanoates (PHA), polybutylene succinate (PBS), PCL and PLA is challenging due to the typically poor intrinsic properties of polymer melts. Firstly, there is often a significant reduction in molecular weight during processing due to hydrolysis initiated by residual water, unzipping reactions due to the depolymerization temperature being too close to the melting temperature, random main-chain scission, and intramolecular and intermolecular transesterification.<sup>10,83–87</sup> Secondly, many polyesters have an inherently lower melt strength compared to polyolefins, which results not only in melt sagging but also low degrees of chain orientation during melt shear.<sup>85,88,89</sup> Thirdly, polyesters often exhibit low homogeneous nucleation rates, resulting in incomplete crystallization during processing and thus requiring an additional annealing step.<sup>90–92</sup>

These obstacles not only impede the processing of the polyesters but also contribute to their high final cost, both of which limit their applications. To address these shortcomings, the following strategies have been attempted: an increase in molecular weight and control over molecular weight distribution; altering chain architectures (e.g., using of chain extenders and branching); dynamic covalent networks and vitrimers; additives (nucleating agents, plasticizers); polymer blends and copolymers and supramolecular networks.

#### *1.2.4 Effects of Molecular Weight and Chain Architecture*

Studies based on PE and PP have shown that a robust entanglement network can significantly increase melt elasticity of linear polymers as the molecular weight increases.<sup>93</sup> An extreme example is ultrahigh molecular weight PE (UHMWPE) with an average number molecular weight well in excess of  $M_n = 1'000'000$  g/mol, which shows rubbery behavior up to its degradation temperature. Broad or even bimodal molecular weight distributions can also show a pronounced strain hardening behavior due the presence of high molar mass fractions thus improving materials processability.<sup>94</sup> Moreover, a broader molecular weight distribution was reported to increase nucleation density of PP,<sup>95,96</sup> probably due to the higher flexibility of the low molecular weight fractions that form nuclei and hence provide a growth front for higher molecular weight fraction. A possible problem of such materials is inhomogeneity caused by phase-separation of high- and low-viscosity polymer fractions, which can lead to melt fracture and significant deterioration of the mechanical properties.<sup>94</sup> Moreover, PE and PP have an entanglement

molecular weight of  $M_e = 1'500$  and  $3'500$  g/mol,<sup>80</sup> respectively, and are thus considerably entangled at molar masses used in typical commercial grades with a molecular weight of  $M_n = 200'000$ – $500'000$  g/mol.

Although high molecular weight aliphatic polyesters can be synthesized in precisely controlled laboratory conditions,<sup>97</sup> mass production is typically limited to molecular weights of up to  $M_n = 100'000$ – $150'000$ . Additionally, aliphatic polyesters often have 3–7 times higher entanglement molecular weights, on the order of  $M_e = 5'000$ – $12'000$  g/mol, which makes these polymers much less entangled compared to the polyolefins and significantly limits not only their melt processability but also their room temperature behavior.<sup>98</sup>

Another method of improving melt processability is the introduction of branching to the polymer backbone, which can be accomplished with a variety of methods, including ROP with multifunctional monomers, functional group polycondensation, chain extension, radical-induced reactions, and dynamic vulcanization.<sup>99</sup> Among different architectures, such as star-shaped, comb-shaped, and hyperbranched polymers, “linear branched” polyesters showed the most useful change in melt strength and elongation for processing.<sup>24</sup> Short, unentangled chain branches showed little to no effect on elongational viscosity and could be described by the Rouse relaxation mode without hydrodynamic or topological interactions.<sup>100,101</sup> On the other hand, long-chain branches, which are defined as branches that are longer than the entanglement molecular weight,  $M_e$ , are characterized by a change in the power law from 3.6 to 6.0 in the viscosity,  $\eta$ , vs. molecular weight dependence, due to the increased entanglement constraints.<sup>101</sup> The effect of long-chain branching on melt elasticity, polymer nucleation, and room temperature mechanical properties was studied for a variety of polyesters, such as PLA,<sup>102–104</sup> PCL,<sup>105–108</sup> and PHAs.<sup>88,109,110</sup> For example, Kontopoulou et al. introduced long-chain branching to a commercial grade of PLLA by peroxide-initiated grafting of a multifunctional coagent (triallyl trimesate, TAM) in the melt.<sup>103</sup> The authors observed not only a pronounced strain hardening behavior but also a significant increase in crystallization temperature from  $T_c = 104$  °C to up to  $133$  °C, which they attributed to the nucleation effect of branching sites (Figure 6).<sup>102</sup> Another example based on the introduction of branching to PCL by  $\gamma$ -irradiation resulted in a rubber-like behavior up to temperatures of  $200$  °C and strain hardening behavior in the melt with only an insignificant change in molecular weight from  $M_n = 90'000$  to  $120,000$  g/mol.<sup>105</sup> Furthermore, the crystallization temperature of PCL increased from  $T_c = 35$  °C to  $41$  °C in the presence of branching produced by reactive melt processing

using benzoyl peroxide.<sup>106</sup> While the introduction of branching has thus proven to be a promising approach, it increases melt viscosity over the whole temperature range, which limits processing where a high flow rate is required, such as in injection molding, and reduces the melting temperature and crystallinity, which can limit its application range.<sup>101,111</sup>

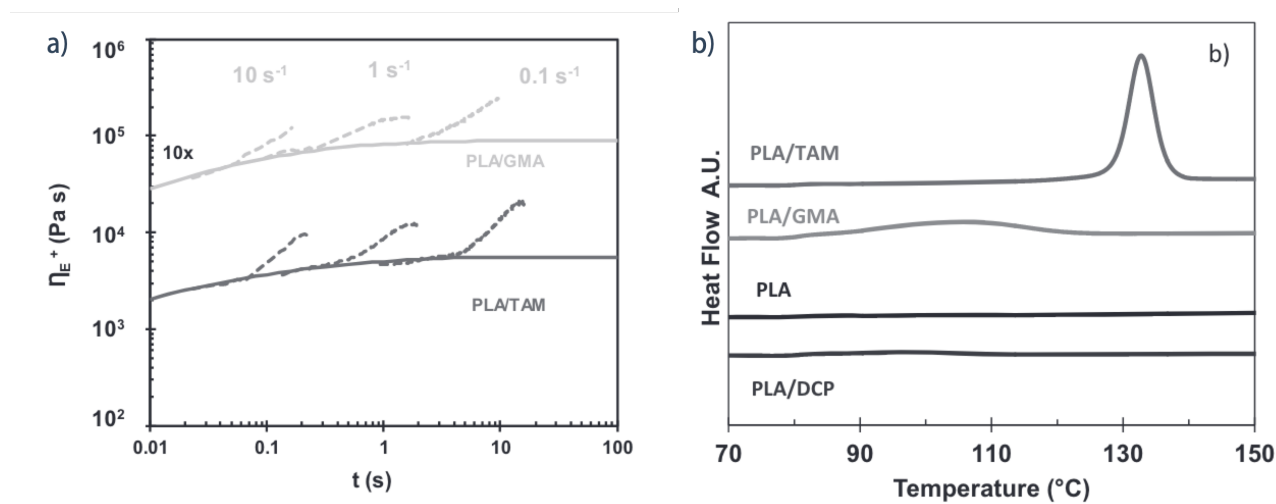


**Figure 6.** Melt behavior of branched PLA. *a)* tensile stress growth coefficient ( $\eta_E$ ) of TAM and GMA modified PLA as a function of strain rate and time at Hencky strain rates of 0.1, 1 and  $10 \text{ s}^{-1}$  at  $180 \text{ }^{\circ}\text{C}$ . *b)* DSC cooling scan at  $5 \text{ }^{\circ}\text{C}/\text{min}$ . Reproduced with permission from reference 103.

## 1.3 Polymer Mixtures

### 1.3.1 Phase Behavior of Polymer Mixtures

Paul Flory and Maurice Huggins were the first to investigate the phase behavior of polymer mixtures using lattice theory to calculate the molar Gibbs free energy of mixing,  $\Delta G_{\text{mix}} = \Delta H_{\text{mix}} - T \Delta S_{\text{mix}}$ , when a polymer is mixed with a low molecular weight solvent.<sup>112-114</sup> They established that, in ideal solutions, where mixing is athermal ( $\Delta H_{\text{mix}} = 0$ ), the entropy of mixing ( $\Delta S_{\text{mix}}$ ) is determinant, so that a positive entropy of mixing leads to a negative  $\Delta G_{\text{mix}}$ , implying the homogeneous mixture to be thermodynamically stable.<sup>114</sup> The original Flory-Huggins theory idealizes polymers as a sequence of  $m_1$  segments, each with a volume equivalent to a molecule of solvent.  $\Delta S_{\text{mix}}$  may then be estimated from the number of distinct arrangements of the polymers and solvent molecules on a lattice comprising  $N$  sites with a volume equal to that of the solvent. This approach results in

$$\Delta G_{\text{mix}} = -T\Delta S_{\text{mix}} = RT \left[ \frac{\phi_1 \ln \phi_1}{m_1} + \phi_2 \ln \phi_2 \right], \quad (1)$$

where  $\phi_1$  and  $\phi_2$  are the fractions of the polymer and solvent, respectively, and  $R$  is the universal gas constant.

In order to account for intermolecular interactions and the term  $\Delta H_{\text{mix}}$  in the free energy of mixing, as well as any entropy terms related to these interactions, Flory and Huggins introduced a contact energy term,  $\Delta G_{\text{mix}}^{\text{contact}} = (z - 2)N_1\phi_2\Delta g_{12}$ , where  $z$  represents the coordination number of the lattice parameter,  $N_1$  is the number of solvent molecules, and  $\Delta g_{12}$  is the Gibbs free energy change for the formation of a single solvent-segment contact. However, determining  $z$  and  $\Delta g_{12}$  is not straightforward, so Flory and Huggins introduced the temperature-dependent Flory-Huggins interaction parameter,  $\chi$ , defined as  $\chi = (z - 2)\Delta g_{12}/kT$ . This allows  $z$  and  $\Delta g_{12}$  to be eliminated, resulting in the Flory-Huggins equation for the molar Gibbs free energy of mixing for a polymer and a solvent: <sup>114</sup>

$$\Delta G_{\text{mix}} = -T\Delta S_{\text{mix}} = RT \left[ \frac{\phi_1 \ln \phi_1}{m_1} + \phi_2 \ln \phi_2 + \chi \phi_1 \phi_2 (1 - \phi_1) \right]. \quad (2)$$

The interaction parameter,  $\chi$ , determines the compatibility of the two components, with a larger value indicating reduced compatibility and a greater likelihood of phase separation. It therefore is of considerable importance for predicting the behavior of polymer-based mixtures, and may be influenced by various factors, including temperature, pressure, and chemical structure.<sup>115,116</sup>

Although the Flory-Huggins equation was originally formulated for binary polymer-solvent systems,<sup>112,113</sup> it was subsequently modified to describe the mixing behavior of two different polymers:

$$\Delta G_{\text{mix}} = -T\Delta S_{\text{mix}} = RT \left[ \frac{\phi_1 \ln \phi_1}{m_1} + \frac{\phi_2 \ln \phi_2}{m_2} + \chi \phi_1 \phi_2 (1 - \phi_1) \right], \quad (3)$$

There have since been numerous theoretical<sup>117-119</sup> and experimental<sup>120,121</sup> developments of the model, e.g., investigations into the temperature and concentration dependences of  $\chi$ , and its extension to block copolymers,<sup>117</sup> However, in all these refinements, materials with very different chemical compositions are expected to form immiscible mixtures because  $\Delta g_{12}$  is expected to be large, leading in turn to large positive values of  $\chi$ , which must be offset by the negative entropy of mixing  $\Delta S_{\text{mix}}$  for a homogeneous mixture to be stable. Phase separation is therefore common in polymer-polymer blends with large segment numbers  $m_1$  and  $m_2$ , because the resulting entropy change,  $\Delta S_{\text{mix}}$ , generally becomes insignificant. For  $\Delta G_{\text{mix}} = \Delta H_{\text{mix}} - T\Delta S_{\text{mix}}$  to be negative, mixing must therefore be exothermic ( $\Delta H_{\text{mix}} < 0$ ), which requires strong specific interactions between the two polymers, such as electrostatic interactions

or hydrogen bonding.<sup>122</sup> In the case of dilute solutions of small molecules in polymers,<sup>123-125</sup> the interaction parameter,  $\chi$ , may be determined using data from the melting point depression of the small molecule in the polymer, assuming an equilibrium transition.<sup>126,127</sup>

### 1.3.2 Polymer-Polymer Blends

To achieve a desired property profile, a polymer can be blended with another polymer that exhibits superior behavior in areas where the former suffers from shortcomings. However, due to the low entropy of mixing of high molecular weight polymers, the resulting blends are often immiscible and thus have poor properties due to weak interfacial adhesion between the two phases. One possible strategy to improve interfacial interactions between the two phases is adding a block copolymer that is localized at the interface and acts as a compatibilizer, which improves the adhesion of the two phases, inhibits coalescence of the dispersed phase, and can result in different blend morphologies (Figure 7).

For instance, blends of PLA with poly(butylene adipate-co-butylene terephthalate) (PBAT), poly(butylene succinate-co-butylene adipate) (PBSA), or PCL with their respective di- or tri-block copolymers have been successfully used to tune the toughness, stiffness, and processability of PLA-based materials.<sup>49,98,128-130</sup> However, the lack of control over the molecular weight and the expensive, multistep preparation of premade block copolymers limit their technological applicability.<sup>128,131</sup> To solve this problem, "A-C" diblock copolymers with a "C" block different from the two materials "A" and "B" in the blend can be used to improve their miscibility, in case "B" and "C" exhibit a high miscibility. For instance, an easily accessible PEG-PLA diblock copolymer was used to successfully increase the elongation at break of PLA/PBAT, PLA/PBSA, and PLA/PBS blends up to 296%, 195%, and 234%, respectively, compared to 30%, 16%, and 45% in the absence of the diblock copolymer.<sup>132</sup> Another way of producing block copolymers can be accomplished *in situ* by reactive mixing of two polymers with a chain extender, transesterification agent, or radical initiator. For example, the melt extrusion of PLLA and 10 wt% of PBAT blend with 0.75 wt% of a multifunctional epoxy chain extender resulted in an increase in elongation at break to 400% with a slight decrease in Young's modulus to 2.75 GPa (compared to 3.25 GPa for pristine PLA).<sup>133</sup>

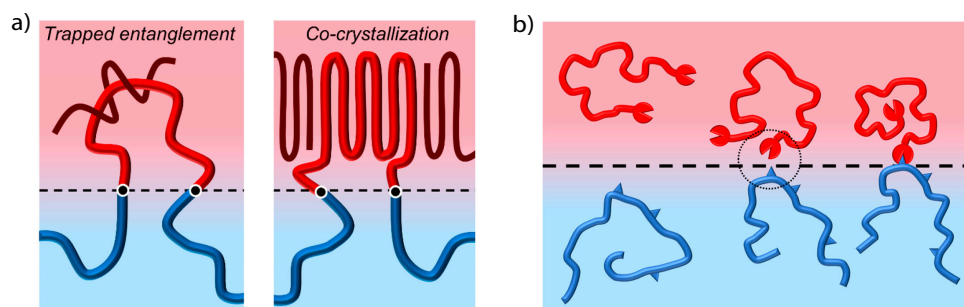


**Figure 7.** Effect of copolymers acting as compatibilizers. *a)* Examples of trapped entanglement and co-crystallization. *b)* Reactive compatibilization of polymers at the interface: a telechelic polymer reacting with a polymer with a grafted functionality. Reproduced with permission from reference 134.

### 1.3.4 Nucleating Agents

Another way to improve polymer processing properties is through the addition of nucleating agents that decrease the nucleation energy barrier by providing crystallization sites and initiating crystallization at higher temperatures. For an efficient nucleating agent, it is desirable to have the following properties: *(i)* a higher melting point than that of the polymer matrix; *(ii)* a crystal structure with some unit cell parameters similar to that of the polymer matrix; *(iii)* favorable miscibility with the matrix, resulting in a fine interfacial interaction; *(iv)* good dispersion in the polymer melt; and *(v)* no toxicity to both humans and the environment.<sup>40</sup>

The effects of classical nucleating agents used for PLLA crystallization are summarized in Table 3, but must be treated with caution due to the different molecular weights, stereopurity, and processing conditions of the PLLA specimens used in the reported studies. Among inorganic nucleating agents, talc exhibits the highest nucleating efficiency, with an up to seven-fold increase in PLLA crystallization half-times.<sup>134,135</sup> This efficiency is attributed to the epitaxy, that is, a match of unit cell parameters between PLLA crystals and talc, which is commonly used as a reference for other nucleating agents. Although clay and calcium carbonate have lower nucleation efficiencies, they are reported to offer other benefits such as an increased thermal stability and elongation at break of the resulting PLLA materials.<sup>39,98,136</sup> However, unless the percolation threshold of the dispersed additive is achieved (usually > 30 wt%), these additives act as a plasticizer, reducing polymer melt viscosity and glass transition temperature, which is detrimental in processes requiring on melt deformation.<sup>136,137</sup>

Nanosopic nucleating agents, such as carbon nanotubes, nanoclay or cellulose nanofibers, are effective nucleating agents, which, thanks to their higher specific surface area and their high aspect ratio, reach the percolation threshold at much lower concentrations and can thus be used at lower content. For

example, using carbon nanotubes as a nucleating agent results in an increase in PLLA crystallization temperatures to  $T_c = 109\text{ }^\circ\text{C}$  at a concentration of 0.08 wt%.<sup>138</sup> Moreover, carbon nanotubes reach the percolation threshold at about 3 wt%, which significantly increases polymer melt viscosity so that at a carbon nanotube contents of 7 wt%, the PLLA melts exhibit a rubber-like behavior.<sup>139-143</sup>

An advantage of organic nucleating agents is their ability to be dissolved in the polymer melt and to recrystallize into highly dispersed crystals at temperatures higher than the polymer crystallization, thus providing nucleation sites and increasing polymer crystallization rates. For example, orotic acid (Figure 8) increases the crystallization temperature of PLLA to  $T_c = 124\text{ }^\circ\text{C}$  at a concentration of 0.3 wt%. Such a strong nucleation effect was attributed to the match of the  $a$  lattice parameter of orotic acid (5,90 Å) and the  $b$  lattice parameter of PLLA (6.04 Å) which thus induced epitaxial growth of PLLA crystals.<sup>144</sup> Other classes of nucleating agents based on oxalamides,<sup>145</sup> hydrazides<sup>146</sup> and 1,3,5-benzenetricarboxylamides (BTA) (Figure 8) showed a significant nucleation of PLLA crystals (Table 3). The structure of these compounds consists of a central part that drives the self-assembly into high aspect ratio crystals and substituents (R) that are used for tuning the miscibility of the compound in the PLA melt.

**Table 3** Nucleation efficiency of various nucleating agents for PLLA.

nucleating agent	$T_c$ , °C	crystallinity, %	concentration, wt%
talc <sup>147</sup>	120	46	2
clay <sup>148</sup>	105	53	4
nanoclay <sup>149</sup>	117	39	1
carbon nanotubes <sup>138</sup>	109	35	0.08
cellulose nanofibers <sup>149</sup>	115	37	1
hydrazide ( <b>h1</b> ) <sup>146</sup>	131	50	1
oxalamide ( <b>o1</b> ) <sup>145</sup>	118	37	1
orotic acid ( <b>o2</b> ) <sup>144</sup>	124	37	0.3
<b>BTA-C6</b>	130	48	0.3
SC <sup>56</sup>	130	57	0.5
SC <sup>56</sup>	141	55	3
hPLLA <sup>40</sup>	141	42	0.5
hPLLA <sup>40</sup>	143	43	5

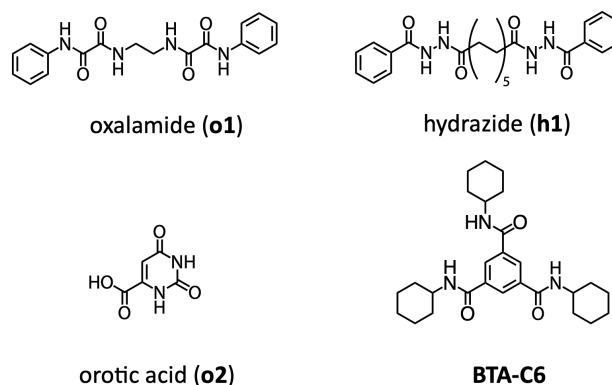


**Figure 8.** Chemical derivatives of oxalamide **o1**, hydrazide (**h1**), orotic acid (**o2**) and cyclohexyl BTA (**BTA-C6**)

BTA derivatives have received particular attention as nucleating agents due to the combination of  $\pi$ -stacking of the central benzene units and the three-fold hydrogen bonding of the amide substituents at their periphery, which enforces a helical arrangement that discourages lateral aggregation and thus provides crystals with high aspect ratio and small lateral dimensions that are well dispersed in the polymer matrix (Figure 9).<sup>150-154</sup> The chemical structure of the peripheral substituents R was found to strongly influence the nucleation efficiency of BTA derivatives. However, no correlation between the nucleation efficiency and either the *a* lattice parameter or the BTA solubility in the polymer melt was found (Figure 10).<sup>150,152,155,156</sup> *N,N,N*-tricyclohexyl benzenetricarboxylamide **BTA-C6** is considered to have the highest nucleation efficiency of all nucleating agents in PLLA and has been used to control the microstructure of PLA crystals to obtain shish-kebab-like and needle-like structures (Figure 11*a,b*).<sup>151,157</sup> Moreover, a pronounced increase in melt elasticity was observed at temperatures of up to 195 °C, which was attributed to the formation of a percolation network of BTA crystals already at a concentration of 0.3 wt% (Figure 11*c*). Furthermore, a decrease in oxygen permeability by two orders of magnitude was attributed to the formation of interlocked PLLA lamellae.

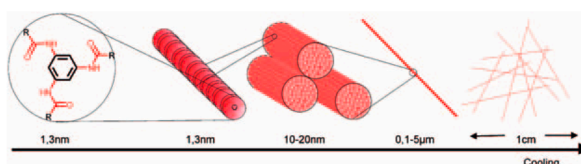


**Figure 9.** Schematic representation of the self-assembly of BTA. Reproduced with permission from reference 158.



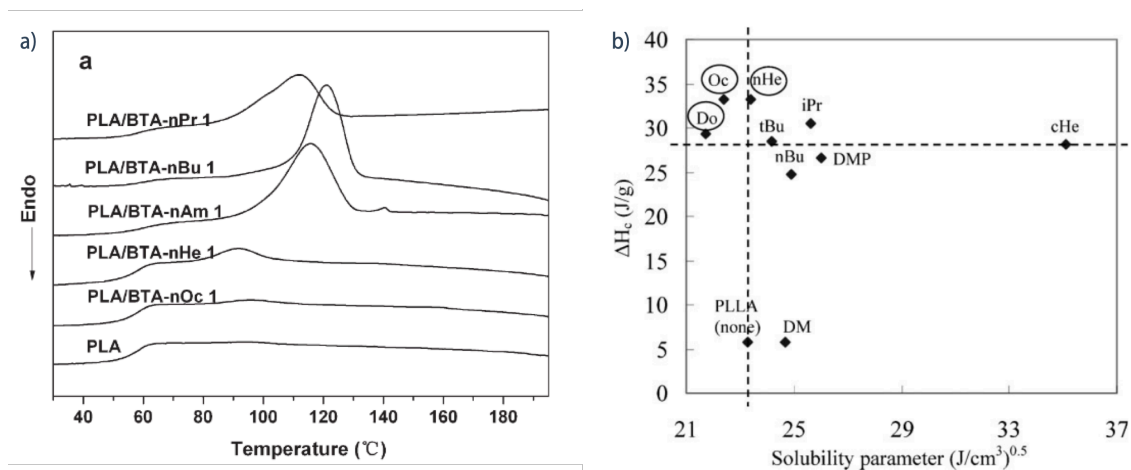


**Figure 10.** Effect of chemical structure of BTA side chains on the crystallization of the PLLA matrix. *a)* DSC cooling curves of PLLA containing various BTA derivatives obtained at cooling rate of 5 °C/min. *b)* Plot of the solubility parameter of BTA derivatives and crystallization enthalpy  $\Delta H_c$  of PLLA containing various BTA derivatives. Reproduced with permission from references 151 and 153.

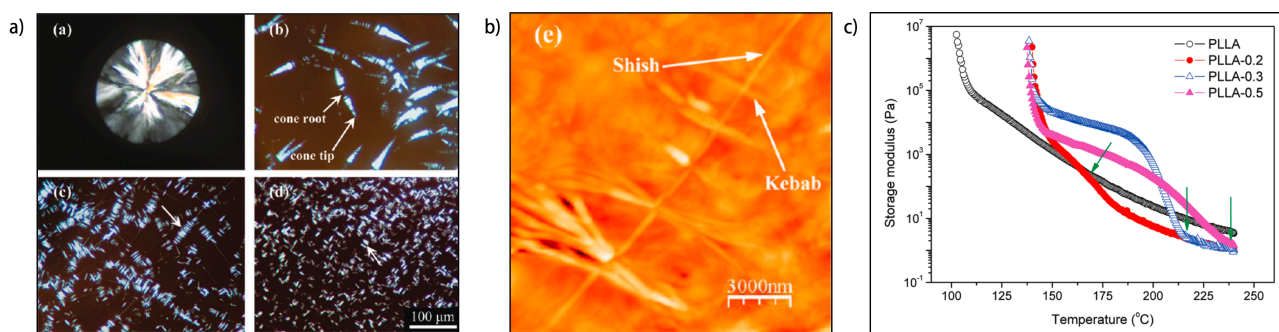


**Figure 11.** Crystallization and melt properties of PLLA. *a)* Polarized optical micrographs of the crystal morphology of PLLA with 0 wt% (top left), 0.2 wt% (top right), 0.3 wt% (bottom left) and 0.5 wt% (bottom right) of **BTA-C6**. *b)* AFM height image of PLLA with 0.2 wt% of **BTA-C6**. *c)* evolution of storage modulus with temperature during crystallization of PLLA blends with 0.2 wt%, 0.3 wt% and 0.5 wt% of **BTA-C6**. Reproduced with permission from reference 158.

## 1.4 Supramolecular Materials

Supramolecular materials are based on discrete building blocks (supramolecular motifs) that thermoreversibly assemble into defined architectures via non-covalent interactions such as hydrogen bonding interactions, metal-ligand coordination, electrostatic and van der Waals forces, or donor-acceptor interactions, which has become a widely used design strategy towards the development of novel polymer materials.<sup>159</sup> In exceptional cases, the interaction of low molecular weight compounds alone can lead to materials featuring polymer-like properties such as a tensile strength of several tens of MPa and extensibilities of up to several 100%, provided that their crystallization into brittle materials is prevented.<sup>160–162</sup> However, since the seminal work of Meijer and coworkers,<sup>163</sup> supramolecular motifs

have been predominantly integrated into numerous covalent polymer systems in order to create materials with tailored structure, dynamic behavior, properties and function.<sup>164</sup> These motifs can be conveniently introduced into covalent polymers in form of, for example, functional end groups,<sup>165</sup> internal main chain segments, or as side chains of branched, grafted or brush polymers.<sup>166</sup> Eventually, their self-assembly physically cross-links the polymer matrix, leading to versatile network structures and thermomechanical property profiles, which allows one to design and to target a broad range of different types of materials, such as thermoplastic elastomers,<sup>167-169</sup> gels,<sup>170</sup> adhesives,<sup>171,172</sup> supramolecular block copolymers,<sup>173</sup> or glassy thermoplastic materials.<sup>161,162,174</sup>

Due to the reversible nature of the underlying supramolecular interactions and an often cooperative self-assembly mechanism, the materials show sharp thermal transitions from an elastic network structure into viscous melt states.<sup>175</sup> Moreover, the dynamic nature of the employed supramolecular interactions, that is their association and dissociation kinetics even in equilibrium conditions,<sup>176</sup> gives a transient character to the network structure, thus often leading to self-healing properties,<sup>177,178</sup> shape memory effects,<sup>179</sup> or enhanced dynamic/viscous energy dissipation. As these features promise (simultaneous) improvements in processability and recyclability<sup>159,180</sup> or even self-repairing mechanisms, the supramolecular modification of covalent polymers holds therefore great promise for materials modification. Indeed, the utilization of well-controlled supramolecular interactions is considered one key element for the development of novel sustainable materials.<sup>159,181</sup> In what follows, we will focus our attention on approaches towards hydrogen-bonded supramolecular materials and their limitations.

#### *1.4.1 Monotopic Hydrogen-Bonded Supramolecular Motifs*

The prospect of high-performance polymer materials that are mechanically robust, thermostable, feature attractive melt properties, and are potentially healable has stimulated ample research on the supramolecular cross-linking of various polymer chain architectures aided by multivalent hydrogen-bonded ligands.<sup>182</sup> Perhaps the most prominent binding motif is the ureidopyrimidinone (UPy) unit, a monotopic self-complementary moiety that dimerizes via four-fold hydrogen bonding interactions. When these units are attached as end groups to a telechelic soft polymer (PDMS,  $M_n = 6'000$ ), they act as supramolecular chain extenders, resulting in strongly temperature-dependent viscosity values that are several orders of magnitude larger than those of a non-functionalized analogue.<sup>163</sup> Such properties are otherwise typical for well-entangled high molecular weight polymers and attributed to the

dimerization of the polymer end groups and the associated increased “virtual” molecular weight. Within a narrow temperature window, the materials display a significant drop in the viscosity above the dissociation temperature of the UPy dimers, above which they show classical melt flow behavior identical to the employed base polymer.<sup>183</sup>

The functionalization of multi-arm polymer chain architectures with UPy-ligands allows one to obtain supramolecular polymer network structures that display rubber-like properties over a large frequency range in oscillatory shear rheology measurements (Figure 12).<sup>163</sup> At sufficiently high temperatures or long experimental time scales, the dynamic character of the dimers becomes evident, and the materials show melt flow behavior typical for low molecular weight polymers. However, in case of too low molecular weights and therefore a comparably high UPy-concentration, the dimerization of the latter leads to formation of glassy domains.<sup>184</sup>

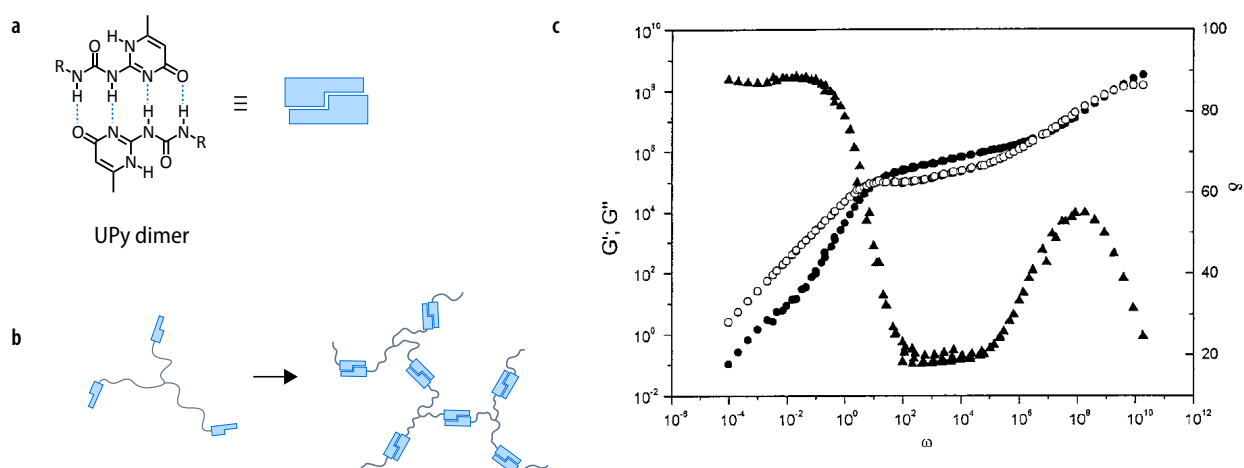


**Figure 12.** a) The end-group functionalization of a soft amorphous three-arm star polymer with ureidopyrimidone (UPy) units and their dimerization leads to b) a supramolecular network with rubber-like properties. c) Due to aggregate dynamics, the material shows a transition into a polymer melt at long experimental time scales. Reproduced with permission from reference 163.

By analogy, the end group modification with UPy units is a straightforward way to affect the melt properties of semi-crystalline polyesters. For example, the dimerization of UPy end groups of functionalized telechelic PCL ( $M_n = 2'900$  g/mol) leads to a qualitatively similar melt behavior like a corresponding non-functionalized polymer of high molar mass ( $M_n = 80'000$  g/mol).<sup>185</sup> Likewise, the disentanglement temperature of soft amorphous polyesters may be considerably increased up to the dissociation temperature of the UPy dimers. For UPy-functionalized poly( $\gamma$ -methyl- $\epsilon$ -caprolactone) (PMCL,  $M_n = 26'000$  g/mol), the associated softening as determined by oscillatory shear rheology was,

for example, up to 70 °C higher than that of its non-functionalized analogue (+40 °C vs. -30 °C), albeit close to room temperature, where the material behaved predominantly as a viscous liquid rather than an elastic solid.<sup>186</sup>

Other important materials parameters like the glass transition temperature,  $T_g$ , are usually not significantly affected by the functionalization. Only when the employed molecular weight is low, the typical drop in  $T_g$ , associated with the increased contribution of the polymer chain ends to the free volume, is prevented in supramolecularly modified telechelic polymers. For instance, the  $T_g$  of pristine PET decreases significantly below a number-average molecular weight of about 7'000 g/mol, whereas the  $T_g$  of UPy-modified PET remains constant at its typical value of  $T_g = 70$  °C.<sup>187</sup> This stabilizing effect of the UPy-modification on  $T_g$  was confirmed in polyisoprene (PI) modified with a UPy analogue<sup>188</sup> and in soft amorphous copolyesters<sup>189</sup> but seems to be important only for low molecular weight polymers.

Similarly, significant effects of UPy-modifications on the polymer crystallization may not be expected because their dissociation and association temperatures of up to  $T_d = 80$  °C remain lower than the melting and crystallization temperatures of many semicrystalline polymers. However, these aggregate structures can severely hinder the polymer crystallization and reduce the degree of crystallinity, if the employed molecular weight is too low and polymer chain mobility restricted, leading to flexible materials with comparably low storage modulus and tensile strength.<sup>190,191</sup> Nevertheless, the presence of the aggregates may promote the formation of metastable crystal structures, as shown for modified PLA, which is apparently the case, when the polymer crystallization temperature coincides with the association temperature of the UPy units.<sup>190</sup> Even though the authors did not report on the resulting room-temperature mechanical properties, one may anticipate that these may be indirectly impacted via differences in the microstructures. With few exceptions,<sup>186</sup> however, drastic effects on the room-temperature mechanical properties have not been reported, although increases in tensile strength and strain-at-break were observed for some polyesters upon UPy modification.<sup>187,189,192</sup> The effects are often marginal, and the materials essentially remain very brittle, presumably because of the low molecular weight of the employed polymer backbone (*vide infra*).

#### 1.4.2 Ditopic Hydrogen-Bonded Supramolecular Motifs

Ditopic ligands are self-complementary ligands that interact with two molecules, and the number of available binding sites for further interactions of the resulting aggregate remains the same. Ditopic ligands *per se* have a strong tendency to form one-dimensionally extended aggregate structures that

serve as crosslinks to the tethered polymer matrix into supramolecular networks. A special case is UPy units that are placed adjacent to hydrogen bonding units such as urea functions. Subsequent to the UPy dimerization, the hydrogen bonding between the urea functions results into the formation of one-dimensionally extended aggregate structures.<sup>193,194</sup> The self-assembly into such anisotropic structures, often fibrillar objects, does not only include the initial formation of nanofibrils but they further tend to laterally aggregate into larger microfibers which can form a percolation network<sup>195,196</sup> and hence result in elastic behavior in small-strain oscillatory shear rheology (Figure 13). By analogy to many organogelators, these latter structures have a typical cross-sectional dimension in the 10–100 nm range, and were also observed in corresponding telechelic PCL materials of low molecular weight ( $M_n = 3'900$  g/mol).<sup>185</sup> Similar structures are observed in case of bisurea-functionalized polymers<sup>196</sup> based on telechelic PDMS<sup>197</sup> or poly(isobutene).<sup>198</sup> These materials can be classified as thermoplastic elastomers (TPEs) in the sense that the aggregate structures represent phase-separated hard microdomains that are interconnected by the soft polymer matrix.<sup>199</sup> However, strong TPEs have not been prepared because polymers too low in molecular weight do not sufficiently entangle and are often even too brittle to be subjected to uniaxial tensile testing.

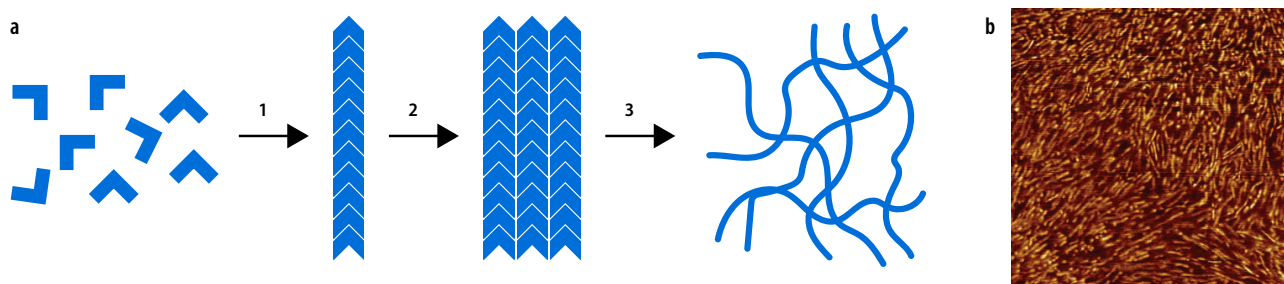


**Figure 13.** a) Typical hierarchical self-assembly process in supramolecular materials based on ditopic self-assembling motifs that (1) are able to form extended nanofibrils, which (2) further undergo lateral interactions into microfibers forming possibly (3) a percolation network. Figure reproduced with permission from reference <sup>195</sup>. b) AFM phase image (scan size: 1  $\mu\text{m}$ ) of a telechelic PCL ( $M_n = 3'900$  g/mol) showing fibrillar aggregate structures. Reproduced with permission from reference 185.

In turn, an increase in the molecular weight led to a reduced bisurea content, and the resulting materials experienced a drop in the storage modulus at temperatures far below the actual dissociation temperature of the bisurea aggregates. This example highlights a general conundrum in supramolecular polymer materials, that is the supramolecular structure formation strongly depends on the molecular weight of the employed polymer segment and becomes increasingly limited as the molecular weight is

increased. However, as will be explained below, high molecular weights are a requirement for obtaining materials with meaningful tensile properties, based on an acceptable yield strength, facilitated plastic deformation, and fracture resistance.

Another prominent ditopic supramolecular motif is the benzene-1,3,5-tricarboxamides (BTAs) unit that reliably forms one-dimensional aggregate structures based on a synergistic interplay of  $\pi$ - $\pi$  stacking between a central benzene core and three-fold hydrogen-bonding of the amide substituents, usually leading to a face-to-face stacking arrangement.<sup>200</sup> In order to accommodate the benzene rings at the van der Waals distance, all amide groups have to be rotationally displaced with respect to the stacking axis, so that a helical one-dimensional aggregate structure is typically observed (Figure 14). This helical arrangement limits the lateral interactions between the stacks, why, depending on the attached substituents, columnar mesophases are likely observed both in bulk and in solution.<sup>201</sup> BTA derivatives usually display high association and dissociation temperatures that can easily exceed 200 °C but are also characterized by a particularly pronounced dynamic behavior because of facile exchange of the building blocks along the aggregate backbone.<sup>202,203</sup>

While self-assembled BTAs are known to be effective gelators for organic or aqueous media, their use as self-assembling ligands in combination with covalent polymers has remained scarce. One reason might be that the self-assembly of BTAs seems to strongly depend on the polarity of the employed polymer matrix. Thus, BTA end groups bearing branched aliphatic side chains only properly aggregate in the apolar polymer poly(ethylene butylene), but no sign of end group association in the more polar aliphatic polyester PCL could be identified.<sup>204</sup> When attached to poly(ethylene butylene) (PEB,  $M_n = 3'500$  g/mol), the self-assembly of BTA end groups gives rise to a brittle supramolecular network that lacks entanglement, whereas incorporation of the BTA unit into a segmented PEB block copolymer yields a thermoplastic elastomer, albeit with a low Young's modulus of  $E = 3.4$  MPa,<sup>205</sup> which confirms the challenge to use the supramolecular modification of polymers as a tool towards useful engineering materials. BTAs are nevertheless interesting because of their reliable formation of extended aggregate structures which renders them highly promising for the design of supramolecular network materials.

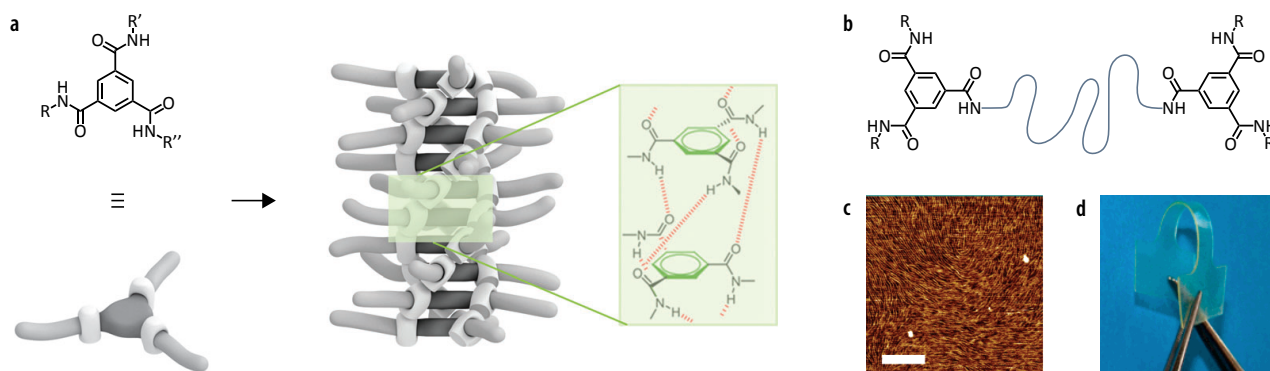


**Figure 14.** *a)* General chemical structure of the benzene-1,3,5-tricarboxamide (BTA) moiety and schematic representation of BTA self-assembly into helical one-dimensional aggregates. Figure reproduced with permission from reference <sup>200</sup>. *b)* BTA end groups of telechelic soft polymers can *c)* self-assemble into extended nanofibrillar aggregates (scale bar: 100 nm) that serve as physical cross-links for the polymer matrix. *d)* The resulting material displays elastic properties. Reproduced with permission from reference 205.

Oligopeptides are a versatile class of ditopic self-complementary self-assembling motifs, as they can be designed from common amino acids, and their binding strength and dynamic behavior can be controlled via their length. Due to their ditopic nature and the highly directional hydrogen-bonding interactions, many oligopeptides have a strong tendency to form 1D or 2D extended nanoscopic aggregates via a cooperative self-assembly mechanism. Our own group has studied mixtures of monofunctional and difunctional polymers with short,  $\beta$ -sheet-forming oligo-L-alanine end groups and demonstrated that their mechanical properties can be tailored over a wide range of target moduli, loss factors, and transition temperatures, depending on the choice and combination of the oligopeptide end groups. For example, reinforced PIB elastomers ( $M_n = 1'200$  g/mol) could be realized in this way that displayed sharp melting transitions at temperatures greater than 150 °C, combined with a high elasticity and a plateau modulus of up to  $G' \approx 5$  MPa (Figure 15). It should be noted, however, that the large strain deformation of these materials could not be investigated due to their brittle behavior in tension.

Other oligopeptides preferentially crystallize into nanofibrous crystals composed of  $\beta$ -sheet aggregates that serve as effective cross-links for soft polymers, as shown, for instance, for a tri-arm polyisobutylene (PIB,  $M_n = 30'000$  g/mol). The transition temperature can be adjusted by the length of the oligopeptide and was as high as 230 °C for a pentapeptide. The resulting material behaved as an elastic solid across a broad frequency range. However, the strain at break of this TPE remained limited to  $\epsilon_{\max} = 130\%$ , again due to the lack of entanglement of the polymer matrix.<sup>206</sup> In marked contrast,  $\beta$ -alanine trimers were grafted to the side-chains of high molecular weight PIB ( $M_w > 400'000$  g/mol), which became cross-linked by the self-assembly of the oligopeptide units into crystalline nanodomains,<sup>207</sup> whose dimensions

could be controlled by the choice of the attached substituents.<sup>208</sup> These crystals acted as a reinforcing element of the elastic network and may facilitate energy dissipation mechanisms based on the reorganization of these aggregates during deformation. As a result, TPE materials extensibilities greater than 1000% and an energy at break of up to  $W = 80 \text{ J/cm}^3$  were obtained.

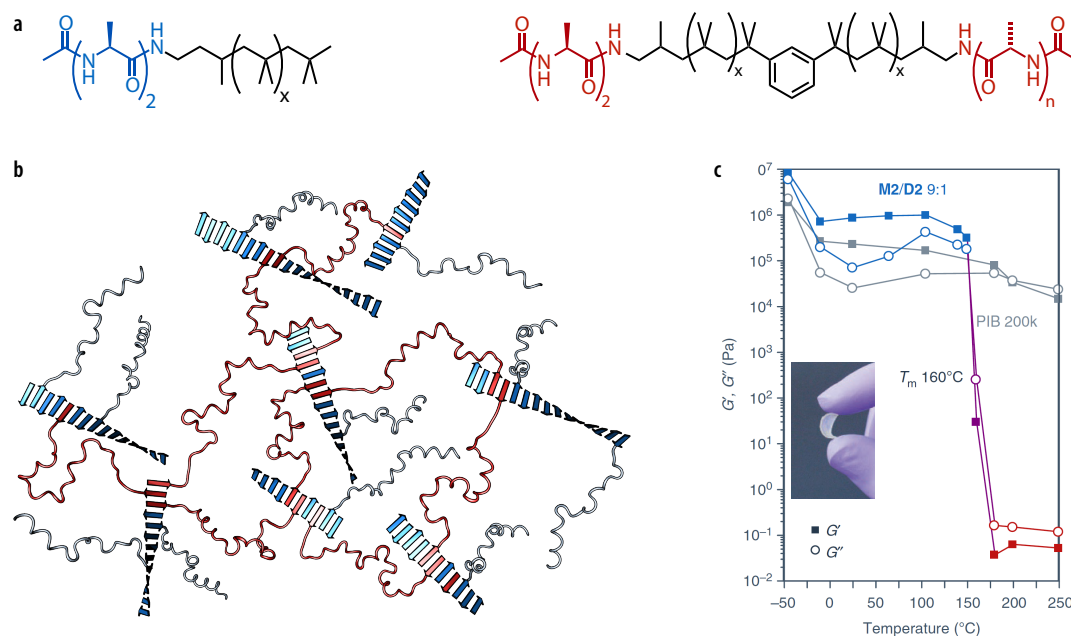


**Figure 15.** a) Chemical structure of mono- and difunctional polyisobutylene (PIB). b) Co-assembly of their end groups into  $\beta$ -sheet-like aggregates results in a supramolecular network. c) As a result, the material forms an elastic rubber-like state similar to that of high molecular weight PIB up to the dissociation temperature of the aggregates, beyond which the material sharply transitions into a low viscosity melt. Reproduced with permission from reference 176.

A similar behavior was found in high-molecular weight polyisoprene ( $M_n$  close to 1'000'000 g/mol) bearing tetra-L-alanines in the side groups that form highly dispersed  $\beta$ -sheet nanostructures. The resulting TPE showed a remarkable tensile strength (15 MPa), toughness ( $46 \text{ J/cm}^3$ ), and extensibility (ca. 900%), associated with pronounced strain hardening due to strain-induced crystallization similar to that of vulcanized natural rubber. By comparison, the non-functionalized but highly entangled base polymer did not strain-harden and displayed a very low energy at break of  $W = 1.3 \text{ J/cm}^3$ .<sup>209</sup> The dynamic reorganization of the aggregate structure during deformation is an important contribution to energy dissipation, particular in case of longer attached oligopeptides like tetra-L-alanines, although they could not fully reversibly adopt their original state within the applied experimental time scale.<sup>210</sup> However, various design parameters need to be considered for optimizing the materials performance in these truly interesting systems, such as the spacer length between the PI backbone and the self-



assembling motif or the oligopeptide length.<sup>211,212</sup> Arguably, a major limitation of this approach is the requirement of side-chains for the functionalization, which are hard to implement into many technologically relevant base polymers.

#### 1.4.3 Molecular Weight Dependence of Polymer End Group Assembly

The functionalization of end groups seems to be the most promising way of attaching supramolecular ligands to existing base polymers. However, the association and dissociation temperatures of supramolecular polymer materials become progressively lower and may often drop below room temperature when the molecular weight of the polymer segment is increased.<sup>197,213</sup> This may be compensated for by increasing the size of the self-assembling unit (which is easily possible in case of oligopeptides or oligoureas). However, the effect of the self-assembly on rheological properties under small strains readily starts to diminish as the molecular weight is increased. As an illustrative example, the plateau modulus  $G'$  of poly(*n*-butyl) acrylate modified with an internal triurea segment decreased by almost one order of magnitude already for  $M_n = 8'000$  g/mol compared to  $M_n = 5'200$  g/mol.<sup>214</sup>

Some studies address moderate molecular weights in the range of 20'000–30'000 g/mol, where pronounced effects on, for instance, rheological properties have been observed. For example, Boothroyd et al. report on the supramolecular modification of polybutadiene ( $M_n = 21'000$  g/mol) with terminal UPy groups that undergoes strain-hardening in elongational viscosity measurements. Such a measurement is not even possible with a corresponding non-functionalized polymer. However, no tensile properties are reported, presumably because the material still shows brittle behavior.<sup>215</sup> Bouteiller and coworkers state that the physical cross-linking of PDMS ( $M_n = 29'000$  g/mol) bearing terminal bisurea units is inefficient, indicated by a low Young's modulus of  $E = 0.55$  MPa despite the reasonably high dissociation temperature of the bisurea aggregates of around  $T_d = 135$  °C.<sup>197</sup>

Consequently, to our knowledge and with the exception of side-chain modified soft amorphous polymers,<sup>207,209</sup> all existing examples in the literature are reported for polymer chain segments that barely exceed the critical molecular weight,  $M_c = 2 M_e$ . This latter is, however, a crucial materials parameter, because it marks the threshold for the molecular weights where the characteristic properties of high molecular weight polymers start to be observed, which is associated with the formation of an entanglement network, which originates from topological constraints of polymer chains imposed by their neighboring chains. This includes the appearance of a rubbery regime at temperatures above  $T_g$ , or both the well-established 3.4-power dependence of the viscosity and the inverse second

power dependence of the diffusion coefficient on the logarithm of the molar mass. Moreover, plastic deformation is no longer stabilized for molecular weights below  $M_c$  and materials become generally brittle, particularly in tension.<sup>216-218</sup> It is noted that  $M_c$  and  $M_e$  are specific parameters of each type of polymer and vary greatly depending on the polymer. As they only mark an onset for the emergence of polymer-typical properties, polymer molecular weights useful for engineering applications are required to exceed the critical molecular weight several times in order to obtain, for instance, an appropriate tensile strength and toughness.<sup>219</sup>

Therefore, it remains a challenge to design supramolecular materials from end-modified polymers with acceptable or good tensile properties, particularly at large strains, because polymer chain entanglement of the polymer matrix and an efficient supramolecular structure formation seem to be mutually exclusive.

#### *1.4.5 Supramolecular Fillers*

The use of "supramolecular fillers" has been proposed to address this conundrum. These are ditopic organic molecules that bind to polymers via specific non-covalent interactions. The few examples so far described in the literature are based on structural motifs such as diurea,<sup>220-224</sup> or diamide<sup>225</sup> derivatives that can bind to a complementary unit of the polymer via multiple hydrogen bonding interactions. The presence of such compounds may improve stiffness without compromising tensile strength or the elongation-at-break,<sup>223</sup> but has mainly been applied to segmented block copolymers with a molecular weight of the polymer chain segments between the hydrogen bonding units that is lower than  $M_e$ . The resulting materials are hence not well entangled, indicated by, for instance, a yield stress below 4 MPa. Notably, however, additives based on UPy-ligands have been designed as well, but because of their monodisperse nature they can only compete with the interactions between UPy polymer chains ends. Their addition leads hence to a break-down of the network.<sup>163,174</sup> Therefore, the potential of this approach for tailoring mechanical properties, particularly of end-group functionalized polymers remains largely unexplored.

#### *1.4.6 Scope and Limitations of Supramolecular Modification for Sustainable Plastics*

In summary, the utilization of hydrogen-bonding units such as amides, urethanes, ureas, or peptide sequences that are self-complementary, highly directional, electronically conjugated, ditopic hydrogen bonded donor and acceptor groups can help to address some of the short comings of existing materials

like, for instance, the often poor processability of aliphatic polyesters. Their incorporation as functional end groups leads to marked increases in the virtual molecular weight or in polymer network formation so that, below the dissociation temperature, such systems usually feature thermomechanical and rheological properties that are otherwise typical of corresponding high molecular weight polymers or chemically cross-linked elastomers. Moreover, the dynamic nature of the aggregates gives rise to self-healing properties, stimuli-responsiveness such as sharp melting transitions into low viscosity melts, which renders these materials potentially highly recyclable. However, current examples rely almost exclusively on short polymer segments with molecular weights well below the threshold required for efficient entanglement, because assembly of polymer end groups becomes progressively thermodynamically disfavored at increasing molecular weights owing to their increased dilution. Consequently, such systems typically show brittle failure at low tensile loads. Moreover, the expansion of self-assembly concepts to solid thermoplastic polymers has so far attracted little interest, because their macroscopic bulk properties are typically assumed to be dominated by polymer crystallinity and/or glass formation. Therefore, conventional approaches to the supramolecular modification of commodity polymers and biodegradable polymers have had little impact on the development of sustainable materials for engineering and packaging applications.

#### **1.4 Scope and Outline of the Thesis**

The plastic waste crisis is one of the most pressing issues facing mankind today. Addressing this issue will require re-evaluation of the materials that are suitable for a future circular plastics economy.<sup>226</sup> One promising class of materials for a circular plastic economy are bio-sourced and biodegradable aliphatic polyesters that can be chemically recycled to monomer via ring-closing depolymerization. Depending on the specific polyester and the target application, however, their scope is often limited by, e.g., low heat resistance, inherent brittleness, or poor processing characteristics, such as low crystallization rates or poor melt strength. One of the most interesting ways of addressing those shortcomings is supramolecular modification with ligands that thermoreversibly assemble by multivalent hydrogen bonding, which offers improved melt strength below the self-assembly temperature, but viscous flow above it. Ligand self-assembly, however, is progressively disfavored as the molecular weight between the functional groups is increased. For this reason, investigations have so far mostly been limited to low molecular weight polymers that are unable to form a robust entanglement network, resulting in brittle failure at low tensile strains in the solid state.

The present thesis work aims to demonstrate that simultaneous improvement of the final mechanical properties, melt behavior, and crystallization rate of high molecular weight aliphatic polyesters may be achieved by blending a polymer end-modified with a ditopic, self-complementary, self-assembling unit, based on three-fold hydrogen bonding, with a low molecular weight additive containing the same supramolecular motif. In the resulting materials, polymer end-groups and the additive co-assemble to form helical, one-dimensional nanofibrils. This replaces macroscopic phase separation of the bulk additive because the polymer-tethered end groups effectively act as a compatibilizer. Instead, a supramolecular network of well-defined polymer-tethered and polymer-bridged nanofibrils is formed, and the material may hence be described as a "supramolecular graft polymer". Because the total concentration of self-assembling units in the blend is determined independently of the polymer molecular weight by varying the additive content, we expect this network formation to remain possible in polymers whose molecular weight, including that of the polymer segments bridging the nanofibrils, is high enough for a robust entanglement network to form. The nanofibril dissociation temperature is also expected to increase with additive concentration, so that the supramolecular network should persist above the glass transitions or melting temperatures of the polymer matrix, depending on the choice of additive. The supramolecular network of nanofibrils hence provides a temperature window of elastic behavior in the molten polymer matrix at elevated temperatures. However, the polymer still shows predominantly viscous behavior above the nanofibril dissociation temperature. Moreover, chain-end tethering is expected to significantly increase polymer relaxation times and hence facilitate molecular orientation during melt stretching, and the nanofibrils may also act as efficient nucleating agents, resulting in enhanced crystallization rates during cooling. Solidified materials prepared by melt stretching may therefore exhibit significantly altered crystalline microstructures and mechanical properties at room temperature in the presence of the nanofibrils.

In the first chapter, we develop the basic concept outlined above and establish detailed structure-property relationships between additive and end-group co-assembly, nanofibril network formation, melt properties, polymer solidification, and molecular orientation. To this end, we use poly( $\epsilon$ -caprolactone) (PCL) as a representative example of a biodegradable polyester with reduced melt strength, a low yield stress, and poor heat resistance in the solid state. We then demonstrate that blending PCL end-modified with acetyl-L-alanyl-L-alanyl amide groups ( $\text{PCL}_{80}(\text{Ala}_2\text{Ac})_2$ ) with the low molecular weight additive 2-octyldodecyl acetyl-L-alanyl-L-alanyl amide (**A**) results in the formation of a network of well-defined nanofibrils homogeneously distributed in the material. The blends show high

melt elasticity and extensibility, and strain-hardening behavior, and can be processed into highly oriented materials characterized by a shift from classical spherulitic to shish-kebab microstructures, and altered mechanical properties at room temperature.

In the second chapter we exploit the high melt elasticity of the **PCL<sub>80</sub>(Ala<sub>2</sub>Ac)<sub>2</sub>/A** blends for the preparation of oriented PCL filaments by melt stretching. Again, the resulting filaments exhibit a shish-kebab morphology, with lamellae oriented perpendicular to the stretching direction and PCL extended chain crystals parallel to the stretching direction, and significantly increased room-temperature Young's modulus, yield stress, and ultimate tensile strength.

In the third chapter, we use the same end groups and a similar additive (2-ethylhexyl acetyl-L-alanyl-L-alanyl amide, **A8**) to modify atactic poly(lactic acid) (**PDLLA-A**) and stereoregular poly(L-lactic acid) (**PDLLA-A**). We do not observe formation of a network of nanofibrils in this case, which we argue to be because the structural similarities of end groups and polymer repeat units lead to too high a solubility of the end groups in the polymer matrix. Instead, the additive **A8** crystals show macroscopic phase separation, but remain well-dispersed in the polymer matrix and hence act as an efficient nucleating agent.

In the fourth chapter, we apply the knowledge gained from the previous investigations to the modification of atactic PDLLA and stereoregular PLLA with *N,N'*-diisopentyl benzene tricarboxamides (**PDLLA-B5** and **PLLA-B5**, respectively), and prepare blends with the additive *N,N,N''*-triiisopentyl BTA (**B5**). We demonstrate that the structure of the end groups and additive are sufficiently different from that of the polymer repeat units to allow successful co-assembly and formation of a network of polymer-tethered nanofibrils. These again act as highly efficient nucleating agents. At the same time, however, a new rubber-like regime is established above the PDLLA glass transition temperature, which again manifests itself through significantly increased melt strength in the semicrystalline **PDLLA-B5/B5** blends at sufficiently high additive concentrations, greatly facilitating melt processing.

Supramolecular Modification for  
High Performance Sustainable Polyesters

The results presented in this chapter are part of a manuscript in preparation:

*“Supramolecular Modification for High Performance Sustainable Polyesters”*, Daniel Görl, Yevhen Hryshunin, Shuichi Haraguchi, Matthieu Wendling, Sophia Thiele, Giorgia Scetta, Alexandre Simula, Nicolas Candau, Torne Tänzer, Marianne Liebi, Christopher Plummer, Holger Frauenrath, *to be submitted*.

H.F. conceived the idea and directed the research. D.G. performed DSC and OM. S.H synthesized all the materials, performed DSC and extensional viscosity. A.S. performed film blowing experiment. C.P. performed AFM and developed the analytical models. T.T. and M.L. performed synchrotron SAXS.

Y.H. performed WAXS and SAXS, prepared melt stretched films and thermoformed cups, performed UTM and polarized IR.

The manuscript was written by D.G., Y.H., M.W., S.T. C.P. and H.F.

## 2. Supramolecular Modification for High Performance Sustainable Polyesters

### 2.1 Introduction

The development of plastic materials has changed our everyday life.<sup>1,226,227</sup> The global plastics production continues to grow exponentially and has surpassed all other man-made materials, with the exception of construction materials.<sup>1</sup> However, only a small fraction of all plastics products is currently recycled, with the remainder ending up in landfill or leaking into the environment.<sup>13</sup> Plastic microparticles have infested the entire food chain, with hitherto unknown consequences for environmental and human health.<sup>8,228</sup> The plastic waste crisis is hence one of the most imminent sustainability challenges mankind is facing today. While there is no singular best strategy to address this complex systemic challenge, polymer standardization, bio-sourcing of materials, biodegradability, and chemical recycling to monomer may be considered as important complementary elements towards a circular plastics economy. Thus, reducing complexity and the number of polymer grades and components will facilitate waste collection, sorting, and recycling.<sup>229</sup> Bio-sourced plastics obtained from second or third generation renewable feedstock, promise to be favorable from a life cycle assessment (LCA) perspective.<sup>17</sup> Biodegradability, while certainly not a universal solution, can provide additional end-of-life options such as composting and, perhaps more importantly, help mitigate problems associated with the inevitable leakage of plastics into the environment.<sup>15</sup> Chemical recycling to monomer by depolymerization under mild conditions will be important as an additional end-of-life option for value recovery with minimal adverse environmental effects.<sup>12</sup> Finally, the development of sustainable materials for the replacement of petroleum-based polyolefins would have the largest impact because the latter represent the vast majority of the global plastics production by volume.<sup>12</sup>

From this perspective, aliphatic polyesters are highly promising materials for a circular plastics economy,<sup>12,16,230</sup> because a wide variety of grades are commercially available from many manufacturers world-wide, they are amenable to chemical recycling to monomer by hydrolysis or ring-closing depolymerization,<sup>12,16,231,232</sup> can, in principle, be sourced from carbohydrate-based second/third generation renewable feedstock,<sup>17,233</sup> often exhibit acceptable biodegradability,<sup>234</sup> and can be designed to have polyolefin-like properties.<sup>235</sup> However, novel sustainable plastics solutions will also have to exhibit materials properties that are at least on par with the materials they intend to replace. Among the typical shortcomings of aliphatic polyesters are their often limited thermal dimensional stability,



low melt strength, elasticity, and/or extensibility for good processability, and their slow crystallization entailing long process cycle times.<sup>17</sup>

The problem of low melt strength, for instance, can be addressed with nanoscopic reinforcements that also provide stiffness and strength.<sup>236</sup> Nucleating agents accelerate the polymer crystallization.<sup>237</sup> Dynamic covalent materials and particularly vitrimers promise to provide a recyclable version of thermosets.<sup>238-240</sup> Moreover, supramolecular polymers and networks have gained considerable attention as a way to obtain materials with versatile thermomechanical properties, ranging from soft gels to thermoplastic elastomers or glassy polymer networks.<sup>241-243</sup> These materials are often composed of linear or star polymers functionalized with multivalent self-complementary hydrogen-bonding chain-internal or end groups that thermoreversibly assemble, resulting in rheological properties that are otherwise typical of corresponding unmodified high molecular weight polymers or covalently cross-linked polymers.<sup>244</sup> Moreover, their sharp melting transitions enable convenient processing from low viscosity melts,<sup>245</sup> which renders these materials potentially highly recyclable,<sup>246,247</sup> and the dynamic nature of the supramolecular aggregation can give rise to self-healing properties<sup>248,249</sup>, stimuli-responsiveness,<sup>250,251</sup> or shape-memory effects,<sup>252</sup> but are also responsible for their potential shortcomings such as poor tensile properties and limited thermal stability under load. The latter can be addressed in supramolecular materials from ditopic hydrogen-bonded ligands that selectively self-assemble into extended one-dimensionally extended nanostructures that provide additional reinforcement, such as benzene tricarboxamides<sup>253-256</sup> or  $\beta$ -sheet-forming oligopeptides. In particular the latter are a useful supramolecular motif that, thanks to its bio-inspired hierarchical structure formation and self-limiting helical aggregation,<sup>257-260</sup> selectively self-assembles into nanofibrils with uniform diameter that can be used to prepare elastomers with tailored elasticity or toughness,<sup>261,262</sup> biomedical scaffolds, multiple-helical polymers,<sup>263,264</sup> or organic nanowires.<sup>265-268</sup> With a few notable exceptions,<sup>269-276</sup> however, research on supramolecular polymers has so far focused polymers at molecular weights well below the entanglement threshold, because the dilution of the polymer end groups with increasing polymer molecular weight renders their aggregation thermodynamically unfavorable.<sup>270-272</sup> Since the presence of a well-developed entanglement network is a critical factor for both melt properties and mechanical resilience in the solid state, the resulting materials typically show low melt strength, as well as low strength and brittle failure in tension. Moreover, supramolecular polymers of semicrystalline or glassy base polymers have generally attracted little interest to date,<sup>277-282</sup> because end group aggregation has to occur above polymer crystallization or vitrification

temperatures, and bulk properties were assumed to be dominated by the solid polymer.<sup>280,281,283</sup> A supramolecular modification strategy that remains effective at technologically relevant molecular weights and in semicrystalline polymers can therefore be seen as one key enabling factor to increase the performance and versatility of novel sustainable polymers.

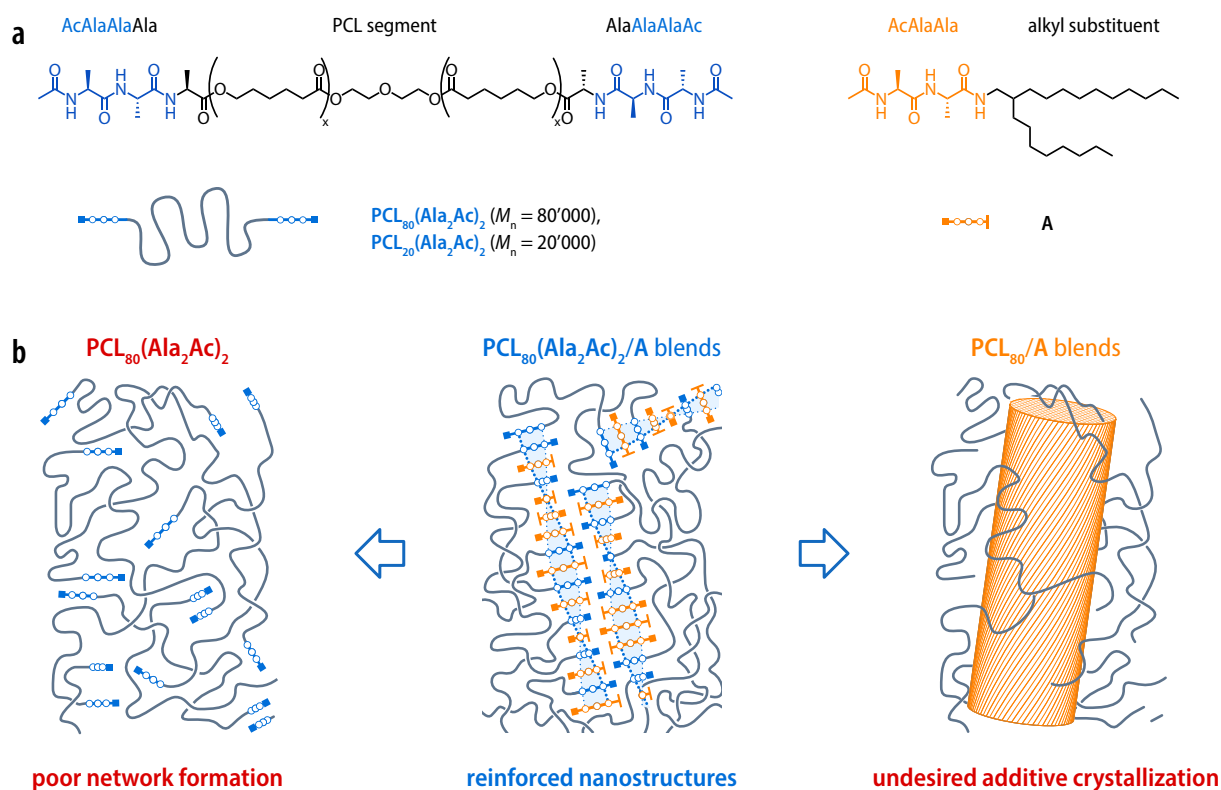


**Figure 16. Supramolecular polymer networks from well-defined nanofibrils.** Decoupling of supramolecular structure formation from the molecular weight of the employed polymer segment is achieved by co-assembly of polymer end groups based on  $\beta$ -sheet-forming oligopeptides (blue) and a matching additive (orange). *a*) Chemical structures of telechelic poly( $\epsilon$ -caprolactone) with different molecular weights,  $\text{PCL}_{20}(\text{Ala}_2\text{Ac})_2$  ( $M_n = 20'000$ ) and  $\text{PCL}_{80}(\text{Ala}_2\text{Ac})_2$  ( $M_n = 80'000$ ), as well as of the additive 2-octyldodecyl acetyl-L-alanyl-L-alanyl amide **A**; it should be noted that the end-modified polymers in fact comprise one more L-alanine repeat unit for synthetic reasons that is, however, linked to the polymer via an ester group that does not participate in hydrogen bonding. *b*) Both, functional polymer chain ends and the additive are mutually necessary for the formation of well-defined polymer-tethered nanofibrils. Without the additive, the polymer end groups are too dilute for efficient self-assembly (left), while without the end groups, the additive undergoes macroscopic phase separation into microfibrinous precipitates (right).

Here, we show that the melt properties and thermomechanical behavior of a biodegradable polyester are drastically improved when modified with  $\beta$ -sheet-forming oligopeptide end groups and then blended with a low molecular weight additive based on the same supramolecular motif (Figure 16). Tuning the additive concentration renders the co-assembly of additive and polymer end groups still

effective at polymer molecular weights many times larger than the entanglement molecular weight where end group assembly alone is already suppressed. The silk-inspired hierarchical structure formation of the oligopeptides prevents additive crystallization and instead results in polymer-tethered nanofibrils with a defined diameter that are arranged with a periodic spacing, homogeneously distributed across the material, and serve multiple roles: The polymer-bridged nanofibrils form a supramolecular network that provides a rubber-like behavior in the polymer melt; they serve as a thermoreversible load-bearing element that facilitates orientation of the material upon melt deformation; and they act as a highly efficient nucleating agent during polymer solidification. With poly( $\epsilon$ -caprolactone) (PCL) as a representative example, we demonstrate that this strategy results in extreme melt extensibility, gives rise to shear-induced polymer crystallization, facilitates processing routes such as thermoforming, film blowing, or film melt-stretching, and provides materials with controlled microstructures translating into a broad range of mechanical property profiles.

## 2.2 Results and Discussion

For our investigations, we have chosen PCL as a representative example because it is a commercially available semicrystalline aliphatic polyester that is prepared by ring opening polymerization (ROP),<sup>64,65</sup> can be recycled to monomer by ring-closing depolymerization (RCD),<sup>12,73</sup> can be obtained from renewable resources,<sup>67,68</sup> and is biodegradable.<sup>284</sup> It is biocompatible and-FDA approved<sup>76</sup> and therefore widely applied in biomedical applications.<sup>77-79</sup> PCL is known to be a highly ductile material<sup>65,80</sup> but is limited by its poor thermal stability and processability due to its low melt strength (Figure 17) and hence not broadly used in engineering or commodity applications, such as packaging.

We have used PCL of two different molecular weights (PCL<sub>80</sub>,  $M_n = 80'000$ ; PCL<sub>20</sub>,  $M_n = 20'000$ ) that are, respectively, 11 and 3 times greater than the entanglement molecular weight ( $M_e = 7'000$ ),<sup>285</sup> and prepared the corresponding end-modified PCL-derivatives **PCL<sub>20</sub>(Ala<sub>2</sub>Ac)<sub>2</sub>** and **PCL<sub>80</sub>(Ala<sub>2</sub>Ac)<sub>2</sub>** (Figure 16). The oligopeptide end groups are known to aggregate via three-fold intermolecular hydrogen-bonds into what we will refer to as “nanofibrils”, that is, one-dimensionally extended aggregates with a well-defined, uniform diameter that consist of helically twisted stacks of antiparallel  $\beta$ -sheet tapes.<sup>261</sup>

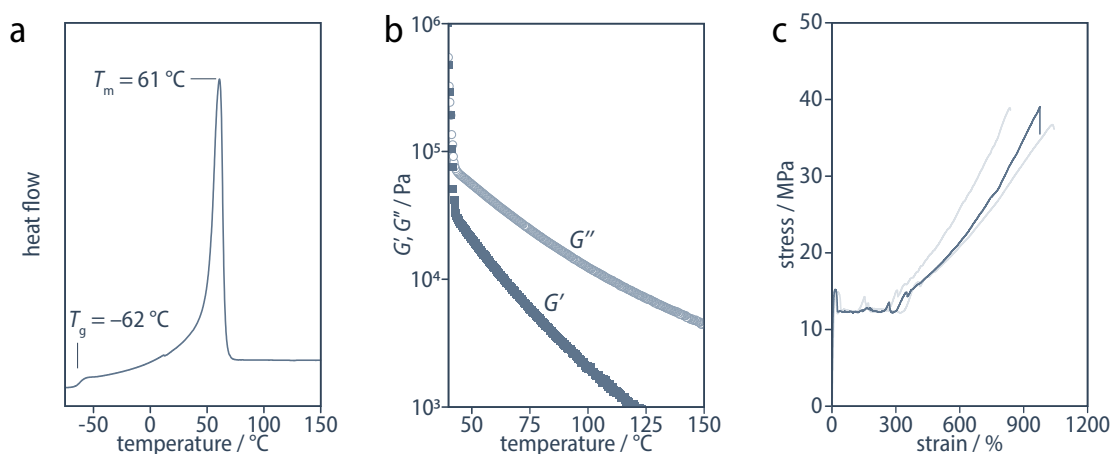


**Figure 17. Thermomechanical properties of poly( $\epsilon$ -caprolactone) PCL<sub>80</sub>.** *a*) DSC heating scan of PCL<sub>80</sub> (scanning rate 10 °C/min), revealing the glass transition at around  $T_g = -62$  °C and the melting transition at  $T_m = +61$  °C. *b*) Temperature-dependent oscillatory shear rheology (strain 5%, frequency 1 rad/s, cooling rate 1 °C/min), indicating that PCL<sub>80</sub> is a rheological liquid ( $G'' > G'$ ) with low melt strength ( $G' < 20$  kPa) at any temperature above its crystallization temperature at  $T_c = 40$  °C. *c*) Tensile testing of three hot-pressed PCL<sub>80</sub> films (room temperature, strain rate 10 mm/min), showing its ductile behavior with a Young's modulus of  $E = 256 \pm 51$  MPa, a yield strength of  $\sigma_y = 15 \pm 0.2$  MPa, an ultimate strength of  $\sigma_{max} = 38 \pm 1.0$  MPa, a strain-at-break of  $\epsilon_{max} = 945 \pm 100$  %, and an energy-at-break of  $W = 195 \pm 22$  MJ m<sup>-3</sup>.

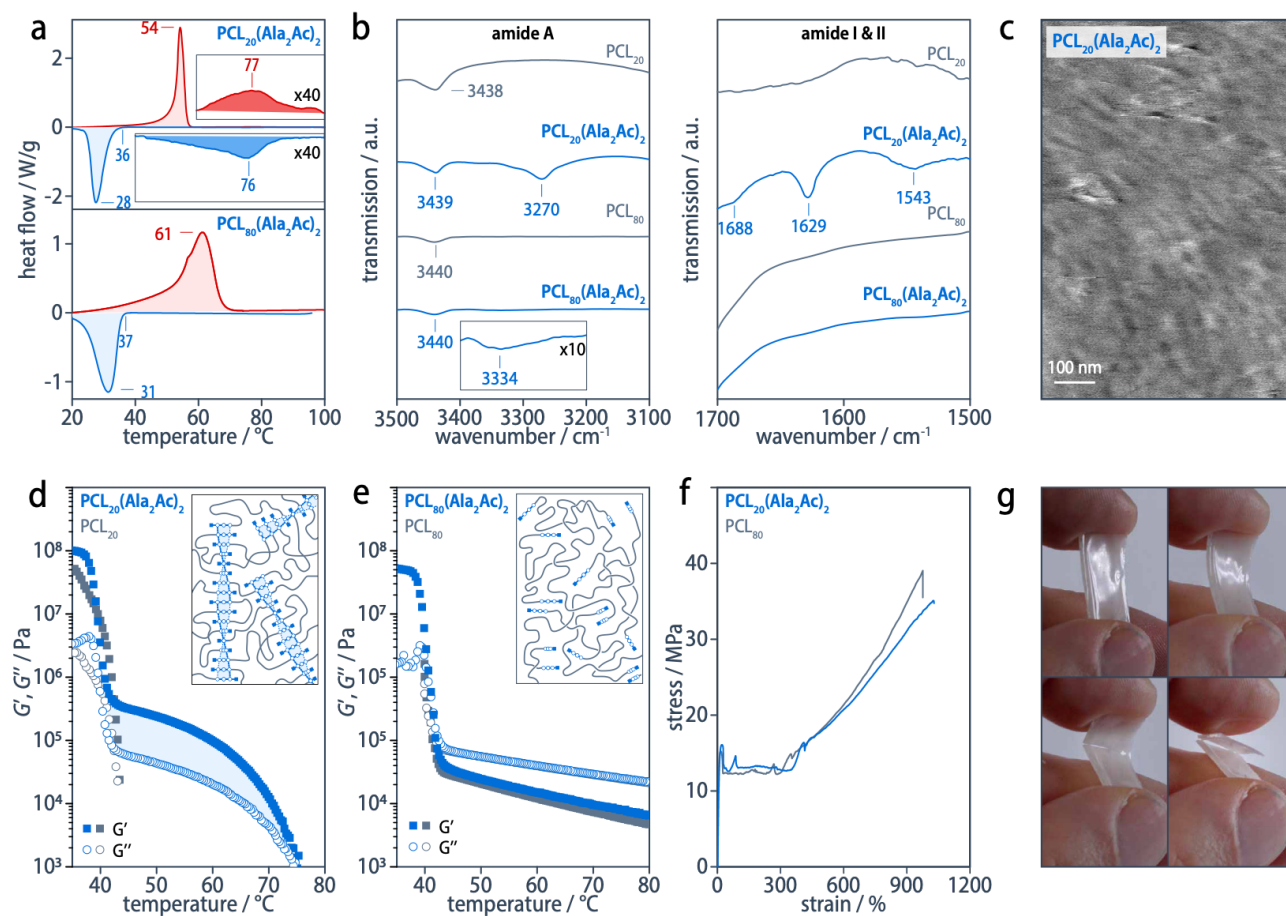


**Figure 18. Molecular weight dependence of end group assembly.** *a*) DSC heating (red) and cooling (blue) scans of PCL<sub>20</sub>(Ala<sub>2</sub>Ac)<sub>2</sub> and PCL<sub>80</sub>(Ala<sub>2</sub>Ac)<sub>2</sub> (scanning rate of 10 °C/min), revealing that PCL<sub>20</sub>(Ala<sub>2</sub>Ac)<sub>2</sub> exhibits an additional reversible endothermic (exothermic) transition at around  $T_d = 77$  °C ( $T_a = 76$  °C), which is above the PCL melting temperature

of  $T_m = 54^\circ\text{C}$  (crystallization onset temperature of  $T_c = 36^\circ\text{C}$ ), respectively. *b*) This transition is attributed to the association (dissociation) of the end groups, as FTIR spectra of  $\text{PCL}_{20}(\text{Ala}_2\text{Ac})_2$  films (blue) obtained on cooling from the melt at  $10^\circ\text{C}/\text{min}$  display a single amide A (N–H stretching) band at  $3270\text{ cm}^{-1}$  with a full-width at half-maximum (FWHM) of  $40\text{ cm}^{-1}$  and a single sharp amide I (C=O stretching) absorption at  $1629\text{ cm}^{-1}$  (FWHM  $12\text{ cm}^{-1}$ ) and a secondary weak component at  $1688\text{ cm}^{-1}$ , the characteristic peak positions for resonance-enhanced arrays of  $\text{N-H}\cdots\text{O}=\text{C}$  hydrogen-bonded amide groups in extended antiparallel  $\beta$ -sheet-like aggregates;<sup>261</sup> these bands are absent in pristine  $\text{PCL}_{20}$  (grey), which show a weak band at  $3440\text{ cm}^{-1}$  that is attributed to bound water, but also in  $\text{PCL}_{80}(\text{Ala}_2\text{Ac})_2$  (blue) that instead shows a weak amide A band at  $3334\text{ cm}^{-1}$ , that can be assigned to ill-defined, loosely hydrogen-bonded aggregates. *c*) AFM phase image obtained from a  $\text{PCL}_{20}(\text{Ala}_2\text{Ac})_2$  film at  $55^\circ\text{C}$  after cooling from  $60^\circ\text{C}$  at a rate of  $0.1^\circ\text{C}/\text{min}$  to avoid crystallization of the polymer matrix, showing aggregates due to the self-assembly of the end groups. *d*) Storage moduli,  $G'$  (closed symbols), and loss moduli,  $G''$  (open symbols), in temperature-dependent oscillatory shear rheology ( $1\text{ rad s}^{-1}$ , cooling rate  $1^\circ\text{C}/\text{min}$ ) show a rubber-like regime ( $G' > G''$ ) between  $T_a$  and  $T_c$  with a plateau modulus of  $G' \approx 0.3\text{ MPa}$  at  $50^\circ\text{C}$  in  $\text{PCL}_{20}(\text{Ala}_2\text{Ac})_2$  (blue) because the association of the end groups results in a supramolecular network where the aggregates serve as physical crosslinks in the (weakly) entangled molten polymer matrix (inset), different from the liquid-like behavior of pristine  $\text{PCL}_{20}$  (grey) above  $T_c$ . *e*) By contrast, both  $\text{PCL}_{80}(\text{Ala}_2\text{Ac})_2$  (blue) and  $\text{PCL}_{80}$  (grey) show viscous behavior ( $G'' > G'$ ) typical of entangled polymer melts (inset) above  $T_c$ . *f*) Representative tensile test of a hot-pressed sheet of  $\text{PCL}_{80}(\text{Ala}_2\text{Ac})_2$  (blue) shows the same behavior as  $\text{PCL}_{80}$  (grey), suggesting the end-group modification not to affect the mechanical properties at room temperature. *g*, Specimens of  $\text{PCL}_{20}(\text{Ala}_2\text{Ac})_2$  are too brittle to allow for tensile testing.

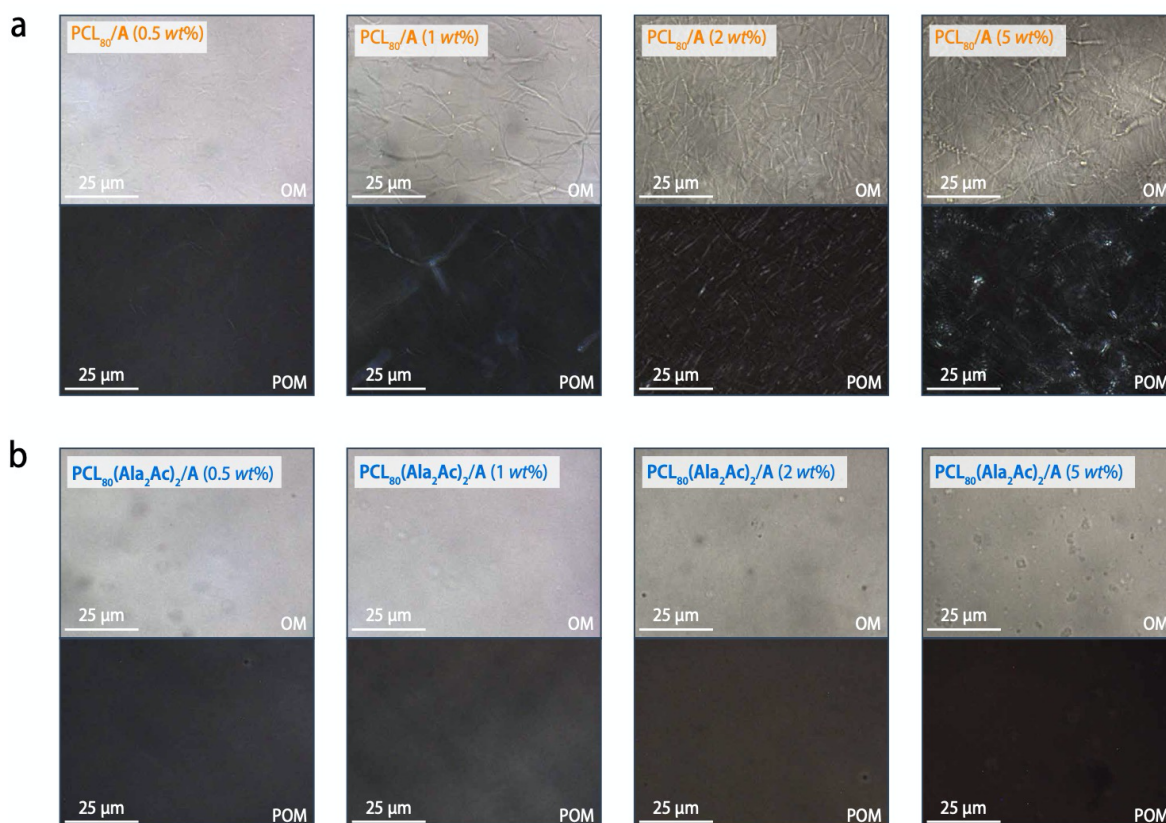


**Figure 19. Optical microscopy of  $\text{PCL}_{80}(\text{Ala}_2\text{Ac})_2/\text{A}$  and  $\text{PCL}_{80}/\text{A}$  blends.** *a*) Optical microscopy images of  $\text{PCL}_{80}/\text{A}$  reference blends of containing 0.5, 1, 2, and 5 wt% of **A** recorded at  $60^\circ\text{C}$  after cooling from the melt at a cooling rate of  $10^\circ\text{C}/\text{min}$ , revealing macroscopic phase separation in the form of birefringent microfibrillar precipitates of the additive that do not change shape or position on crystallization and re-melting of the polymer matrix. *b*) By contrast, blends of the modified  $\text{PCL}_{80}(\text{Ala}_2\text{Ac})_2$  containing 0.5, 1, and 2 wt% of the additive **A** remain optically homogeneous. At an additive concentration of

5 wt%, isotropically shaped features slowly emerge over extended periods of time and at a significantly lower volume fraction compared to the precipitates in the reference blend.

While the lower molecular weight  $\text{PCL}_{20}(\text{Ala}_2\text{Ac})_2$  (end group concentration of 2 wt%) indeed shows end group aggregation into ill-defined nanofibrils, exhibits rubber-like behavior above the PCL crystallization temperature but is highly brittle due to insufficient entanglement, materials based on the higher molecular weight  $\text{PCL}_{80}(\text{Ala}_2\text{Ac})_2$  (end group concentration of 0.5 wt%) are ductile but show no sign of end-group aggregation and hence properties identical to non-modified  $\text{PCL}_{80}$  (Figure 18). However, we addressed this problem by blending  $\text{PCL}_{80}(\text{Ala}_2\text{Ac})_2$  with the low molecular weight additive 2-octyldodecyl acetyl-L-alanyl-L-alanyl amide **A** that is based on the same oligopeptide motif.

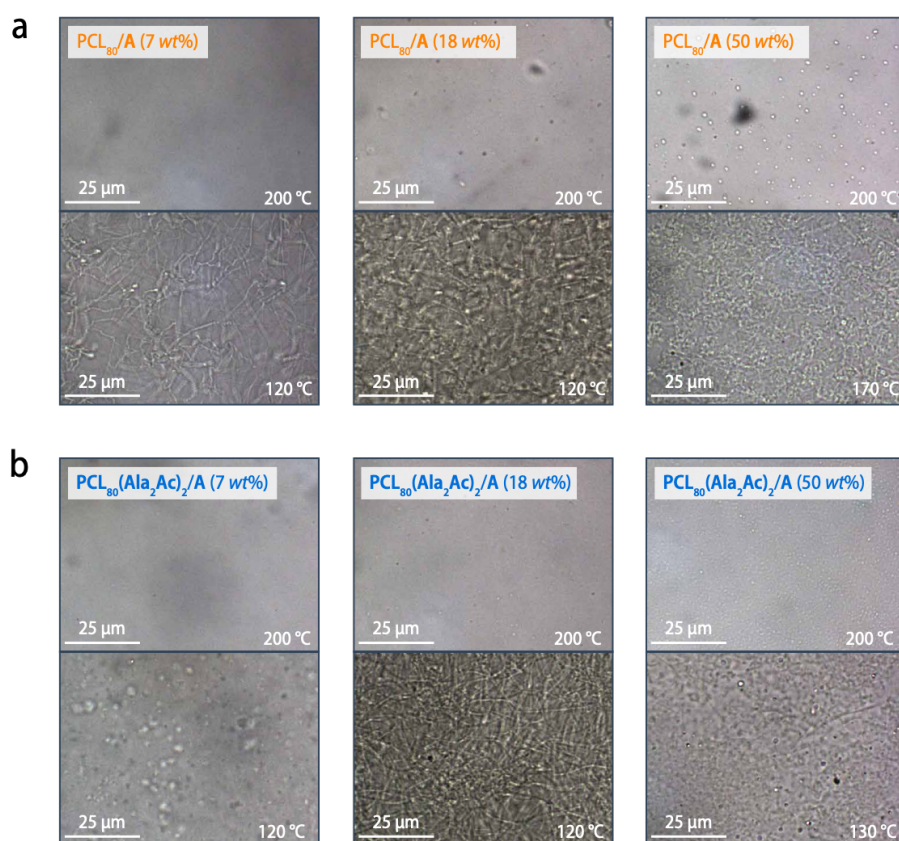


**Figure 20. Macroscopic phase separation in  $\text{PCL}_{80}(\text{Ala}_2\text{Ac})_2/\text{A}$  and  $\text{PCL}_{80}/\text{A}$  blends at high additive concentrations.**

*a)* Optical microscopy images of  $\text{PCL}_{80}/\text{A}$  reference blends of containing 7, 18, and 50 wt% of **A** recorded in the melt state at 200 °C and after cooling to 120 °C at a cooling rate of 10 °C/min, revealing macroscopic phase separation in the form of birefringent microfibrillar precipitates of the additive that do not change shape or position on crystallization and re-melting of the polymer matrix. At high additive contents, liquid-liquid phase separation of additive-rich droplets from the polymer melt occurs. While the droplets solidify, the additive of the polymer-rich phase forms microfibrillar precipitates upon cooling below the association temperature. *b)* Macroscopic phase separation in the form of birefringent microfibrillar precipitates similar to those in the reference blends is also observed  $\text{PCL}_{80}(\text{Ala}_2\text{Ac})_2/\text{A}$  blends at high concentrations of **A**.

In marked contrast to reference blends of unmodified PCL<sub>80</sub> and the additive **A** that show macroscopic phase separation of the additive in the form of microfibrinous and birefringent precipitates at any concentration of **A** visible in (polarized) optical microscopy, the PCL<sub>80</sub>(Ala<sub>2</sub>Ac)<sub>2</sub>/A blends remain optically homogeneous at additive concentrations of up to a threshold concentration of roughly 5 wt%, above which macroscopic additive precipitates similar to those in the reference blends are formed (Figure 19).

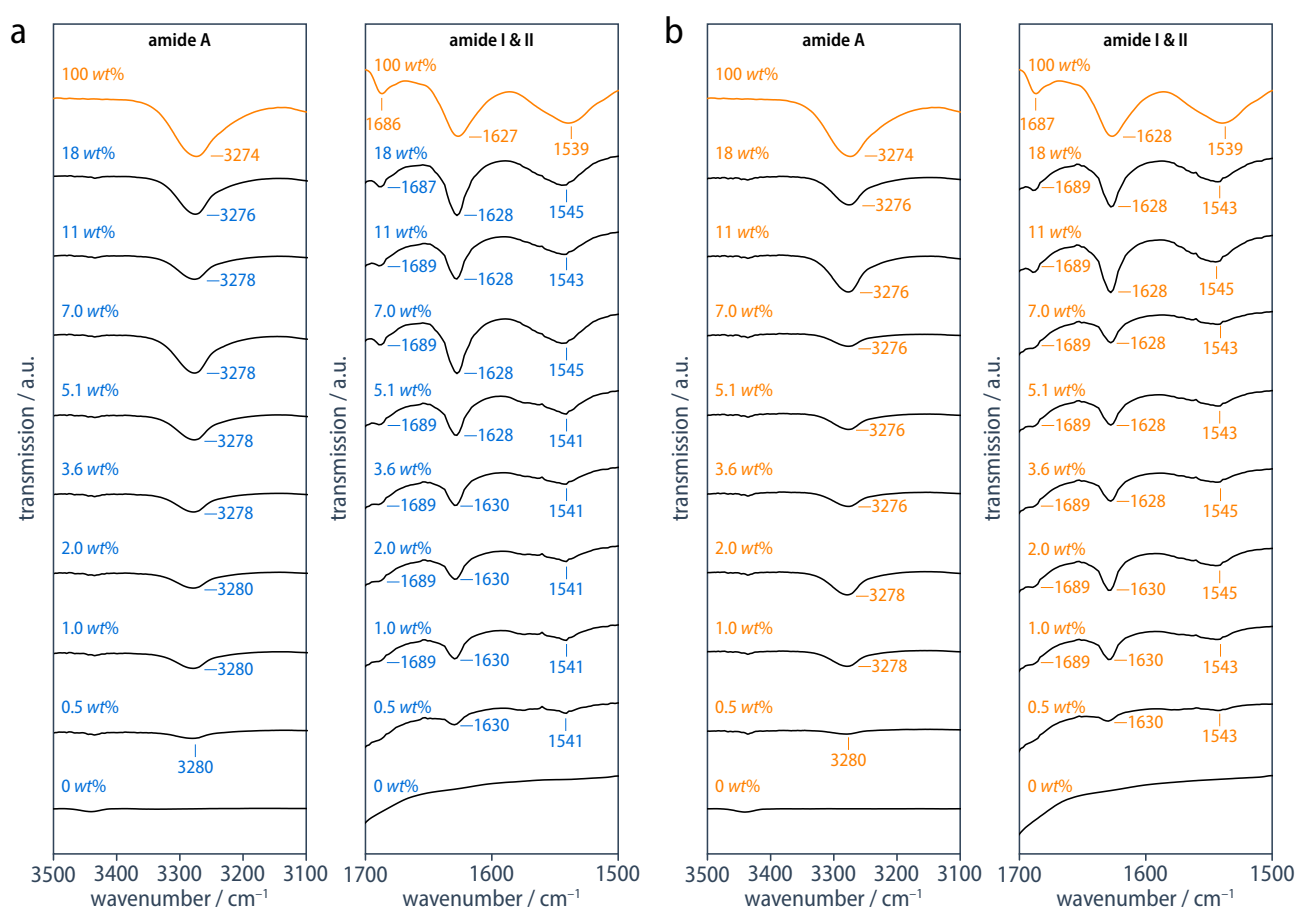


**Figure 21. IR spectroscopy of PCL<sub>80</sub>(Ala<sub>2</sub>Ac)<sub>2</sub>/A blends.** *a)* FTIR spectra of PCL<sub>80</sub>(Ala<sub>2</sub>Ac)<sub>2</sub>/A as well as *b)* of PCL<sub>80</sub>/A specimens obtained upon cooling from the melt (10 °C/min) show single amide A (N–H stretching) bands at 3276–3280 cm<sup>-1</sup> (FWHM 46–60 cm<sup>-1</sup>), single sharp amide I (C=O stretching) bands at 1628–1630 cm<sup>-1</sup> (FWHM 14–20 cm<sup>-1</sup>) along with a weaker secondary component at 1687–1689 cm<sup>-1</sup>, and amide II (C=O bending) bands at 1541–1545 cm<sup>-1</sup>, which are the characteristic peak positions of resonance-enhanced arrays of N–H···O=C hydrogen-bonded amide groups in a hydrophobic polymer matrix, The additional small feature at 3450 cm<sup>-1</sup> is also observed in pristine PCL<sub>80</sub> and can be attributed to bound water.

Nevertheless, even in the homogeneous PCL<sub>80</sub>(Ala<sub>2</sub>Ac)<sub>2</sub>/A blends below that threshold concentration, FTIR spectra (Figure 21) show single amide A (N–H stretching) bands at 3276–3280 cm<sup>-1</sup> (FWHM 46–60 cm<sup>-1</sup>), single sharp amide I (C=O stretching) bands at 1628–1630 cm<sup>-1</sup> (FWHM 14–20 cm<sup>-1</sup>) along

with a weaker secondary component at 1687–1689  $\text{cm}^{-1}$ , and amide II (C=O bending) bands at 1541–1545  $\text{cm}^{-1}$ , which are the characteristic peak positions of resonance-enhanced arrays of N–H $\cdots$ O=C hydrogen-bonded amide groups, with no sign of free amide groups or ill-defined aggregates. This proves that both additive and end groups remain quantitatively assembled into extended antiparallel  $\beta$ -sheet-like aggregates, which, in turn, implies that the materials undergo nanophase separation in this low additive concentration range.

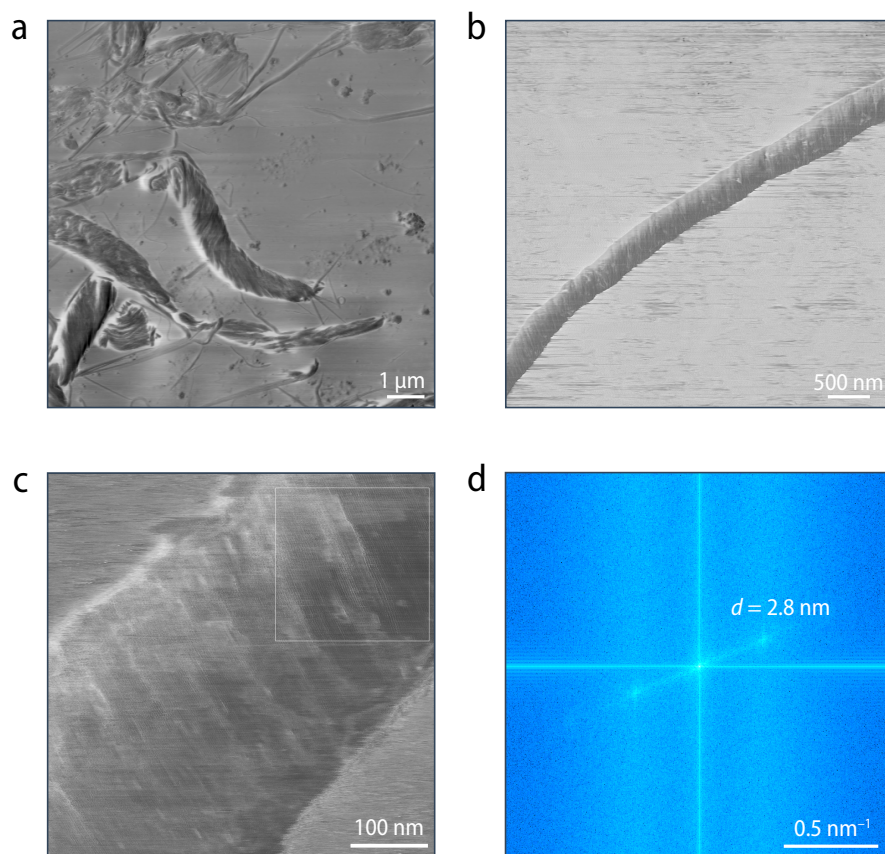


**Figure 22. Microfibrillar precipitates of A in PCL<sub>80</sub>/A reference blends.** *a–c*), AFM phase images of PCL<sub>80</sub>/A (5 wt%) recorded at 65 °C, that is, above the PCL melting temperature, confirm the presence of macroscopically phase-separated additive domains in PCL<sub>80</sub>/A reference blends, mostly in the form of microfibrils with lengths on the order of tens of micrometers and diameters and widths of at least several hundred nanometers. These microfibrils consist of a chiral columnar mesophase of close-packed additive columns that are helically twisted around the microfibril axis. *d*) Power spectrum of the inset in *c* shows the aggregates to have a periodic spacing of  $d_A = 2.8\text{nm}$ .

The microfibrillar precipitates of **A** in the reference blends have a chiral columnar mesophase structure of close-packed additive columns that are helically twisted around the microfibril axis with a characteristic intercolumnar spacing of  $d_A = 2.8\text{nm}$  in both AFM imaging and XRD analysis (Figure 22).



While the corresponding Bragg reflection is well visible in the  $\text{PCL}_{80}/\text{A}$  reference blends, it is absent in  $\text{PCL}_{80}(\text{Ala}_2\text{Ac})_2/\text{A}$  blends up to an additive content of 2 wt%, above which it starts to emerge albeit significantly weaker than in the reference materials. This reflection can hence be used to qualitatively evaluate the transition from the nanophase-separated regimes to macroscopic phase separation that occurs in the range of additive concentrations of 2–5 wt% (Figure 23). Even at 5 wt%, however, homogeneous nanophase-separated materials are obtained if one ensures proper mixing of the test specimen in the melt, such as in a rheometer or during melt deformation.

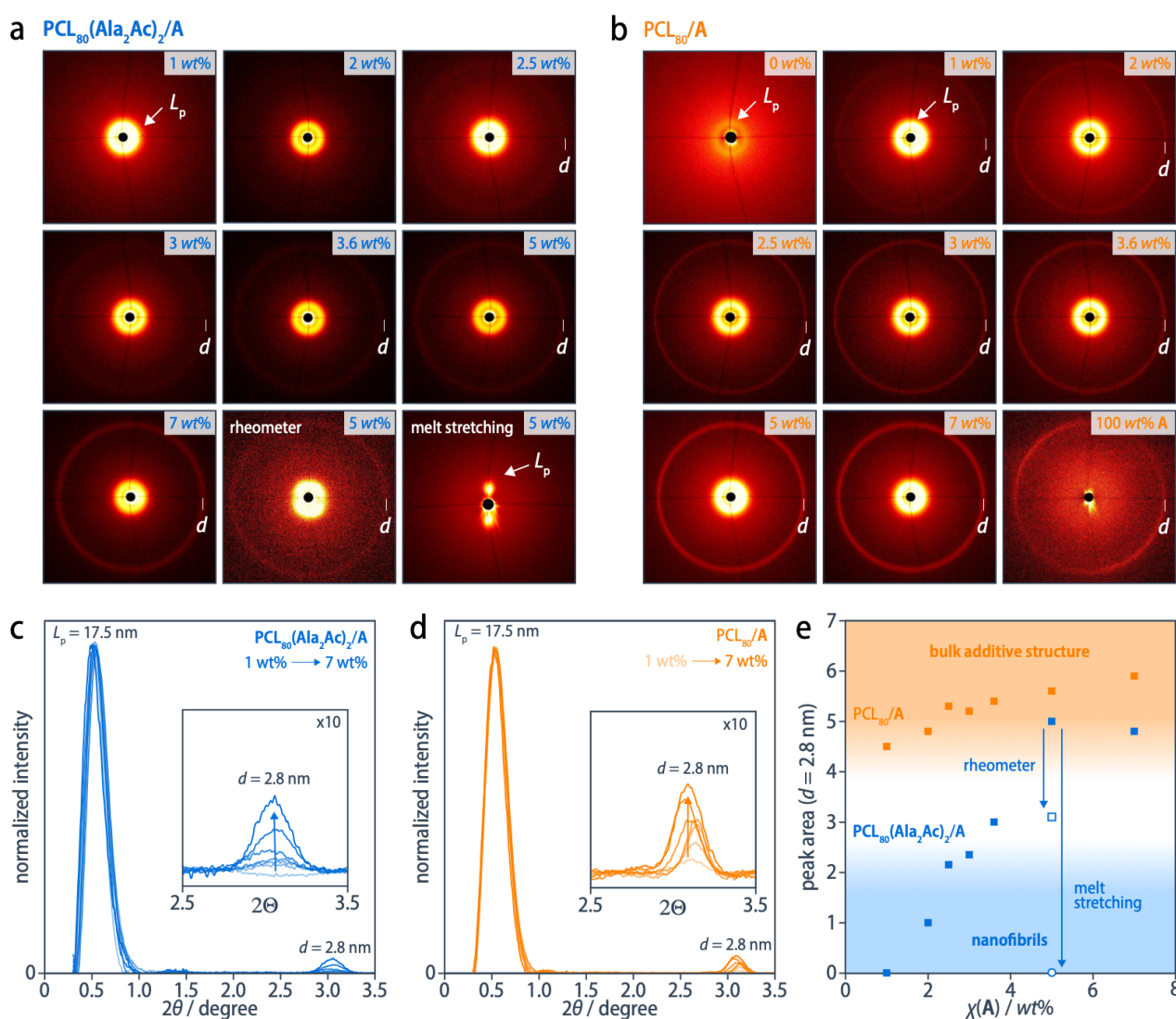


**Figure 23.** The onset of the macroscopic phase separation in  $\text{PCL}_{80}(\text{Ala}_2\text{Ac})_2/\text{A}$  blends. a–b, 2D SAXS patterns of non-oriented  $\text{PCL}_{80}(\text{Ala}_2\text{Ac})_2/\text{A}$  blends and  $\text{PCL}_{80}/\text{A}$  reference blends, respectively, obtained after cooling from the melt at 10 °C/min. 2D SAXS patterns of specimens of  $\text{PCL}_{80}(\text{Ala}_2\text{Ac})_2/\text{A}$  (5 wt%) after simultaneous cooling and melt shearing or melt deformation are also shown. All patterns except of that of the pure additive show an intense low-angle Bragg reflection corresponding to the lamellar long period,  $L_p$ , of the PCL matrix of about 17.5 nm. All the  $\text{PCL}_{80}/\text{A}$  reference blends, irrespective

of the concentration of **A**, show a Bragg reflection corresponding to the spacing of  $d_A = 2.8$  nm characteristic of the pure additive **A** and its microfibrillar precipitates (Figure 22). This reflection is practically absent in **PCL<sub>80</sub>(Ala<sub>2</sub>Ac)<sub>2</sub>/A** blends up to an additive content of 2 wt%, above which it starts to emerge albeit significantly weaker than in the **PCL<sub>80</sub>/A** reference blends. **c-d**, Corresponding intensity profiles normalized with respect to the maximum intensity of the lamellar long period ( $L_p = 17.5$  nm). **e**, A plot of the areas of the Bragg reflection corresponding to  $d_A = 2.8$  nm, normalized using the reflection of the lamellar long period and divided by the additive content, as a function of additive contents qualitatively shows the transition from homogeneous (nanophase-separated) materials to macroscopic phase separation towards the threshold concentration of 5 wt%. It is worth noting that establishing any form of mixing, such as small-strain melt shearing in a rheometer (open square) or large-strain melt-stretching (open circle) of **PCL<sub>80</sub>(Ala<sub>2</sub>Ac)<sub>2</sub>/A** (5 wt%) blends during cooling results in, respectively, a substantial reduction or even a complete disappearance of the  $d_A = 2.8$  nm feature.

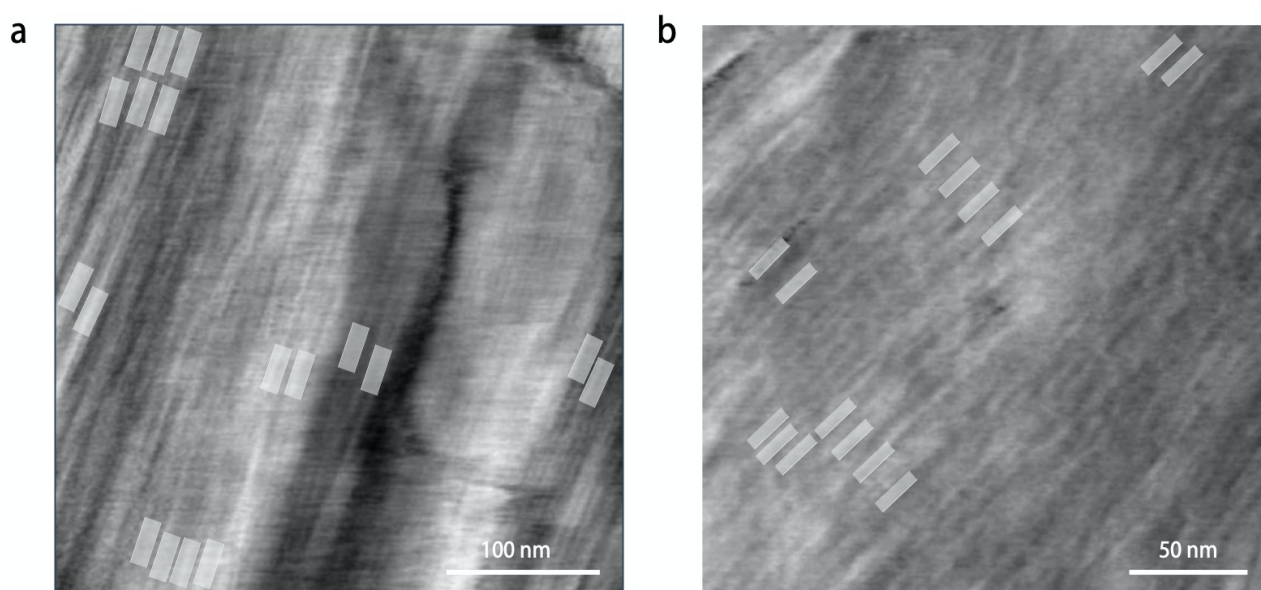


**Figure 24. Uniform nanofibrils in **PCL<sub>80</sub>(Ala<sub>2</sub>Ac)<sub>2</sub>/A**.** *a*) AFM phase images of **PCL<sub>80</sub>(Ala<sub>2</sub>Ac)<sub>2</sub>/A** (2 wt%) on film specimens (prepared by hot pressing 80 °C) recorded at 65 °C, and *b*) of **PCL<sub>80</sub>(Ala<sub>2</sub>Ac)<sub>2</sub>/A **PCL<sub>80</sub>(Ala<sub>2</sub>Ac)/A** (5 wt%) recorded at 55 °C after cooling *in situ* from 70 °C, revealing well-defined nanofibrils with lengths of at least several micrometers that are homogeneously distributed throughout the material; these nanofibrils are compliant objects that are locally aligned with a periodic spacing of  $d_{nf} = 18.7 \pm 2.5$  nm (averaged over the distances between the indicated white lines) for **PCL<sub>80</sub>(Ala<sub>2</sub>Ac)<sub>2</sub>/A** (2 wt%) and  $d_{nf} = 13.1 \pm 3.0$  nm for **PCL<sub>80</sub>(Ala<sub>2</sub>Ac)<sub>2</sub>/A **PCL<sub>80</sub>(Ala<sub>2</sub>Ac)/A** (5 wt%) on film specimens (prepared by hot pressing at 80 °C).****

In this nanophase-separated regime, the co-assembly of additive and end groups and their bioinspired hierarchical structure formation effectively suppresses additive crystallization. Thus, AFM images of **PCL<sub>80</sub>(Ala<sub>2</sub>Ac)<sub>2</sub>/A** blends recorded at 60°C, that is, above the PCL melting temperature, reveal a network of what is best described well-defined nanofibrils that are homogeneously distributed across the entire sample and have a uniform width of below 5 nm, lengths of at least several micrometers, a high persistence length, and occasionally show a helical fine structure (Figure 24). It is important to note that these nanofibrils are unlike nanocrystals or mesophase precipitates but compliant one-

dimensional nanoscopic objects that can bend, entangle, and locally align with one another. Comparing the nanofibril dimensions, their morphology and rigidity with previous examples,<sup>258,260,261</sup> they are most likely constituted of a helically twisted stack of a defined number of  $\beta$ -sheet tapes. This is a manifestation of hierarchical structure formation, as also known from silk materials or amyloid fibers where lateral aggregation is self-limiting due to the inherent helicity of the aggregates and therefore results in equilibrium structures with a defined, uniform diameter.

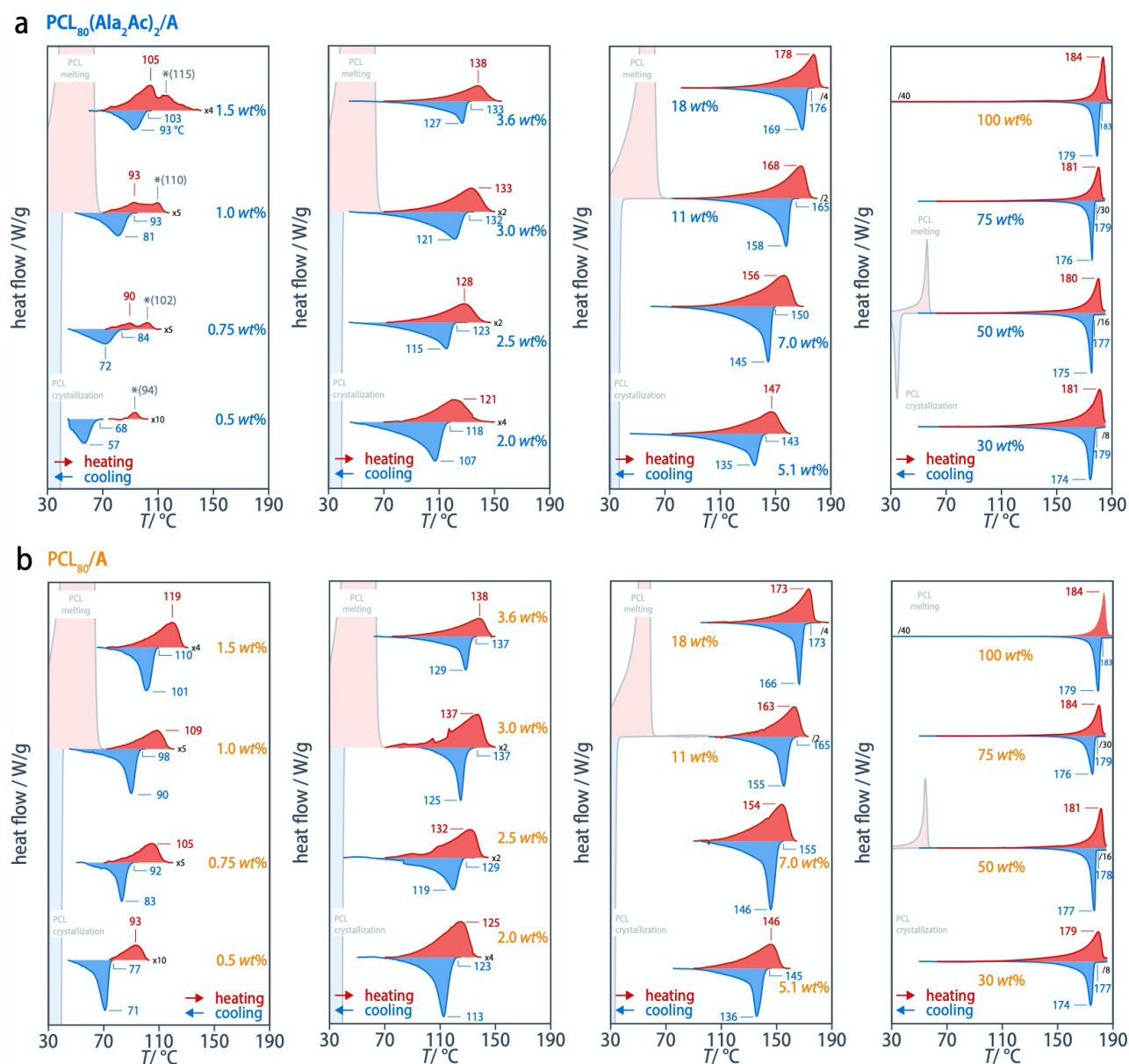


**Figure 25. Thermal Transitions in  $\text{PCL}_{80}(\text{Ala}_2\text{Ac})_2/\text{A}$  and  $\text{PCL}_{80}/\text{A}$  Blends.** First DSC cooling (blue, with indicated onset and peak association temperatures) and second heating (red, with indicated dissociation temperatures) scans (scanning rate 10 °C/min) for *a)*  $\text{PCL}_{80}(\text{Ala}_2\text{Ac})_2/\text{A}$  blends and *b)*  $\text{PCL}_{80}/\text{A}$  reference blends from. Each blend exhibits an enthalpic peak at temperatures above the PCL melting and crystallization transition (shown for one composition only per panel for clarity), associated with dissociation and association of the additive and end groups. This peak shifts to higher temperatures with increasing additive contents and approaches the dissociation temperature of the pure additive at high additive contents. At

concentrations of up to 2 wt%, the dissociation and association transitions occur at significantly lower temperatures than in the PCL<sub>80</sub>/A reference blends. At concentrations of 5 wt%, 7 wt%, and 11 wt%, an additional shoulder can be identified in the PCL<sub>80</sub>(Ala<sub>2</sub>Ac)<sub>2</sub>/A blends (Figure 26), while no differences between the two types of blends are observed at higher additive contents. The endotherms marked with an asterisk in **a** for PCL<sub>80</sub>(Ala<sub>2</sub>Ac)<sub>2</sub>/A with additive contents less than 2 wt% occur at temperatures similar to the additive dissociation peaks in the reference blends and are hence identified with dissociation of bulk additive structures; however, since there is no corresponding exothermic transition in the cooling scans (neither in heating-cooling cycles to temperatures immediately above the onset of the main cooling exotherm), it is attributed to a “cold crystallization” of additive after their release from the nanofibrils upon their dissociation. For PCL<sub>80</sub>(Ala<sub>2</sub>Ac)<sub>2</sub>/A (0.5 wt%), only this melting of recrystallized additive is observed, whereas the dissociation of the co-assembled nanofibrils is probably obscured by the dominant PCL melting transition (not shown).

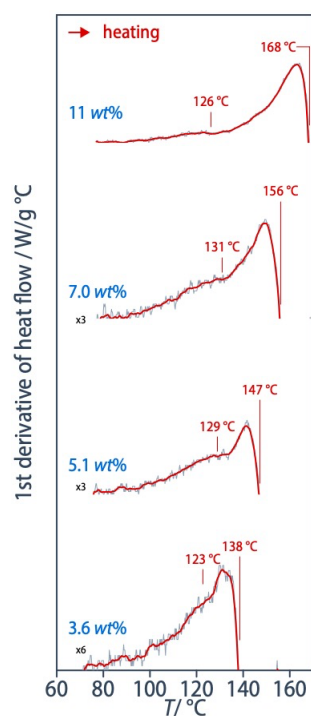


**Figure 26. Thermal Transitions in PCL<sub>80</sub>(Ala<sub>2</sub>Ac)<sub>2</sub>/A and PCL<sub>80</sub>/A Blends at Moderate Additive Contents.** First derivative of the DSC heating curves (red curves are smoothed data) for PCL<sub>80</sub>(Ala<sub>2</sub>Ac)<sub>2</sub>/A at concentrations of 3.6, 5.1, 7.0, and 11 wt% reveals a local maximum at around 123 °C, 129 °C, 131 °C, and 126 °C, respectively, which is assigned to dissociation of the co-assembled nanofibrils. This maximum precedes the main endothermic peak at 138 °C, 147 °C, 156 °C, and 168 °C, respectively, which is assumed to be due to dissociation of bulk additive domains. For PCL<sub>80</sub>(Ala<sub>2</sub>Ac)<sub>2</sub>/A blends with additive contents of 2–5 wt%, no shoulder is distinguishable because the bulk and nanofibril endotherms strongly overlap.

Moreover, they are placed at a periodic interfibrillar distance that appears to decrease with increasing additive concentration, for instance, from  $d_{nf} = 13.0 \pm 3.6$  nm at 2 wt% to  $d_{nf} = 10.5 \pm 2.7$  nm at 5 wt% of A. This dependence can be straightforwardly explained by the fact that, with increasing additive concentration in the nanofibrils, the polymer tethering density decreases.

The co-assembled nanofibrils constitute a new phase in the phase diagram of the blends PCL<sub>80</sub>(Ala<sub>2</sub>Ac)<sub>2</sub>/A, that we construct from DSC heating curves (Figure 25Figure 26), starting from a

description of the melting points observed in the PCL<sub>80</sub>/A reference blends according to a Flory-Huggins approach (Figure 27). The equilibrium dissociation temperature,  $T_d$ , of the additive in the PCL<sub>80</sub>/A reference blends is significantly lower than the equilibrium dissociation temperature of the pure additive  $T_d(\mathbf{A}) = 184$  °C in regions of the phase diagram where the binodal falls below  $T_d(\mathbf{A})$ . If the Flory-Huggins interaction parameter is of the form  $\chi = \chi_0/T + \chi_1$ , and the molar volume of the PCL is much greater than that of the additive, the variation of the additive dissociation temperature  $T_d$  with additive volume fraction,  $\phi$ , at low  $\phi$  may be expressed as

$$T_d = \frac{T_d(\mathbf{A}) + \frac{RT_d\chi_0}{\Delta H_d}(1 - \phi)^2}{1 - \frac{RT_d(\mathbf{A})}{\Delta H_d}(1 - \phi + \ln \phi + \chi_1(1 - \phi)^2)}, \quad (4)$$

where  $\Delta H_d = 32$  kJ/mol is the molar enthalpy of dissociation of the pure additive. The assumption that molar volume of the PCL is very much greater than that of the additive also implies the liquid additive-rich domains corresponding to the binodal to contain very little polymer, so that the low- $\phi$  branch of the binodal may be expressed roughly as

$$T_{bin} \approx -\frac{\chi_0(1 - \phi)^2}{1 - \phi + \ln \phi + \chi_1(1 - \phi)^2}. \quad (5)$$

Fitting of Equation 4 to the observed  $T_d$  for PCL<sub>80</sub>/A blends gives  $\chi_0 = 2756$  K and  $\chi_1 = -5.17$ , and liquid-liquid phase-separation according to Equation 5 occurs when  $T_d$  exceeds the melting point of the pure additive (184 °C), i.e., for  $\phi$  greater than about 40 wt%.

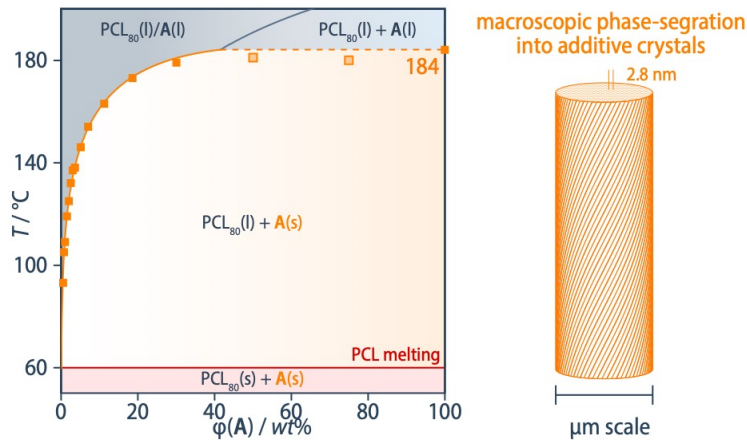


**Figure 27. Phase Diagram of PCL<sub>80</sub>/A Reference Blends.** Blends of the non-modified polymer PCL<sub>80</sub> and the additive show upper critical solution temperature-type behavior, forming an optically transparent, homogeneous melt at sufficiently high temperatures, PCL/A(l), where the suffix indicates a liquid state. At additive contents below about 40 wt%, solid bulk additive domains precipitate from the liquid phase on cooling, (PCL/A)<sub>(l)</sub>+ A<sub>(s)</sub>. The dissociation temperatures of these domains

(filled orange squares) are generally higher than the association onset temperature during cooling, implying it to be more representative of equilibrium conditions. Its concentration dependence below about 40 wt% of **A** may hence be described analytically (solid orange curve) using the Flory-Huggins approach (Equation 4). The resulting additive structures persist on further cooling below the polymer melting temperature (60 °C), where the morphology is dominated by the lamellar crystalline domains of the polymer matrix ( $\text{PCL}_{(s)} + \text{A}_{(s)}$ ). At additive contents higher than about 40 wt% (open squares), the additive solidifies directly from a liquid-liquid phase-separated state, consisting of a highly additive-rich liquid phase and a polymer-rich liquid phase,  $(\text{PCL}/\text{A})_{(l)} + \text{A}_{(l)}$ . It therefore solidifies at temperatures close to the melting temperature of the pure additive (dashed orange line). The grey solid curve is the binodal line for liquid-liquid phase separation calculated from Equation 5 using the above values for  $\chi_0$  and  $\chi_1$ .

Similar to the reference blends, the  $\text{PCL}_{80}(\text{Ala}_2\text{Ac})_2/\text{A}$  blends show upper critical solution temperature-type behavior, forming an optically transparent, homogeneous melt at sufficiently high temperatures, but precipitation of solid bulk additive domains from the liquid phase on cooling. The concentration dependence of the additive dissociation temperatures  $T_d$  in the concentration range of 5–40 wt% of **A** follows the Flory-Huggins curve of the reference blends (Figure 28). Below about 2.5 wt%, however, the dissociation temperatures start to deviate significantly from this behavior and show reversible transitions at lower temperatures that, according to the optical microscopy and AFM results, can be attributed to the reversible formation of the nanofibrils.

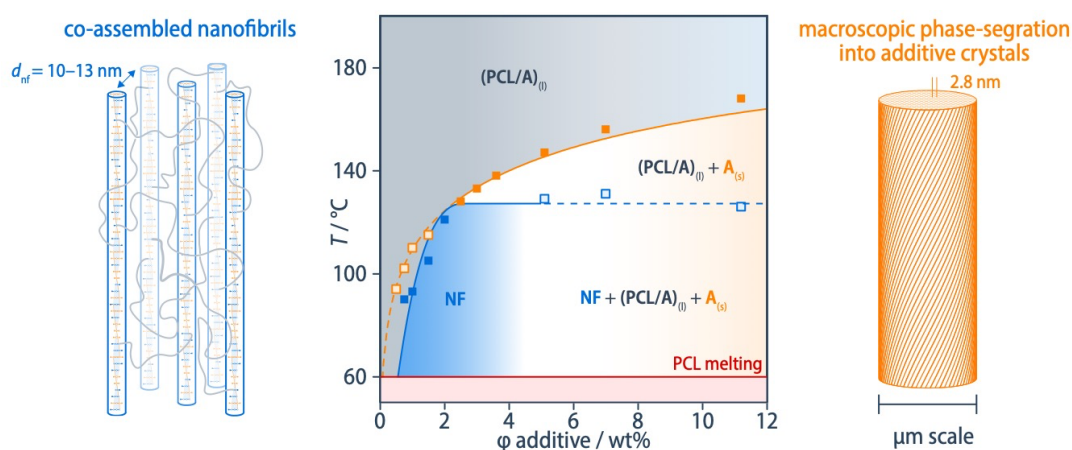


**Figure 28. Phase diagram of  $\text{PCL}_{80}(\text{Ala}_2\text{Ac})_2/\text{A}$  blends.** Also the  $\text{PCL}_{80}(\text{Ala}_2\text{Ac})_2/\text{A}$  blends show upper critical solution temperature-type behavior, forming an optically transparent, homogeneous melt at sufficiently high temperatures, but precipitation of solid bulk additive domains precipitate from the liquid phase on cooling,  $(\text{PCL}/\text{A})_{(l)} + \text{A}_{(s)}$ . The concentration dependence of the additive dissociation temperatures  $T_d$  in the concentration range of 5–40 wt% of **A** (filled orange squares) can be described analytically using the Flory-Huggins approach (Equation 4, solid orange line, corrected for the end group concentration of 0.5 wt%). However, unlike the reference blends based on the non-modified polymer, at low additive contents the morphology is dominated by nanofibrils (**NF**) resulting from co-assembly of the polymer end groups and additive. The dissociation temperature of the co-assembled nanofibrils, identified with the lower of the two additive endotherms observed in DSC heating scans (Figure 25) at low additive contents (filled blue squares), are significantly lower than the bulk additive dissociation temperatures in the  $\text{PCL}_{80}/\text{A}$  reference blends and Equation 4 (hatched orange line). These reduced dissociation

temperatures are attributed to the high specific interfacial area of the nanofibrils, and the free energy cost associated with polymer chain attachment. The upper additive endotherms (empty orange squares), on the other hand, follows Equation 4 closely over most of the composition range shown, and is identified with dissociation of the bulk additive as a result of “cold crystallization” of additive released upon dissociation of the nanofibrils formed during the previous cooling cycle. The nanofibrils are hence exclusively present in the phase domain marked **NF**, up to about 5 wt%.

We can thus conclude that the end-modified polymer **PCL<sub>80</sub>(Ala<sub>2</sub>Ac)<sub>2</sub>** acts like a compatibilizer and suppresses the formation of macroscopically phase-separated microfibrillar precipitates of **A** (at sufficiently low concentrations). Moreover, due to the bio-inspired hierarchical structure formation, this co-assembly process results in well-defined nanofibrils with uniform diameter, constituted of a helically twisted stack of a defined number of  $\beta$ -sheet tapes that, rather than nanocrystals, should be regarded as compliant “supramolecular graft copolymers” with tethered polymer “side chains” whose molecular weight is many times larger than their entanglement molecular weight. At the same time, the nanofibrils are homogeneously distributed in the material, and their semi-ordered network bears resemblance to a “cylindrical phase” typical of an ABA triblock copolymer, albeit with domain diameters of a few nanometers, which implies that an estimated 60% of the tethered polymer segments are in fact bridging two nanofibrils.<sup>286–289</sup>

The co-assembled nanofibrils are a highly effective nucleating agent for PCL crystallization, supposedly due to both their maximized dispersion and polymer tethering. Thus, PCL crystallization half-times according to isothermal DSC at 45 °C decrease from  $\tau_{1/2} = 4060$  s for pristine PCL<sub>80</sub> to 1410 s for PCL<sub>80</sub>/**A** (2wt%) and continue to decrease to 970 s for additive concentrations as high as 18 wt%. However, they are reduced by almost one order of magnitude to  $\tau_{1/2} = 660$  s for the pure modified **PCL<sub>80</sub>(Ala<sub>2</sub>Ac)<sub>2</sub>**, and further to 160 s for the blend **PCL<sub>80</sub>(Ala<sub>2</sub>Ac)<sub>2</sub>/**A** (2 wt%) (Figure 29). This overall 25-fold decrease in crystallization half-times thus demonstrates the synergistic effect of end group modification and nanofibril formation. The nanofibrils do not limit the polymer crystallization though, as indicated by an unaffected degree of crystallinity of about 40% (Figure 29c) and the preserved orthorhombic crystal structure (Figure 30).**

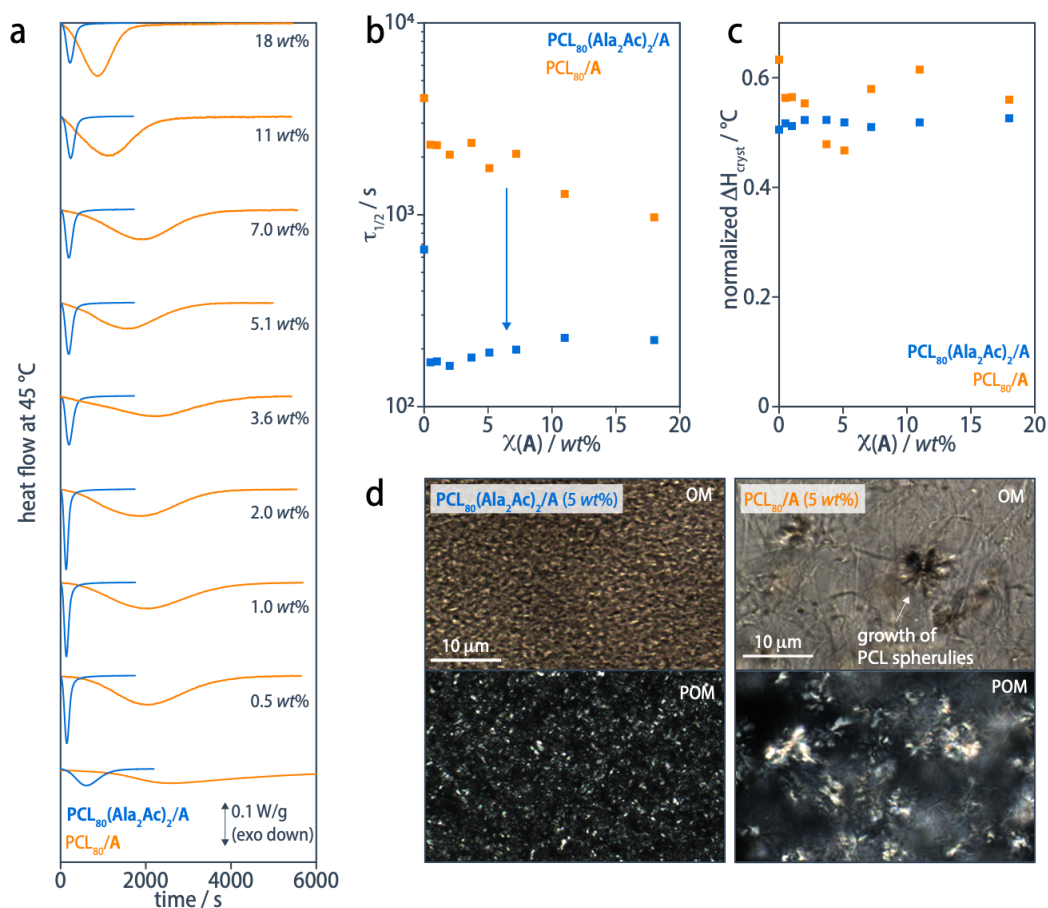


**Figure 29. Nucleation of PCL crystallization.** *a*) Isothermal DSC curves recorded at 45 °C after cooling from the melt state (10 °C/min), revealing that polymer crystallization for any  $\text{PCL}_{80}(\text{Ala}_2\text{Ac})/\text{A}$  blend (blue) occurs drastically faster than in the corresponding  $\text{PCL}_{80}/\text{A}$  reference blends (orange); for clearer visualization, the heat flow of the reference blends was multiplied by a factor of 5. *b*) The crystallization half times,  $\tau_{1/2}$ , of the  $\text{PCL}_{80}(\text{Ala}_2\text{Ac})/\text{A}$  blends are one order of magnitude shorter half-times than those of the corresponding  $\text{PCL}_{80}/\text{A}$  blends. *c*) The degree of crystallinity of the PCL phase, determined by integration of second DSC heating curves after cooling from the melt at 10 °C/min remains around 40% for all  $\text{PCL}_{80}(\text{Ala}_2\text{Ac})/\text{A}$  and  $\text{PCL}_{80}/\text{A}$  blends, indicating that it is independent on the type and amount of additive structures. The melting enthalpy of an ideal PCL crystal is assumed to be 139.5 J/g.<sup>290</sup> *d*) Optical microscopy images recorded at 45 °C, revealing a crystalline texture based on small spherulitic structures for  $\text{PCL}_{80}(\text{Ala}_2\text{Ac})/\text{A}$  (5 wt%) already after 3 min (left), but a yet incomplete crystallization into large spherulites for the  $\text{PCL}_{80}/\text{A}$  (5 wt%) after 18 min (right).



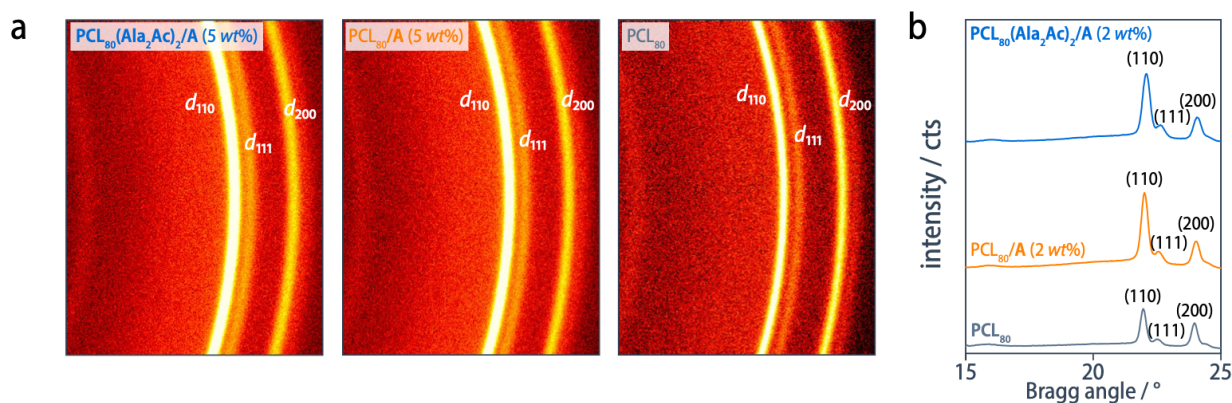


**Figure 30. PCL crystallization.** *a)* Representative WAXD patterns and *b)* corresponding plots of intensity versus Bragg angle of  $\text{PCL}_{80}(\text{Ala}_2\text{Ac})_2/\text{A}$  blends, of  $\text{PCL}_{80}/\text{A}$  reference blends, and of pristine PCL show reflections associated with Miller indices (110), (111) and (200), indicative of the orthorhombic crystal structure of PCL, indicating that the polymer crystal structure is not affected by the presence of the nanofibrillar co-aggregates found in the  $\text{PCL}_{80}(\text{Ala}_2\text{Ac})_2/\text{A}$  (2 wt%), neither by the microfibrillar precipitates in  $\text{PCL}_{80}/\text{A}$  (2 wt%).

As we will show in what follows, the hierarchical structure formation into semirigid but still compliant nanofibrils with uniform diameter and tethered polymer segments well above the entanglement molecular weight, described above, is a unique feature that distinguishes our system from the few examples of “supramolecular reinforcement” of hydrogen-bonded polymers with low molecular weight additives reported previously<sup>275,276</sup> and that is critically important for the remarkable melt properties and subsequent solidification of the  $\text{PCL}_{80}(\text{Ala}_2\text{Ac})_2/\text{A}$  blends that opens new melt processing pathways proceeding under deformation.

Oscillatory shear rheology temperature sweeps (1 rad/s, cooling at 10 °C/min) demonstrate that the  $\text{PCL}_{80}(\text{Ala}_2\text{Ac})_2/\text{A}$  blends exhibits a new rubbery regime at temperatures well above the PCL crystallization temperature, where the materials continue to show elastic behavior, with a storage modulus,  $G'$ , larger than the loss modulus,  $G''$  (Figure 31). Both the softening temperature,  $T_s$  (defined as the  $G'/G''$  crossover temperatures indicating the end of the rubbery plateau and the onset of predominantly viscous flow) and the plateau modulus (defined as  $G'$  at 60°C) can be systematically modulated with the additive concentration (Figure 32).

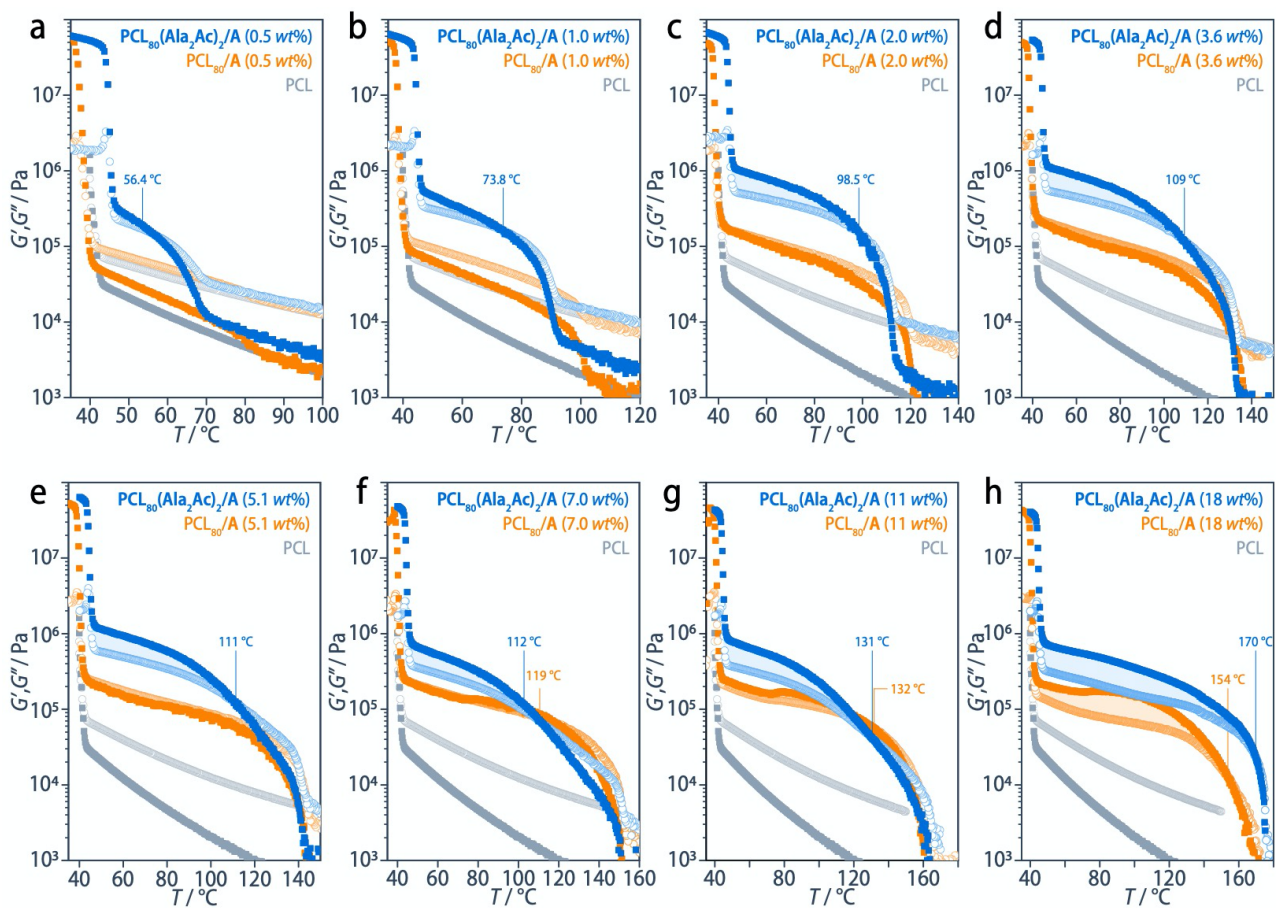


**Figure 31. Temperature-dependent oscillatory shear rheology.** *a–h*) A comparison of storage modulus,  $G'$  (filled squares), and loss modulus,  $G''$  (open circles), determined from oscillatory shear rheology temperature sweeps (frequency 1 rad/s, cooling rate 1 °C/min) reveals that the  $\text{PCL}_{80}(\text{Ala}_2\text{Ac})_2/\text{A}$  blends (blue) exhibit a rubbery regime, defined as  $G' > G''$  (blue area), above the PCL crystallization onset temperature,  $T_c = 36$  °C. Both the plateau modulus, defined as  $G'$  at 60°C, and the rheological softening temperature,  $T_s$ , indicated in the plots and defined as the  $G'/G''$  cross-over temperatures, can be tailored with the additive concentration (Figure 32). Above  $T_s$ , the melt modulus sharply drops towards the values observed for non-modified PCL (grey). By comparison, the  $\text{PCL}_{80}/\text{A}$  reference blends show a gradual transition from a rheological liquid ( $G' < G''$ ) at  $[\text{A}] = 0.5$  wt% to a rheological gel ( $G' \approx G''$ ) at  $[\text{A}] \approx 5$  wt%; finally, at additive contents  $[\text{A}] > 7$  wt%, elastic behavior is observed in  $\text{PCL}_{80}/\text{A}$ , supposedly because the threshold concentration for the formation of a percolation network of the macroscopically phase-separated microfibrillar additive precipitates is exceeded. Even in this high concentration regime, however, the melt moduli remain one order of magnitude lower than those observed in  $\text{PCL}_{80}(\text{Ala}_2\text{Ac})_2/\text{A}$  blends.

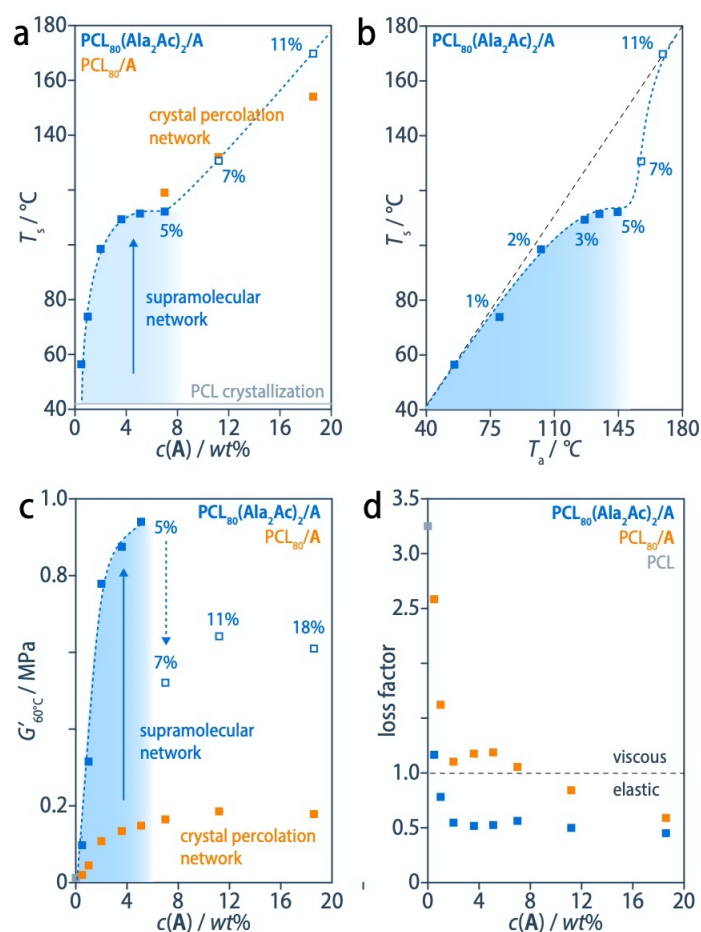


**Figure 32. Reinforced supramolecular network of  $PCL_{80}(Ala_2Ac)_2/A$  blends.** *a*) Plot of rheological softening temperatures,  $T_s$ , defined as the  $G'/G''$  cross-over temperatures (Figure 31) as a function of additive contents. For the  $PCL_{80}(Ala_2Ac)_2/A$  blends (blue),  $T_s$  increases steeply at low additive contents and then levels off towards  $T_s = 110$  °C at an additive concentration of 4–5 wt%; further increasing the additive concentration initially does not affect  $T_s$ ; only in the high additive contents regime ( $\geq 18$  wt%),  $T_s$  increases again which we attribute, by comparison to the  $PCL_{80}/A$  blends (orange) and the optical microscopy results (Figure 19), to the formation of a percolation network of the microfibrillar precipitates. *b*) Comparison of rheological softening temperatures,  $T_s$ , with the association temperatures,  $T_a$ , obtained by DSC analysis (Figure 25), revealing an excellent match in the nanofibrillar regime at additive concentrations  $\leq 2$  wt%, which implies that all additive molecules contribute to a rheologically active network, whereas this ceases to be the case when approaching the additive threshold concentration of 5 wt% for macroscopic phase separation according to optical microscopy (Figure 19). *c*) Plot of the plateau modulus  $G'$  at 60 °C as a function of additive concentration, showing the progressive reinforcement of the rubbery phase of the  $PCL_{80}(Ala_2Ac)_2/A$  materials up to almost 1 MPa at  $[A] = 5$  wt%; the subsequent decrease implies that the macroscopic phase separation at higher additive concentration disrupts the network; by comparison, the  $PCL_{80}/A$  reference blends show a substantially smaller increase in  $G'$ . *d*) Moreover, a plot of the loss factor,  $\tan \delta$ , at 60 °C as a function of additive contents demonstrates that only the  $PCL_{80}(Ala_2Ac)_2/A$  materials show elastic behavior ( $\tan \delta < 1$ ) at concentrations lower than the threshold concentration of 5 wt%; the reference blends  $PCL_{80}/A$  show elastic behavior only at high additive concentrations ( $\geq 11$  wt%), which we attribute to the formation of a percolation network of the microfibrillar precipitates.

Thus,  $T_s$  initially increases steeply with increasing additive concentration up to the threshold concentration for exclusive nanofibril formation of 2 wt%, and then converges to about 110 °C for 5 wt%, which provides an up to 50 °C wide processing window above the PCL melting temperature. The resulting plateau value of ca. 110 °C can, hence, be interpreted as the equilibrium aggregation temperature of the fully developed nanofibril network. Likewise,  $G'$  at 60 °C monotonously increases from 0.10 MPa at 0.5 wt% to reach a maximum of 0.94 MPa at 5 wt% of **A**, representing a more than two orders of magnitude increase in melt strength over pristine PCL. Different from most other melt thickening approaches, however, the melt modulus sharply drops to the  $10^4$  kPa range at temperatures above  $T_s$ , that is, to the level of melt properties of pristine PCL. As a result, the materials now exhibit two distinct temperature windows, one with high melt strength and elasticity above the polymer melting point, and an additional one of low melt viscosity, the combination of which renders the materials amenable to a broad range of processing techniques. By contrast, the additive precipitates in the PCL<sub>80</sub>/**A** reference blends act as a classical melt-reinforcing filler leading to a gradual transition to a gel state but at significantly lower melt strength ( $G' \approx G'' = 0.15$  MPa at 60 °C for 5 wt%) and with no evident elastic response (except at high additive loadings  $\geq 18$  wt%, due to the formation of a percolation network of the microfibrillar precipitates in both PCL<sub>80</sub>(Ala<sub>2</sub>Ac)<sub>2</sub>/**A** and PCL<sub>80</sub>/**A** reference blends).

These results demonstrate that the polymer-bridged nanofibrils synergistically serve as reinforcing elements and physical cross-links for the molten polymer chains so that the materials are transformed into reinforced supramolecular networks at additive concentrations of 5 wt% or below. Moreover, while changes in rheological behavior are commonly observed in supramolecular polymers and networks,<sup>244</sup> they typically do not translate into meaningful properties at large strains and under tensile loads. In our case, however, the presence of well-defined polymer-tethered nanofibrils in the PCL<sub>80</sub>(Ala<sub>2</sub>Ac)<sub>2</sub>/**A** materials, and their interconnection with well-entangled polymer segments, gives rise to continued thermoplastic behavior at temperatures well above the polymer melting temperature, and results in strain hardening and extreme melt extensibilities.

Thus, uniaxial extensional viscosity measurements on hot-pressed films at a strain rate of 2 s<sup>-1</sup> at 70 °C, that is, well above the PCL melting temperature, reveal a more than one order of magnitude larger viscosity in PCL<sub>80</sub>(Ala<sub>2</sub>Ac)<sub>2</sub>/**A** (5 wt%) than in PCL<sub>80</sub>/**A** (5 wt%), while this experiment is impossible to perform with pristine PCL due to its low melt strength (Figure 33a). Importantly, while PCL<sub>80</sub>/**A** (5 wt%) exhibits viscous flow at larger strains, PCL<sub>80</sub>(Ala<sub>2</sub>Ac)<sub>2</sub>/**A** (5 wt%) shows pronounced strain hardening.

As can be seen from the corresponding stress-strain plots (Figure 33b), the material effectively behaves like a thermoplastic solid at temperature where the PCL matrix is completely molten.

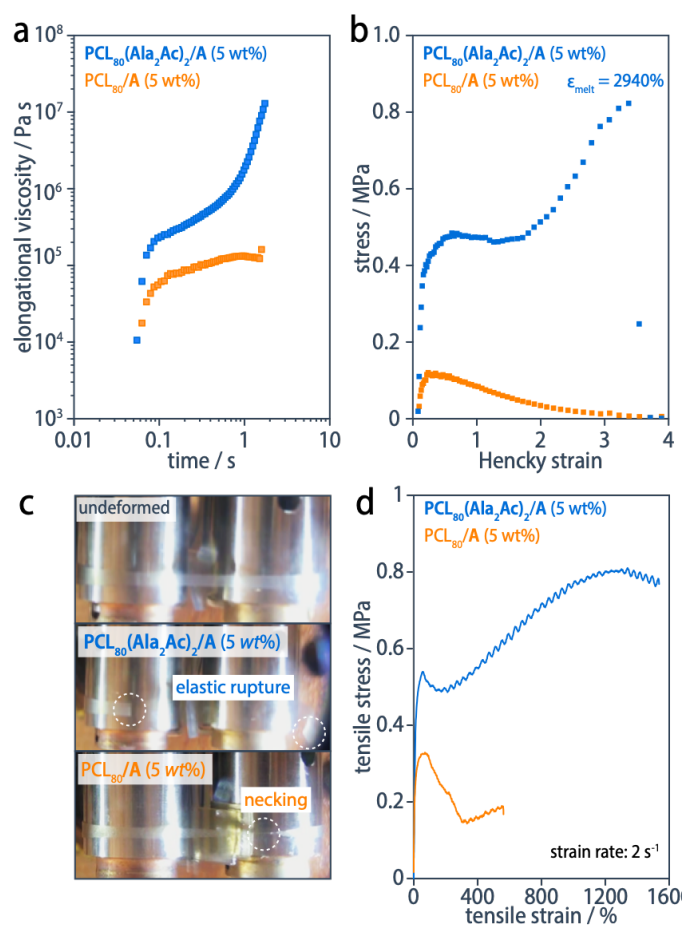


**Figure 33. Thermoplastic behavior of PCL<sub>80</sub>(Ala<sub>2</sub>Ac)/A above the PCL melting temperature.** *a*) Elongational viscosity measurements performed on hot-pressed sheets of the blend PCL<sub>80</sub>(Ala<sub>2</sub>Ac)/A (5 wt%) (blue) and the PCL<sub>80</sub>/A (5 wt%) reference blend (orange) 70 °C (strain rate 2 s<sup>-1</sup>), that is, significantly above the PCL melting temperature; no data for pristine PCL are shown because the material already disintegrated on pre-heating before the actual experiment. The uniaxial extensional flow of the PCL<sub>80</sub>(Ala<sub>2</sub>Ac)/A (5 wt%) blend is characterized by a more than one order of magnitude higher extensional viscosity compared to the reference blend and pronounced strain-hardening behavior. *b*) Corresponding stress-strain curves at 70 °C shows an initially elastic behavior with a comparably high stiffness of  $E = 6.1$  MPa, then yielding at a yield strength of  $\sigma_y = 0.48$  MPa at a yield strain of  $\epsilon_y = 120\%$ , and finally significant strain hardening above a Hencky strain of 1.72 ( $\epsilon = 560\%$ ), up to an ultimate strength of  $\sigma_y = 0.82$  MPa at a Hencky strain of 3.38 ( $\epsilon_{\max} = 2940\%$ ). By contrast, in spite of the melt reinforcement observed for PCL<sub>80</sub>/A (5 wt%) in oscillatory shear rheology (Figure 31), the material exhibits viscous behavior under these conditions. *c*) Only the PCL<sub>80</sub>(Ala<sub>2</sub>Ac)/A (5 wt%) blend shows an elastic rupture with a clean fracture edge, whereas PCL<sub>80</sub>/A (5 wt%) exhibits necking and flow before rupture. *d*) Stress-strain curves in the melt state of PCL<sub>80</sub>(Ala<sub>2</sub>Ac)<sub>2</sub>/A (5 wt%) in comparison to PCL<sub>80</sub>/A (18 wt%) recorded during tensile testing at 70 °C (strain rate 2 s<sup>-1</sup>) shows that while PCL<sub>80</sub>(Ala<sub>2</sub>Ac)<sub>2</sub>/A (5 wt%) reproduces elongational viscosity results, including initial elastic behavior and strain hardening, the PCL<sub>80</sub>/A (18 wt%) blend that shows elastic behavior in oscillatory shear rheology, attributed to a percolation network of the additive precipitates, does not predominantly shows viscous behavior and starts to flow before rupture.

It initially shows elastic behavior with a comparably high stiffness of  $E = 6.1$  MPa, then yields with a yield strength of  $\sigma_y = 0.48$  MPa at a strain of  $\varepsilon_y = 120\%$ , undergoes plastic deformation without melt rupture up to a strain of about  $\varepsilon = 610\%$ , and eventually shows significant strain hardening up to an ultimate strength of  $\sigma_{\max} = 0.82$  MPa, along with a truly remarkable total strain-at-break of  $\varepsilon_{\max} = 2940\%$  and a 22-fold increased energy-at-break of  $W = 18$  MJ/m<sup>3</sup> compared to the reference blends. Accordingly, **PCL<sub>80</sub>(Ala<sub>2</sub>Ac)<sub>2</sub>/A (5 wt%)** at 70 °C still undergoes elastic rupture as the dominant failure mode (Figure 33c), while the reference blends exhibit the viscous behavior typical of an entangled polymer melt, show necking, and starts to flow before rupture, even at high additive loadings (18 wt%, Figure 33d), which demonstrates that a mere melt reinforcement is not sufficient.

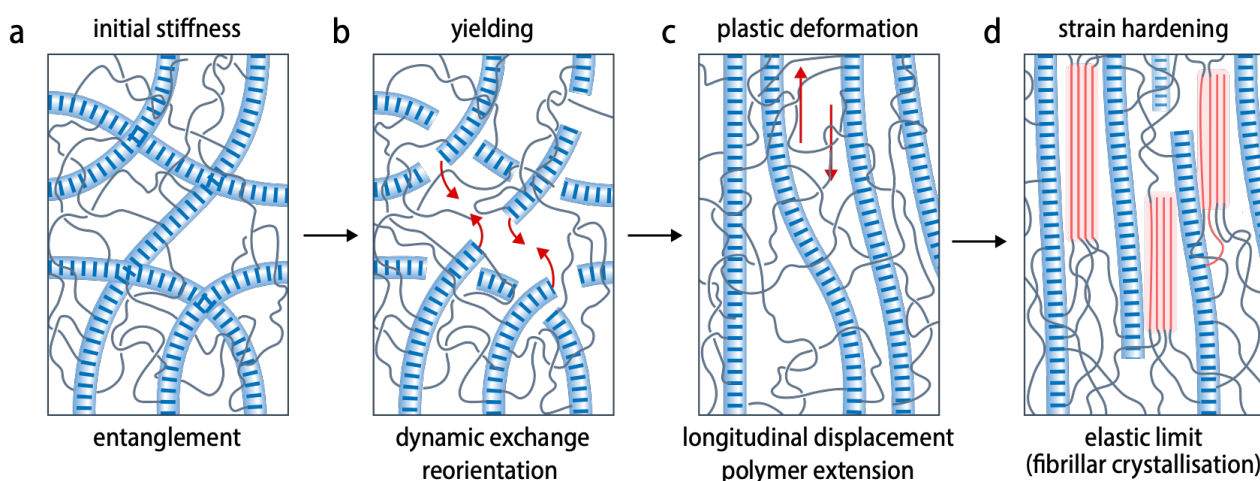


**Figure 34. Proposed synergistic interplay of entanglement and nanofibril dynamics.** *a)* We attribute the initial elastic behavior and the high initial stiffness of the **PCL<sub>80</sub>(Ala<sub>2</sub>Ac)<sub>2</sub>/A** blends above the PCL melting temperature to the nanofibrils being trapped in the well-entangled polymer matrix and potentially entangled themselves. *b)* The subsequent yielding of the material requires a break-down of the load-bearing elements in the preceding elastic regime, which we associate with the dynamic exchange of co-assembled hydrogen-bonded end groups and additive molecules at 70 °C, that facilitates disentanglement and reorientation of the nanofibrils. *c)* Consequently, the well-defined nanofibrils become aligned and do not interlock when sliding along each other, providing a mechanism for plastic deformation up to large strains, under conformational extension of the tethered polymer chains. *d)* Strain hardening occurs either due to the polymer network reaching its elastic limit, or due to strain-induced crystallization into fibrillar crystals, at least, upon cooling

Instead, the **PCL<sub>80</sub>(Ala<sub>2</sub>Ac)<sub>2</sub>/A** blends appear to show a synergistic interplay of the transient supramolecular network, melt reinforcement, and efficient coupling to polymer matrix (Figure 34). Thus, we attribute the initial elastic behavior and high stiffness to the nanofibrils being entrapped in polymer entanglement network and possibly entangled themselves. We interpret the subsequent yielding to be associated with a break-down of the nanofibril network due to entanglement-enforced load transfer to the nanofibrils, resulting in dynamic end group exchange (at sufficiently elevated

temperatures) and (partial) disentanglement. This process should allow for nanofibril reorientation and alignment in the applied mechanical field. The well-defined nature of the aligned nanofibrils and their semirigid nature is then relevant for the subsequent plastic deformation where they become the load-bearing elements and can be longitudinally displaced relative to one another without interlocking, different from, for instance, the hard domains in TPUs. This process proceeds under conformational extension of the weakly entangled bridging polymer segments of the softer polymer matrix. At sufficiently high strain rates (and at low temperatures where end group exchange is sufficiently slow) to not allow the bridging polymer chains to completely relax, strain hardening finally occurs when the polymer network reaches its elastic limit, or fibrillar crystallization occurs, at least, upon cooling (see below).

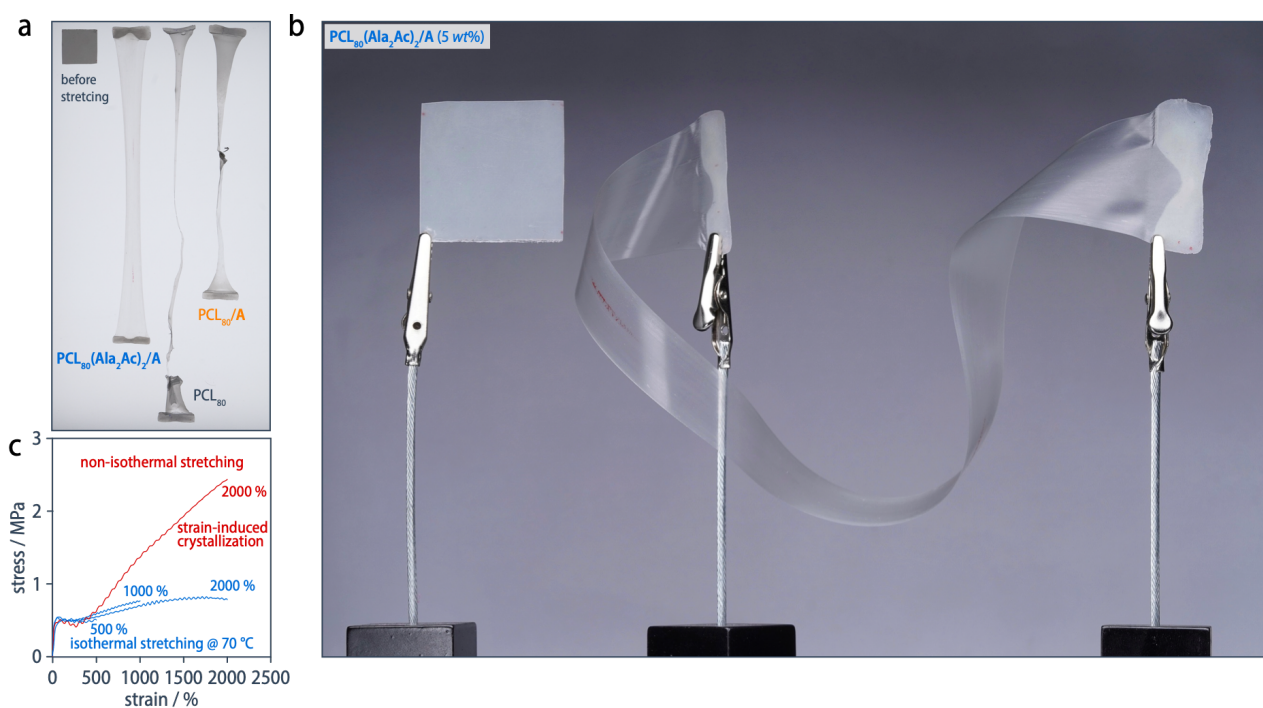


**Figure 35. Facilitated film melt stretching.** *a)* Photograph of sheet specimens (prepared by hot-pressing at 80 °C and cooling to room temperature at a rate of 10 °C/min) uniaxially deformed in tension at 70 °C and a strain rate of 2 s<sup>-1</sup> using an ultimate testing machine (UTM). Only the PCL<sub>80</sub>(Ala<sub>2</sub>Ac)<sub>2</sub>/A (5 wt%) blends display strain hardening under these conditions and can hence be melt-stretched up to large deformations into films with uniform thickness and materials distribution. Reference materials from PCL<sub>80</sub>/A (5 wt%) or pristine PCL show necking and viscous flow. *b)* Photograph confirming the uniform melt deformation of a hot-pressed sheet from PCL<sub>80</sub>(Ala<sub>2</sub>Ac)<sub>2</sub>/A (5 wt%) into an extended film. *c)* In-situ stress-strain curves recorded during film preparation by uniaxial melt-stretching of PCL<sub>80</sub>(Ala<sub>2</sub>Ac)<sub>2</sub>/A (5 wt%) sheets (strain rate 2 s<sup>-1</sup>). The stretching was performed at 70 °C (blue) and to different stretching ratios of 500%, 1000%, and 2000%. The latter is close to the maximum extensibility as determined from elongational viscosity data (Figure 33). The measurements confirm the initially stiff behavior, yielding, and strain hardening of PCL<sub>80</sub>(Ala<sub>2</sub>Ac)<sub>2</sub>/A (5 wt%) materials in film drawing above the PCL melting temperature. The strain-hardening was particularly pronounced in case of non-isothermal stretching conditions (red), that is, simultaneous melt stretching and cooling below the crystallization temperature of PCL.

The observed tensile properties and large-strain response at temperatures above the polymer melting temperature, in combination with accelerated polymer crystallization, are highly relevant for the application of industrial processing techniques that proceed under deformation, such as film blowing, injection stretch blow molding, thermoforming, or foaming. The pronounced strain hardening, for instance, provides a self-leveling effect on deformation, leading to a uniform thickness, which is the key feature for the success of PET in bottle manufacturing.<sup>291</sup> Indeed, the **PCL<sub>80</sub>(Ala<sub>2</sub>Ac)<sub>2</sub>/A** blends can be subjected to a variety of demanding melt processing conditions that proceed under large deformations or require high thermal stability. For example, film drawing of hot-pressed sheets of **PCL<sub>80</sub>(Ala<sub>2</sub>Ac)<sub>2</sub>/A** (5 wt%) at 70 °C at a strain rate of 2 s<sup>-1</sup> (Figure 35) results in homogeneous anisotropic films with a high degree of orientation, well-controlled microstructure, and a tailorable mechanical response at room temperature (*vide infra*). This is impossible with pristine PCL or **PCL<sub>80</sub>/A** reference blends, as they can only be deformed into inhomogeneous filaments.



**Figure 36. Facilitated film blowing.** Film blowing experiment at 70 °C, demonstrating that, upon application of an overpressure of 0.1 bar, sheets (prepared by hot-pressing at 80 °C and cooling to room temperature at a rate of 10 °C/min) from **PCL<sub>80</sub>(Ala<sub>2</sub>Ac)<sub>2</sub>/A** (5 wt%) form stable bubbles with a uniform materials distribution up to substantial deformations, which is not possible with either **PCL<sub>80</sub>/A** blends or pristine PCL.



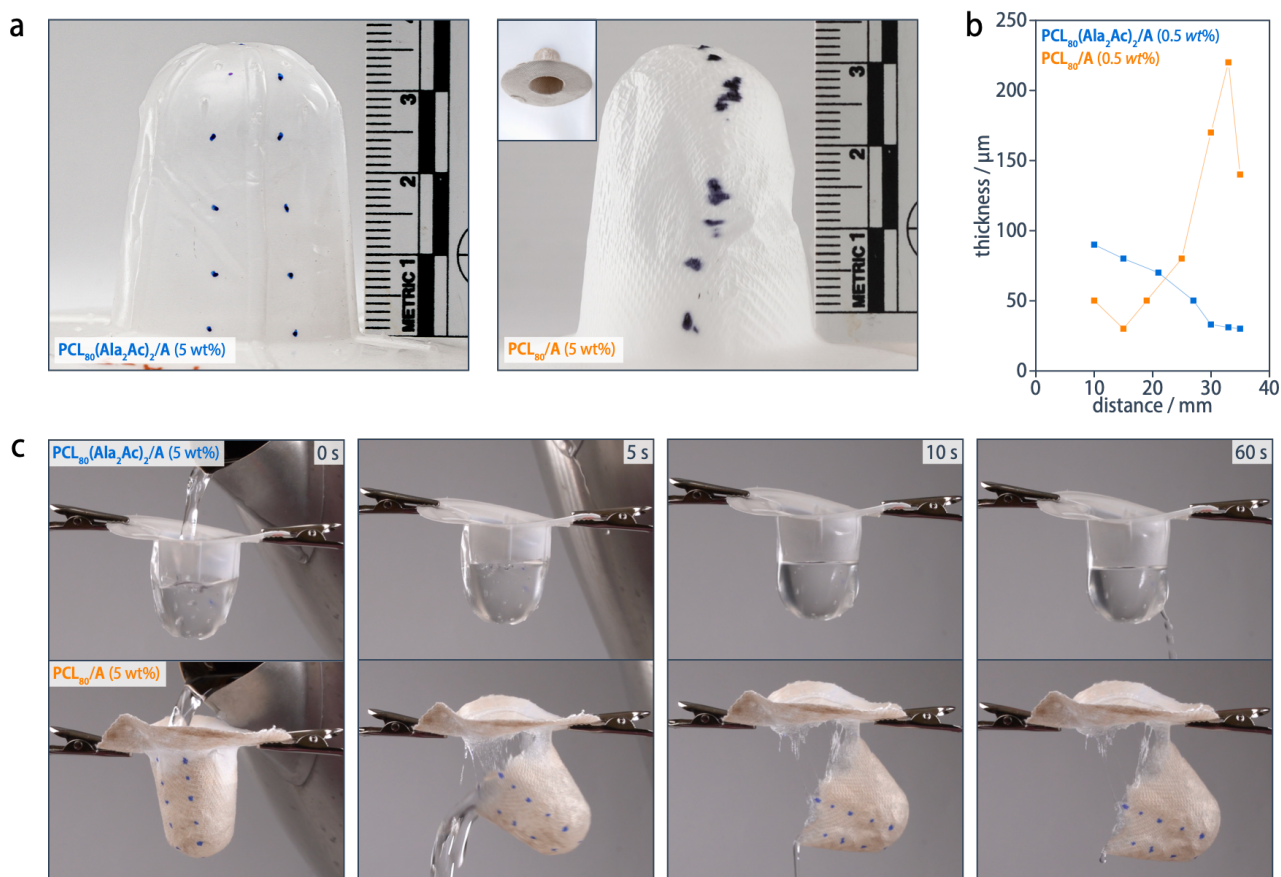


**Figure 37. Facilitated thermoforming and increased thermal stability.** *a–b*), Photographs of cup-shaped specimens from **PCL<sub>80</sub>(Ala<sub>2</sub>Ac)<sub>2</sub>/A (5 wt%)** and **PCL<sub>80</sub>/A (5 wt%)** prepared by thermoforming of hot-pressed sheets at 80 °C. Only the **PCL<sub>80</sub>(Ala<sub>2</sub>Ac)<sub>2</sub>/A** blend can be thermoformed into self-standing specimens with a wall thickness of 30–90 μm. By contrast, the **PCL<sub>80</sub>/A** material could only be thermoformed using a paper support (inset), which leads to a comparably inhomogeneous wall thickness ranging from 30–220 μm. *c*) Moreover, cup-shaped specimens prepared from **PCL<sub>80</sub>(Ala<sub>2</sub>Ac)<sub>2</sub>/A** retain thermal dimensional stability at temperatures well above the polymer melting temperature; for instance, upon filling with boiling water, the cups immediately turn transparent as a result of the PCL melting but remain shape-persistent for minutes, even under load; the leakage after 60 s can be attributed to a defect where the mold was connected to the vacuum line. By contrast, the **PCL<sub>80</sub>/A (5 wt%)** specimen immediately disintegrates.

Moreover, film-blowing of hot-pressed sheets of **PCL<sub>80</sub>(Ala<sub>2</sub>Ac)<sub>2</sub>/A (5 wt%)** at 70°C gives rise to stable bubble formation, whereas holes emerge in sheets of pristine PCL immediately upon deformation (Figure 36). Furthermore, thermoforming of hot-pressed sheets of **PCL<sub>80</sub>(Ala<sub>2</sub>Ac)<sub>2</sub>/A (5 wt%)** results in objects with high feature fidelity that can be easily removed from the mold, are self-standing, and exhibit a homogeneous film thickness of 30–90 μm (Figure 37), in contrast to **PCL<sub>80</sub>/A** reference blends that can only be thermoformed against a cup-shaped paper support and leads to more inhomogeneous thickness distribution (30–140 μm). Moreover, the thermoformed **PCL<sub>80</sub>(Ala<sub>2</sub>Ac)<sub>2</sub>/A** cups exhibit thermal dimensional stability at up to 100 °C, as evidenced by the fact that, when filled with boiling water, the cups become transparent, due to the melting of the PCL matrix, but remain shape persistent

even under the weight of the hot water, which is a remarkable achievement for a PCL-based material, given the PCL melting temperature of  $T_c = 61\text{ }^\circ\text{C}$  (Figure 37c).

One can utilize the extraordinary melt extensibility to prepare highly anisotropic PCL materials from melt-stretched films with a high degree of orientation, well-controlled microstructure, and a tailorable mechanical response at room temperature. To this end, hot-pressed sheets of **PCL<sub>80</sub>(Ala<sub>2</sub>Ac)<sub>2</sub>/A (5 wt%)** have been stretched isothermally at 70 °C to draw ratios of  $\epsilon_{\text{melt}} = 500\%$ , 1000% and 2000%, or non-isothermally to 2000% under cooling from 70 °C to room temperature to ensure that the materials undergo strain-hardening, which is particularly pronounced for the latter condition (Figure 35c).

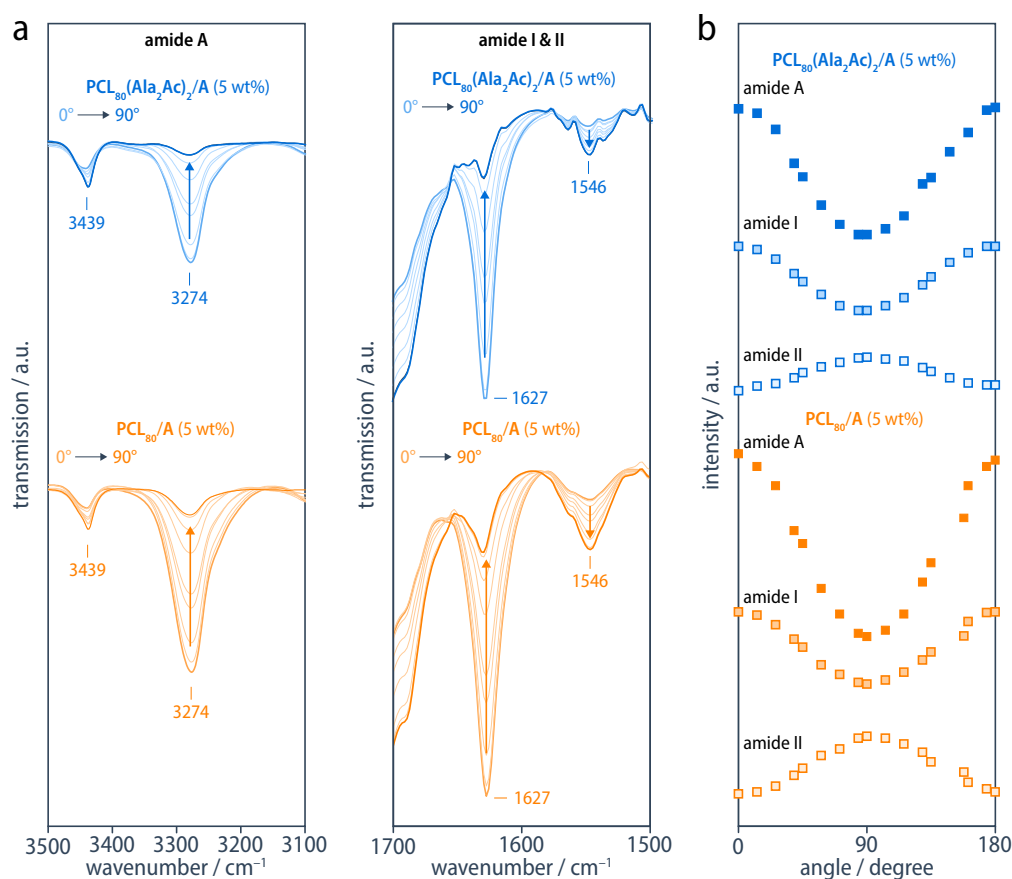


**Figure 38. Oriented aggregate structures.** *a*) Polarized IR spectra of melt-stretched film from **PCL<sub>80</sub>(Ala<sub>2</sub>Ac)<sub>2</sub>/A (5 wt%)** and **PCL<sub>80</sub>/A (5 wt%)** showing Amide A, I, and II regions at different polarizer positions, and *b*) a plot of the transmission intensity of the band maxima against the angle between polarizer and the stretching direction. The Amide A and Amide I bands showed a maximum absorption intensity parallel to the stretching direction, and the Amide II band showed a maximum absorption intensity perpendicular to the stretching direction in both cases, which is consistent with an average orientation of the hydrogen-bonded aggregates parallel to the stretching direction.

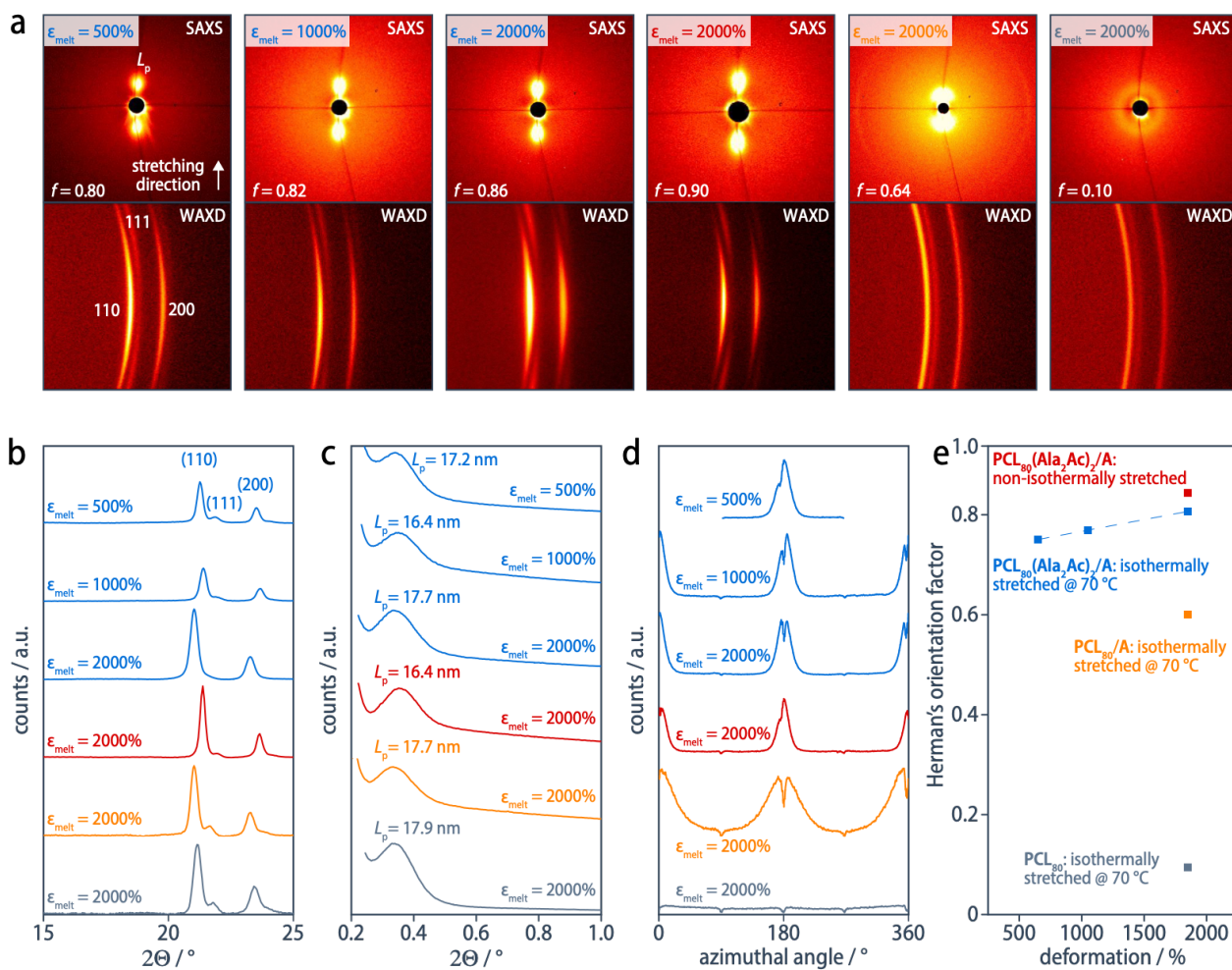


**Figure 39. X-ray characterization of melt-stretched PCL materials.** *a*) SAXS and WAXD diffraction patterns of  $\text{PCL}_{80}(\text{Ala}_2\text{Ac})_2/\text{A}$  (5 wt%), prepared via melt-stretching at 70 °C at different stretching ratios (500%, 1000%, and 2000%) or upon stretching to 2000% and simultaneous cooling from 70 °C to below the PCL crystallization temperature. The resulting materials are highly oriented as indicated by the strongly anisotropic meridional scattering signal of the lamellar long periods,  $L_p$ , and the equatorial 110 and 200 reflections. By comparison, a melt-stretched  $\text{PCL}_{80}/\text{A}$  (5 wt%) reference and PCL filaments (Figure 35) exhibit a comparably low degree of orientation and nearly isotropic scattering signals, respectively. *b*) Corresponding 1D equatorial WAXD profiles show that the crystallization of PCL into its usual orthorhombic crystal structure is maintained with lattice parameters  $d_{110} = 0.42$  nm,  $d_{111} = 0.41$ ,  $d_{200} = 0.38$  nm observed for all materials. *c*) 1D meridional SAXS profiles indicating marginally lamellar long periods,  $L_p = 16$ –18 nm. *d*) azimuthal plot of the lamellar long period,  $L_p$ , show narrow diffraction signals for the melt-stretched  $\text{PCL}_{80}(\text{Ala}_2\text{Ac})_2/\text{A}$  (5 wt%) materials, a significantly broader signal for the  $\text{PCL}_{80}/\text{A}$  (5 wt%) reference blend, and isotropic scattering for pristine PCL. *e*) Herman's orientation factor,  $\langle P \rangle$ , for the orientation of PCL lamellae of the different PCL materials as a function of the stretching ratio as calculated from the SAXS data reveals a high degree of orientation for all melt-stretched  $\text{PCL}_{80}(\text{Ala}_2\text{Ac})_2/\text{A}$  (5 wt%) materials as compared to  $\text{PCL}_{80}/\text{A}$  (5 wt%) or pristine PCL.

Polarized solid-state FTIR spectroscopy reveals an intensification of the amide A ( $3276 \text{ cm}^{-1}$ ) and amide I ( $1627 \text{ cm}^{-1}$ ) bands in parallel polarizer orientation, and of the amide II absorption ( $1546 \text{ cm}^{-1}$ ) in perpendicular polarizer orientation, which indicates an average orientation of the nanofibrils parallel

to the film stretching axis (Figure 38). Integration over the Amide A band allows for calculating the Herman's orientation factor,  $\langle P \rangle$ , for the hydrogen-bonded aggregates using<sup>292</sup>

$$\langle P \rangle = \frac{D - 1}{D + 2} \frac{2}{3 \cos^2 \alpha - 1}, \quad (6)$$

where  $D$  is the dichroic ratio, defined as the ratio of the respective absorbances under perpendicular and parallel polarization, and  $\alpha$  is the angle between the  $\beta$ -sheet long axis and the transition dipole moment of the N-H stretching band and is assumed to be  $0^\circ$ . This gives  $\langle P \rangle = 0.86$  for the nanofibrils in **PCL<sub>80</sub>(Ala<sub>2</sub>Ac)<sub>2</sub>/A** and  $\langle P \rangle = 0.85$  for the microfibrinous precipitates in **PCL<sub>80</sub>/A**.

While 2D WAXS patterns show that the PCL keeps its orthorhombic crystal structure with polymer chains oriented along the stretching direction, corresponding 2D SAXS patterns show a meridional reflection corresponding to the lamellar long period at  $L_p = 16\text{--}18$  nm, which indicates a lamellar orientation perpendicular and a lamellar stacking parallel to the film stretching direction (Figure 39). With increasing draw ratio,  $L_p$  remains unchanged but the azimuthal width is reduced, as indicated by the associated Herman's orientation factor that increases linearly from  $\langle P \rangle = 0.80$  at  $\epsilon_{\text{melt}} = 500\%$  to  $\langle P \rangle = 0.86$  at  $\epsilon_{\text{melt}} = 2000\%$ , whereas the non-isothermally drawn films exhibit a particularly high  $\langle P \rangle = 0.90$ . By comparison, the inhomogeneous filaments that result from film drawing experiments with **PCL<sub>80</sub>/A** (5 wt%) or pristine PCL only show marginal orientation with  $\langle P \rangle = 0.64$  and  $\langle P \rangle = 0.1$ , respectively, because of fast polymer chain relaxation during melt deformation.

Furthermore, 2D synchrotron SAXS patterns show an evolution with melt stretching ratio from an isotropic scattering distribution in non-oriented films to highly anisotropic streak-like scattering pattern at  $\epsilon_{\text{melt}} = 2000\%$  (Figure 40), which is commonly attributed to the formation of "shish-kebab" structures,<sup>293</sup> that is, extended "fibrillar" polymer chain crystals and epitaxially grown folded chain lamellar crystals. These crystallographic features are particularly pronounced in the non-isothermally stretched films, where the polymer chains extended by longitudinal displacement of the nanofibrils during melt deformation can undergo strain-induced crystallization upon cooling (Figure 35Figure 35).

The formation of shish-kebab structures was further confirmed by AFM imaging performed on the surface of the deformed films, which showed a combination of (i) highly oriented fibrillar structures parallel to the drawing direction with an average spacing of about 25 nm that we attribute to fibrillar polymer crystals that (ii) occasionally show a fine structure with a spacing of 5 nm may be assigned to oriented nanofibrils (the reduced interfibrillar spacing compared to non-oriented samples being due to

the lateral shrinking of the films upon longitudinal deformation); as well as *(iii)* features protruding from the fibrillar structures and oriented perpendicular to the stretching direction that can be assigned to broken-up PCL lamellae with a periodicity of  $18 \pm 2$  nm (along the stretching direction) in excellent agreement with the lamellar long period,  $L_p$ , determined in the SAXS measurements (Figure 39).

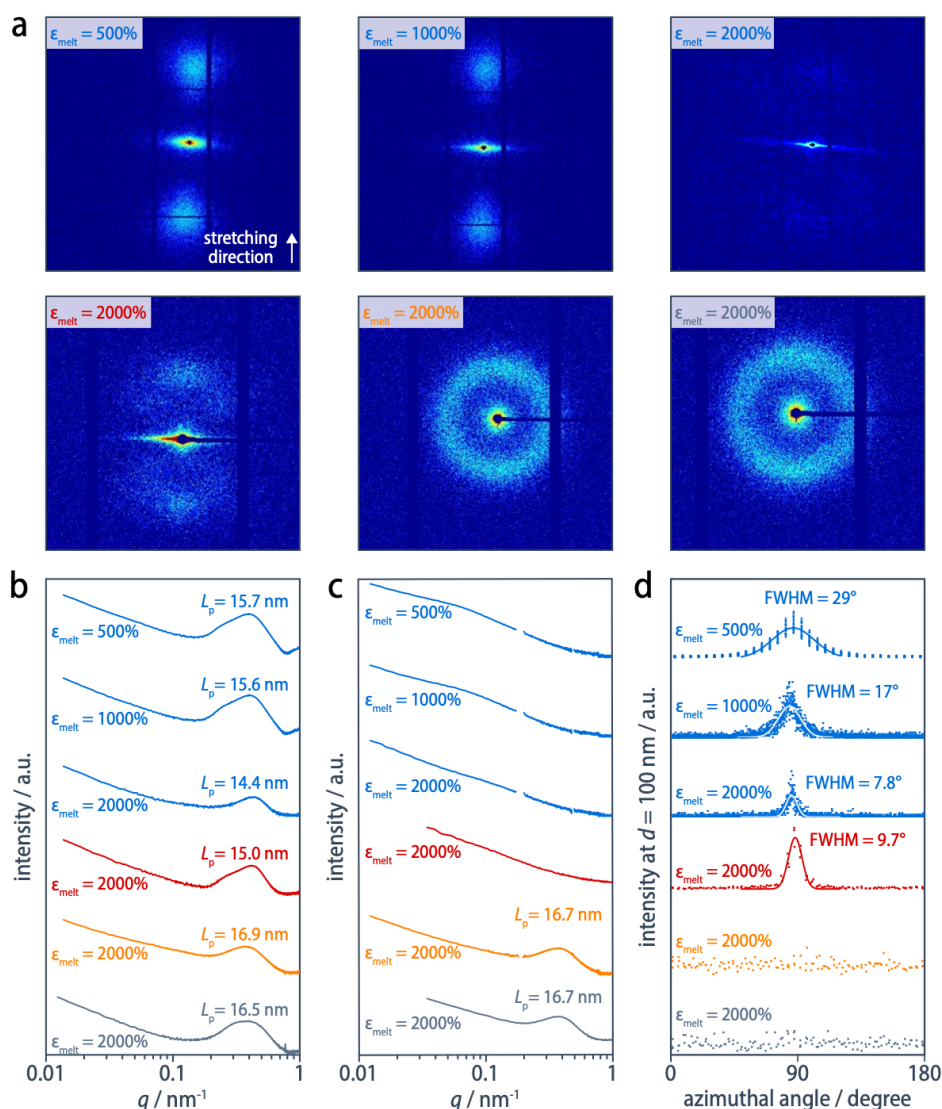


**Figure 40. Synchrotron X-ray diffraction of melt-stretched PCL materials.** *a)* 2D SAXS patterns of  $\text{PCL}_{80}(\text{Ala}_2\text{Ac})_2/\text{A}$  (5 wt%), prepared via melt-stretching at  $70^\circ\text{C}$  at different stretching ratios  $\epsilon_{\text{melt}} = 500\%$ ,  $1000\%$ , and  $2000\%$ , (blue) or upon stretching to  $\epsilon_{\text{melt}} = 2000\%$  and simultaneous cooling from  $70^\circ\text{C}$  to below the PCL crystallization temperature (red), in comparison to melt-stretched filaments from  $\text{PCL}_{80}/\text{A}$  (5 wt%) (orange) and pristine PCL (grey). In addition to the meridional scattering signal of the lamellar long period, only the  $\text{PCL}_{80}(\text{Ala}_2\text{Ac})_2/\text{A}$  (5 wt%) materials show an streak-like equatorial scattering feature that is commonly assigned to the formation of shish-kebab structures. *b–c)* Corresponding 1D meridional and equatorial SAXS profiles showing the lamellar long period,  $L_p = 14\text{--}17$  nm, for lamellae oriented perpendicular to the melt-stretching direction in the melt-stretched  $\text{PCL}_{80}(\text{Ala}_2\text{Ac})_2/\text{A}$  (5 wt%) specimens, whereas the  $\text{PCL}_{80}/\text{A}$  (5 wt%) and PCL (grey) samples are isotropic. *d)* Azimuthal plot of the streak-like feature (determined at a  $d$ -spacing of  $100$  nm) reveals that the full width at half maximum (FWHM) decreases with increasing draw ratio, indicating increasing orientation of the fibrillar polymer crystals.

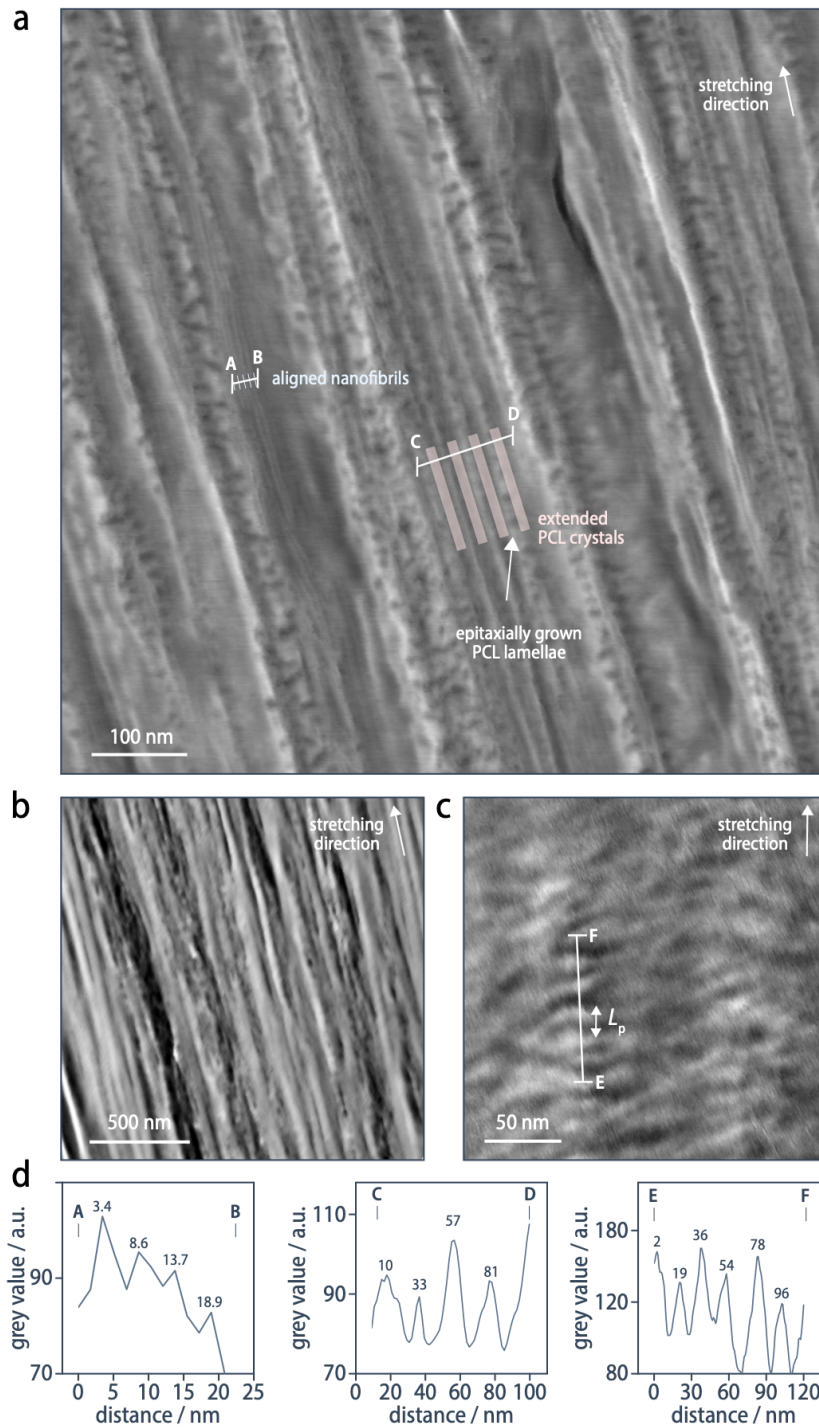


**Figure 41. Shish-kebab structures in highly oriented PCL<sub>80</sub>(Ala<sub>2</sub>Ac)/A materials.** *a)* AFM phase image of the non-isothermally melt-stretched PCL<sub>80</sub>(Ala<sub>2</sub>Ac)<sub>2</sub>/A (5 wt%) films, revealing a highly oriented material composed of shish-kebab structures and aligned nanofibrils oriented along the melt-stretching direction. Their reduced average interfibrillar spacing of 5 nm (profile A–B) compared to the non-oriented state (13 nm) is attributed to the lateral shrinking of the films upon uniaxial deformation. The strain-induced crystallization leads to the formation of fibrillar PCL structures oriented parallel to the melt-drawing direction, which are spaced at an average distance of 25 nm (profile C–D). *b)* Corresponding profiles of the AFM phase images. *c)* The AFM phase image of the same material at lower magnification shows highly oriented fibrillar PCL structures. *d)* AFM phase image showing epitaxially grown PCL lamellae that periodically stack at an average distance of 18 ± 2 nm (profile E–F), which is in excellent agreement with the lamellar long period,  $L_p$ , observed in XRD measurements

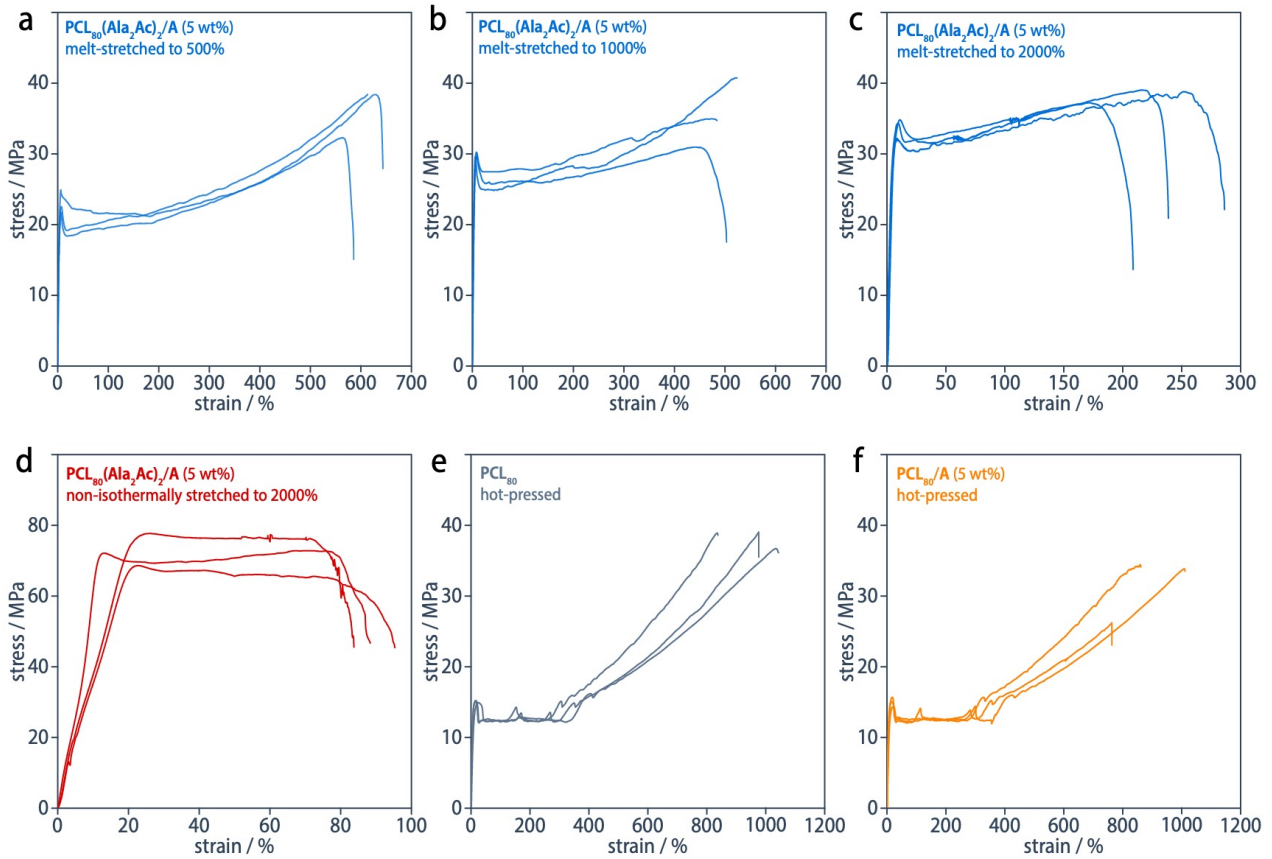


**Figure 42. Ensembles of tensile testing results of PCL-based materials.** Tensile testing stress-strain curves (strain rate  $2 \text{ s}^{-1}$ ) of *a-c*)  $\text{PCL}_{80}(\text{Ala}_2\text{Ac})_2/\text{A}$  (5 wt%) prepared by melt-stretching at  $70 \text{ }^\circ\text{C}$  and different draw ratios (blue); *d*)  $\text{PCL}_{80}(\text{Ala}_2\text{Ac})_2/\text{A}$  (5 wt%) material prepared via non-isothermal stretching conditions (red), that is, simultaneous melt stretching and rapid cooling below the crystallization temperature of PCL; *e*) pristine PCL (grey); and *f*) the  $\text{PCL}_{80}/\text{A}$  (5 wt%) reference blend (orange).

Although shish-kebab structures have been observed in electro-spun PCL microfibers,<sup>294,295</sup> they have never been obtained by bulk melt shear.<sup>296,297</sup> The increasing degree of orientation and microstructure evolution from a classical spherulitic morphology to a shish-kebab microstructures results in drastic changes in tensile properties (Figure 42, 0). Thus, the materials display up to three times higher Young's moduli (up to  $E = 740 \text{ MPa}$  at  $\epsilon_{\text{melt}} = 1000\%$ ) compared to the corresponding reference  $\text{PCL}_{80}/\text{A}$  blend or pristine PCL. At the same time, the yield strength systematically increases with stretching ratio  $\epsilon_{\text{melt}}$  from  $\sigma_y = 15 \text{ MPa}$  (non-oriented PCL) to  $34 \text{ MPa}$  at  $\epsilon_{\text{melt}} = 2000\%$ , approaching the ultimate strength of all samples of  $\sigma_{\text{max}} = 40 \text{ MPa}$ , albeit accompanied with a decrease in the elongation at break, from  $\epsilon_{\text{max}} = 945\%$  (non-oriented PCL) to  $\epsilon_{\text{max}} = 220\%$  (Figure 43). Particularly, the non-isothermally drawn films exhibit a remarkably high yield strength of  $\sigma_y = 72 \text{ MPa}$ , which is a more than five-fold increase compared to pristine PCL, and an ultimate strength of  $\sigma_{\text{max}} = 73 \text{ MPa}$ , almost twice as high as that of

pristine PCL. The increases in stiffness and yield strength can be attributed to fibrillar crystals that act as rigid reinforcement and promote the resistance towards plastic deformation. Moreover, an increased orientation of the lamellae perpendicular to the stretching direction means that their preferred slip direction becomes oriented parallel to the stretching direction, which significantly diverges from the direction of maximum shear stress ( $45^\circ$ ) so that the oriented lamellae require more stress to yield.

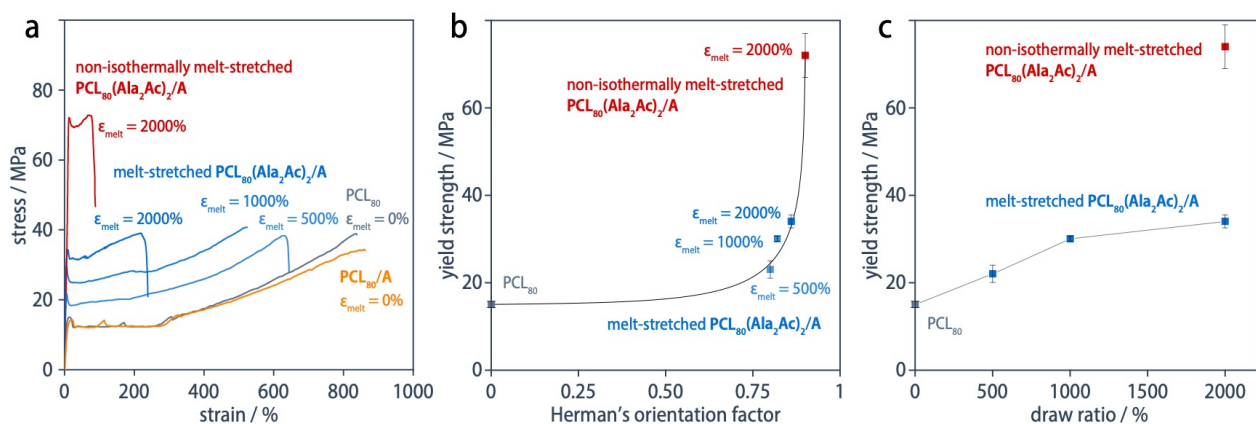


**Figure 43. Mechanical Properties of Melt-Stretched PCL Materials.** *a)* Representative stress-strain curves (room temperature, strain rate  $2 \text{ cm s}^{-1}$ ) taken from the ensembles of tensile testing results (Figure 42) of  $\text{PCL}_{80}(\text{Ala}_2\text{Ac})_2/\text{A}$  (5 wt%) melt-stretched at  $70^\circ\text{C}$  (blue) show that yield strength increases and extensibility decreases with increasing melt stretching ratio, as imposed by different draw ratios during the melt-stretching; particularly, non-isothermal stretching conditions (red), that is, simultaneous melt stretching and rapid cooling from  $70^\circ\text{C}$  below the crystallization temperature of PCL results in strongly increased stiffness, yield strength, and ultimate strength. By comparison, a hot-pressed  $\text{PCL}_{80}/\text{A}$  (5 wt%) (orange) reference blend (orange) exhibited tensile properties similar to non-oriented pristine PCL (grey). *b)* The yield strength,  $\sigma_y$ , systematically increases with melt stretching ratio,  $\epsilon_{\text{melt}}$ , but is particularly increased by non-isothermal melt stretching. The solid line serves as guide to the eyes. *c)* Corresponding plot of yield strength,  $\sigma_y$ , against Herman's orientation factor,  $\langle P \rangle$ , shows the correlation between the mechanical strength and the degree of orientation.

**Table 4** Tensile yield strength,  $\sigma_y$ , tensile strength,  $\sigma_{\text{max}}$ , tensile strain at break,  $\epsilon_{\text{max}}$ , Young's modulus,  $E$ , tensile energy at break,  $W$ , for  $\text{PCL}_{80}(\text{Ala}_2\text{Ac})_2/\text{A}$  (5 wt%) materials melt-stretched to 500%, 1000% and 2000% isothermally at  $70^\circ\text{C}$  and to 2000% non-isothermally (NI); hot pressed PCL and  $\text{PCL}_{80}/\text{A}$  (5 wt%).

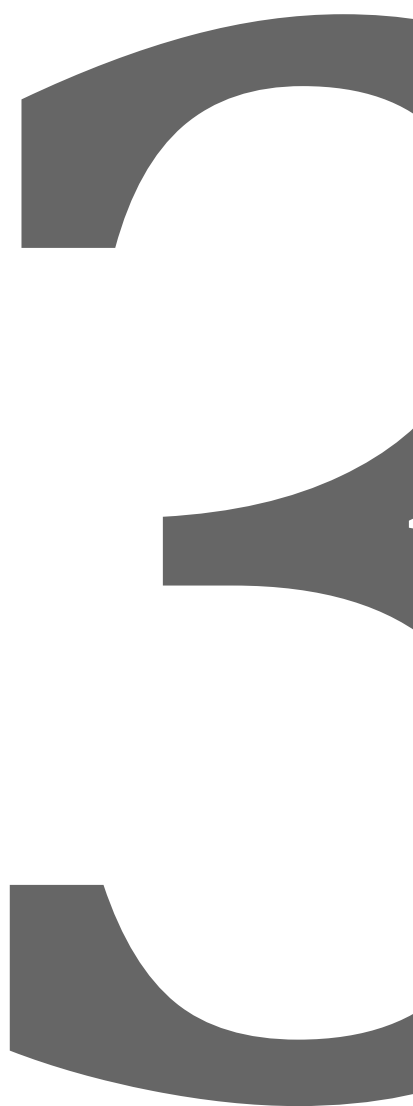
	$\text{PCL}_{80}(\text{Ala}_2\text{Ac})_2/\text{A}$ (5 wt%), 500 %	$\text{PCL}_{80}(\text{Ala}_2\text{Ac})_2/\text{A}$ (5 wt%), 1000 %	$\text{PCL}_{80}(\text{Ala}_2\text{Ac})_2/\text{A}$ (5 wt%), 2000 %	$\text{PCL}_{80}(\text{Ala}_2\text{Ac})_2/\text{A}$ (5 wt%), 2000 %NI	$\text{PCL}_{80}$ hot- pressing	$\text{PCL}_{80}/\text{A}$ (5 wt%) hot- pressing
preparation conditions	melt-stretching to 500 %	melt-stretching to 1000 %	melt-stretching to 2000 %	melt-stretching to 2000 % (non-isothermally)	hot-pressing	hot-pressing
$\sigma_y$ (MPa)	$23 \pm 2$	$29.6 \pm 0.6$	$33.6 \pm 1.5$	$72 \pm 5$	$15.0 \pm 0.2$	$14.8 \pm 0.7$
$\sigma_{\text{max}}$ (MPa)	$36 \pm 3$	$36 \pm 5$	$38.6 \pm 1.5$	$70 \pm 7$	$38 \pm 1$	$31 \pm 5$
$\epsilon_b$ (%)	$600 \pm 36$	$485 \pm 37$	$218 \pm 37$	$79 \pm 7$	$945 \pm 100$	$876 \pm 125$
$E$ (MPa)	$633 \pm 107$	$736 \pm 45$	$646 \pm 41$	$566 \pm 20$	$256 \pm 51$	$250 \pm 36$
$W$ (MJ/m <sup>3</sup> )	$155 \pm 10$	$148 \pm 10$	$83 \pm 14$	$56 \pm 1$	$195 \pm 22$	$164 \pm 34$



## 2.3 Conclusions

In summary, we have demonstrated that the co-assembly of oligopeptide-based polymer end groups and a corresponding low-molecular weight additive is an excellent approach to address what we deem the most important shortcomings in terms of processing properties and final product performance limiting the broader technological application of typical aliphatic polyesters, for which we have chosen PCL as a representative example. Our results demonstrate that the silk-inspired hierarchical structure formation of a supramolecular network of well-defined and nanofibrils bridged with polymer chains well above their entanglement molecular weight are critical features that determine these properties. In this way, we have improved the melt strength of PCL by two orders of magnitude into the MPa range that is typically used for processing. We have introduced large-strain melt elasticity and stiffness, plastic deformation without melt rupture, and an extreme melt extensibility of up to almost 3'000 % into the material at temperatures where the polymer matrix is fully molten. This renders the polymer amenable to processing techniques that require large melt deformations and are impossible to pursue with typical soft aliphatic polyesters. Moreover, the heat resistance of PCL was elevated to temperatures of at least 100 °C, which is relevant for many consumer applications. We have reduced crystallization half-times by a factor of 20, which is relevant for process cycle times, will be particularly for polyesters with hindered crystallization. Finally, these properties have allowed us to produce oriented materials with altered polymer microstructure and significantly increased stiffness and yield strength, which is, again, difficult with the pristine polymer. The combined results are highly relevant for the manufacturing of, for instance, sustainable packaging films, thermoplastic elastomers, or elastomer foams, based on aliphatic polyesters.<sup>298</sup> More generally speaking, since the end group and additive co-assembly should be possible in other types of polymer, as long as they are not too polar or directly compete for hydrogen bonding, we regard the chosen approach as a versatile method for the modification of polymers at technologically relevant molecular weights. As a circular plastics economy will demand to reduce the number of employed polymer grades to facilitate reverse logistics and recycling, this is relevant. because one will still have to cover the broad range of properties covered by the materials that are to be replaced.

# Supramolecular Modification for Poly( $\epsilon$ -caprolactone) Filaments



The results presented in this chapter are part of a manuscript in preparation:

*“Reinforced Supramolecular Networks for Tailoring Mechanical Properties of Poly( $\epsilon$ -caprolactone) Filaments”, Yevhen Hryshunin, Shuichi Haraguchi, Holger Frauenrath<sup>1\*</sup>, to be submitted.*

H.F. conceived the idea and directed the research. S.H. synthesized the materials. Y.H. prepared all the mixtures and performed all testing unless otherwise stated. The manuscript was written by Y.H. and H.F.

## Introduction

The production of plastics worldwide continues to increase, reaching over 460 million metric tons in 2021, with around 75% of all plastics produced being petroleum-based polymers.<sup>1-3</sup> Currently, open-loop recycling streams for post-consumer waste plastics are only available for a limited number of polymers, including polyethylene (PE), polypropylene (PP), and bottle-grade polyethylene terephthalate (PET), with only PET being recycled in significant quantities.<sup>12,299</sup> As a result, less than 14% of all plastics are currently collected for recycling, and the majority ends up in landfills or leaks into the environment, posing a significant threat to ecosystems globally.<sup>226</sup> To address this problem, a future circular plastics economy will need to consider alternative materials such as biodegradable or bio-sourced plastics and chemical recycling to monomer. Biodegradable polyesters obtained via ring-opening polymerization (ROP) of monomers from renewable resources can be seen as an attractive class of materials class for a circular plastics economy because there is a clear and selective depolymerization pathway by ring-closing depolymerization (RCD).<sup>12,20</sup> Moreover, PCL is a biodegradable aliphatic polyester with a glass transition of  $T_g = -60\text{ }^\circ\text{C}$  and a melting temperature of  $T_m = 60\text{ }^\circ\text{C}$  and is known to be a highly ductile material with an elongation at break of up to 1000%, a Young's modulus of approximately 200 MPa, and a yield strength and ultimate strength of 15 MPa and 40 MPa, respectively.<sup>65,80</sup> However, the mechanical properties of PCL can be drastically altered, for instance by melt and room temperature drawing. Recently, Selli *et al.* showed that PCL fibers can achieve a yield and ultimate strength of 300 MPa and 450 MPa, respectively, with a concomitant decrease in elongation at break to 70%.<sup>77,81</sup> Despite the many advantages of PCL, it is not broadly used in engineering or commodity applications mostly due its insufficient thermal stability and its poor processability because of its very low melt strength.

One method of improving melt processability is the introduction of long-chain branching to the polymer backbone, which can be accomplished with a variety of methods, including ROP with multifunctional monomers, functional group polycondensation, chain extension, radical-induced reactions, and dynamic vulcanization.<sup>99</sup> For example, the introduction of branching to PCL by  $\gamma$ -irradiation resulted in a rubber-like behavior up to temperatures of 200 °C and strain hardening behavior in the melt with only an insignificant change in molecular weight from  $M_n = 90'000$  to 120,000 g/mol.<sup>105</sup> Furthermore, the crystallization temperature of branched PCL produced by reactive melt processing using benzoyl peroxide was increased from  $T_c = 35\text{ }^\circ\text{C}$  to 41 °C.<sup>106</sup> While the introduction of branching has thus proven

to be a promising approach, it increases melt viscosity over the whole temperature range, which limits processing where high flow rates is required, such as in injection molding, and decreases polymer melting temperature and crystallinity, which can in turn limit the range of target applications.<sup>101,111</sup>

Multivalent hydrogen-bonded ligands have been used for the supramolecular modification of PCL. For example, Yu *et al.* prepared ureidopyrimidinone end-functionalized PCL ( $M_n = 4,000$ ), which showed self-healing properties.<sup>300</sup> However, due to the utilization of low molecular weight PCL, the mechanical properties of the resulting material were limited, exhibiting a yield strength  $\sigma_y = 5$  MPa and strain at break  $\varepsilon_{max} = 20\%$ . Recently, it was found that the poor end-group self-assembly of high molecular weight PCL ( $M_n = 80,000$ ) functionalized with oligopeptide end groups can be overcome by selective co-assembly with a low molecular weight additive based on the same oligopeptide motif, to form well-defined, polymer-tethered self-assembled helically twisted antiparallel  $\beta$ -sheet tapes. The obtained materials demonstrated an order of magnitude crystallization half-times, elastomeric strain-hardening behavior of the polymer melt, significantly higher Young's modulus and yield strength, as well as a drastically increased heat resistance.

Here, we prepared filaments by rapid stretching of a blend of **PCL<sub>80</sub>(Ala<sub>2</sub>Ac)<sub>2</sub>**, modified with acetyl-L-alanyl-L-alanyl end groups, and the additive 2-octyldodecyl acetyl-L-alanyl-L-alanyl amide **A** in the melt. Our results demonstrate that, first of all, the network of polymer-tethered  $\beta$ -sheet tapes can significantly facilitate the orientation of the crystalline PCL lamellae and formation of extended PCL crystals, which results in shish-kebab structures. Secondly, the newly obtained material's morphology leads to an increase in Young's modulus, yield, and ultimate strength to 1 GPa, 323 MPa, and 555 MPa, respectively, compared to 0.5 GPa, 110 MPa, and 300 MPa of pristine PCL<sub>80</sub>.

## 3.2 Results and Discussion

### 3.2.1 Materials Design, Structural and Mechanical Analysis of Melt-Stretched Fibers

For our studies, we chose PCL<sub>80</sub> ( $M_n = 80,000$ ) and a blend of **PCL<sub>80</sub>(Ala<sub>2</sub>Ac)<sub>2</sub>** with 5 wt% of the low molecular weight additive **A** (Figure 44), which were previously shown to aggregate into one-dimensionally extended polymer-tethered  $\beta$ -sheet nanofibrils.<sup>261</sup> This material was previously shown to exhibit an elongation at break,  $\varepsilon_{max} = 2940\%$ , and ultimate strength,  $\sigma_{max} = 0.82$  MPa, at a temperature of  $T = 70$  °C, that is, well above the PCL melting temperature.<sup>301</sup> Making use of these remarkable melt properties, fibers of **PCL<sub>80</sub>(Ala<sub>2</sub>Ac)<sub>2</sub>/A** (5 wt%) and PCL<sub>80</sub> were drawn from an extruder at constant

torque and at three different melt temperatures of 200 °C, 120 °C and 70 °C, which are, respectively, above, close to, and below the  $\beta$ -sheet aggregation temperature of 111 °C for the **PCL<sub>80</sub>(Ala<sub>2</sub>Ac)<sub>2</sub>/A** (5 wt%) blend, according to oscillatory shear rheology.<sup>301</sup> The fiber diameter was determined by optical microscopy, and fibers with diameters,  $d = 300\text{--}400\ \mu\text{m}$  were chosen for further structural and mechanical characterization.

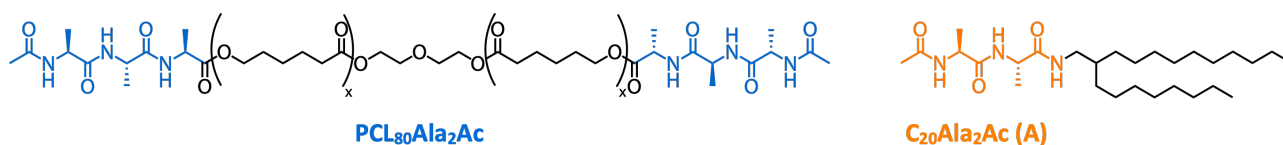


**Figure 44.** Chemical structures of telechelic poly( $\epsilon$ -caprolactone) end modified with acetyl-L-alanyl-L-alanine end groups **PCL<sub>80</sub>(Ala<sub>2</sub>Ac)** ( $M_n = 80'000$ ), as well as of the additive 2-octyldodecyl acetyl-L-alanyl-L-alanyl amide **A**

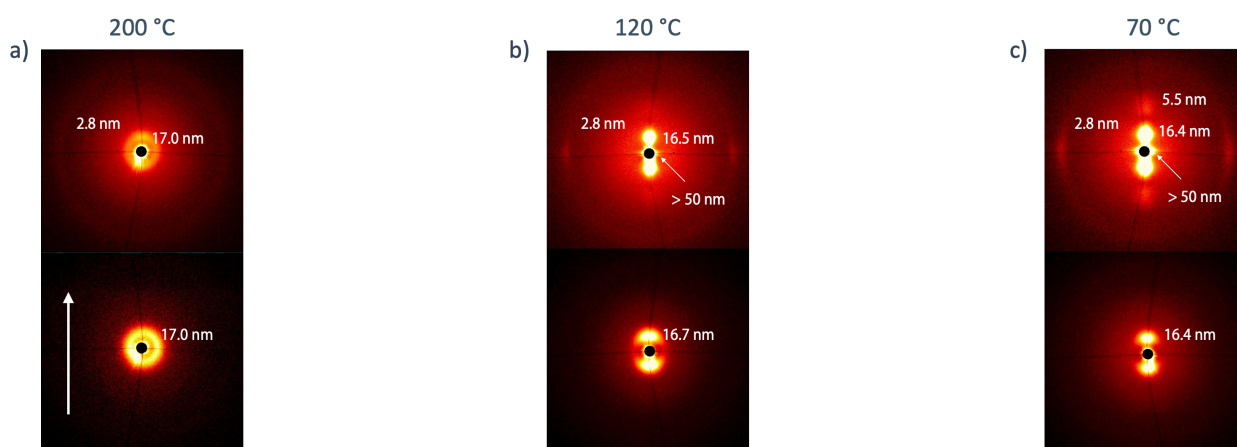


**Figure 45.** 2D small-angle X-ray scattering from fibers drawn at a) 200 °C b) 120 °C and c) 70 °C of **PCL<sub>80</sub>(Ala<sub>2</sub>Ac)<sub>2</sub>/A** (5 wt%) (top) and PCL<sub>80</sub> (bottom) showing the  $d$ -spacings corresponding to the Bragg peaks. The arrow on the bottom left indicates the drawing direction.

The uniform azimuthal intensity of the SAXS Bragg peak identified with the long period of the PCL lamellae of about 17.0 nm indicated there to be no preferential orientation in PCL<sub>80</sub> fibers drawn at 200 °C, and only slight orientation of lamellar trajectories perpendicular to the draw direction in **PCL<sub>80</sub>(Ala<sub>2</sub>Ac)<sub>2</sub>/A** (5 wt%) (Figure 45). However, for the lower drawing temperatures of 120 and 70 °C, the PCL<sub>80</sub>-based fibers showed a 2-point SAXS pattern with a meridional Bragg peak corresponding to a  $d$ -spacing of 16.5 nm, indicating preferential orientation of the lamellae perpendicular to the draw direction, with a Herman's orientation function of  $\langle P \rangle = 0.55$  and  $\langle P \rangle = 0.65$ . This suggests that the PCL chains did not completely relax their conformations during drawing at these temperatures. The orientation of the PCL lamellae perpendicular to the draw direction significantly increased further in

**PCL<sub>80</sub>(Ala<sub>2</sub>Ac)<sub>2</sub>/A (5 wt%)** fibers drawn at 120 and 70 °C, with a Herman's orientation function of  $\langle P \rangle = 0.95$  and  $\langle P \rangle = 0.94$ , respectively). It may hence be concluded that relaxation of the PCL chains is inhibited when they are tethered to the nanofibrillar network via the end groups. (Figures 45b and 45c). At the lowest drawing temperature of 70 °C, **PCL<sub>80</sub>(Ala<sub>2</sub>Ac)<sub>2</sub>/A (5 wt%)** also showed an additional broad meridional Bragg peak corresponding to a *d*-spacing of 5.5 nm, which is assigned to a higher order reflection of PCL lamellae, can be explained by the higher degree of orientation of PCL lamellae compared to the fibers drawn at 120 °C where this reflection is absent (Figure 45c). Moreover, **PCL<sub>80</sub>**, **PCL<sub>80</sub>(Ala<sub>2</sub>Ac)<sub>2</sub>/A (5 wt%)** showed a marked equatorial streak at low angles which became more pronounced at lower drawing temperatures, and was absent from the PCL<sub>80</sub> fibers. This combination of equatorial streaking and a meridional Bragg peak is commonly attributed to the formation of "shish kebab" structures. Shish kebab structures arise from orthogonal, epitaxial growth of lamellae from fibrillar extended polymer chain crystals, which in the case of fibers, are oriented parallel to the drawing direction. However, while PCL shish-kebab structures can be readily obtained by electro-spinning,<sup>294,295</sup> they have not so far been reported for shearing of the bulk melt. Finally, additional low angle Bragg scattering in the SAXS patterns for **PCL<sub>80</sub>(Ala<sub>2</sub>Ac)<sub>2</sub>/A (5 wt%)** corresponding to a *d*-spacing of 2.8 nm was attributed to the close packing distance columnar additive structures found in bulk additive precipitates. These showed no orientation in fibers drawn at 200 °C, but became oriented parallel to the draw direction in fibers drawn at 70 °C and 120 °C. To conclude, consistent with extensional viscosity experiments, **PCL<sub>80</sub>(Ala<sub>2</sub>Ac)<sub>2</sub>/A (5 wt%)** may be oriented more efficiently during melt spinning than pristine PCL<sub>80</sub> owing to the end-group tethering of the polymer chains to the nanofibrillar network, particularly at lower temperatures, where the self-assembled aggregates are presumably sufficiently stable on the time-scale of the process to restrict chain relaxation.

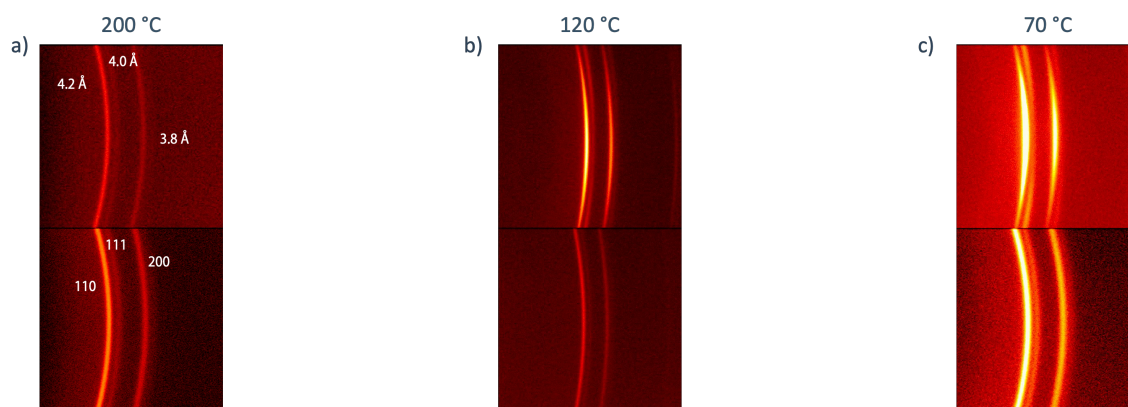


**Figure 46.** Equatorial 2D wide-angle X-Ray diffraction of fibers drawn at a) 200 °C b) 120 °C and c) 70 °C of **PCL<sub>80</sub>(Ala<sub>2</sub>Ac)<sub>2</sub>/A (5 wt%)** (top) and PCL<sub>80</sub> (bottom), showing the *d*-spacings corresponding to the Bragg peaks.

According to the PCL melting enthalpies measured from DSC first heating scans at 10 °C/min, the crystallinity of the drawn fibers remained roughly constant at around 40%. In each case, WAXD patterns showed the PCL to adopt its typical orthorhombic crystal structure with lattice parameters  $a = 7.50 \text{ \AA}$ ,  $b = 4.97 \text{ \AA}$ ,  $c = 17.3 \text{ \AA}$ , such that the  $d$ -spacings associated with the (110), (111), and (200) planes were  $d_{110} = 4.2 \text{ \AA}$ ,  $d_{111} = 4.0 \text{ \AA}$ , and  $d_{200} = 3.8 \text{ \AA}$ , respectively (Figures 46).<sup>75</sup> The PCL<sub>80</sub> fibers showed little crystallographic texture regardless of the drawing temperature, in contrast with the PCL<sub>80</sub>(Ala<sub>2</sub>Ac)<sub>2</sub>/A (5 wt%) fibers drawn at 70 °C and 120 °C which showed a strong equatorial scattering produced by crystallized PCL chains oriented parallel to the drawing direction.

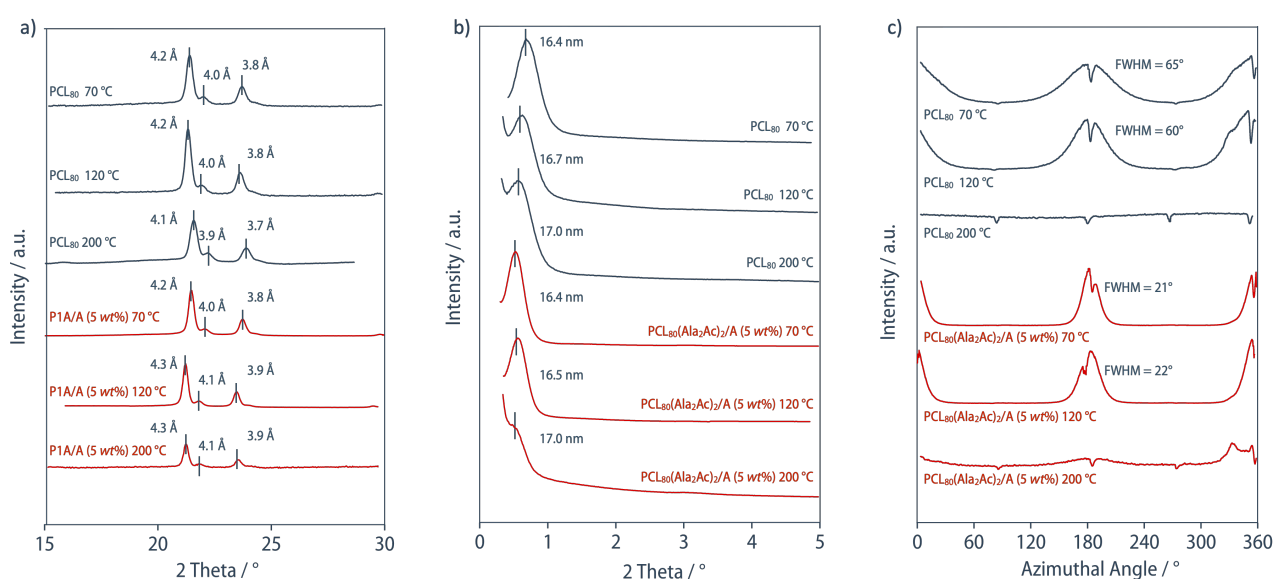


**Figure 47.** a) Equatorial wide-angle and b) meridional small-angle X-ray scattering of fibers drawn at various temperatures; c) azimuthal angle analysis of the lamellar long period indication full width at half-maximum (FWHM).

The orientation of the melt-stretched fibers was correlated with their tensile mechanical response at room temperature. All the fibers showed ductile behavior, with development of an optically visible neck, followed by strain-hardening behavior after propagation of the neck along the gauge length. The tensile properties of the PCL<sub>80</sub> fibers, which were consistent with those reported in the literature,<sup>302</sup> varied little with the degree of lamellar orientation obtained by varying the drawing temperature. The PCL<sub>80</sub>(Ala<sub>2</sub>Ac)<sub>2</sub>/A (5 wt%) fibers drawn at 200 °C and 120 °C showed only slight increases in Young's modulus, yield strength, and ultimate strength compared with the PCL<sub>80</sub> fibers, while the differences in the extension at break remained within the measuring error (Figure 48, Table 5). Moreover, although the higher lamellar orientation of the PCL<sub>80</sub>(Ala<sub>2</sub>Ac)<sub>2</sub>/A (5 wt%) fibers drawn at 70 °C was reflected by significant further increases in Young's modulus and yield strength, these were accompanied by



decreases in the strain at break and ultimate strength compared with PCL<sub>80</sub> fibers drawn at the same temperature.

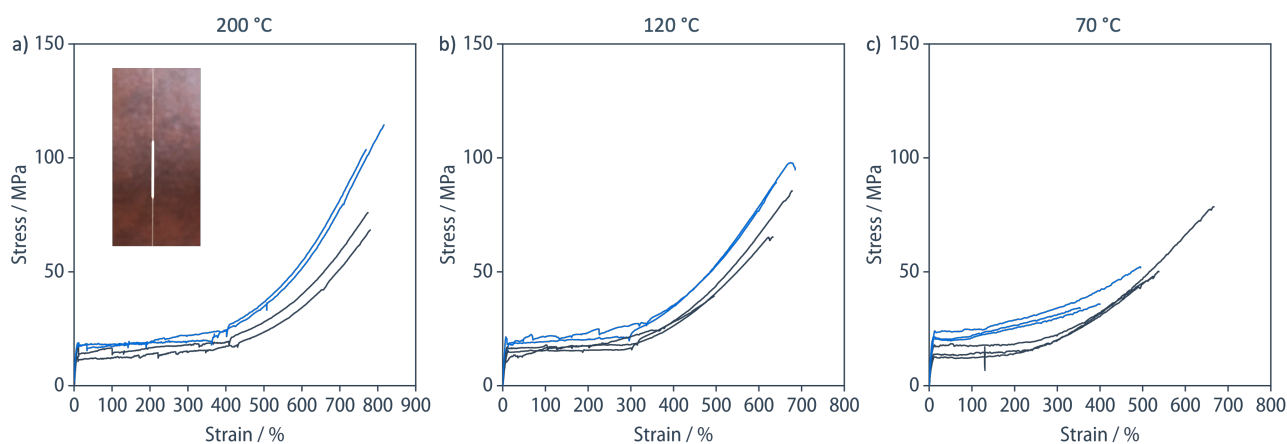


**Figure 48.** Tensile stress-strain curves of PCL<sub>80</sub>(Ala<sub>2</sub>Ac)<sub>2</sub>/A (5 wt%) (blue) and PCL<sub>80</sub> (black) fibers drawn at a) 200 °C b) 120 °C and c) 70 °C. The inset shows the neck formed after yielding.

**Table 5.** Tensile yield strength,  $\sigma_y$ , tensile strength,  $\sigma_{max}$ , tensile strain at break,  $\epsilon_b$ , Young's modulus,  $E$ , and tensile energy at break,  $W$ , for the PCL<sub>80</sub> and PCL<sub>80</sub>(Ala<sub>2</sub>Ac)<sub>2</sub>/A (5 wt%) fibers melt-stretched at 70 °C, 120 °C and 200 °C

	PCL <sub>80</sub> , 200 °C	PCL <sub>80</sub> , 120 °C	PCL <sub>80</sub> , 70 °C	PCL <sub>80</sub> (Ala <sub>2</sub> Ac) <sub>2</sub> /A (5 wt%), 200 °C	PCL <sub>80</sub> (Ala <sub>2</sub> Ac) <sub>2</sub> /A (5 wt%), 120 °C	PCL <sub>80</sub> (Ala <sub>2</sub> Ac) <sub>2</sub> /A (5 wt%), 70 °C
$\sigma_y$ (MPa)	13 ± 1	15 ± 2	15 ± 2	20 ± 1	20 ± 2	23 ± 1
$\sigma_{max}$ (MPa)	68 ± 19	63 ± 23	58 ± 17	109 ± 8	94 ± 6	41 ± 10
$\epsilon_b$ (%)	777 ± 20	595 ± 95	574 ± 79	792 ± 33	658 ± 25	414 ± 73
$E$ (MPa)	280 ± 25	252 ± 39	220 ± 40	312 ± 20	340 ± 39	383 ± 38
$W$ (MJ/m <sup>3</sup> )	207 ± 31	166 ± 59	152 ± 55	309 ± 20	255 ± 23	111 ± 26

### 3.2.2 Preparation, Structural Characterization, and Mechanical Analysis of Cold-Stretched Fibers

To further understand the mechanical response described in the previous section, melt-drawn fibers were stretched at room temperature until complete propagation of the neck along the gauge length. The  $d$ -spacings of the (110) and (200) WAXS reflections from the resulting cold-stretched PCL<sub>80</sub> and PCL<sub>80</sub>(Ala<sub>2</sub>Ac)<sub>2</sub>/A (5 wt%) fibers remained at 4.2 Å and 3.8 Å, respectively, but in all cases showed a strong equatorial peak, regardless of the initial state of the fiber (Figure 49). SAXS revealed a concomitant change from the isotropic or two-point patterns and a lamellar long period of 16.5 nm observed in the as-spun fibers to a four-point scattering pattern at 12.6 nm in the meridional direction (Figure 50). This was interpreted to reflect lamellar slippage and tilt, which commonly results in the

formation of chevron-type lamellar arrangements.<sup>303</sup> The cold-stretched **PCL<sub>80</sub>(Ala<sub>2</sub>Ac)<sub>2</sub>/A** (5 wt%) fibers also showed low-angle streaks in the equatorial direction whose intensity was significantly greater than for the as-spun fibers. The high intensity of this streaking implied a high concentration of scattering entities, which would be inconsistent with scattering from oriented self-assembled nanofibers alone. Notably, the streak is absent in all cold drawn PCL<sub>80</sub> fibers, which suggests a facilitated formation of the shish-like structures in **PCL<sub>80</sub>(Ala<sub>2</sub>Ac)<sub>2</sub>/A** (5 wt%) materials.

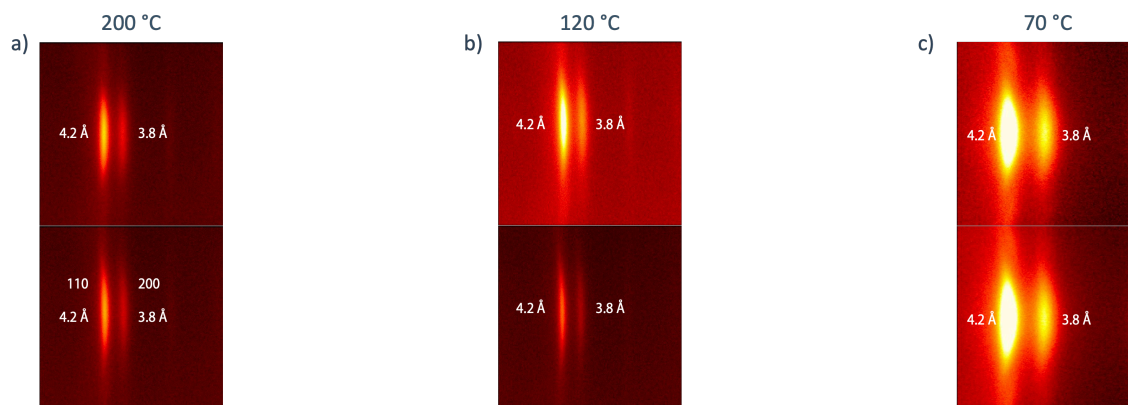


**Figure 49.** 2D wide angle X-Ray scattering of fibers stretched at *a)* 200 °C, *b)* 120 °C and, *c)* 70 °C followed by stretching at room temperature until neck depletion of **PCL<sub>80</sub>(Ala<sub>2</sub>Ac)<sub>2</sub>/A** (5 wt%) (top) and PCL<sub>80</sub> (bottom), along with the *d*-spacings of the scattering peak maxima.

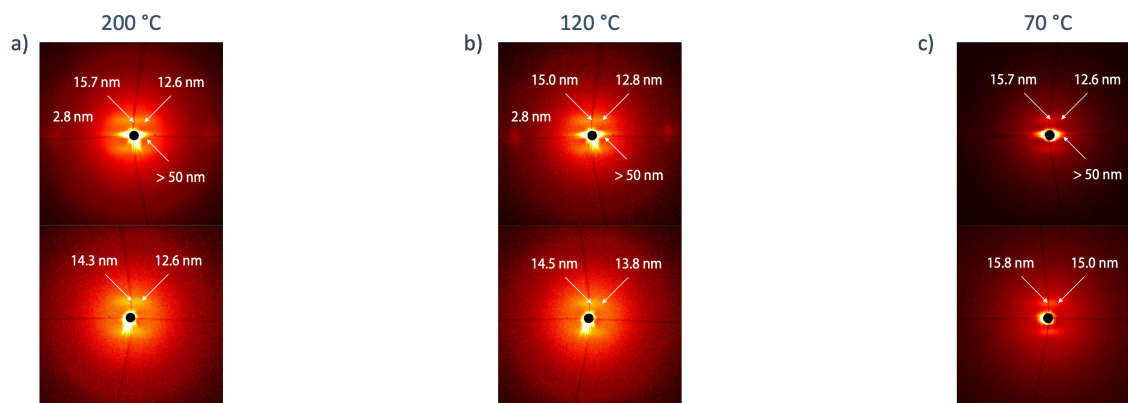


**Figure 50.** 2D small angle X-Ray scattering of fibers stretched at *a)* 200 °C, *b)* 120 °C and, *c)* 70 °C followed by stretching at room temperature until neck depletion of **PCL<sub>80</sub>(Ala<sub>2</sub>Ac)<sub>2</sub>/A** (5 wt%) (top) and PCL<sub>80</sub> (bottom), along with the *d*-spacings of the scattering peak maxima.

As in the case of the as-spun fibers, the tensile properties of the cold stretched PCL<sub>80</sub> fibers showed little variation with the original drawing temperature, with the exception of Young's modulus of  $307 \pm 10$  MPa,  $484 \pm 46$  MPa and  $440 \pm 9$  MPa for fibers drawn at 200 °C, 120 °C and 70 °C (Figure 51, Table 6). However, regardless of the structural similarities revealed by WAXS and SAXS, cold-drawn **PCL<sub>80</sub>(Ala<sub>2</sub>Ac)<sub>2</sub>/A** (5 wt%) fibers materials showed a significant variation in tensile behavior,

depending on the temperature in the previous melt stretching step. Cold-drawn  $\text{PCL}_{80}(\text{Ala}_2\text{Ac})_2/\text{A}$  (5 wt%) fibers that had initially been melt-stretched at 200 °C showed only slight increase in Young's modulus, yield strength, and ultimate strength with a concomitant decrease in strain at break.

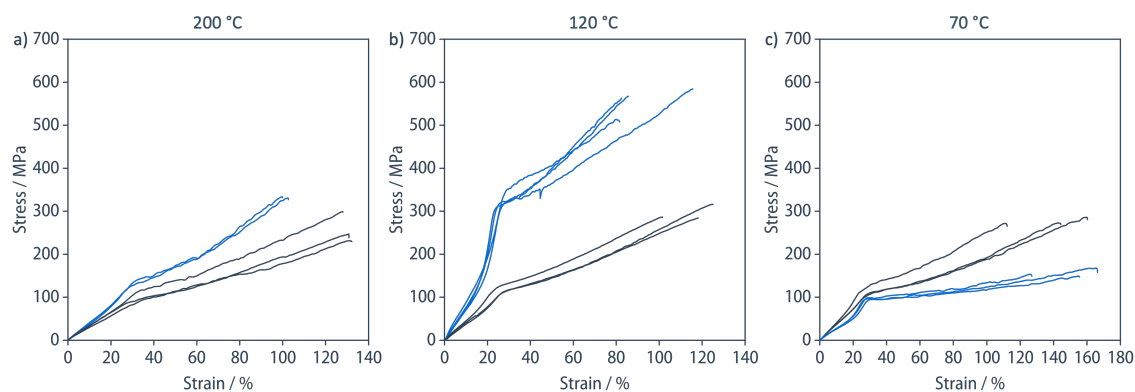


**Figure 51.** Tensile stress-strain curves of fibers stretched at a) 200 °C, b) 120 °C, and c) 70 °C followed by stretching at room temperature until neck depletion of  $\text{PCL}_{80}(\text{Ala}_2\text{Ac})_2/\text{A}$  (5 wt%) (blue) and  $\text{PCL}_{80}$  (black)

**Table 6.** Tensile yield strength,  $\sigma_y$ , tensile strength,  $\sigma_{max}$ , tensile strain at break,  $\epsilon_b$ , Young's modulus,  $E$ , tensile energy at break,  $W$  of the  $\text{PCL}_{80}$  and  $\text{PCL}_{80}(\text{Ala}_2\text{Ac})_2/\text{A}$  (5 wt%) fibers stretched at room temperature until neck depletion and initially drawn at 70 °C, 120 °C and 200 °C

	$\text{PCL}_{80}$ 200 °C	$\text{PCL}_{80}$ 120 °C	$\text{PCL}_{80}$ 70 °C	$\text{PCL}_{80}(\text{Ala}_2\text{Ac})_2/\text{A}$ (5 wt%), 200 °C	$\text{PCL}_{80}(\text{Ala}_2\text{Ac})_2/\text{A}$ (5 wt%), 120 °C	$\text{PCL}_{80}(\text{Ala}_2\text{Ac})_2/\text{A}$ (5 wt%), 70 °C
$\sigma_y$ (MPa)	$96 \pm 16$	$114 \pm 5$	$110 \pm 9$	$132 \pm 10$	$323 \pm 17$	$93 \pm 4$
$\sigma_{max}$ (MPa)	$259 \pm 35$	$295 \pm 18$	$276 \pm 7$	$332 \pm 6$	$555 \pm 30$	$157 \pm 7$
$\epsilon_b$ (%)	$129 \pm 2$	$115 \pm 12$	$138 \pm 25$	$100 \pm 2$	$91 \pm 17$	$147 \pm 21$
$E$ (MPa)	$307 \pm 10$	$484 \pm 46$	$440 \pm 9$	$403 \pm 10$	$959 \pm 127$	$307 \pm 17$
$W$ (MJ/m <sup>3</sup> )	185.18	$191 \pm 24$	$220 \pm 41$	$174 \pm 6$	$312 \pm 74$	$158 \pm 27$

On the other hand, cold-drawn  $\text{PCL}_{80}(\text{Ala}_2\text{Ac})_2/\text{A}$  (5 wt%) fibers that had been melt-stretched at 70 °C showed a slight decrease in both Young's modulus and ultimate strength. The most prominent difference is observed in the cold-drawn  $\text{PCL}_{80}(\text{Ala}_2\text{Ac})_2/\text{A}$  (5 wt%) fibers that had been melt-stretched at 120 °C (Figure 51). These fibers demonstrated an increase in Young's modulus and ultimate strength to  $959 \pm 127$  MPa and  $555 \pm 30$  MPa, respectively, which is an almost two-fold increase compared to pristine  $\text{PCL}_{80}$  fibers prepared in the same conditions. Additionally, the yield strength increased to  $323 \pm 17$  MPa with a slight decrease in strain at break to  $91 \pm 17\%$  compared to  $114 \pm 5$  MPa and

115 ± 12%, respectively, demonstrated by PCL<sub>80</sub> fibers prepared in this work, and 290 MPa and 69 ± 13%, respectively, compared to the PCL fibers reported in the literature.<sup>304</sup> Such a drastic change in mechanical response is explained by the orientation of the lamellar easy slip direction, which is normal to their plane, and parallel to the stretching direction and thus diverts from the maximum shear stress direction, which is at 45° to uniaxial stretching. As a result, the lamellae require higher stress to yield as they become more oriented. Moreover, the extended PCL chain crystals are fully stretched and act as rigid reinforcements, further increasing the yield strength of the obtained materials.

### 3.3 Conclusions

In summary, it was shown that the presence of a network of polymer-tethered  $\beta$ -sheet nanofibrils significantly facilitates the orientation of PCL chains in filaments prepared by rapid stretching of **PCL<sub>80</sub>(Ala<sub>2</sub>Ac)<sub>2</sub>/A** (5 wt%) compared to PCL<sub>80</sub>. SAXS revealed that **PCL<sub>80</sub>(Ala<sub>2</sub>Ac)<sub>2</sub>/A** exhibited a shish-kebab morphology with lamellae perpendicular to the stretching direction and PCL extended chain crystal parallel to the stretching direction. Fibers with this newly obtained morphology demonstrated an increase in Young's modulus, yield strength, and ultimate strength to 959 ± 127 MPa, 323 ± 17 MPa, and 555 ± 30 MPa, respectively, compared to 484 ± 46 MPa, 114 ± 5 MPa, and 295 ± 18 MPa, respectively, demonstrated by pristine PCL<sub>80</sub>.

Supramolecular Modification of Poly(lactic acid)  
for Improved Nucleation



The results presented in this chapter are part of a manuscript in preparation:

*“Supramolecular Modification of Poly(lactic acid) for Improved Thermal Stability and Melt Strength”,*  
Yevhen Hryshunin,<sup>1</sup> Daniel Görl,<sup>1</sup> Christopher Plummer,<sup>1</sup> Holger Frauenrath<sup>1\*</sup>. *To be submitted.*

H.F. conceived the idea and directed the research. C.P. performed AFM. Y.H. prepared all the mixtures and performed all testing unless otherwise stated. The manuscript was written by Y.H. and H.F.

## 4. Supramolecular Modification of Poly(lactic acid) for Improved Nucleation

### 4.1 Introduction

Global plastic production continues to increase without restraint and has surpassed 460 Mt in 2021.<sup>1-3</sup> The majority of plastics produced, around 75%, are derived from petroleum-based polymers, with polyolefins comprising more than 50% by volume. At present, open-loop recycling systems for post-consumer plastic waste are only available for poly(ethylene) (PE), poly(propylene) (PP), and bottle-grade poly(ethylene terephthalate) (PET), with only the latter being recycled in significant quantities.<sup>12,299</sup> As a result, less than 9% of plastics are currently collected for recycling, while 12% of plastic waste is incinerated, and the remainder ends up in landfills or is released into the environment.<sup>226</sup> The incomplete degradation of plastic waste and microplastic particles contributes significantly to pollution and poses a severe threat to virtually every ecosystem on our planet.<sup>7,305</sup> Therefore, the plastic waste crisis is one of the most pressing problems that humanity needs to address, and we must reconsider which materials are appropriate for a circular plastics economy in the future.<sup>226</sup> Although there is no single optimal approach to address this complex systemic problem, bio-sourced and/or biodegradable materials, as well as chemical recycling to monomer, are promising complementary elements towards a circular plastics economy. Bio-sourced plastics, particularly those obtained from second or third-generation renewable feedstock, are expected to be more favorable from a life cycle assessment (LCA) perspective as they help conserve fossil fuel resources and decrease the carbon footprint.<sup>17</sup> Biodegradability, while not a universal solution, is important to provide additional end-of-life alternatives such as composting and to mitigate issues associated with the inevitable release of polymers into the environment during production, use, and disposal or recycling.<sup>18</sup> Finally, chemical recycling to monomer through depolymerization under mild conditions is crucial as an additional end-of-life option for value recovery with minimal adverse environmental effects.<sup>12</sup>

Looking at it from a circular plastics economy perspective, biodegradable polyesters produced through ring-opening polymerization (ROP) of monomers from renewable resources can be an attractive category of materials. However, for sustainable alternatives to commodity plastics to be successful, they must also be competitive in terms of processability and final product performance. Among the potential candidates to replace petroleum-based polymers in packaging and other commodity applications, poly(lactide) or poly(lactic acid) (PLA) is considered one of the most promising.<sup>306</sup> PLA is a

biodegradable, compostable, chemically recyclable, and biocompatible thermoplastic polyester that is stiff and has tensile strength similar to those of polystyrene (PS) or PET. In 2021, PLA production amounted to 400 kT per year, which is about 20% of all bioplastics produced, and this is expected to double by 2026.<sup>307</sup> However, inherent brittleness and slow crystallization, which leads to poor heat resistance, post-processing aging or creep caused by insufficient crystallinity obtained during fast industrial processing, restrict widespread adoption of PLA.

Adding a nucleating agent that lowers the surface energy penalty during the formation of a polymer nucleus can significantly accelerate polymer crystallization. For example, the melting temperature,  $T_m$ , of poly (L-lactide) (PLLA) can be tuned between 120 °C and the thermodynamic melting point of around 200 °C depending on the D-lactide content, molecular weight, and crystallization conditions.<sup>39,40,50,51</sup> Blending 0.1 wt% of high-melting-point PLLA (hPLLA,  $T_m = 187$  °C) with a standard commercial PLLA grade (e.g., NatureWorks LLC, trade name 4032D,  $T_m = 169$  °C) led to an increase in crystallization temperature of the latter from 105 to 141 °C, which was attributed to self-nucleation effect.<sup>40</sup> Another example of efficient nucleating agent is PLA stereocomplex obtained by mixing PLLA with 0.5–5 wt% with poly (D-lactide) (PDLA). The stereocomplex has a melting temperature of 215 °C and thus do not only reduce the surface energy for nucleation of PLLA crystallization but also act as physical crosslinks in the melt state and thus significantly increase melt strength.<sup>56,58</sup> However, D,D-lactide is currently not readily available on an industrial scale.<sup>63</sup> Alternatively, modifications to the chain architecture have been explored, including chain extenders, branching, or covalent cross-linking.<sup>99,308</sup> For instance, introducing long-chain branches with a segment length above the entanglement length improves the nucleation of PLA crystallization, increases melt strength and introduces strain hardening during melt deformation.<sup>99,102</sup>

Addition of inorganic additives such as clay or talc increase the crystallization temperature up to 20 °C and result in an up to seven-fold increase in crystallization half times.<sup>39</sup> However, unless the percolation threshold of the dispersed additive is achieved (usually > 30 wt%), these additives act as a plasticizer, reducing polymer melt viscosity and glass transition temperature, which is detrimental in processes requiring on melt deformation.<sup>136,137</sup> Nanoscopic fillers such as carbon nanotubes, nanoclay, or cellulose nanofibers are effective nucleating agents that, thanks to their higher surface area can be used at lower contents.<sup>139–143</sup> Moreover, such nanoscopic nucleating agents act as reinforcing elements that increase melt viscosity and, at sufficiently high concentrations, melt elasticity.<sup>98</sup> The use of organic nucleating



agents such as *N,N,N*-tricyclohexyl benzenetricarboxylamide<sup>144</sup> that are soluble in the PLA melt and recrystallize upon cooling is beneficial because they form reversibly. Moreover, they typically exhibit better interfacial adhesion and remain better dispersed in the polymer matrix at higher concentrations. Multivalent hydrogen-bonded ligands have also been used for the supramolecular modification of PLA. End-modification with self-complementary ureidopyrimidinone (UPy) ligands, for instance, resulted in the conversion of amorphous PDLLA with an actual molecular weight of 7'000 into materials with an apparent molecular weight of  $M_n = 70'000$ .<sup>277</sup> However, the reported dissociation temperature of UPy dimers of about 87 °C limits the use of UPy ligands for the modification of semicrystalline PLLA because it is well below the melting temperature of the latter. In fact, the application of “supramolecular polymer” concepts to semicrystalline or glassy polymers has generally attracted little interest to date,<sup>277-282</sup> because end group aggregation has to occur above polymer crystallization or vitrification temperatures, and bulk properties were assumed to be dominated by the solid polymer.<sup>280,281,283</sup> Moreover, due to the increasing dilution of the polymer end groups with increasing polymer molecular weight, their aggregation becomes thermodynamically unfavorable<sup>270-272</sup> so that, with a few notable exceptions,<sup>270-276</sup> most investigations have focused polymers at molecular weights well below the entanglement threshold. Consequently, since the presence of a well-developed entanglement network is a critical factor both for melt properties and mechanical resilience in the solid state,<sup>217,309,310</sup> the resulting materials typically show low melt strength, as well as low strength and brittle failure in tension. We have recently shown that these limitations of supramolecular networks can be overcome by the specific co-assembly of ditopic hydrogen-bonded end groups and a low molecular weight additive based on the same supramolecular motif into well-defined nanofibrils whose aggregation temperatures can be tailored to be well above 150 °C even in high molecular weight polymers.<sup>301</sup>

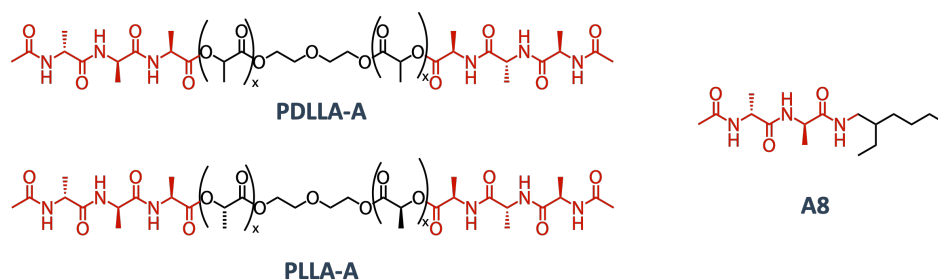
Here, we show that blending of PLA modified with ditopic hydrogen-bonded end groups with low molecular weight additive based on the same supramolecular motif results in 1,5 orders of magnitude decreases in crystallization half-times of PLLA. Such a drastic increase in the crystallization rate enables fast processing from the melt directly to the temperatures around the glass transition, at the same time, achieving high crystallinity. To this end, we modified amorphous PDLLA and semicrystalline PLLA, both of  $M_n = 60'000$ , with acetyl-L-alanyl-L-alanyl amide **A** end groups (**PDLLA-A** and **PLLA-A**, respectively) which are ditopic, self-complementary self-assembling unit based on three-fold hydrogen bonding. We then demonstrate that the blends of **PDLLA-A** and 2-ethylhexyl acetyl-L-alanyl-L-alanyl amide (**A8**)

exhibit a three-fold decrease in the width of **A8** crystals compared to non-modified PDLLA/**A8** blends due to the compatibilization effect of the end-groups.

## 4.2 Results and Discussion

### 4.2.1 Materials Design and Synthesis

We synthesized both atactic PDLLA and stereoregular PLLA by bidirectional ring-opening polymerization of D,L-lactide and L,L-lactide, respectively, starting from diethylene glycol. A molecular weight of  $M_n = 60'000$  was chosen in both cases because it was considered to be sufficiently above the entanglement molecular weight of PLA of about  $M_e = 9'000$  to have a fully developed entanglement network and possess mechanical properties similar to commercial PLA.<sup>26</sup> The corresponding telechelic **PDLLA-A** and **PLLA-A** (Figure 52), both end-modified with acetyl-L-alanyl-L-alanine end groups with a nominal weight fraction of  $\approx 1$  wt%, were then synthesized by Steglich esterification the hydroxyl end groups of PDLLA and PLLA, respectively, with *N*-Cbz-L-alanine using DMAP/DCC as coupling promoter, followed by deprotection using  $\text{Me}_3\text{SiI}$ , and a final amide coupling with acetyl-L-alanyl-L-alanine using PyBOP/DIPEA as the coupling reagent. **PDLLA-A** and **PLLA-A** were obtained in yields of 37% and 53% over three steps, with a degree of functionalization of  $f = 2.0$  according to  $^1\text{H}$  NMR spectroscopy (Figure 53). The dipeptide end groups were chosen as self-complementary and ditopic ligands that mimic the nanofibril-forming L-alanine-rich segments in silk materials,<sup>311</sup> and are expected to self-assemble into helically twisted  $\beta$ -sheet nanofibrils.<sup>312</sup> These aspects are relevant to allow for dynamic co-assembly with a corresponding low-molecular weight additive, 2-ethylhexyl *N*-acetyl-L-alanyl-L-alanyl-amide **A8** in the blends **PDLLA-A/A8** and **PLLA-A/A8**. The blends of the additive **A8** and non-functionalized polymers PDLLA/**A8** and PLLA/**A8** served as reference materials to investigate the effect of the polymer end groups on materials structure and properties.



**Figure 52.** Chemical structures of telechelic **PDLLA-A** and **PLLA-A** ( $x = 420$ ), functionalized with acetyl-L-alanyl-L-alanine end groups and the corresponding additive 2-ethylhexyl *N*-acetyl-L-alanyl-L-alanyl-amide **A8**.

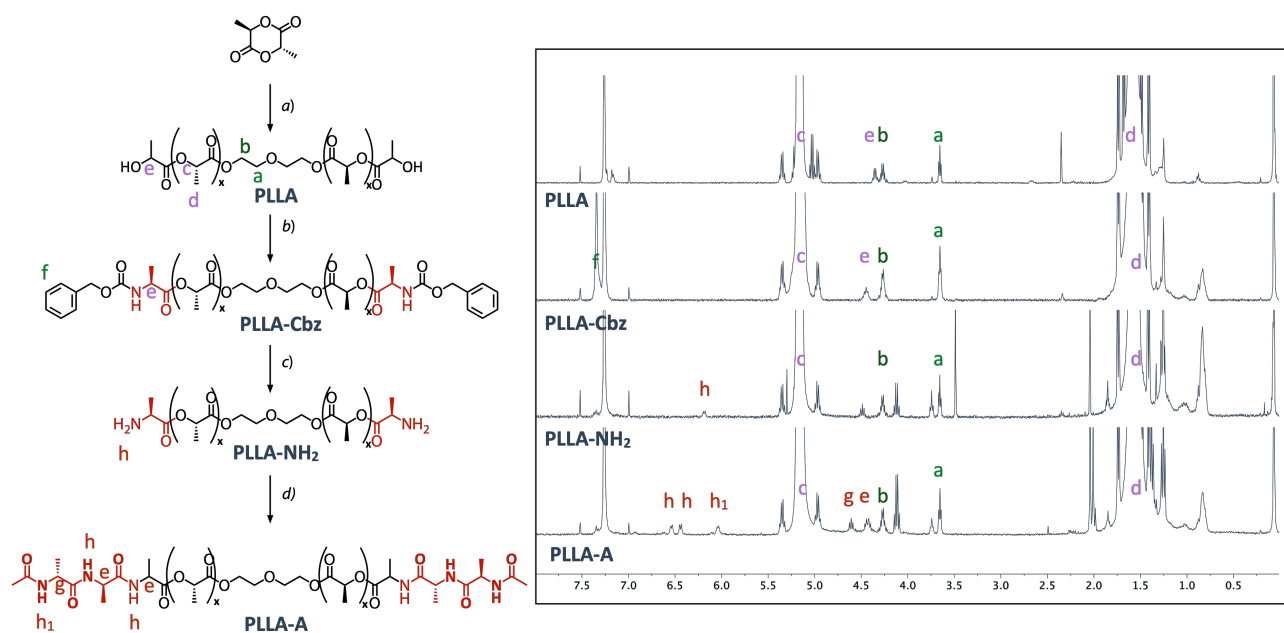


**Figure 53.** Synthesis of end-modified polymers. *Reagents and conditions:* a) L,L-lactide or D,L-lactide (416.0 equiv.), diethylene glycol (1.0 equiv.), tin(II) 2-ethylhexanoate (0.8 equiv.), toluene, reflux, 4 h, yields 82.5 % (PLLA), 71.7 % (PDLLA); b) PLLA-OH or PDLLA-OH (1.0 equiv.), *N*-carbobenzoxy-L-alanine (20 equiv.), *N,N'*-dicyclohexylcarbodiimide (10 equiv.), 4-*N,N*-dimethylamino)pyridine (12 equiv.), dry DCM, 12 h, yields 92.9 % (PLLA), 81.3 % (PDLLA); c) PLA-Cbz (1.0 equiv.), trimethylsilyl iodide (40 equiv.), dry DCM, 2 h, yields 82.9 % (PLLA), 71.6 % (PDLLA); d) PLA-NH<sub>2</sub> (1.0 equiv.), PyBOP, DIPEA, THF, acetyl-L-alanyl-L-alanine (2.1 equiv.) room temperature, 16 h, yields 80.3% (PLLA), 70.1% (PDLLA). <sup>1</sup>H NMR spectra (CDCl<sub>3</sub>, 400 MHz) of PLLA, PLLA-Cbz, PLLA-NH<sub>2</sub> and PLLA-B5.

#### 4.2.2 Morphology and Thermal Properties of PDLLA-A/A and PDLLA/A blends

Solid-state IR spectroscopy of PDLLA-A/A8 and PLLA-A/A8 blends as well as PDLLA/A8 and PLLA/A8 reference blends at room temperature showed single amide A (N-H stretching) and single sharp amide I (C=O stretching) bands at around 3280 cm<sup>-1</sup> and 1630 cm<sup>-1</sup>, respectively, which are the same as those in pure A8 (Figure 54). These peak positions are characteristic of N-H and C=O stretching vibrations of amide groups that are part of resonance-enhanced arrays of N-H...O=C hydrogen bonds in antiparallel  $\beta$ -sheet-like aggregates and are further confirmed by the absence of additional amide A bands around 3290 cm<sup>-1</sup> that would indicate the presence of parallel  $\beta$ -sheet aggregates. Notably, neither the pure PDLLA-A nor pure PLLA-A materials showed absorption peaks corresponding to the formation of antiparallel  $\beta$ -sheet-like aggregates, thus implying that acetyl-L-alanyl-L-alanine end groups with a nominal concentration of 1 wt% did not self-assemble in the PLA matrix, in the absence of the reinforcement provided by the A8 additive.

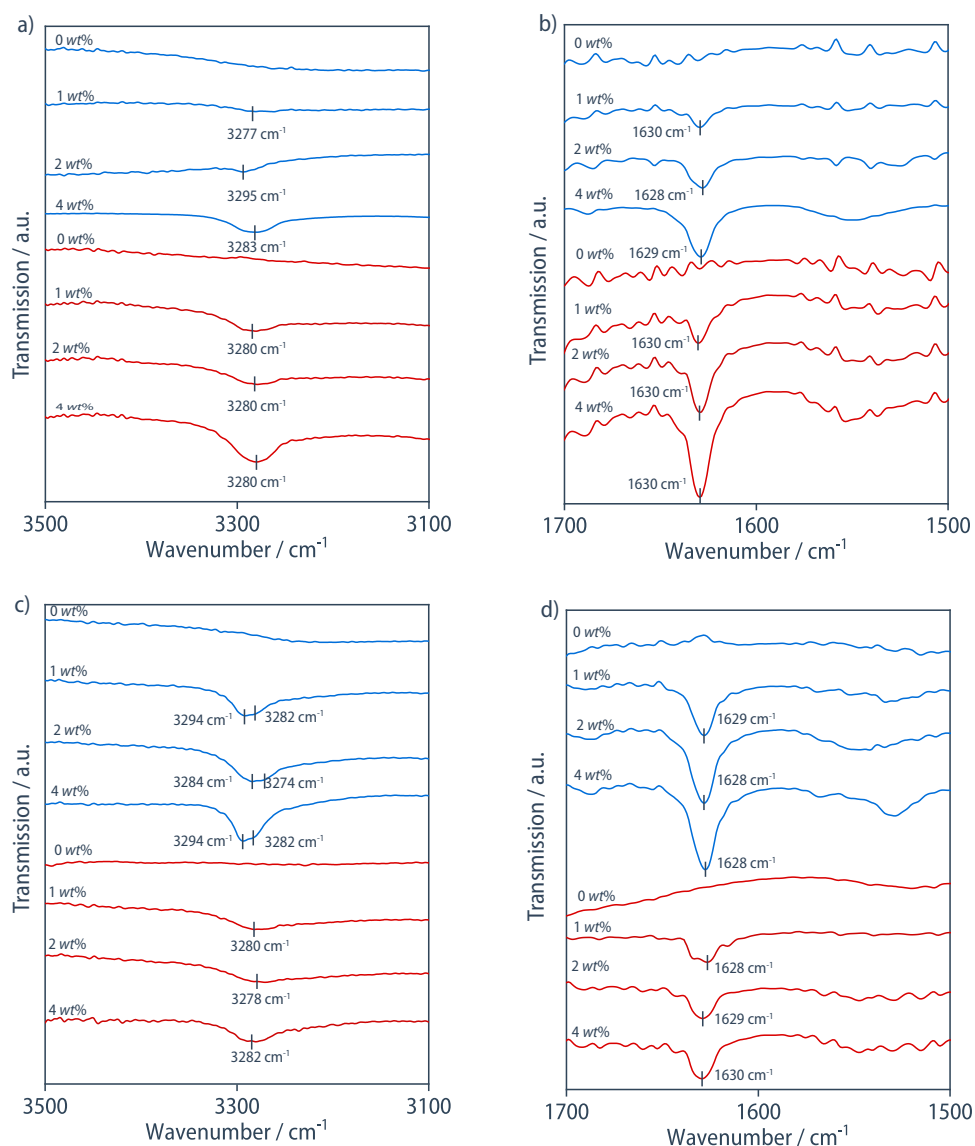


**Figure 54.** Solid-state FTIR spectra measured in transmission of film samples of *a,b*) **PDLLA-A/A8** blends (red) and **PDLLA/A8** reference blends (blue), and of *c,d*) **PLLA-A/A8** blends (red) and **PDLLA/A8** reference blends (blue) at different concentrations of the additive **A8** obtained upon cooling from the melt to room temperature (10 °C/min), showing the positions of the N–H stretching (3278–3282 cm<sup>-1</sup>) and C=O stretching (1628–1630 cm<sup>-1</sup>) vibrations of amide groups that are part of antiparallel  $\beta$ -sheet-like structures.

Thermal transitions of **PDLLA/A8** and **PDLLA-A/A8** blends were characterized by DSC heating and cooling scans performed at a rate of 10 °C/min. Neither **PDLLA/A8** nor **PDLLA-A/A8** demonstrated a shift in PLA glass transition, which remained at 53 °C at all concentrations, suggesting that molecularly dissolved **A8** did not act as an antiplasticizer in the polymer matrix. While the bulk melting temperature of the pure additive **A8** was observed at  $T_{A8} = 229$  °C, the additive showed a pronounced melting point depression in the blends **PDLLA/A8**, with  $T_{blend} = 143$  °C at an additive concentration of 0.5 wt% which first increased with additive concentration and then leveled off at a concentration of 4 wt% towards a temperature of  $T_{blend} = 185$  °C. Again, the pure end-modified **PDLLA-A** showed no additional thermal

transition, suggesting the absence of the aggregated end groups, in agreement with FTIR spectroscopy. Upon the addition of **A8**, however, the **PDLLA-A/A8** blends showed an even larger melting point depression and lower melting enthalpies compared to the **PDLLA/A8** reference blends at the same concentrations (Figure 55). These observations can, for instance, be explained by a higher degree dispersion of the **A8** aggregates caused by polymer end-groups acting as a surfactant, which leads to a higher surface area. Additionally, there may be the presence of additional defects in **A8** aggregates caused by the inclusion of the polymer end-groups, as well as a loss of conformational entropy of the polymer chain in the vicinity of the end-group tethering to the **A8** aggregates.

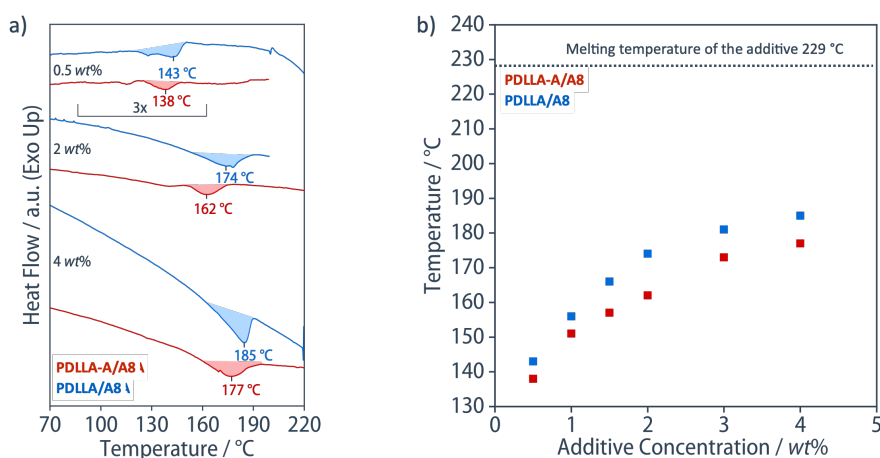


**Figure 55.** a) DSC heating scans (heating rate 10 °C/min) of **PDLLA-A/A8** blends (red) and **PDLLA/A8** reference blends (blue), indicating melting of the **A8** aggregates at different concentrations. b) Phase diagram of the blends derived from endothermal transitions in DSC heating scans.

Optical microscopy experiments were performed to understand the phase behavior at elevated temperatures. At all investigated concentrations, **PDLLA/A8** blends showed macroscopic phase separation of **A8** into a network of needle-like crystals at temperatures up to the dissociation temperatures  $T_{\text{blend}}$  observed in DSC, and optically homogeneous solutions of **A8** in the polymer melt above that temperature. Similarly, **PDLLA-A/A8** blends at additive concentrations  $> 2 \text{ wt}\%$  showed macroscopic phase separation into spherically shaped domains at temperatures up to  $T_{\text{blend}}$ . By contrast, the **PDLLA-A/A8** blends at additive concentrations  $\leq 2 \text{ wt}\%$  remained homogeneous at any temperature, suggesting the formation of the nanoscopic aggregates (Figure 56). Atomic force microscopy (AFM) imaging (Figure 57) of **PDLLA-A/A8** blends at additive concentrations below (0.5 wt%), around (1.5 wt%), and above (4 wt%) the threshold for macroscopic phase separation showed the formation of needle-like crystals with lateral dimensions of  $31 \pm 5 \text{ nm}$ ,  $34 \pm 4 \text{ nm}$  and  $38 \pm 7 \text{ nm}$ , respectively.

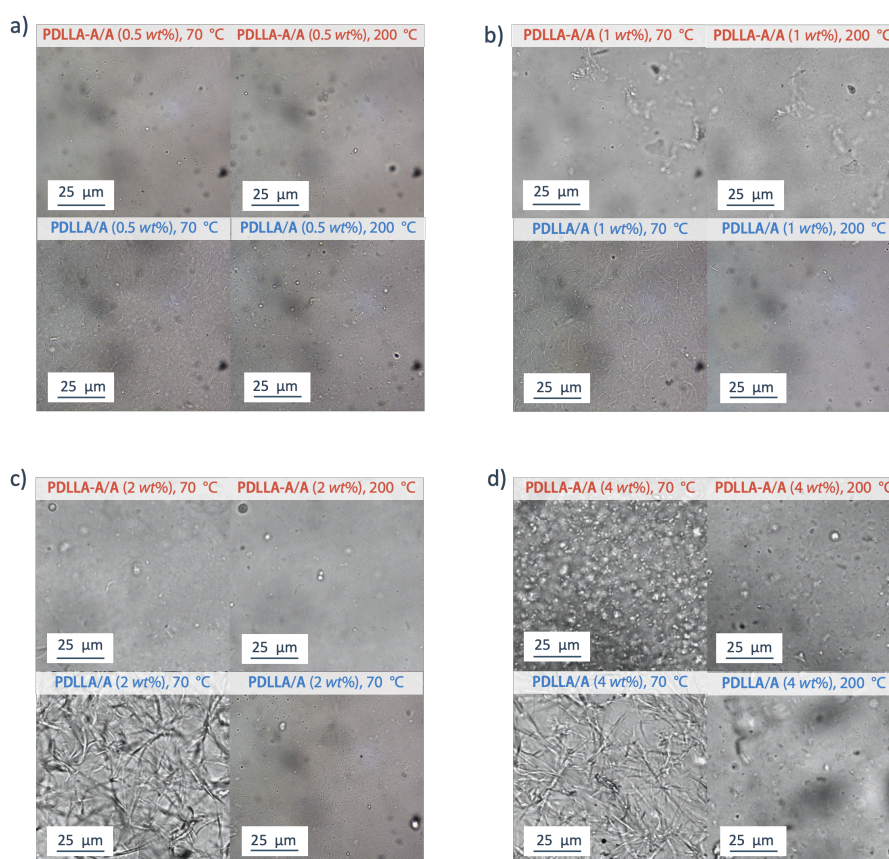


**Figure 56.** Optical micrographs (bright field) obtained at *a,c*) 70 °C and at *b,d*) 200 °C of **PDLLA-A/A8** blends (top) and of **PDLLA/A8** reference blends (bottom), each below the onset of **PDLLA-A/A8** macrophase separation at 2 wt% (*a* and *b*) and above the onset at 4 wt% (*c* and *d*)

These crystals were thus significantly smaller than those observed in the reference blends at the same additive concentrations, of  $114 \pm 32$  nm (0.5 wt%),  $135 \pm 39$  nm (1.5 wt%), and  $104 \pm 45$  nm (4 wt%). Nevertheless, the additive precipitates in the **PDLLA-A/A8** blends exhibited the same needle-like crystal morphology, a very similar aspect ratio, and lateral dimensions that were many times larger than the width of a single stack of an individual **A8**  $\beta$ -sheet tape of about 1.5 nm, implying that they were crystalline structures albeit with nanoscale dimensions. This is in marked contrast with PDLLA materials end-modified with benzenetricarboxamide (BTA) end groups and their blends with a triamyl benzenetricarboxamide additive investigated previously, where we had observed a network of nanofibrils that had much significantly smaller lateral dimensions, were compliant, and aligned with one another at a periodic spacing commensurate with the dimensions of employed polymer segments and hence interpreted as formed from a single stack of co-assembled polymer end groups and additive molecules. We attribute this difference in behavior to the fact that the solubility of the acetyl-L-alanyl-L-alanine end groups in the PDLLA matrix is too high for them to be effective as a surfactant, due to their

structural similarity with the PDLLA repeating unit, featuring even an identical spacing and orientation of the respective carbonyl groups as hydrogen-bond acceptors. In good agreement with this interpretation, temperature-dependent oscillatory shear rheology revealed a noticeable increase in the melt modulus compared to pristine PDLLA, but no significant difference between PDLLA/A8 and PDLLA-A/A8 (Figure 58)

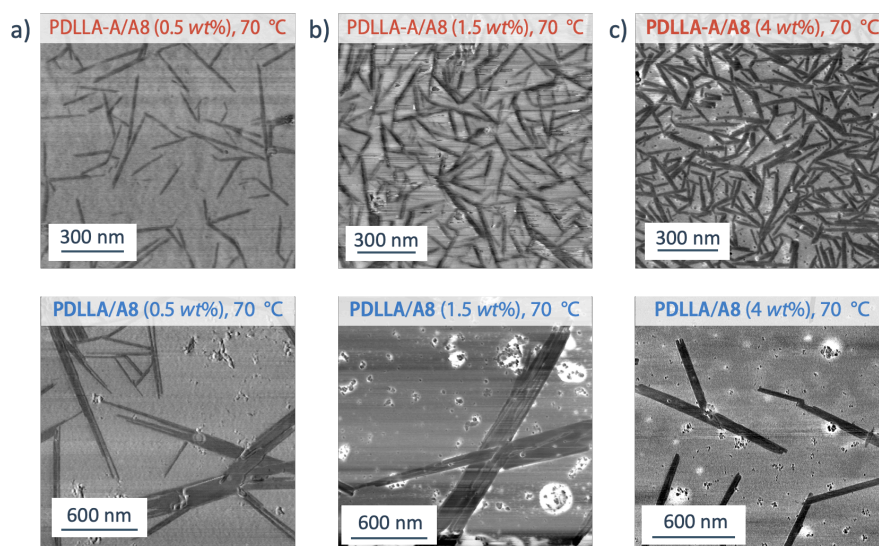


**Figure 57.** AFM phase images of PDLLA-A/A8 blends (top) and PDLLA/A8 reference blends (bottom) at 70 °C at *a*) 0.5 wt%, *b*) 1.5 wt%, and *c*) 4 wt% of A8 revealed better dispersion of the needle-like crystals of A8 in the PDLLA-A/A8 blends with widths of  $31 \pm 5$  nm,  $34 \pm 4$  nm, and  $38 \pm 7$  nm, respectively, compared to widths of  $114 \pm 32$  nm,  $135 \pm 39$  nm and  $104 \pm 45$  nm, respectively, in the PDLLA/A8 reference blends.

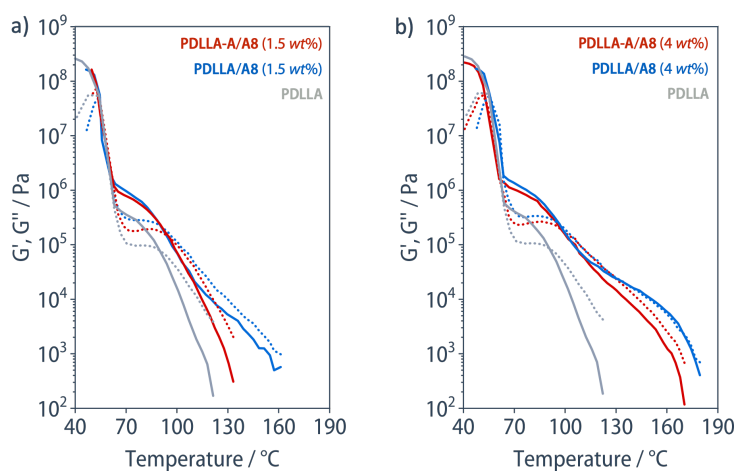


**Figure 58.** Temperature-dependent oscillatory shear rheology (cooling rate 10 °C/min, 1 rad/s, strain 1%) of PDLLA-A/A8 blends (red), PDLLA/A8 reference blends (blue), and pristine PDLLA (grey) at *a*) 1.5 wt% and *b*) 4 wt% of A8; storage modulus – solid line; loss modulus – dotted line.

### 4.2.3 Thermal Properties of **PLLA-A/A** and **PLLA/A** blends

Although AFM imaging in the semicrystalline **PLLA-A/A8** blends and **PLLA/A8** reference blends was impeded by the crystalline domains of the PLLA matrix, the fact that both the FTIR band positions and DSC transition temperatures were virtually identical to those observed in the amorphous **PDLLA-A/A8** and **PDLLA/A8** materials (see above) gives confidence that the phase behavior of the additive **A8** remained the same, implying a better dispersion of **A8** nanocrystals in the **PLLA-A/A8** blends than in non-modified PLLA materials. Accordingly, while the pure end-modified **PLLA-A** exhibited similar crystallization onset temperature of  $T_c = 124\text{ }^\circ\text{C}$  as non-modified PLLA ( $T_c = 122\text{ }^\circ\text{C}$ ), according to the DSC cooling scans at a rate of  $10\text{ }^\circ\text{C}/\text{min}$  (Figure 59), the crystallization temperatures steeply increased with additive concentration in the blends **PLLA-A/A8** and leveled off at  $T_c = 149\text{ }^\circ\text{C}$  for additive concentrations  $\geq 2\text{ wt}\%$ . This increase in crystallization temperatures was significantly more pronounced than in the **PLLA/A8** reference blends where they leveled off at  $T_c = 138\text{ }^\circ\text{C}$ . Moreover, it is interesting to note that, for additive concentrations  $\leq 2\text{ wt}\%$ , the crystallization onset of PLLA coincided exactly with the dissociation temperatures  $T_{A8}$  that had been observed in the amorphous **PDLLA-A/A8** blends, suggesting that the formation of nanoscopic aggregates instantaneously nucleated PLLA crystallization (Figure 59c).

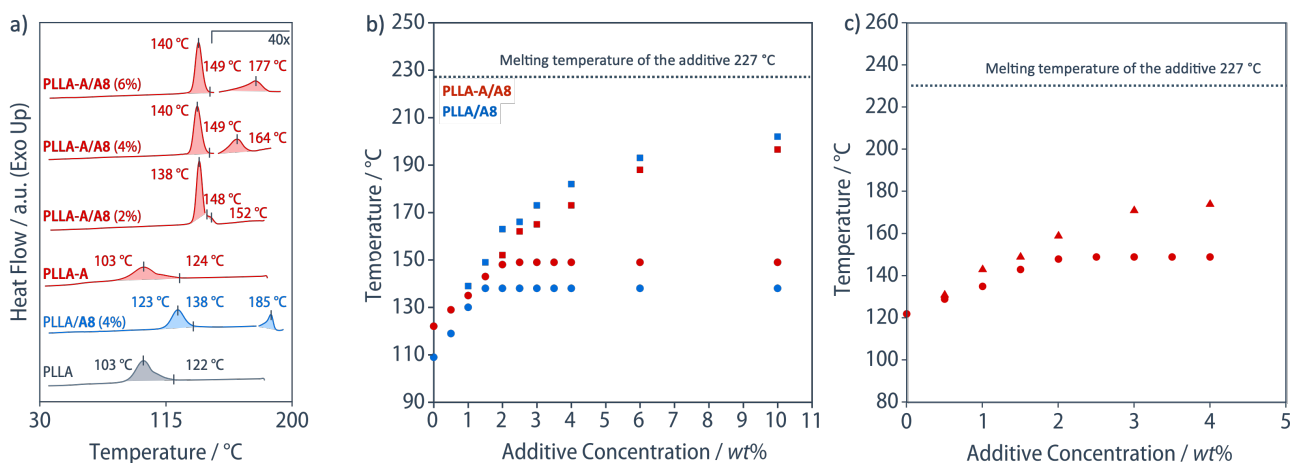


**Figure 59.** a) DSC cooling scans (cooling rate  $10\text{ }^\circ\text{C}/\text{min}$ ) of **PLLA-A/A8** blends (red), **PLLA/A8** reference blends (blue), and PLLA (black), indicating the crystallization temperatures of the PLLA matrix and **A8** crystals at different concentrations of **A8**. b) Exothermal transition temperatures observed in DSC of **A8** (squares) and onset of PLLA crystallization (circles) in **PLLA-A/A8** blends and **PLLA/A8** reference blends. c) Exothermal transition temperatures of **A8** crystallization in **PDLLA-A/A8** blends (triangles) and onset of PLLA crystallization in **PLLA-A/A8** blends (circles).



Isothermal crystallization experiments were performed by rapidly cooling the polymer melt to the desired crystallization temperature of 140 °C (Figure 60). Crystallization half-times on the order of  $\tau_{1/2} = 0.4\text{--}1$  min and an average spherulite size of 8  $\mu\text{m}$  were observed for all **PLLA-A/A8** blends, irrespective of additive concentration. The crystallization half times were thus more than one order of magnitude lower than those observed for the PLLA/**A8** reference blends at additive concentrations  $\geq 2$  wt% ( $\tau_{1/2} = 10$  min, spherulite size 30  $\mu\text{m}$ ) and a PLLA blend with 2 wt% of talc ( $\tau_{1/2} = 7.6$  min).

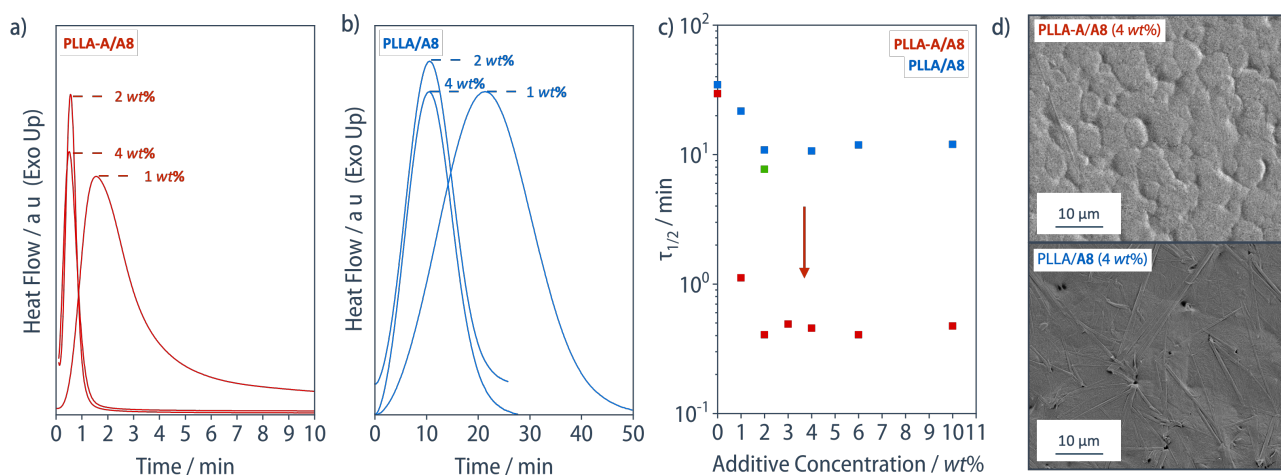


**Figure 60.** DSC isothermal crystallization curves at 140 °C for *a)* **PLLA-A/A8** blends (red) and *b)* PLLA/**A8** reference blends (blue) at different concentrations of **A8**. *c)* Crystallization half times determined from isothermal DSC experiments for **PLLA-A/A8** blends (red), PLLA/**A8** reference blends (blue), and PLLA/talc (2 wt%) (green). *d)* SEM images of **PLLA-A/A8** blends (top) and PLLA/**A8** reference blends (bottom) at 4 wt% of **A8**.

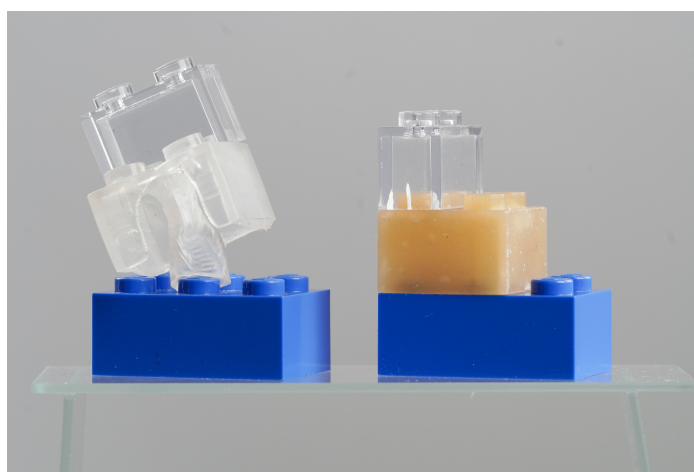


**Figure 61.** Injection molding from the melt 200 °C into a toy brick-shaped mold at a mold temperature of 80 °C of PLLA (left) and **PLLA-A/A8** (4 wt%) (right).

The superior processing properties of the **PLLA-A/A8** (4 wt%) materials compared to PLLA were demonstrated by injection molding from the melt at 200 °C into a toy brick mold at a mold temperature

of 80 °C (Figure 61). The resulting material fully crystallized immediately, maintained its shape upon demolding, and exhibited excellent feature fidelity as well as perfect “clutch work” with commercial toy bricks. By comparison, injection-molded specimens using PLLA apparently only partially crystallized and therefore remained softer, so that they deformed upon removal from the mold.

### 4.3 Conclusions

In summary, atactic PDLLA and stereoregular PLLA, both of  $M_n = 60'000$ , were modified with acetyl-L-alanyl-L-alanyl end-groups (**PDLLA-A** and **PLLA-A**, respectively) and blended with the low molecular weight additive 2-ethylhexyl *N*-acetyl-L-alanyl-L-alanyl amide **A8**. The **PDLLA-A/A8** blends showed a three-fold decrease in the width of **A8** crystals compared to non-modified PDLLA/**A8** blends, which led to an increase in crystallization onset temperature of PLLA matrix up to  $T_c = 148$  °C and a decrease in crystallization half-times to  $\tau_{1/2} = 0.5$  min, compared to  $T_c = 138$  °C and  $\tau_{1/2} = 10$  min of non-modified PDLLA/**A8** blends. Such a drastic increase in the crystallization rate enables fast processing from the melt directly to the temperatures around the glass transition, at the same time, achieving high crystallinity should significantly reduce in cycle times and increase the heat resistance and creep of the obtained items.

Supramolecular Modification of Poly(lactic acid)  
for Improved Nucleation and Melt Strength



The results presented in this chapter are part of a manuscript in preparation:

*“Supramolecular Modification of Poly(lactic acid) for Improved Thermal Stability and Melt Strength”, Yevhen Hryshunin,<sup>1</sup> Michael Giffin,<sup>1</sup> Daniel Görl,<sup>1</sup> Christopher Plummer,<sup>1</sup> Holger Frauenrath<sup>1\*</sup>, to be submitted.*

H.F. conceived the idea and directed the research. M.G. and Y.H. synthesized the additive. C.P. performed AFM and developed the analytical models. Y.H. prepared all the mixtures and performed all testing unless otherwise stated. The manuscript was written by Y.H., C.P. and H.F.

## 5. Supramolecular Modification of Poly(lactic acid) for Improved Nucleation and Melt Strength

### 5.1 Introduction

Global plastics production continues to grow unabatedly and has reached over 460 Mt in 2021.<sup>1-3</sup> About 75% of the all plastics produced are based on petroleum-based polymers, with polyolefins amounting to more than 50% by volume. Open-loop recycling streams for post-consumer waste plastics currently only exist for poly(ethylene) (PE), poly(propylene) (PP), and bottle-grade poly(ethylene terephthalate) (PET), but only the latter is recycled in meaningful amounts.<sup>12,299</sup> Consequently, less than 9 % of all plastics are currently collected for recycling, another 12% of plastic waste is incinerated, while the remainder ends up in landfill or leaks into the environment.<sup>226</sup> The pollution with plastic waste and microplastic particles as a result of incomplete degradation poses a severe threat to virtually any ecosystem on this planet.<sup>7,305</sup> The plastic waste crisis is hence one of the most imminent problems for mankind to address and will require reconsidering which materials are suitable for a future circular plastics economy.<sup>226</sup>

While this is a complex systemic problem for which there is no singular best strategy, bio-sourced and/or biodegradable materials, as well as chemical recycling to monomer may be considered as promising complementary elements towards a circular plastics economy. Thus, bio-sourced plastics, particularly those where the monomers are obtained from second or third generation renewable feedstock, promise to be more favorable from a life cycle assessment (LCA) perspective, mainly because they help save fossil fuel resources and reduce carbon footprint.<sup>17</sup> Biodegradability, while perhaps not a universal solution due to the complexities of controlling degradation in various environments, will nevertheless be important to both provide additional end-of-life options such as composting and to help mitigate problems associated with the inevitable leakage of polymers into the environment during production, use, and disposal or recycling.<sup>18</sup> Finally, chemical recycling to monomer by depolymerization under mild conditions will be important as an additional end-of-life option for value recovery with minimal adverse environmental effects.<sup>12</sup>

From that perspective, biodegradable polyesters obtained via ring-opening polymerization (ROP) of monomers from renewable resources can be seen as an attractive class of materials for a circular plastics economy. However, sustainable alternatives to commodity plastics will also have to be

competitive in terms of processability and final product performance, which may explain why bio-sourced and biodegradable plastics currently account for far less than 1% of the global plastics production. Poly(lactide), commonly also referred to as poly(lactic acid) (PLA), is considered one of the most promising candidates to replace petroleum-based polymers in packaging and other commodity applications.<sup>306</sup> It is a biodegradable, compostable, chemically recyclable, and biocompatible thermoplastic polyester that is glassy at room temperature, resulting in stiffness and tensile strength similar to those of polystyrene (PS) or PET. PLA production amounted to 400 kT per year in 2021, which corresponds to about 20% of all bioplastics produced and is expected to double by 2026.<sup>307</sup> High molecular weight PLA is produced by ring-opening polymerization of enantiopure L,L-lactide, D,D-lactide or achiral D,L-lactide, resulting in semicrystalline stereoregular PLLA and PDLA or amorphous atactic PDLLA, respectively.<sup>313,314</sup> Among the performance limitations of PLA materials that have so far limited their wider adoption are poor melt strength, slow crystallization, poor heat resistance, post-processing ageing or creep, as well as their inherently brittle behavior.<sup>306,315–317</sup>

Various approaches have been explored to address some of these shortcomings. For instance, PLA stereocomplex obtained by mixing PLLA with 0.5–5 wt% PDLA have a melting temperature of 215 °C and thus do not only reduce the surface energy for nucleation of PLLA crystallization but also act as physical crosslinks in the melt state and thus significantly increase melt strength.<sup>56,58</sup> However, D,D-lactide is currently not readily available on an industrial scale.<sup>63</sup> Alternatively, modifications to the chain architecture have been explored, including chain extenders, branching, or covalent cross-linking.<sup>99,308</sup> For instance, introducing long-chain branches with a segment length above the entanglement length improves the nucleation of PLA crystallization, increases melt strength and introduces strain hardening during melt deformation.<sup>99,102</sup>

Blends of PLA with other sustainable polymers like poly(butylene adipate-*co*-butylene terephthalate) (PBAT), poly(butylene succinate-*co*-butylene adipate) (PBSA), or poly( $\epsilon$ -caprolactone) (PCL) have been used to increase toughness and melt strength,<sup>98</sup> typically complemented with the use of nucleating agents to simultaneously increase the PLA crystallization rate. To this end, inorganic additives such as calcium carbonate, clay, or talc increase the crystallization temperature by up to 20 °C and result in an up to seven-fold increase in crystallization half times.<sup>39</sup> Nanoscopic fillers such as carbon nanotubes, nanoclay, or cellulose nanofibers are effective nucleating agents that, thanks to their higher surface area can be used at lower contents.<sup>139–143</sup> Moreover, such nanoscopic nucleating agents act as reinforcing

elements that increase melt viscosity and, at sufficiently high concentrations, melt elasticity.<sup>98</sup> The use of organic nucleating agents that are soluble in the PLA melt and recrystallize upon cooling is beneficial because they form reversibly, which improves recyclability. Moreover, they typically exhibit better interfacial adhesion and remain better dispersed in the polymer matrix at higher concentrations. Particularly beneficial are hydrogen-bonded organic nucleating agents, such as 1,3,5-benzenetricarboxylamide (BTA) derivatives that form crystals with high aspect ratio driven by the combination of  $\pi$ -stacking of the central benzene units and three-fold hydrogen bonding of the amide substituents.<sup>150-154</sup> For instance, tricyclohexyl BTA has been found to both significantly increase crystallization rate and change the PLA microstructure to, for instance, shish-kebab-like and needle-like structures.<sup>151,157</sup> Moreover, the addition of tricyclohexyl BTA increases melt strength, which has been attributed to the formation of percolation networks of BTA crystals. Very often, however, it is only possible to address a subset of the perceived shortcomings; for instance, the melt processing of PLLA under large melt deformation typically requires starting from specimens quenched into an amorphous state and processing upon reheating to below the melting temperature, but this precludes the use of nucleation agents and thus comes at the expense of undesirably high cycle times, lower thermal stability, and post-processing ageing and creep.

Multivalent hydrogen-bonded ligands have also been used for the supramolecular modification of PLA. End-modification with self-complementary ureidopyrimidinone (UPy) ligands, for instance, resulted in the conversion of amorphous PLA with an actual molecular weight of 7'000 into materials with an apparent molecular weight of  $M_n = 70'000$ ,<sup>277</sup> or for the formation of supramolecular block copolymers with poly( $\gamma$ -methyl- $\epsilon$ -caprolactone)<sup>24</sup> and poly(butadiene)<sup>25</sup> that exhibited a significant increased ductility. However, the reported dissociation temperature of UPy dimers of about 87 °C limits the use of UPy ligands for the modification of semicrystalline PLLA because it is well below the melting temperature of the latter. While BTA derivatives have successfully been used for the supramolecular modification of other types of polymer,<sup>320</sup> and although they are important as nucleating agents for PLA, the supramolecular modification of PLA with BTA end groups has never been explored to date. In fact, the application of "supramolecular polymer" concepts to semicrystalline or glassy polymers has generally attracted little interest to date,<sup>277-282</sup> because end group aggregation has to occur above polymer crystallization or vitrification temperatures, and bulk properties were assumed to be dominated by the solid polymer.<sup>280,281,283</sup>

Here, we show how end group modification of PLLA with ditopic hydrogen-bonded end groups and their co-assembly with a low molecular weight additive based on the same supramolecular motif results in materials that synergistically combine the processing and performance advantages of chain extenders, nucleating agents, and melt reinforcing elements. To this end, we modified amorphous PDLLA and semicrystalline PLLA, both of  $M_n = 60'000$ , with diisopentyl BTA end groups (**PDLLA-B5** and **PLLA-B5**) and blended them with triisopentyl BTA (**B5**). Our results demonstrate that the specific co-assembly of BTA polymer end groups and the BTA additive results in a supramolecular network of polymer-bridged self-assembled “single-stack” nanofibrils. The polymer-tethered nanofibrils, first of all, serve as highly efficient nucleating agents for PLLA crystallization. Secondly, the physical network acts like a supramolecular chain extender and drastically increases the melt strength of PLLA, which opens a new processing temperature window for non-quenched PLLA above the PLLA melting temperature. The combination of these features has allowed us to melt-process well-nucleated PLLA specimens under realistic processing conditions that show drastically improved thermal stability and low ageing or creep.

## 5.2 Results and Discussion

### 5.2.1 Materials Design and Synthesis

We synthesized hydroxy-telechelic atactic PDLLA and stereoregular PLLA by ring-opening polymerization of D,L-lactide and L,L-lactide, respectively, initiated with diethylene oxide. A molecular weight of  $M_n = 60'000$  was chosen in both cases because it was considered to be sufficiently above the entanglement molecular weight of PLA of around  $M_e = 9'000$  to have a fully developed entanglement network and possess mechanical properties similar to commercial PLA.<sup>26</sup> The corresponding telechelic **PDLLA-B5** and **PLLA-B5** (Figure 62), both modified with *N,N'*-diisopentyl BTA end groups, were then synthesized by coupling of *N*-Cbz-L-alanine to the PDLLA or PLLA end groups by a Steglich esterification using *N,N'*-dicyclohexylcarbodiimide followed by deprotection using  $\text{Me}_3\text{SiI}$ , and a final amide coupling to 3,5-Bis(3-methylbutylcarbonyl)benzoic acid using PyBOP/DIPEA as the coupling reagent. **PDLLA-B5** and **PLLA-B5** were obtained in yields of 40% and 60% over three steps, respectively, both with a degree of functionalization of  $f = 2.0$  according to  $^1\text{H}$  NMR spectroscopy ( $M_n = 70'500$ , dispersity of  $\mathcal{D} = 1.22$  and  $M_n = 67'000$ ,  $\mathcal{D} = 1.20$ , respectively, according to GPC) (Figure 63). We chose this type of end groups because BTA derivatives are self-complementary and ditopic ligands known to reversibly form one-dimensionally extended aggregates via three-fold intermolecular hydrogen bonding, whose inherent helicity disfavors further lateral crystallization and thus promotes the formation of “single-



stack” nanofibrils in sufficiently dilute systems.<sup>157</sup> All of these aspects are relevant to allow for dynamic co-assembly with the low-molecular weight additive *N,N,N'*-triisopentyl BTA **B5**, to form the blends **PDLLA-B5/B5** and **PLLA-B5/B5**. The corresponding non-modified blends **PDLLA/B5** and **PLLA/B5** served as reference materials to investigate the effect of the polymer end groups on materials structure and properties.

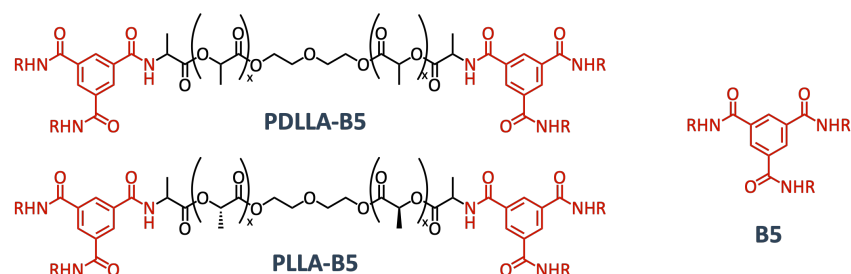


**Figure 62.** Chemical structures of telechelic poly(lactide)s **PDLLA-B5** and **PLLA-B5** ( $x = 420$ ), end-modified with *N,N'*-diisopentyl BTA, and of the additive *N,N,N'*-triisopentyl BTA (**B5**); R = isopentyl.

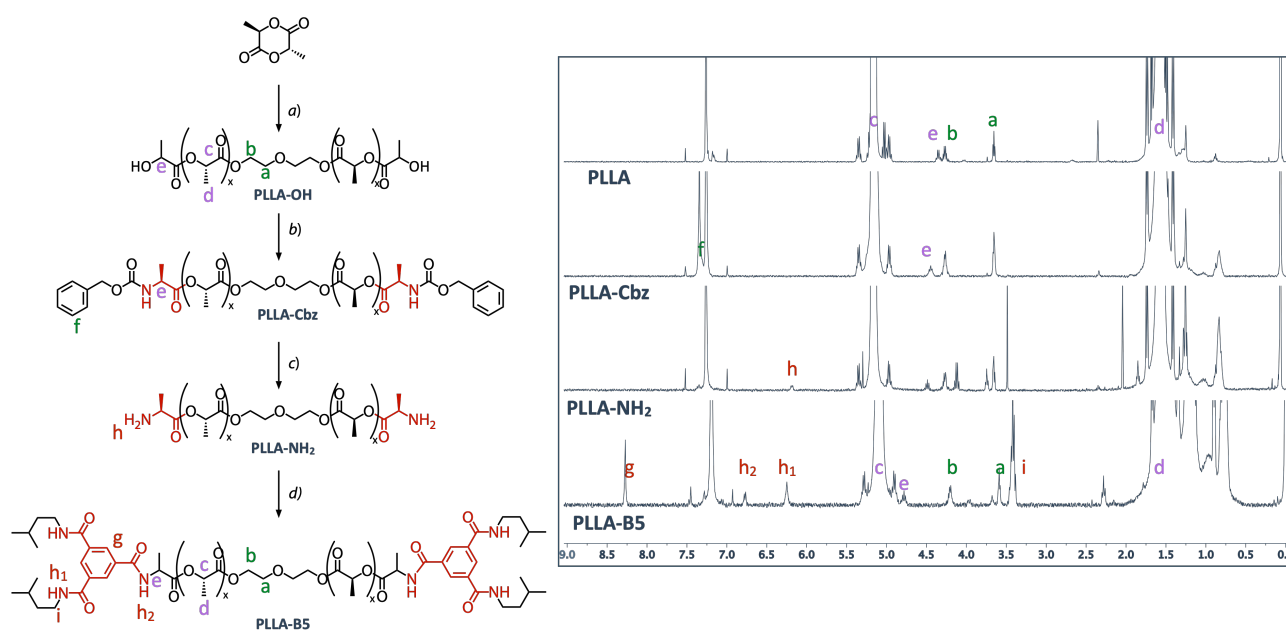


**Figure 63.** Synthesis of end-modified PLLA and PDLLA (not shown). *Reagents and conditions:* a) lactide (416.0 equiv.), diethylene glycol (1.0 equiv.), tin(II) 2-ethylhexanoate (0.8 equiv.), toluene, reflux, 4 h, 83 % (PLLA), 72 % (PDLLA). b) PLA-OH (1 equiv.), *N*-carbobenzoxy-L-alanine (20 equiv.), *N,N'*-dicyclohexylcarbodiimide (10 equiv.), 4-dimethylaminopyridine (12 equiv.), dry DCM, 12 h, 93 % (PLLA), 81 % (PDLLA). c) PLA-Cbz (1 equiv.), trimethylsilyl iodide (40 equiv.), dry DCM, 2 h, 83 % (PLLA), 72 % (PDLLA). d) PLA-NH<sub>2</sub> (1 equiv.), benzotriazol-1-yloxytripyrrolidinophosphonium hexafluorophosphate (PyBOP, 3 equiv.), 3,5-Bis(3-methylbutylcarbamoyl)benzoic acid (2.2 equiv.), *N,N*-diisopropylethylamine (DIPEA), THF, r. t., 16 h, 84 % (PLLA), 82 % (PDLLA). <sup>1</sup>H NMR spectra (CDCl<sub>3</sub>, 400 MHz) of **PLLA**, **PLLA-Cbz**, **PLLA-NH<sub>2</sub>** and **PLLA-B5** (right).

### 5.2.2 Morphology and Thermal Properties of **PDLLA-B5/B5** Blends

Temperature-dependent optical microscopy (OM) experiments were performed to understand the phase behavior of the **PDLLA-B5/B5** blends and the **PDLLA/B5** reference materials. At all investigated concentrations, the **PDLLA/B5** reference blends showed macroscopic phase separation of the additive **B5** into a network of needle-like crystals below their melting temperature observed in DSC (see below), and optically homogeneous solutions of **B5** in the polymer melt above that temperature (Figure 64) Similarly, **PDLLA-B5/B5** blends at concentrations above 2 wt% of **B5** showed macroscopic phase separation into needle-like crystals below their DSC melting temperature. In marked difference to the reference blends, however, **PDLLA-B5/B5** blends with  $\text{B5} \leq 1 \text{ wt\%}$  remained optically homogeneous both above and below the melting temperature of **B5**.

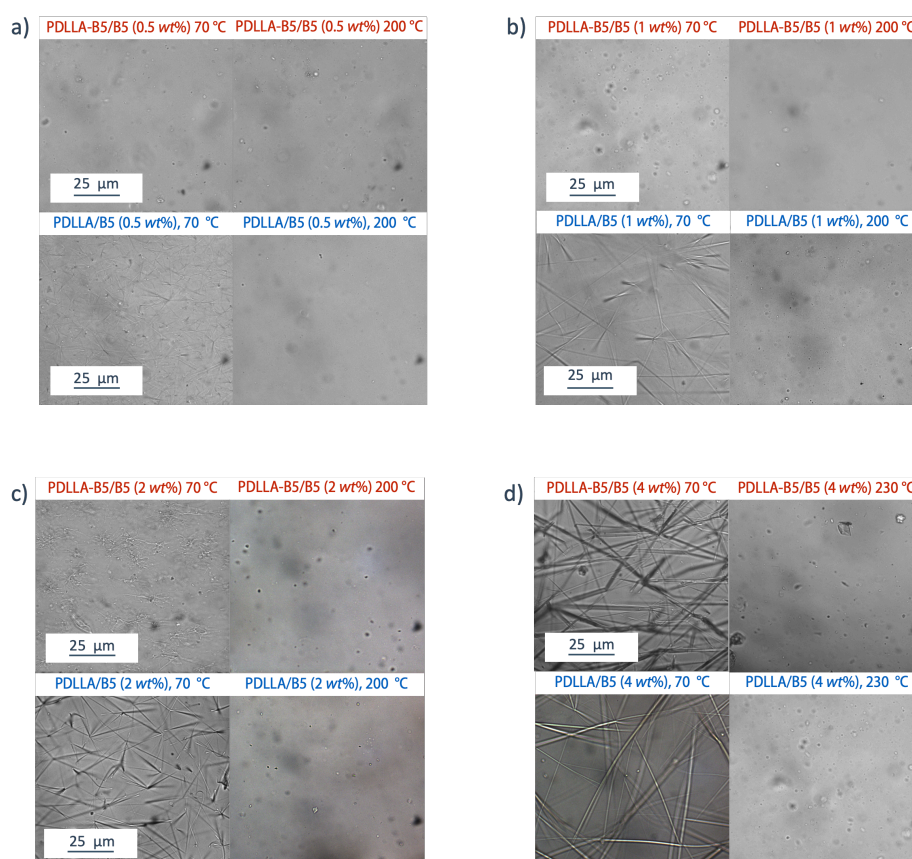


**Figure 64.** Optical micrographs in bright field of **PDLLA-B5/B5** and **PDLLA/B5** blends at additive concentrations of *a)* 0,5 wt%, *b)* 1 wt%, *c)* 2 wt%, and *d)* 4 wt% at 70 °C after cooling from the melt at 10 °C/min and in the melt at 200 °C or 230 °C

At the same time, however, the solid-state IR spectra of **PDLLA-B5/B5** at room temperature showed sharp N–H and C=O stretching bands at 3232–3236  $\text{cm}^{-1}$  and 1638–1640  $\text{cm}^{-1}$ , respectively, the same as those in pure **B5** (Figure 65). This proves that the end groups and the additive both remained

quantitatively aggregated into strongly N–H···C=O hydrogen-bonded stacks even in the optically homogeneous materials at low additive concentrations and thus implies that the additive still undergoes nanophase separation. Notably, however, the pure end-modified **PDLLA-B5** showed broad featureless absorptions in the N–H and C=O regions, demonstrating that the BTA end groups alone, in the absence of additional **B5** additive, did not aggregate at their nominal concentration of 1.1 wt% high molecular weight PDLLA.

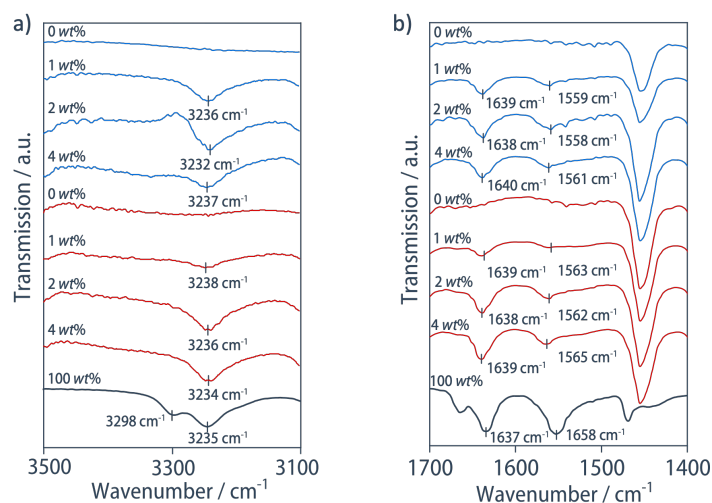


**Figure 65.** Solid-state FT-IR spectra (transmission) of **PDLLA-B5/B5** (red) **PDLLA/B5** (blue) blends at different additive concentrations at room temperature, with the positions of the characteristic N–H stretching (3232–3236  $\text{cm}^{-1}$ ), C=O stretching (1638–1640  $\text{cm}^{-1}$ ), and C=O bending (1558–1565  $\text{cm}^{-1}$ ) vibrations of hydrogen-bonded BTA stacks indicated.

AFM images (Figure 66) of the **PDLLA/B5** reference blends showed well-dispersed nanoscopic needle-like crystals with, for instance, an average width of  $40 \pm 10$  nm for a concentration of **B5** of 1 wt%, which is much larger than a single stack of BTA molecules, which is on the order of 1.5 nm.<sup>321</sup> In marked contrast, while the pure **PDLLA-B5** showed short, ill-defined, rod-like nanostructures, the addition of 1 wt% of **B5** resulted in a network of nanofibrils with widths on the order of a few nanometers and a very high aspect ratio that were homogeneously distributed across the entire sample. It is important to note that these nanofibrils did not have a crystalline morphology with straight edges and defined angles, but were compliant one-dimensional nanoscopic objects that were locally aligned parallel to one another with a periodic spacing. Histogrammic analysis of the interfibrillar distances (Figure 67a–d) showed that these distances systematically decreased with additive concentration, from  $13 \pm 2$  nm in pure **PDLLA-B5** to finally  $10 \pm 2$  nm at 4 wt% **B5**. This dependence could be successfully described with a simple space-filling model assuming a hexagonal close-packing of single stacks formed from BTA end

groups and additive molecules, which qualitatively confirms end group and additive co-assembly into nanofibrils with little to no lateral aggregation in **PDLLA-B5/B5** materials at concentrations  $< 2 \text{ wt}\%$  (Figure 67e-f). We can thus conclude that the presence of polymer **B5** end-groups suppresses typical macroscopic phase separation of the BTA additive **B5** and instead results in the formation of a network of homogeneously dispersed, polymer-tethered (and bridged) self-assembled nanofibrils that should hence be regarded as a physical network of “supramolecular graft copolymers”.

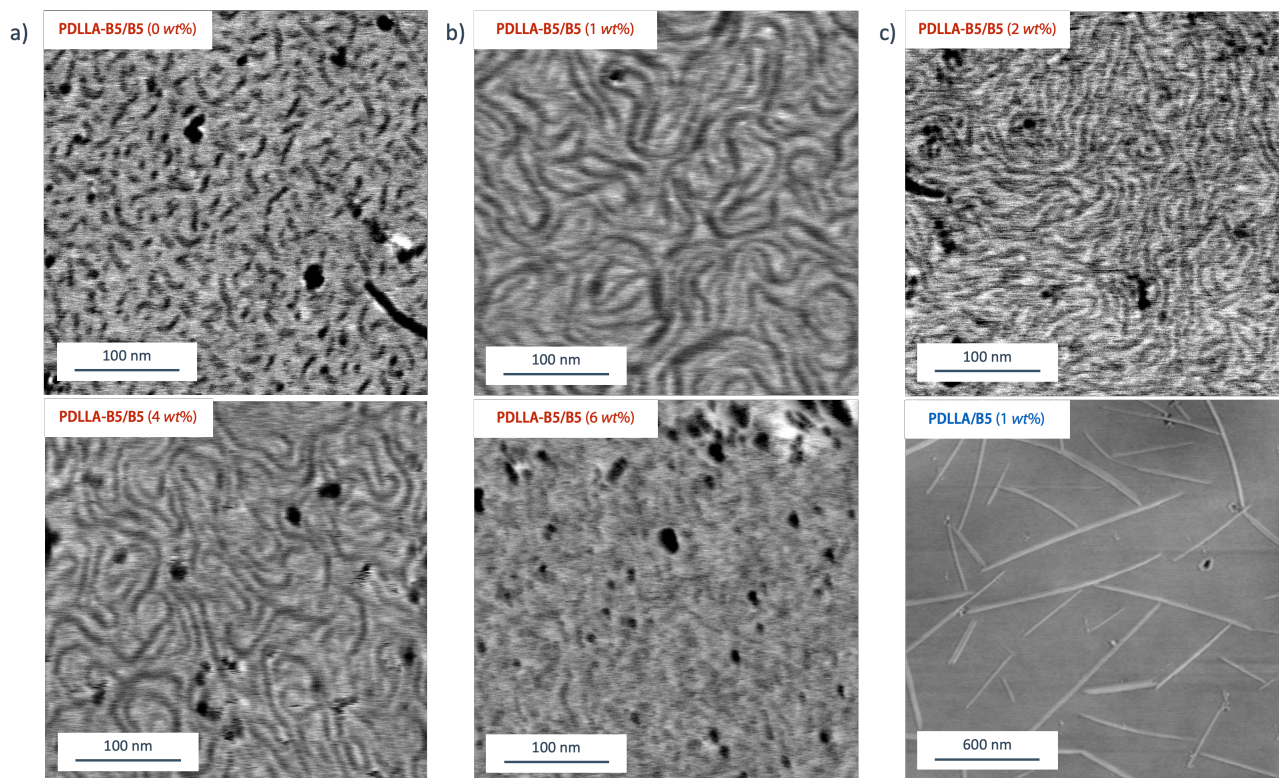


**Figure 66.** AFM phase images of the **PDLLA-B5/B5** blends at 70 °C at different additive concentrations revealed the formation of a network of nanofibrils, while the **PDLLA/B5** reference blends showed needle-like crystals of the additive.

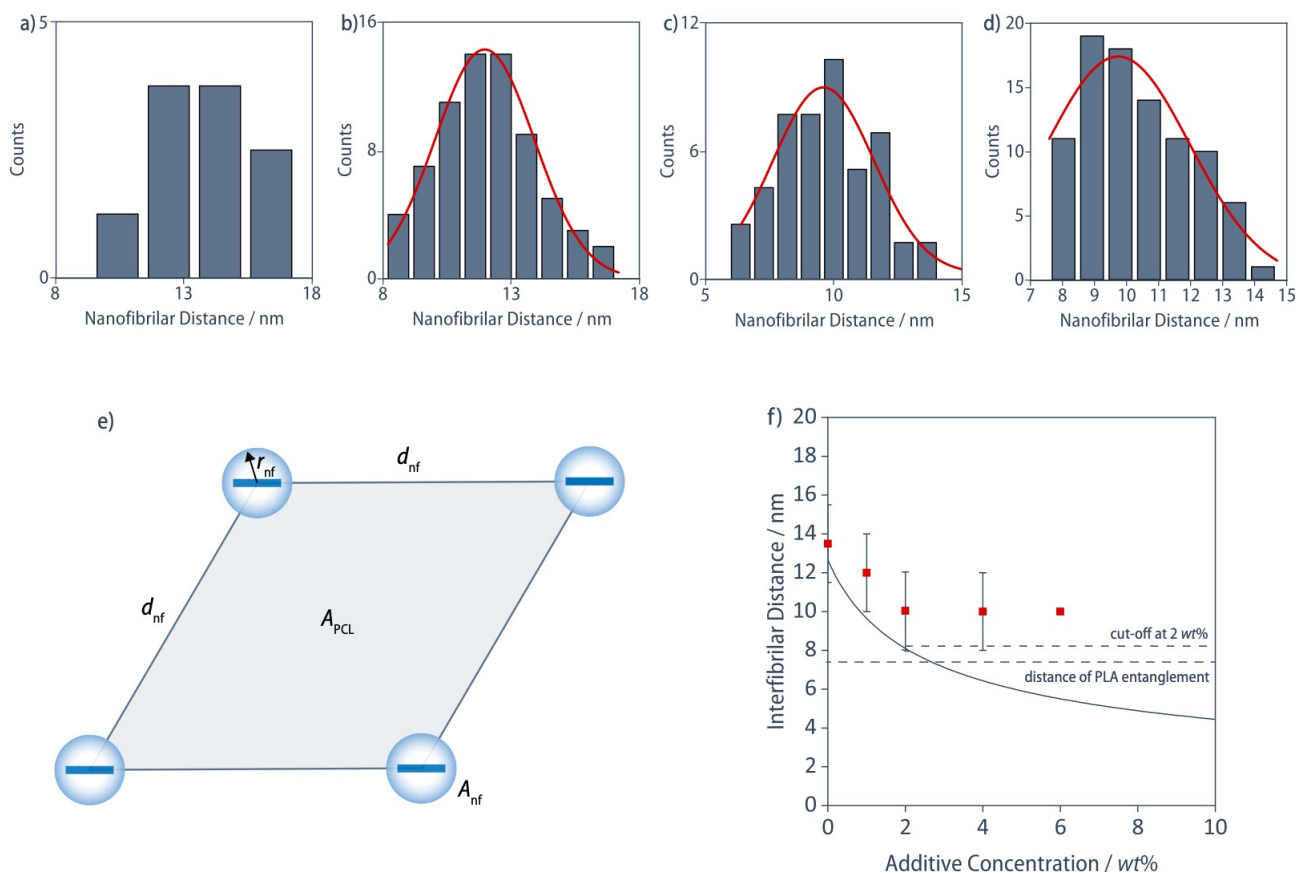


**Figure 67.** Histograms of nanofibrillar (NF) distances and Gaussian fit (red line) for *a*) PDLLA-B5, *b*) PDLLA-B5/B5 (1 wt%), *c*) PDLLA-B5/B5 (2 wt%), and *d*) PDLLA-B5/B5 (4 wt%); the histogram for PDLLA-B5/B5 (6 wt%) blend could not be plotted to due to poor contrast in AFM images of the blend. *e*) Space-filling model of the interfibrillar distance; the nanofibrils are assumed to be arranged on a hexagonal lattice whose basal lattice parameter,  $d_{nf}$ , corresponds to the interfibrillar distance,  $A_{nf}$  is the cross-sectional area of a nanofibril, and  $A_{PCL} = d_{nf}^2 \cos 30^\circ$  is the basal area of the unit cell, assumed to be equal to  $A_{nf}$  divided by the nanofibril volume fraction. *f*) Interfibrillar distance determined theoretically from a model based on hexagonal packing and equal special distribution (solid line) and experimentally from AFM images plotted versus the weight fraction of the **B5** additive. At concentrations  $\geq 2$  wt%, the additive **B5** phase-separates macroscopically and does not participate in nanofibrillar formation (upper dashed line). End-to-end distance of PLA entanglement points (lower dashed line) calculated using  $R = l\sqrt{NC_\infty} = 7.5$  nm (bond length  $l = 1.5$  Å, number of bonds  $N$  between entanglements, characteristic ratio  $C_\infty = 6.5$ ).

DSC heating scans of the pure additive **B5** showed two endothermic peaks at  $T_{meso} = 209$  °C and  $T_{B5} = 267$  °C. The lower temperature transition was associated with a transition from a crystalline phase to a columnar mesophase, attributed to a loss in three-dimensional order of the aliphatic moieties, while  $T_{B5}$  corresponded to a transition from the mesophase to the isotropic melt.<sup>321</sup> In the DSC heating scans of the PDLLA/**B5** blends, the temperature of the higher endothermic peak, which we refer to in what follows as  $T_{blend}$ , progressively diverges to temperatures far lower than  $T_{B5}$  as the additive concentration in the blend is decreased, while the lower one remains at  $T_{meso} = 209$  °C and is only observed for additive concentrations  $\geq 3$  wt% where  $T_{blend} > T_{meso}$  (Figure 68). Assuming the DSC observations to represent

the equilibrium behavior of the system, this depression in the melting temperature of the **B5** mesophase may be expressed in terms of its volume fraction in the homogeneous melt,  $\phi$ , using the Flory-Huggins model:<sup>114</sup>

$$T_{\text{blend}} \approx \frac{T_{\text{B5}} + \frac{RT_{\text{B5}}\chi_0}{\Delta H_{\text{B5}}}(1-\phi)^2}{1 - \frac{RT_{\text{B5}}}{\Delta H_{\text{B5}}}(1-\phi + \ln \phi + \chi_1(1-\phi)^2)}, \quad (7)$$

where  $\Delta H_{\text{B5}}$  is the molar enthalpy of the **B5** mesophase-isotropic transition, the Flory-Huggins interaction parameter is assumed to be of the form  $\chi = \chi_0/T + \chi_1$ , the reference volume is the molar volume of **B5**, and the molar volume of the polymer is assumed to be much greater than that of **B5**. The volume fraction,  $\phi$ , was estimated from the additive weight fraction, taking the melt densities of **B5** and PLA to be  $\rho_{\text{B5,L}} = 0.9 \text{ g/cm}^3$ , which is 80 % of the room temperature crystal density determined by WAXD,<sup>321</sup> and  $\rho_{\text{PLA,L}} = 1.07 \text{ g/cm}^3$ .<sup>322</sup> For  $T_{\text{blend}} < T_{\text{meso}}$ , however,  $\Delta H_{\text{B5}}$  must be replaced by  $\Delta H_{\text{B5}} + \Delta H_{\text{meso}}$ , where  $\Delta H_{\text{meso}}$  is the molar enthalpy of the **B5** crystalline-mesophase transition. Similarly,  $T_{\text{B5}}$  must be replaced by  $(\Delta H_{\text{B5}} + \Delta H_{\text{meso}})/(\Delta S_{\text{B5}} + \Delta S_{\text{meso}})$ , where the  $\Delta S$  terms are the respective molar transition entropies. Linear regression of the experimental  $T_{\text{blend}}$  gave  $\chi_0 = 1'708 \text{ K}$  and  $\chi_1 = -1.65$ .  $T_{\text{blend}}[\phi]$  and the binodal for phase separation of liquid additive-rich domains at  $T > T_{\text{B5}}$  could then be determined analytically (Figure 68c).

This analysis provided a semi-quantitative basis for the more involved discussion of the blends **PDLLA-B5/B5**, for which we assume initially that the end groups are homogeneously distributed in the liquid phase at any  $T > T_{\text{blend}}$ , the effective chain-end molar volume is equal to the additive molar volume, and the free energy of interaction between the chain ends and the additive is zero. To calculate the interaction term in the Flory-Huggins equation for phase separation of bulk **B5** from end-modified **PDLLA-B5**, firstly,  $\phi$  in the equation  $RT\chi\phi(1-\phi)$  for the unmodified PDLLA blends, must be replaced with  $\phi + (1-\phi)f$  to account for the presence of end groups. Secondly, the free energy associated with interactions between the chain ends only and PDLLA, which remains unchanged after phase separation of **B5** must be subtracted to finally give Equation (8):

$$RT\{\chi(\phi + (1-\phi)f)(1-\phi - (1-\phi)f) - f(1-f)(1-\phi)\} = RT(1-f)^2\chi\phi(1-\phi), \quad (8)$$

where  $f \approx 0.0167$  is the end-group volume fraction in **PDLLA-B5**. Indeed, replacing  $\chi$  by  $(1-f)^2\chi$  in Equation (7) provided an adequate description of the experimentally determined  $T_{\text{blend}}$  for  $\phi \gtrsim 0.02$  (Figure 68d), which corresponds to the threshold concentration below which optical microscopy and

AFM imaging indicated macroscopic phase separation of bulk **B5** to be fully suppressed in favor of nanofibril formation.

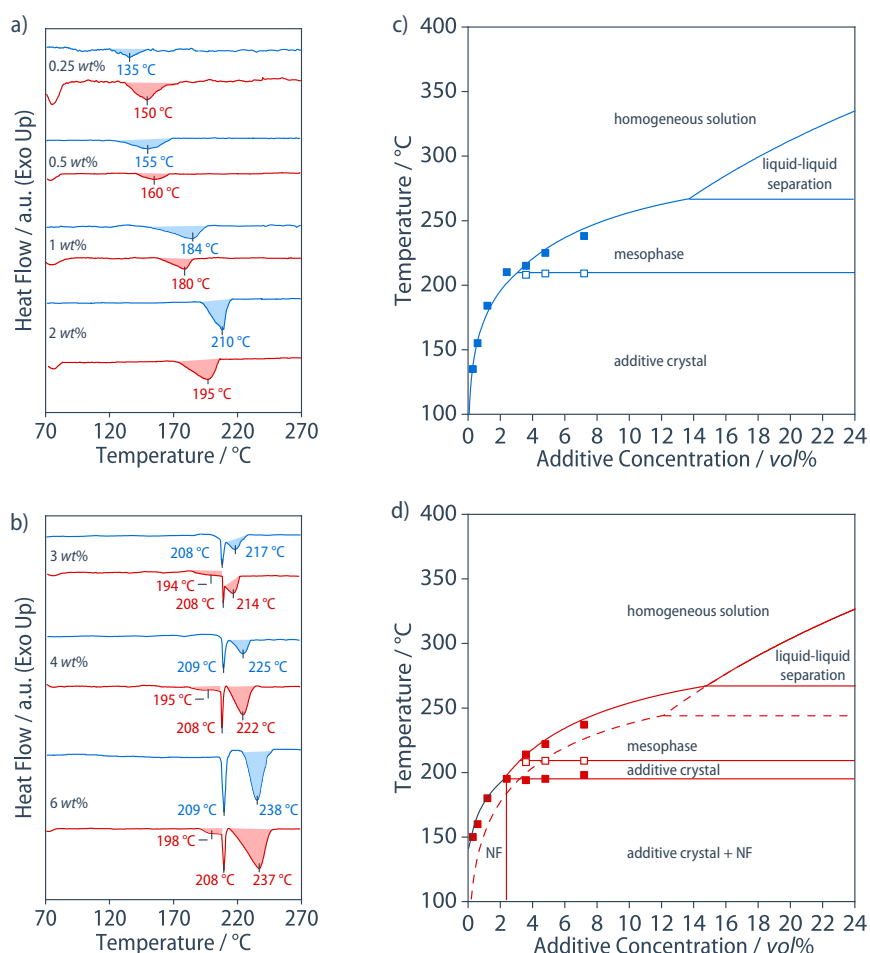


**Figure 68.** *a–b*) DSC heating scans (scanning rate 10 °C/min) of **PDLLA-B5/B5** (red) or **PDLLA/B5** (blue) blends, indicating the endothermal transition temperatures of the **B5** nanofibrils or crystals at different concentrations. *c*) Phase diagram of **PDLLA/B5** blends derived from endothermal transitions in DSC, and *d*) phase diagram of the blends derived from endothermal transitions in DSC marking the concentration limit of the nanofibrillar regime (NF) at 2 wt% at 195 °C above which excess of **B5** additive in **PDLLA-B5/B5** materials showed macrophase separation into additive crystals and thus an additional endothermal peak characterized by temperatures that are almost identical to melting of **B5** crystals in **PDLLA/B5** materials. Full symbols represent a transition from the mesophase of **B5** aggregates to the isotropic melt, empty symbols represent a transition from a crystalline phase of **B5** aggregates to a columnar mesophase

The formation of nanofibrils whose core is made up of single extended BTA stacks from pure **B5** is assumed not to occur under equilibrium conditions in the unmodified PDLLA blends, because pure **B5** nanofibrils would be associated with a significant interfacial energy penalty with respect to the bulk **B5** phases. It is nevertheless instructive to consider the notional dissociation temperature,  $T_{nf}$ , of pure **B5** nanofibrils (Figure 68d, hatched curve), which was calculated from Equation (8), assuming for the sake of illustration that interfacial interactions result in a reduction in  $\Delta H_{B5}$  by 1.2 kJ/mol, implying that the

bulk melting temperature of the additive,  $T_{B5}$ , must be replaced by a fictive limiting dissociation temperature,  $T_{nf\infty} = 244$  °C, which represents the temperature at which dispersed nanofibrils would be in equilibrium with bulk **B5** crystals, if the transition entropy remained unchanged. In the case of **PDLLA-B5**, the end groups are able to self-assemble to form nanofibrils in the absence of any additive, with a dissociation temperature  $T_{nf0} \approx 140$  °C. The temperatures of the endothermic transitions in the DSC heating scans associated with nanofibril dissociation then increase rapidly with  $\phi$  for  $\phi \lesssim 0.02$ . This may be attributed to the formation of mixed nanofibrils made up of co-assembled end groups and **B5** molecules. The main driving force for the formation of such nanofibrils at temperatures greater than both  $T_{nf0}$  and  $T_{blend}$  is inferred to be the gain in the effective free energy of dissociation per **B5** molecule on incorporation of chain ends into pure **B5** nanofibrils. Hence, the dissociation temperature of the mixed nanofibrils (Figure 68d, black curve) is expected to tend to  $T_{nf0} \approx 140$  °C as  $\phi \rightarrow 0$ , and to converge with  $T_{nf}$  for pure **B5** nanofibrils (Figure 68d, hatched curve) if  $\phi \gg f$ , where the end-group contribution becomes small. We experimentally observed that the value of  $\phi$  corresponding to the transition from the low- $\phi$  nanofibrillar regime to the regime in which nanofibrils coexist with the bulk **B5** mesophase or crystalline phase, *i.e.*, the point at which the dissociation temperature of the nanofibrils becomes equal to  $T_{blend}$ , is  $\phi \approx 0.02$ . This value is very close to  $f \approx 0.0167$ , the volume fraction of the end groups. It is therefore tempting to hypothesize that it is not a coincidence that this transition occurs at an additive to end-group ratio of 1. Moreover, the nanofibril dissociation temperature and volume fraction should remain constant at about 195 °C and 0.037, respectively, as  $\phi$  increases further. At  $\phi \gtrsim 0.02$  **B5** phase-separates macroscopically in **PDLLA-B5/B5** blends and does not participate in nanofibril formation. In turn, the thermodynamic description implies that macroscopic phase separation of bulk **B5** to be fully suppressed in favor of nanofibril formation at concentration of  $\phi \lesssim 0.02$  in **PDLLA-B5/B5** blends.

### 5.2.3 Morphology and Thermal Properties of **PLLA-B5/B5** Blends

We observed virtually identical thermal transitions in DSC heating scans of the blends of end-modified semicrystalline **PLLA-B5/B5** as in the blends of amorphous **PDLLA-B5/B5** described above (Figure 69) implying the formation of a nanofibril network in the polymer melt and its presence in the amorphous phase at room temperature also in **PLLA-B5/B5** blends, although its imaging by AFM was impeded by the PLLA crystalline domains in this case. Both non-modified **PLLA** and pure modified **PLLA-B5** showed a similar crystallization onset at  $T_c = 114$  °C in DSC cooling scans at a cooling rate of 10 °C/min,



suggesting that the presence of the end groups alone in **PLLA-B5** had little effect on polymer crystallization (Figure 69a). Since BTA derivatives are commonly used as nucleating agents,<sup>152,155</sup> the addition of the additive **B5**, as expected, increased the crystallization onset in the reference materials **PLLA/B5** materials to reach  $T_c = 124$  °C at all concentrations  $\geq 0.5$  wt%. Remarkably, however, this increase in crystallization onset temperature was significantly more pronounced in the blends **PLLA-B5/B5**, where it reached 141 °C for additive concentrations  $\geq 1$  wt%, which is among the highest crystallization temperatures reported in the literature (Figure 69).<sup>134,157</sup> This may indicate that the single-stack nanofibrils may be significantly more effective as nucleating agents than even the highly dispersed nanoscopic needle-like crystals of **B5**, supposedly both because of their optimal dispersion and the PLLA segments tethered to the nanofibrils. It is interesting to note that, while the reference materials **PLLA/B5** containing  $\geq 6$  wt% of **B5** continued to show a well-nucleated polymer crystallization with the same  $T_c = 124$  °C as the blends with less additive, the modified blend **PLLA-B5/B5** (6 wt%) did not crystallize at all under the same cooling conditions. As will be demonstrated later, **PLLA-B5/B5** (6 wt%) has significantly higher melt elasticity compared to the blends with less additive, and thus, supposedly, prevents polymer chains from disentanglement and slows down the crystallization process.

In order to investigate the nucleation effect of the nanofibril network in the blends **PLLA-B5/B5** in more detail, we conducted isothermal crystallization experiments by rapid cooling from the polymer melt to the desired crystallization temperature of 140 °C. Crystallization half-times on the order of  $\tau_{1/2} = 6$ –8 min were observed for the reference materials **PLLA/B5**, that were significantly lower than the  $\tau_{1/2} = 34$  min of pure PLLA but increased again slightly towards higher additive concentrations, supposedly due to the increased melt viscosity. A similar  $\tau_{1/2} = 7.6$  min was determined for a PLLA blend with talc (2 wt%). By contrast, the blends **PLLA-B5/B5** exhibited an additional order of magnitude lower crystallization half-times of  $\tau_{1/2} = 0.8$ –1 min at all additive concentrations  $< 6$  wt%.

Scanning electron microscopy (SEM) images of both **PLLA/B5** and **PLLA-B5/B5** samples containing with 0 or 1 wt% of **B5** crystallized at 140 °C showed homogeneously distributed spherulites with straight boundaries where they impinge in all cases, indicating simultaneous heterogeneous nucleation (Figure 70d-f). However, the spherulites in the case of the modified blend **PLLA-B5/B5** (1 wt%) had average diameters  $d = 8$   $\mu\text{m}$  and nucleation densities  $ND = 7.8 \cdot 10^5$   $\text{mm}^{-3}$ , both differing substantially from those in the non-modified reference blends **PLLA/B5** (1 wt%) where  $d = 105$   $\mu\text{m}$  and  $ND = 6.9 \cdot 10^2$   $\text{mm}^{-3}$ .

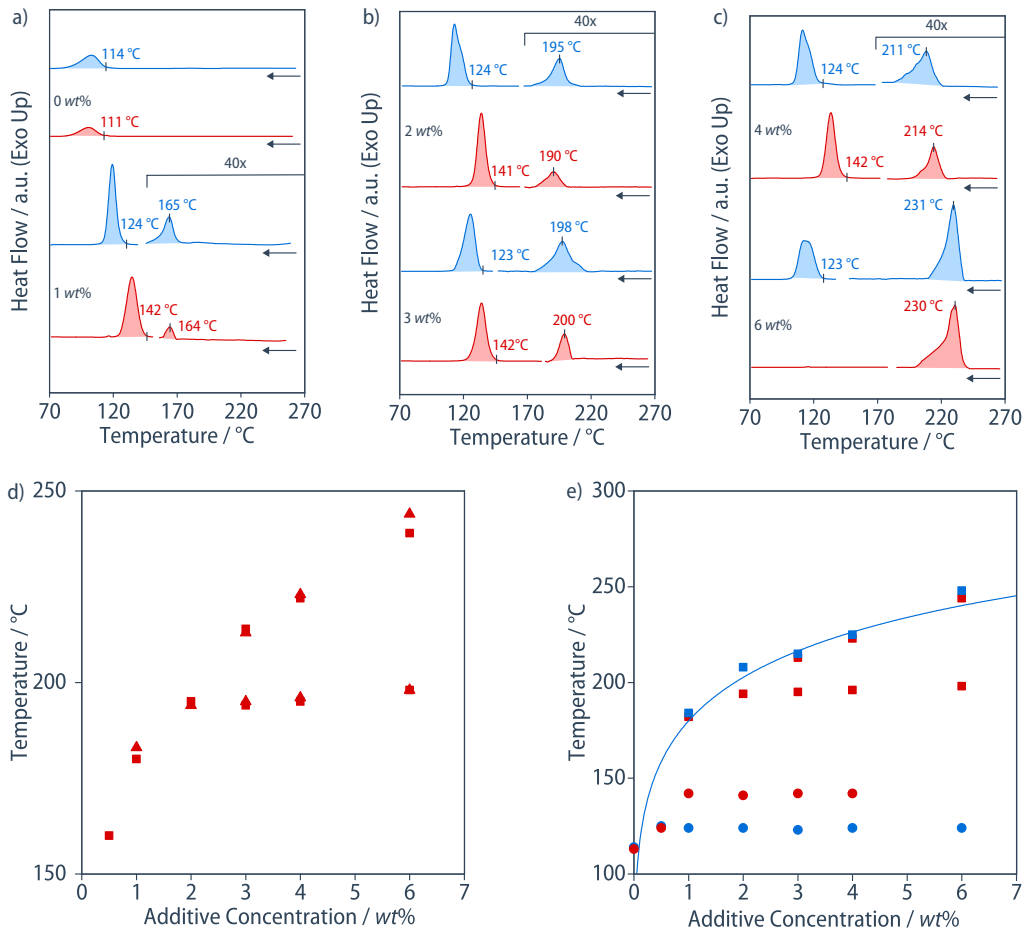


**Figure 69.** *a–c)* DSC cooling scans at 10 °C/min of **PLLA-B5/B5** (red) or **PLLA/B5** (blue) blends, indicating self-assembly temperature of the **B5** aggregates and onset temperature of PLLA crystallization at different concentrations. *d)* DSC cooling scans at 10 °C/min of **PLLA-B5/B5** (red) and **PLLA/B5** (blue) blends indicating crystallization of PLLA matrix and **B5** aggregates. *e)* Phase diagram of the blends derived from endothermal transitions of **B5** aggregates (squares) in DSC marking the concentration limit of the nanofibrillar regime at 2 wt% at 195 °C above which excess of **B5** additive in **PLLA-B5/B5** materials showed macro-phase separation and thus an additional endothermal peak characterized by temperatures that are almost identical to melting of **B5** crystals in PLLA/B5 blends. PLLA crystallization onset (circles) is shown to demonstrate increase in crystallization temperature of PLLA-**B5/B5** and PLLA/B5 blends.

To estimate the size of spherulites at other additive concentrations, the spherulite growth constant,  $k$ , was determined by fitting the integrated degree of crystallization  $X[t]$  at 140 °C using Johnson-Mehl-Avrami-Kolmogorov model

$$X[t] = 1 - e^{-kt^n}, \quad (8)$$

assuming a dimensionality parameter  $n = 3$  for three-dimensional spherulite growth (Figure 70i).

Nucleation density  $N$  could then be calculated determined by

$$N = 3k/(4\pi c^3), \quad (9)$$

and using growth rates,  $c$ , determined by optical microscopy (Table7).

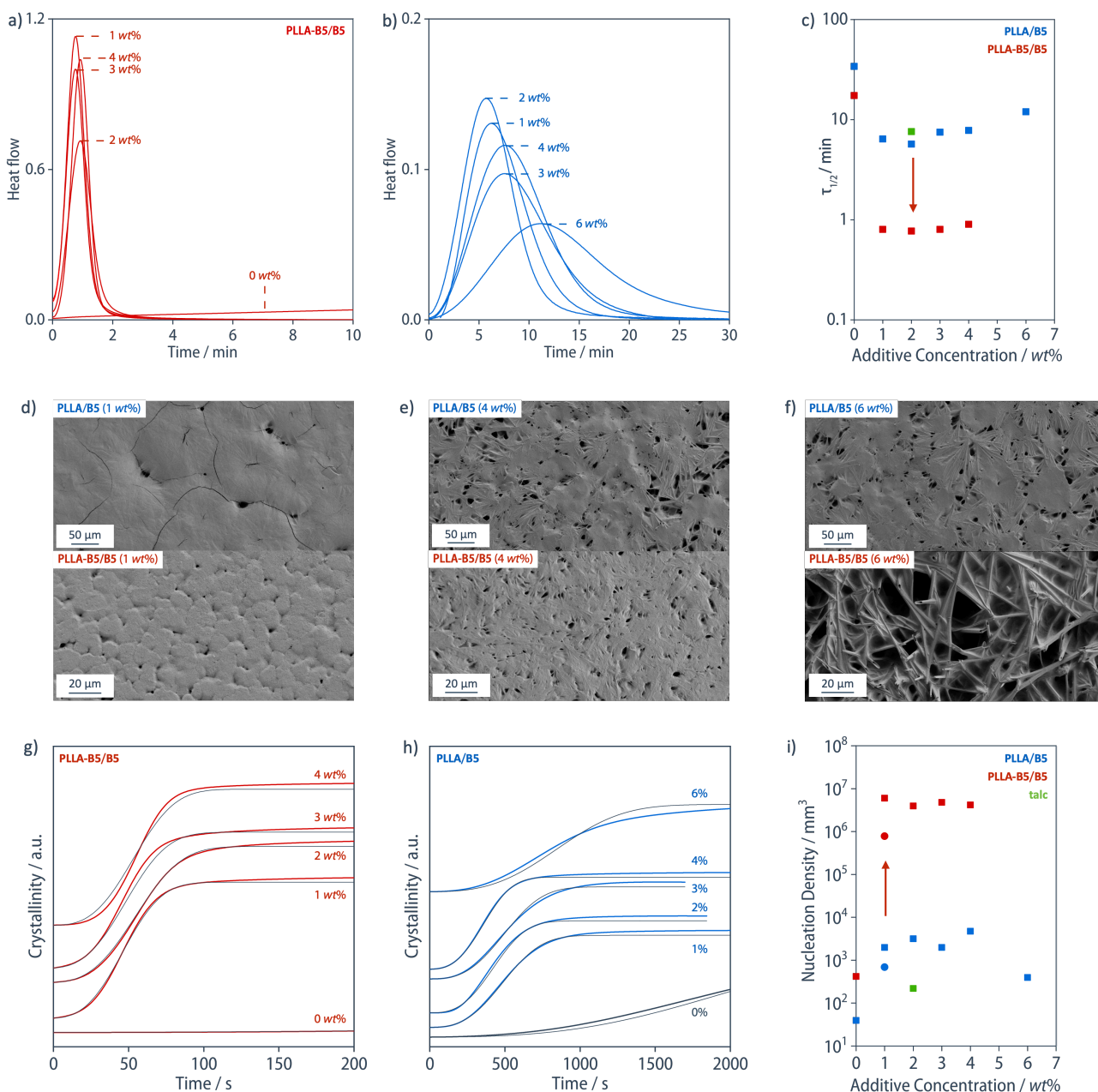


**Figure 70.** DSC isothermal crystallization curves at 140 °C for *a)* **PLLA-B5/B5** (red) and *b)* **PLLA/B5** (blue) blends at various concentration. *c)* Crystallization half times determined from DSC isothermal crystallization for **PLLA-B5/B5** (red), **PLLA/B5** (blue) and **PLLA/talc** (2 wt%) (green). *d-f)* SEM images of **PLLA-B5/B5** (bottom) and **PLLA/B5** (top) of 1 wt%, 4 wt% and 6 wt% of **B5** prepared by isothermal crystallization at 140 °C. *g-h)* Integration of DSC isothermal crystallization curves at 140 °C of **PLLA-B5/B5** (red) and **PLLA/B5** (blue) blends with the corresponding fitting using Johnson-Mehl-Avrami-Kolmogorov model (black). *i)* Calculated (squares) and measured from SEM (circles) nucleation density for **PLLA-B5/B5** (red), **PLLA/B5** (blue) and **PLLA/talc** (2 wt%) (green)

The nucleation densities were thus found to be three orders of magnitude higher in the modified **PLLA-B5/B5** blends compared to the non-modified **PLLA/B5** reference materials at all additive concentrations (Figure 70g-i). Considering that BTA derivatives such as **B5** on their own are among the most efficient nucleating agents used for PLLA materials,<sup>157</sup> this unprecedentedly efficient nucleation

effect in the **PLLA-B5/B5** blends can probably be explained not only by the yet improved dispersion of **B5** aggregates but also by the improved interaction between nucleating agent and the tethered polymer chains.

**Table 7** Spherulite growth rates for **PLLA-B5/B5** and **PLLA/B5** at 140 °C determined by optical microscopy, in  $\mu\text{m}/\text{min}$ .

	0 wt%	1 wt%	2 wt%	3 wt%	4 wt%	6 wt%
<b>PLLA-B5/B5</b>	3.3	3.6	3.0	3.3	3.3	3.3
<b>PLLA/B5</b>	5.7	10	4.8	5.3	5.5	5.3

#### 5.2.4 Melt Properties of the Blends

Oscillatory shear rheology temperature sweeps were performed at a frequency of 1 rad/s and a cooling rate of 10 °C/min to demonstrate the effect of the polymer chain tethering to the nanofibrillar network on the viscoelastic properties of the materials. Due to entanglement, pristine PDLA showed a rubbery plateau above its glass transition temperature of  $T_g = 60$  °C with a storage modulus  $G' = 0.3$  MPa at 75 °C (loss factor  $\tan \delta = G''/G' = 0.3$ ) and a rheological softening temperature  $T_s = 90$  °C ( $G' = G''$ ) above which PDLA showed viscous behavior ( $G'' > G'$ ). The addition of **B5** in the PDLA/**B5** reference materials resulted in a slightly increased melt modulus of, e. g.,  $G' = 0.9$  MPa and 1.0 MPa at 1 wt% and 6 wt% of **B5**, respectively, that we attributed to melt reinforcement by the needle-like crystals of **B5**, but otherwise unaltered rheological behavior. In marked contrast, the modified blends **PDLA-B5/B5** demonstrated a rubbery regime that extended far beyond the softening temperature of the entanglement network in PDLA and its blends, with a melt modulus of about  $G' = 5$  MPa at 75 °C and up to rheological softening temperatures,  $T_s$ , defined as the cross-over temperature where  $G'' = G'$ , that systematically increased with additive concentration to  $T_s = 111, 120, 154,$  and 198 °C at 1, 2, 4, and 6 wt% of **B5** (Figure 71), as did the plateau moduli that reached up to  $G'(130$  °C) = 0.19, 0.14, 0.67, and 1.5 MPa at these concentrations. Additionally,  $\tan \delta$  decreased to 1.8, 1, 0.8 and 0.4 in **PDLA-B5/B5** blends at 1, 2, 4, and 6 wt% of **B5** compared to 2.2, 1.6, 1.2 and 0.9 in PDLA/**B5** reference materials, showing higher melt elasticity due to polymer chains being covalently tethered to the nanofibrillar network preventing relaxation under load.

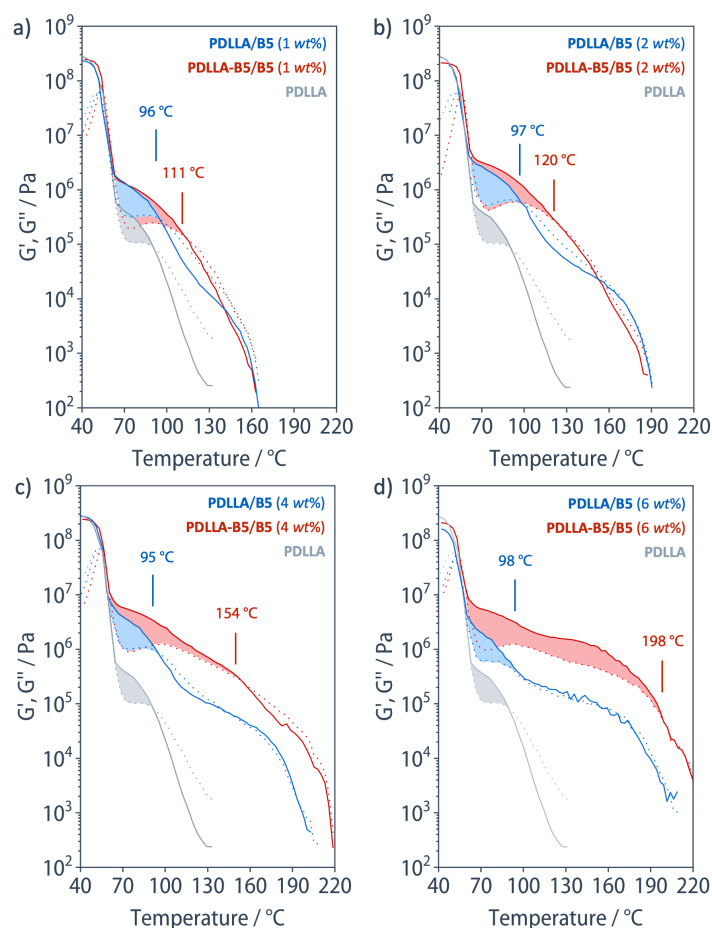


**Figure 71.** Storage modulus (solid line) and loss modulus (dotted line) from temperature-dependent oscillatory shear rheology (cooling rate 10 °C/min, frequency 1 rad/s, strain 1%) of **PDLLA-B5/B5** (red), **PDLLA/B5** (blue) and pristine **PDLLA** (grey) at different additive concentrations. Rheological softening temperatures,  $T_s$ , defined as the cross-over temperature where  $G'' > G'$ , indicated in the graphs.

Oscillatory shear oscillatory temperature sweep experiments under the same conditions were also performed with semicrystalline PLLA materials. While no significant difference in melt properties was observed for **PLLA-B5/B5** and **PLLA/B5** mixtures at additive contents below 4 wt%, where the amorphous materials had shown softening temperatures,  $T_s$ , below the PLLA melting temperature of 175 °C, **PLLA-B5/B5** (4 wt%) showed a more than one order of magnitude increase in melt strength and elasticity, with  $G' = 12$  kPa and  $\tan \delta = 1.3$  at 180 °C, compared to the **PLLA/B5** reference material where  $G' = 0.7$  kPa and  $\tan \delta = 2.7$  (Figure 72a-d).

Moreover, elongational viscosity measurements performed on thin films of **PLLA-B5/B5** (4 wt%) at an extension rate of 2 s<sup>-1</sup> at 180 °C showed melt strength of 90 kPa which is an order of magnitude higher than its non-modified analog (8.5 kPa), and was further increased to 175 kPa and a melt extensibility of up to 500 % at 160 °C, which is lower than  $T_m$  but above  $T_c$  of the PLLA matrix (Figure 72d). To showcase

processability of the obtained materials, **PLLA-B5/B5** (4 wt%) and PLLA were injection molded from the melt  $T = 200\text{ }^{\circ}\text{C}$  into a toy brick mold at  $80\text{ }^{\circ}\text{C}$ . While the injection-molded PLLA toy brick was apparently too soft and deformed upon demolding, the toy brick produced from **PLLA-B5/B5** (4 wt%) could be straightforwardly removed from the mold, exhibited excellent feature fidelity, as well as good “clutch work” in bonding with commercial toy bricks (Figure 72e-f).

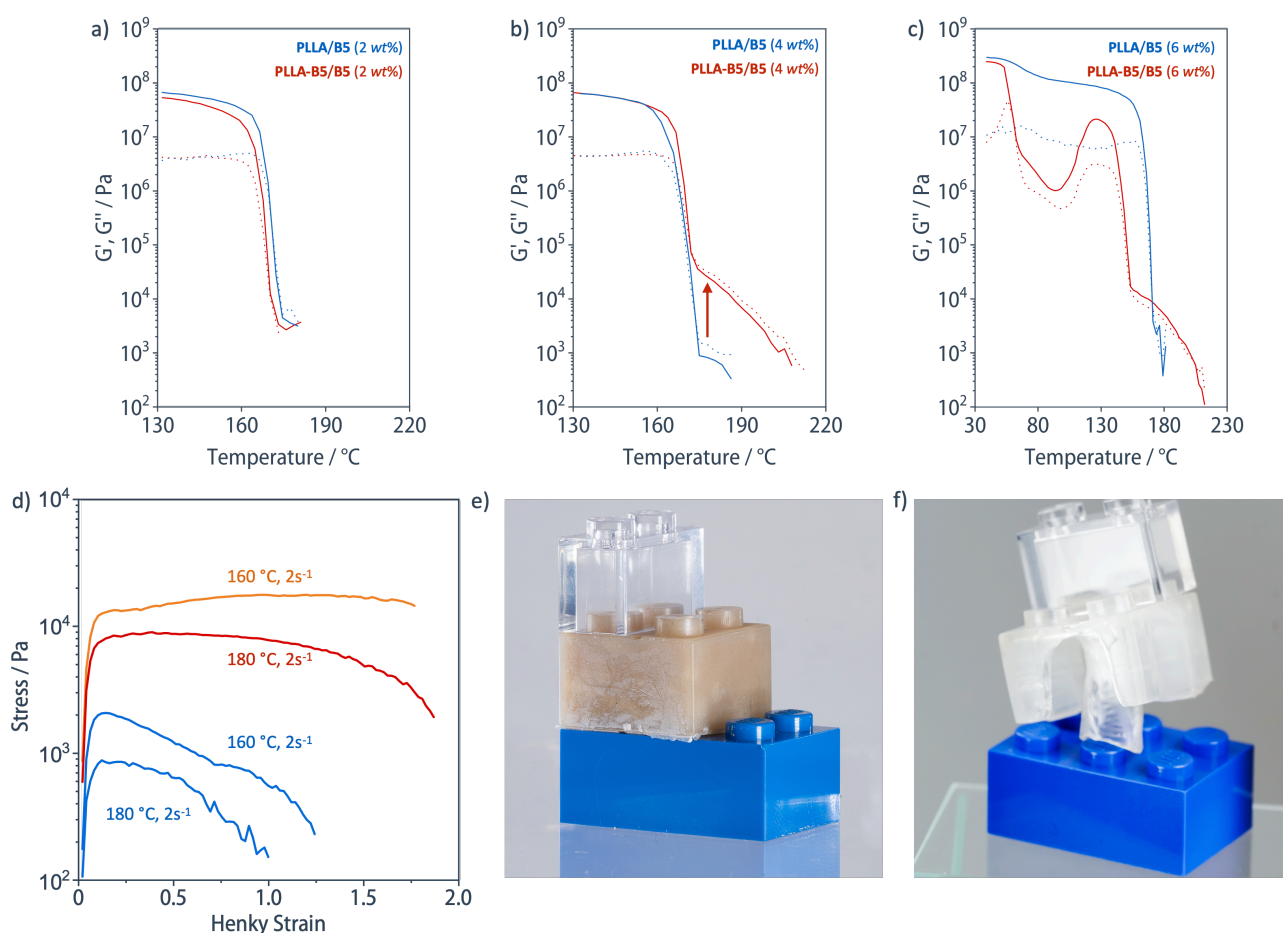


**Figure 72.** *a-c*) Oscillatory shear rheology (heating rate  $10\text{ }^{\circ}\text{C}/\text{min}$ ,  $1\text{ rad/s}$ , strain 1%) of **PLLA-B5/B5** (red), **PLLA/B5** (blue) and pristine **PLLA** (grey) at various concentrations; storage modulus – solid line; loss modulus – dotted line. *d*) extensional viscosity experiments of **PLLA-B5/B5** (4 wt%) (red), **PLLA/B5** (4 wt%) (blue) at  $180\text{ }^{\circ}\text{C}$  and **PLLA-B5/B5** (4 wt%) (orange) and **PLLA/B5** (4 wt%) (blue) at  $160\text{ }^{\circ}\text{C}$  as a function of Henky strain showing significantly higher melt strength of the **PLLA-B5/B5** blends. *e*) **PLLA-B5/B5** (4 wt%) and *f*) PLLA used for the preparation of an injection molded LEGO brick prepared from the melt  $200\text{ }^{\circ}\text{C}$  (mold temperature  $80\text{ }^{\circ}\text{C}$ ).

### 5.3 Conclusions

It was shown that the co-assembly of the end groups of high molecular weight **PLLA-B5** and **PDLLA-B5** ( $M_n = 60'000$ ) and **B5** additive suppressed the macroscopic phase separation of the additive into needle-like crystals and instead yielded a network of compliant, polymer-tethered nanofibrils that were placed

at a periodic distance of 10–12 nm. This nanofibrillar network was found to be a highly efficient nucleating agent for PLLA crystallization, resulting in crystallization temperatures as high as  $T_c = 140$  °C, and an increase in nucleation density by three orders of magnitude. Simultaneously, a new rubber-like regime is established in the amorphous **PDLLA-B5/B5** blends above the PDLLA glass transition, which manifested itself also in a one order of magnitude increase in melt strength in the semicrystalline **PDLLA-B5/B5** blends at sufficiently high additive concentration, and is also observed at large melt deformations. The combination of improved nucleation efficiency and increased melt strength opens new avenues for PLA processing, for instance, by injection molding, thermoforming, film-blowing, or foaming, and promises improved cycle times and product performance in terms of heat resistance and ageing.

## **Conclusions and Outlook**



## Conclusions and Outlook

In the present thesis, it was demonstrated that a simultaneous improvement of final mechanical properties, melt behavior, and crystallization rate of high molecular weight aliphatic polyesters can be achieved when one blends a polymer end-modified with a ditopic, self-complementary self-assembling unit based on three-fold hydrogen bonding and a low molecular weight additive based on the same supramolecular motif. Co-aggregation of the polymer end-groups and the additive resulted in the formation of helical, one-dimensional nanofibrils which, due to polymer tethering, suppressed macroscopic phase separation of the additive and resulted in a supramolecular network of nanofibrils. The use of the additive allowed efficient control over the concentration of the self-assembling units independent of the molecular weight of the polymer so that the polymer matrix, including the polymer segments bridging the nanofibrils, could still develop a robust entanglement network. Due to the high melting temperatures of the nanofibrils, the supramolecular network persisted above the glass transitions or melting temperatures of the employed base polymers. The supramolecular network of nanofibrils provided a window of elastic behavior in the molten polymer matrix at elevated temperatures up to their dissociation temperature and a regime of low melt viscosity above that temperature. Additionally, the nanofibrils acted as efficient nucleating agents and thus increased nucleation density and reduced crystallization half-time. Moreover, chain end tethering significantly increased polymer relaxation time and allowed for facilitated orientation during melt deformation.

In the first chapter, we synthesized PCL end-modified with acetyl-L-alanyl-L-alanyl end groups (**PCL<sub>80</sub>(Ala<sub>2</sub>Ac)<sub>2</sub>**) and blended with the low molecular weight additive 2-octyldodecyl acetyl-L-alanyl-L-alanyl amide (**A**). The blends demonstrated the formation of a network of nanofibrils that were aligned and placed at a periodic distance of 8 nm. The supramolecular network decreased crystallization half-times of PCL matrix by more than one order of magnitude compare to non-modified PCL. Above the melting temperature of PCL, the blends exhibited a high melt elasticity and a melt extensibility of up to almost 3000%. As revealed by SAXS measurements, oriented films prepared by melt stretching exhibited a shift from the standard spherulitic morphology to shish-kebab structures, which increased Young's modulus 550 MPa and a yield strength of 72 MPa, respectively, compared to 250 and 15 MPa for the non-oriented pristine PCL films.

In the second chapter, we made use of the high melt elasticity of the **PCL<sub>80</sub>(Ala<sub>2</sub>Ac)<sub>2</sub>/A** blends and demonstrated that this facilitates the preparation of oriented PCL filaments by melt stretching. Again,

SAXS revealed that the obtained filaments exhibited a shish-kebab morphology, with lamellae oriented perpendicular to the stretching direction, and PCL extended chain crystals parallel to the stretching direction. Fibers with this newly obtained morphology demonstrated an increase in Young's modulus, yield strength, and ultimate strength to  $959 \pm 127$  MPa,  $323 \pm 17$  MPa, and  $555 \pm 30$  MPa, respectively, compared to  $484 \pm 46$  MPa,  $114 \pm 5$  MPa, and  $295 \pm 18$  MPa, respectively, demonstrated by pristine PCL<sub>80</sub>.

In the third chapter, we applied the same end groups and a similar additive (2-ethylhexyl acetyl-L-alanyl-L-alanyl amide, **A8**) to modify atactic poly(DL-lactic acid) (**PDLLA-A**) and stereoregular poly(L-lactic acid) (**PDLLA-A**). We demonstrated that, in this case, no network of nanofibrils is formed, supposedly due to the too high solubility of the end groups in the polymer matrix because of the structural similarities of end groups and polymer repeat units. Instead, the additive **A8** crystals showed macroscopic phase separation but exhibited a three-fold decrease in the width of **A8** crystals compared to non-modified PDLLA/**A8** blends, which led to an increase in crystallization onset temperatures of the PLLA matrix up to  $T_c = 148$  °C, and a decrease in crystallization half-times to  $\tau_{1/2} = 0.5$  min compared to  $T_c = 138$  °C and  $\tau_{1/2} = 10$  min of non-modified PDLLA/**A8** blends.

In the fourth chapter, we finally modified atactic PDLLA and stereoregular PLLA with *N,N'*-diisopentyl benzene tricarboxamides (**PDLLA-B5** and **PLLA-B5**, respectively), and prepare blends with the additive *N,N,N''*-triisopentyl BTA (**B5**). We demonstrated that the co-assembly of the end groups and the **B5** additive successfully suppressed macroscopic phase separation of the additive into needle-like crystals and instead yielded a network of compliant, polymer-tethered nanofibrils that were placed at a periodic distance of 10–12 nm. This nanofibrillar network was found to be a highly efficient nucleating agent for PLLA crystallization, resulting in crystallization temperatures as high as  $T_c = 140$  °C, and an increase in nucleation density by three orders of magnitude. Simultaneously, a new rubber-like regime is established in the amorphous **PDLLA-B5/B5** blends above the PDLLA glass transition, which manifested itself also in a one order of magnitude increase in melt strength in the semicrystalline **PDLLA-B5/B5** blends at sufficiently high additive concentration, and is also observed at large melt deformations.

In conclusion, we have shown that blending of the polymer with a ditopic, self-complementary self-assembling unit based on three-fold hydrogen bonding and a low molecular weight additive based on the same supramolecular motif enabled the efficient self-assembly of high molecular weight polymers.

As a consequence, the presence of both a robust entanglement network in the polymer matrix and a supramolecular network that persists above polymer glass transition or melting temperatures opened up new avenues for materials processing and tuning room temperature mechanical properties. We demonstrated that this concept can be applied to biodegradable aliphatic polyesters like PCL and PLA, which can undergo chemical recycling via ring closing depolymerization and thus are promising for plastics circular economy. This concept can be further applied to other hydrophobic polymers whose end-groups can be functionalized with a ditopic self-assembling unit.

## **Experimental**



## 7. Experimental Part

### *Materials and Methods*

*Materials.* All materials and solvents for reactions were purchased from commercial suppliers and used without further purification unless otherwise stated.

*Gel Permeation Chromatography (GPC).* The number-average molecular weight,  $M_n$ , the weight-average molecular weight,  $M_w$ , and the dispersity,  $\mathcal{D}$ , were determined by dissolving 3–5 mg of sample in 1 mL tetrahydrofuran and filtering the solution through 0.220  $\mu\text{m}$  Nylon filter before injection. The elution was performed in tetrahydrofuran at 40 °C with flow rate of 1 mL/min, using an Agilent 1260 Infinity instrument coupled to 390-MDS equipped with a refractive index detector, one precolumn PSS SDV and either two columns PLgel 5  $\mu\text{m}$  MIXED-C Analytical or two columns PSS SDV Analytical Linear XL. The calibration was performed with PS samples with molecular weights in the range  $M_n = 682\text{--}2'520'000$  g/mol.

*Differential Scanning Calorimetry (DSC).* DSC measurements were performed using a Mettler Toledo DSC 3+ in nitrogen atmosphere (flow rate 200 mL/min) with 4–8 mg specimens and at a scanning rate of typically 10 °C/min. A total of four heating and three cooling cycles were applied to each specimen to check for reproducibility, but only the second heating and first cooling scans are typically shown. Isothermal experiments were conducted by heating the specimens to 200 – 230 °C followed by rapid cooling to the isothermal temperature and maintaining this temperature until the end of the crystallization process, followed by a heating scan at 10 °C/min to estimate melting temperature and crystallinity.

*Scanning Electron Microscopy (SEM).* SEM specimens were heated to 5 °C above the highest temperature endothermic transition according to DSC heating scans, followed by rapid cooling to the desired isothermal temperature and maintaining this temperature until the end of the crystallization process using a Linkham TMS600 hot-stage. The specimens were coated with a 10 nm gold layer using a Quorum Q150T S/E/ES Specimen preparation system. SEM images were recorded on a Zeiss Gemini SEM300 (Zeiss, Göttingen, Germany) at 2.0 keV using a standard Everhart-Thornley secondary electron detector. Spherulite size distributions were determined using the ImageJ software package. Average spherulite size was calculated by counting the number of spherulites on the image and dividing the number by the area of the whole image.

*Infrared Spectroscopy (IR).* Specimens for IR spectroscopy were typically prepared by cooling a few milligrams from the melt 200 – 230 °C to ambient temperature at 10 °C/min. IR spectra of solid samples were typically recorded in attenuated total reflectance (ATR mode) on a JASCO FT/IR 6300 spectrometer using the Miracle ATR accessory from PIKE. IR was recorded via attenuated total reflectance (ATR) averaging over 100 scans. All PCL-based films were recorded in transmission mode using a Bruker Vertex 70v FTIR Spectrometer attached to a Bruker Hyperion 3000 microscope with an N<sub>2</sub> cooled MCT detector with a KBr beam splitter and a ZnSe-based wire grid polarizer, averaging over 100 scans.

*Atomic Force Microscopy (AFM).* Selected materials were cooled from the melt at 200–230 °C to ambient temperature at 10 °C/min. Flat surfaces were prepared by hot-pressing the specimens directly onto a steel AFM stub at the required temperature (above the glass transition in the case of PLA, and between the matrix melting point and the dissociation temperature of the fibrils in the case of PCL) with the aid of a Kapton release film and a Linkham THS600 hot-stage, and cooling to room temperature at 10 °C/min. Images were obtained using an Asylum Research Cypher VRS AFM equipped with a heating stage and a laser-excited MikroMasch aluminum-coated NC14 probe (resonance frequency 160 kHz, and force constant 5 N/m) in intermittent contact mode, with a typical scanning frequency of 5 Hz and amplitude ratios of 0.1–0.3. PLA and PCL samples were generally imaged at temperatures immediately above the glass transition and melting temperatures, respectively. Image analysis was performed using ImageJ software by setting the scale to the one mentioned on the images, smoothing, and plotting a grey profile of a chosen line.

*Optical Microscopy (OM).* Specimens of a few milligrams were compressed between glass cover slides in the melt at 200–230 °C, followed by cooling at a nominal rate of 10 °C/min to the desired observation temperature using a Linkham TMS600 hot-stage. Images were recorded using an Olympus BX60 optical microscope equipped with crossed polarizers once the temperature had stabilized.

*Shear Rheology and Extensional Viscosity.* Dynamic shear rheology was performed using a parallel plate TA Instruments ARES 2 rheometer. 8 mm diameter steel plates were used throughout, with a gap set to 0.8–1.3 mm. The specimens were loaded in the melt at the temperature of 200 – 230 °C from which a cooling ramp was initiated at 10 °C/min unless otherwise stated, with a fixed radial frequency of 1 rad/s and a variable strain of 1%. A standard test fixture from TA Instruments was used for the extensional viscosity measurements. The specimens were prepared by hot-pressing for 5 min at 60 N/m and 200–

230 °C using a Lauffer Pressen UVL 5.0 laboratory press. They were then cut into 20 × 7 × 0.3 mm strips, placed in the test fixture, and held at the testing temperature for 3 min before starting the measurement.

*1D NMR Spectroscopy.* <sup>1</sup>H and <sup>13</sup>C NMR spectra were obtained at 298 K using a Bruker Avance III 400 spectrometer at frequencies of 400 MHz and 100 MHz, respectively, and were calibrated with respect to the residual solvent peaks of DMSO-*d*<sub>6</sub> (2.50 ppm <sup>1</sup>H NMR; 39.52 ppm <sup>13</sup>C NMR), CDCl<sub>3</sub> (7.26 ppm <sup>1</sup>H NMR; 77.16 ppm <sup>13</sup>C NMR) and toluene-*d*<sub>8</sub> (7.10 ppm, 2.19 ppm <sup>1</sup>H NMR; 137.52 ppm, 20.43 ppm <sup>13</sup>C NMR).

*Tensile Testing (UTM).* Room temperature tensile tests were performed using a Zwick Roell 5 kN UTM at a nominal extension rate of 10% of the initial length ( $L_0 = 17\text{--}23$  mm) per minute with a pre-stretch of 0.1 MPa. The specimens were punched out from the hot-pressed or melt-stretched films using a dog-bone shaped steel punch with the width of the clamping zone of 1 cm and of the testing zone of 0.5 cm, a total length of 4 cm, and a testing length of 2 cm. Unless otherwise stated, the specimens were mounted using standard 500 N clamps. PCL filaments were measured by placing additional PCL films between the filaments and the clamps. The Young's modulus was calculated from the slope of the nominal stress-strain curve in the linear elastic regime (0.5–1.5 % strain). UTM experiments at elevated temperatures were performed in the Zwick Roell heating chamber. The specimens were maintained for 5 min at the required experiment temperature and tested at a strain rate of 2 s<sup>-1</sup> unless otherwise stated. Non-isothermally melt stretched **PCL<sub>80</sub>(Ala<sub>2</sub>Ac)<sub>2</sub>/A** (5 wt%) was prepared by opening the oven door 5 s after the stretching began. Typically, 2–4 specimens were tested for each material.

*2D Small and Wide-Angle X Ray Scattering (SAXS/WAXS).* Powder patterns were obtained using a Bruker D8 Discover Plus system with a TXS Cu rotating anode and a Göbel mirror for focusing. A 0.5 mm pinhole and a 0.3 mm collimator were placed in the primary beam path to select a beam of approximately 300 × 400 μm<sup>2</sup> in area at the specimen position. 2D scans were carried out using a micro source using a Cu K<sub>α</sub> radiation ( $\lambda = 1.54$  Å) in transmission mode at 300 mm, calibrated using silver behenate as standard and detector distance with an Eiger2 500K detector. The intensity profiles were obtained by azimuthal or radial integration of the 2D patterns using Bruker Difrac Eva software. The orientation distribution of the crystalline structure in polymers can be mathematically expressed as a series expansion in spherical harmonics. Assuming transverse isotropy of the distribution of the molecular chain axis in the samples, the mathematical expression reduces to the description of the orientation of the unique chain axis *c*, with respect to a reference direction, chosen here as the injection axis, *z*. For

distributions of such cylindrical symmetry, the distribution of molecular orientation can be characterized by using a series of Legendre polynomials are generally described by its second-order coefficient:

$$\langle P_2 \rangle = \frac{1}{2} (3 \langle \cos^2 \theta \rangle - 1), \quad (9)$$

where  $\theta$  is the azimuthal angle and  $\langle \cos^2 \theta \rangle$  is given by

$$\langle \cos^2 \theta \rangle = \frac{\int_0^\pi I_\theta \cos^2 \theta \sin \theta d\theta}{\int_0^\pi I_\theta \sin \theta d\theta}. \quad (10)$$

$\langle P_2 \rangle$  is accessible by SAXD from the azimuthal profiles as

$$\langle P_2 \rangle = \frac{\langle P_2 \rangle_0}{P_2 \cos \chi} \quad (11)$$

*Synchrotron Scanning Small Angle X-Ray Scattering (SAXS).* Scanning SAXS was performed at the cSAXS (X12SA) beamline at the Paul Scherrer Institut (PSI, Switzerland). The X-ray beam was monochromated by a fixed-exit double crystal Si (111) monochromator to 12.4 keV and focused to  $20 \times 7 \mu\text{m}^2$  for samples A, and to  $45 \times 6 \mu\text{m}^2$  for samples B. To minimize the air scattering and absorption, a flight tube was placed between the sample and detector. The scattering signal was recorded by a Pilatus 2M detector and the transmitted beam was measured with a photodiode on a beamstop placed inside the flight tube. The sample-to-detector distance was 7.12 m, as calibrated by silver behanate. The exposure time was 0.1s for all the measured samples. The 2D scattering patterns were radially integrated to obtain 1D scattering curves in 64 azimuthal detector segments with the cSAXS Matlab analysis package. The azimuthal plots were calculated either from the radially integrated data or directly from the pixel intensities, depending on the measured intensity and statistics in the q-range of interest.

*Extrusion, Injection Molding and Fiber Drawing.* Materials were dried at room temperature in vacuum for at least 12 h before extrusion. The materials were loaded into a micro-extruder Xplore MC5 with co-rotating twin-screws equipped with a nitrogen inlet and at a screw speed of 50 rpm and compounded for 5 min at 200 °C with a screw speed of 100 rpm. The extrudates were injected using a miniature injection molding machine Xplore IM5.5 with melt and mold temperatures at 80 °C for PLLA toy bricks, and an injection pressure of 8 bar. PCL fibers were drawn directly from the extruder at constant torque of 5 N, and the extruder chamber was set to 200 °C while the exit nozzle was set to 70, 120, or 200 °C.



The filament was collected with a spinneret with diameter of 15 cm, rotating at 20 rpm and. Fiber cold stretching was performed by hand until visible neck depletion. The fiber diameter was determined using an Olympus BX60 optical microscope.

*Hot Pressing.* The specimens were placed in an aluminum mold with dimensions of 25 × 25 × 0.03 cm and a square (5 × 5 cm) or circular ( $d = 7$  cm) hole in the center, and placed between Teflon plates of lateral dimensions of 50 × 50 cm. A Lauffer Pressen UVL 5.0 laboratory press was loaded at 30 °C and evacuated to 1 mbar before heating to 200–230 °C at 10 °C/min. After the melt temperature was reached, a pressure of 60 N/m was applied for 5 min, followed by cooling to ambient temperature at 10 °C/min.

*Film Melt Stretching.* Hot-pressed films of lateral dimensions of 3 × 5 cm were placed in the oven of the Zwick Roell 5 kN UTM using 500 N clamps and equilibrated at 70 °C for 5 min. The stretching rate was set to 2 s<sup>-1</sup> and maximum extension was set to 500, 1000, or 2000%. Non-isothermally melt-stretched **PCL<sub>80</sub>(Ala<sub>2</sub>Ac)<sub>2</sub>/A** (5 wt%) was prepared by opening the oven door 5 s after the stretching began. Typically, 2–4 specimens were tested for each material.

*Thermoforming.* Hot pressed circular shaped specimens with a diameter of  $d = 7$  cm were thermoformed using Formech HD686 by heating for 20–30 s using an infrared oven, followed by a delay of 0.4 s and using 100% plug assist, 50% vacuum power, 0% air pressure and 0% pre-stretch into the 40 °C heated mold. **PCL<sub>80</sub>** and **PCL<sub>80</sub>/A** (5 wt%) specimens were thermoformed using a paper assist placed directly into the mold with a depth of 35 mm and diameter  $d = 30$  mm, while **PCL<sub>80</sub>(Ala<sub>2</sub>Ac)<sub>2</sub>/A** (5 wt%) were thermoformed without the paper assist without it.

*Heat Stability Testing.* To test the heat stability of the thermoformed specimens were filled with boiling water, and a video recording for the analysis.

### *Synthetic Procedures*

**5-Methoxycarbonylbenzene-1,3-dicarboxylic acid (1).** Trimethyl benzene-1,3,5-tricarboxylate (80.2 g, 160 mmol) was added to MeOH (800 mL) in a 2 L round-bottom flask. The mixture was stirred to create a slurry. Sodium hydroxide (28.16 g 704 mmol) was dissolved in MeOH (400 mL) and then added to the slurry. The reaction mixture was heated to reflux and turned into a clear solution. After 16 h, the volume was reduced by half by rotary evaporation, and the solution was poured into 1 M HCl (3 L). The solution was then extracted with diethyl ether (4 × 800 mL). The combined organic phases

were washed once with 1 M HCl (500 mL), and the solvent was removed in vacuo to give a white powder (72.0g) that was a mixture of products. This mixture was purified slightly by refluxing in CHCl<sub>3</sub> (1 L) and EtOH (500 mL) for 15 min, followed by hot filtration. The filter cake was collected, and the procedure was repeated twice, to give a crude white powder in a yield of 46.5 g (92%), which was used without further purification. <sup>1</sup>H NMR (400 MHz, DMSO-*d*<sub>6</sub>): δ 8.66 (s, 1H), 8.64(s, 2H), 3.93(s, 3H).

**Methyl 3,5-bis(3-methylbutylcarbamoyl)benzoate (2).** Crude **1** (7.0 g, 31.2 mmol), 3-methylbutanamine (6.80 g, 78.0 mmol), PyBOP (40.6 g, 78.0 mmol), and THF (300 mL) were combined in a 500 mL round-bottom flask. DIPEA (20 g, 156.0 mmol) was added to the mixture, which was then stirred at room temperature. After 16 h, the volume was reduced to 75 mL by rotary evaporation, and the solution was precipitated into water (400 mL). The precipitate was collected, redissolved in MeOH (50 mL), and precipitated into water again (400 mL) to yield a portion of the crude product as a white powder (8.5 g). More water (1 L) was added to the THF/water filtrate, and the THF was allowed to slowly evaporate from the solution for 16 h, resulting in further solid precipitate (2.0 g). The two fractions were combined to give the crude product **2** in a yield of 10.5 (93%), which contained minor contaminations of tris(3-methylbutyl) benzene-1,3,5-tricarboxamide and was used without further purification. <sup>1</sup>H NMR (400 MHz, CDCl<sub>3</sub>): δ 8.50 (s, 2H), 8.39 (s, 1H), 6.38 (s, 2H), 3.95 (s, 3H), 3.49 (m, 4H), 1.68 (m, 2H), 1.52 (q, *J* = 6.5 Hz, 4H), 0.95 (d, *J* = 6.6 Hz, 12H).

**3,5-Bis(3-methylbutylcarbamoyl)benzoic acid (3).** Crude **2** (10.5 g, 29 mmol) was dissolved in MeOH (200mL), and the resulting mixture was filtered to remove any insoluble material. LiOH (1.8 g, 75 mmol) was added to the solution, followed by water (15 mL) and MeOH (50 mL) to aid in solubilizing both compounds. The reaction mixture was stirred for 16 h at room temperature, then more LiOH was added (200 mg, 8.4 mmol), and the mixture was stirred for another 2 h. The mixture was then acidified with 1 M HCl until pH 2 was reached (≈150 mL). The white precipitate that formed was collected and dried to give a white powder (9.5 g). The crude product was then added to CHCl<sub>3</sub> (200 mL). The resulting suspension was refluxed for 10 min under vigorous stirring, allowed to cool to room temperature, and filtered. This process was repeated twice, until TLC indicated the complete removal of *N,N,N*-tri(3-methylbutyl) benzene-1,3,5-tricarboxamide (*R*<sub>f</sub> = 0.3, heptane/EtOAc, 3:2). Pure **3** was obtained as a white powder in a yield of 8.0 g (80%). <sup>1</sup>H NMR (400 MHz, toluene-*d*<sub>8</sub>, 375 K): δ 12.72 (br, 1H), 8.82 (s, 2H), 8.75 (s, 1H), 8.09 (br, 2H), 3.43 (q, *J* = 6.9 Hz, 4H), 1.63 (m, 2H), 1.50 (q, *J* = 6.9 Hz, 4H), 0.88 (d, *J* = 6.5 Hz, 12H). <sup>13</sup>C NMR (100 MHz, DMSO-*d*<sub>6</sub>): δ 166.52, 164.86, 135.34, 131.10, 130.35, 130.08, 37.99,

37.60, 25.24, 22.41. HRMS (nanochip-ESI/LTQ-Orbitrap)  $m/z$ :  $[M + H]^+$  Calcd. for  $C_{19}H_{29}N_2O_4^+$  349.2122; Found 349.2118. EA: Calcd. for  $C_{19}H_{28}N_2O_4$ : C, 65.49; H, 8.10; N, 8.04. Found: C, 65.31; H, 8.10; N, 8.01.

***N,N,N*-Tri(3-methylbutyl) benzene-1,3,5-tricarboxamide (B5).** 3-Methylbutylamine (0.785 g, 9.0 mmol), triethylamine (5.08 g, 50.0 mmol) and THF (150 mL) were added to a flask at 0 °C. 1,3,5-benzenetricarbonyl trichloride (0.664 g, 2.5 mmol) was added slowly to the reaction mixture over 10 min. The reaction mixture was stirred at 0 °C for 1 h and then at room temperature for 16 h. Its volume was reduced to about 50 mL by rotary evaporation. The product was precipitated into water (500 mL), collected by filtration, washed with 0.5 M KOH (25 mL) and water (50 mL), and dried in high vacuum to give **B5** as a white powder in a yield of 0.84 g (81%).  $^1H$  NMR (400 MHz,  $CDCl_3$ ):  $\delta$  8.29 (s, 3H), 6.54 (t,  $J = 5.8$  Hz, 3H), 3.48 (dd,  $J = 13.8, 6.7$  Hz, 6H), 1.73 – 1.65 (m, 4H), 1.50 (q,  $J = 7.1$  Hz, 6H), 0.95 (d,  $J = 6.6$  Hz, 18H).  $^{13}C$  NMR (100 MHz,  $CDCl_3$ ):  $\delta$  166.46, 135.72, 127.83, 38.79, 38.58, 26.12, 22.59. HRMS (nanochip-ESI/LTQ-Orbitrap)  $m/z$ :  $[M + H]^+$  Calcd. for  $C_{24}H_{40}N_3O_3^+$  418.3064; Found 418.3058. EA: Calcd. for  $C_{24}H_{39}N_3O_3$ : C, 69.03; H, 9.41; N, 10.06. Found: C, 67.96; H, 9.28; N, 9.78.

***N*-(9-Fluorenylmethoxycarbonyl)-L-alanyl-L-alanine *tert*-butyl ester (4).** PyBOP (120 g, 231 mmol, 1.2 equiv.) and diisopropylethylamine (100 mL, 578 mmol, 3 equiv.) were added to a solution of *N*-(9-fluorenylmethoxycarbonyl)-L-alanine (60 g, 192 mmol, 1 equiv.) and L-alanine *tert*-butyl ester (35.0 g, 192 mmol, 1 equiv.) in THF (700 mL). After stirring the reaction mixture overnight, it was concentrated to 100 mL and poured into water. The solid residue was filtered and redissolved again in THF. The precipitation was repeated twice. The solid crude product was dissolved in DCM. The solution was dried over  $MgSO_4$  and finally evaporated to dryness in vacuo. The resulting solid was dissolved once more in DCM and purified by column chromatography (AcOEt/*n*-hexane, 1:3). After drying in high vacuum, pure *N*-(9-fluorenylmethoxycarbonyl)-L-alanyl-L-alanine *tert*-butyl ester **4** was obtained as a colorless solid in a yield of 54 g (64%).  $^1H$  NMR (400 MHz, DMSO- $d_6$ ):  $\delta$  8.19 (d,  $J = 7.0$  Hz, 1H), 7.89 (d,  $J = 7.5$  Hz, 2H), 7.73 (t,  $J = 6.4$  Hz, 2H), 7.52 (d,  $J = 7.9$  Hz, 1H), 7.42 (t,  $J = 7.5$  Hz, 2H), 7.33 (t,  $J = 7.4$  Hz, 2H), 4.34–3.97 (m, 5H), 1.37 (s, 9H), 1.23 (t,  $J = 6.5$  Hz, 6H).  $^{13}C$  NMR (400 MHz,  $CDCl_3$ ):  $\delta$  171.85, 171.54, 141.31, 141.30, 127.72, 127.09, 125.10, 120.00, 82.17, 77.35, 77.03, 76.72, 67.08, 50.45, 48.78, 47.14, 27.96, 19.03, 18.54. HRMS (ESI-TOF, positive):  $m/z$  461.2045  $[M + Na]^+$ , calculated for  $C_{25}H_{30}N_2NaO_5^+$ : 461.2047.

***N*-(9-Fluorenylmethoxycarbonyl)-L-alanyl-L-alanine (5).** *N*-(9-Fluorenylmethoxycarbonyl)-L-alanine-L-alanine *tert*-butyl ester **1** (5.27 g, 12.0 mmol, 1.0 equiv.) was dissolved in chloroform (15 mL),

followed by the addition of trifluoroacetic acid (24.8 mL, 324 mmol, 27 equiv.). After stirring the reaction mixture for 3 h, the trifluoroacetic acid was removed by azeotropic evaporation in vacuum by the repeated addition of CHCl<sub>3</sub>. The obtained solid was washed with DCM and dried in high vacuum. *N*-(9-Fluorenylmethoxycarbonyl)-*L*-alanyl-*L*-alanine **5** was obtained as colorless solid in a yield of 3.57 g (78%), which was used without further purification. <sup>1</sup>H NMR (400 MHz, DMSO-d<sub>6</sub>): δ = 12.50 (s, 1H), 8.11 (d, *J* = 7.3 Hz, 1H), 7.89 (d, *J* = 7.5 Hz, 2H), 7.73 (t, *J* = 7.3 Hz, 2H), 7.49 (d, *J* = 7.9 Hz, 1H), 7.42 (t, *J* = 7.5 Hz, 2H), 7.33 (t, *J* = 7.4 Hz, 2H), 4.31–4.13 (m, 4H), 4.08 (d, *J* = 7.4 Hz, 1H), 1.27 (d, *J* = 7.3 Hz, 3H), 1.22 (d, *J* = 7.1 Hz, 3H). <sup>13</sup>C NMR (400 MHz, DMSO-d<sub>6</sub>): δ 174.45, 172.73, 156.04, 144.34, 144.21, 141.12, 128.04, 127.48, 125.72, 120.51, 65.99, 55.33, 40.35, 40.15, 39.94, 39.73, 39.52, 18.58, 17.57. HRMS (ESI-TOF, positive): *m/z* 405.1427 [M + Na]<sup>+</sup>, calculated for C<sub>21</sub>H<sub>22</sub>N<sub>2</sub>NaO<sub>5</sub><sup>+</sup>: 405.1421.

**L-Alanyl-L-alanine (6).** *N*-(9-Fluorenylmethoxycarbonyl)-*L*-alanyl-*L*-alanine **5** (33 g, 86.29 mmol, 1.0 equiv.) was dissolved in 200 mL of DMF followed by the addition of piperidine (34 mL, 345 mmol, 4 equiv.). After stirring the reaction mixture overnight, DCM was added. Upon stirring for an additional 1 h, the resulting solid was filtered off, washed with DCM, and recrystallized from IPA/H<sub>2</sub>O. Drying in high vacuum afforded pure *L*-alanyl-*L*-alanine **6** in a yield of 9.71 g (70%). <sup>1</sup>H NMR (400 MHz, DMSO-d<sub>6</sub>): δ 12.48 (s, 1H), 8.13 (d, *J* = 7.3 Hz, 1H), 7.99 (d, *J* = 7.8 Hz, 1H), 4.30 (p, *J* = 7.0 Hz, 1H), 4.17 (p, *J* = 7.3 Hz, 1H), 2.50 (q, *J* = 3.6, 2.8 Hz, 2H), 1.81 (s, 3H), 1.26 (d, *J* = 7.3 Hz, 3H), 1.17 (d, *J* = 7.1 Hz, 3H). <sup>13</sup>C NMR signals in solvent could not be resolved. HRMS (ESI-TOF, negative): *m/z* 159.0779 [M + H-1]<sup>-</sup> calculated for C<sub>6</sub>H<sub>11</sub>N<sub>2</sub>O<sub>3</sub><sup>-</sup>: 159.0775.

***N*-Acetyl-L-alanyl-L-alanine (7).** *L*-Alanyl-*L*-alanine **6** (8.65 g, 54 mmol, 1.0 equiv.) was dissolved in water (170 mL) followed by the addition of acetic anhydride (38.3 mL, 405 mmol, 7.5 equiv.). After stirring the reaction mixture overnight, the solvent was removed in vacuum. The obtained solid was washed with DCM and dried in high vacuum to afford *N*-acetyl-*L*-alanyl-*L*-alanine **7** in a yield of 10.5 g (95%) that was used without further purification with the. <sup>1</sup>H NMR (400 MHz, DMSO-d<sub>6</sub>): δ 8.12 (d, *J* = 7.3 Hz, 1H), 8.00 (d, *J* = 7.8 Hz, 1H), 4.41–4.25 (m, 1H), 4.17 (t, *J* = 7.3 Hz, 1H), 1.81 (s, 3H), 1.26 (d, *J* = 7.3 Hz, 3H), 1.17 (d, *J* = 7.1 Hz, 3H). <sup>13</sup>C NMR (400 MHz, DMSO-d<sub>6</sub>): δ 174.49, 172.65, 169.34, 48.15, 47.88, 40.14, 39.93, 39.73, 22.93, 18.71, 17.58. HRMS (ESI-TOF, positive): *m/z* 225.0846 [M + Na]<sup>+</sup>, calculated for C<sub>8</sub>H<sub>14</sub>N<sub>2</sub>NaO<sub>4</sub><sup>+</sup>: 225.0846.

**2-Ethylhexyl *N*-acetyl-*L*-alanyl-*L*-alanyl amide (A8).** PyBOP (3.6 g, 6.92 mmol 1.4 equiv.) and diisopropylethylamine (3.45 mL, 19.8mmol 4 equiv.) to a solution of *N*-acetyl-*L*-alanyl-*L*-alanine **7** (1 g,

4.95 mmol, 1 equiv.) and 2-ethylhexyl-1-amine (639 mg, 4.95 mmol, 1 equiv.) in THF (15 mL). After stirring the reaction mixture overnight, it was concentrated to one third of its original volume and poured into water. The solid precipitate was filtered off and redissolved in THF. The precipitation was repeated twice. The resulting solid was dissolved in DCM, and the solution was dried over MgSO<sub>4</sub>. After filtration, the solvent was finally evaporated in vacuo, and the resulting solid was dried in high vacuum. 2-Ethylhexyl *N*-acetyl-L-alanyl-L-alanyl amide **A8** was obtained as a colorless solid in a yield of 1.10 g (68%). <sup>1</sup>H NMR (400 MHz, CDCl<sub>3</sub>) R (400 MHz, CDCl<sub>3</sub>): δ = 6.99 (s, 1H), 6.37 (d, J = 50.5 Hz, 2H), 4.52 (d, J = 30.8 Hz, 2H), 3.19 (s, 3H), 2.03 (s, 3H), 1.66 (s, 3H), 1.53–1.00 (m, 16H), 1.00–0.70 (m, 6H). <sup>13</sup>C NMR (400 MHz, DMSO-d<sub>6</sub>): δ 172.43, 169.66, 48.75, 48.60, 41.65, 30.70, 28.77, 23.99, 22.96, 18.87, 18.50, 14.42, 11.19. HRMS (ESI-TOF, positive): *m/z* 336.2326 [M + Na]<sup>+</sup>, calculated for C<sub>16</sub>H<sub>31</sub>N<sub>3</sub>NaO<sub>3</sub><sup>+</sup>: 2336.22576. DSC: *T*<sub>m</sub> = 228 °C, *T*<sub>c</sub> = 227 °C. TGA (N<sub>2</sub>): 260 °C, TGA (air): 250 °C.

**2-Octyldodecyl *N*-acetyl-L-alanyl-L-alanine amide (A20).** 2-Octyldodecyl-1-amine (2.01 g, 6.72 mmol) was dissolved in THF (50 mL). *N*-acetyl-L-alanyl-L-alanine (1.64 g, 8.11 mmol), PyBOP (4.87 g, 9.36 mmol), and DIEA (3.5 mL) were added, and the reaction mixture was stirred at room temperature overnight. Then, the mixture was poured into 1 M HCl (1 L). The precipitate was redissolved in THF, and the solution was again precipitated into 1 M HCl. The precipitate was finally washed with water (50 mL) and acetone (50 mL) to yield 2-octyldodecyl *N*-acetyl-L-alanyl-L-alanine amide (**7**) as a colorless solid in a yield of 2.97 g (92%). <sup>1</sup>H NMR (400 MHz, CDCl<sub>3</sub>): δ = 7.51 (d, 1H), 7.09 (d, 1H), 6.77 (t, 1H), 4.71 (m, 1H), 4.60 (m, 1H), 3.23 (m, 1H), 3.15 (m, 1H), 2.08 (s, 3H), 1.51 (m, 1H), 1.38 (m, 6H), 1.25 (bs, 32H), 0.87 (m, 6H) ppm. HRMS (ESI-TOF, positive): *m/z* 504.4145 [M + Na]<sup>+</sup>, calculated for C<sub>28</sub>H<sub>55</sub>N<sub>3</sub>O<sub>3</sub>Na: 504.4141. DSC: *T*<sub>m</sub> = 186 °C.

**PCL<sub>20</sub>-AlaFmoc (8).** Hydroxy-telechelic poly(ε-caprolactone) (*M*<sub>n</sub> = 20'000, 100 g) was dissolved in THF (700 mL). *N*-(9-Fluorenylmethoxycarbonyl)-L-alanine (17.7 g, 113 mmol), DMAP (3.45 g, 28.2 mmol), and DCC (35.3 g, 171 mmol) were added, and the reaction mixture was stirred at room temperature for 3 d. The mixture was poured into MeOH. The precipitate was dried in high vacuum to yield Fmoc-**PCL<sub>20</sub>-AlaFmoc 8** as a colorless solid in a yield of 97 g (97%). <sup>1</sup>H NMR (400 MHz, CDCl<sub>3</sub>): δ = 7.80 (d, 2H), 7.61 (m, 3H), 7.41 (m, 3H), 7.34 (m, 4H), 5.42 (bs, 1H), 4.40 (brs, 7H), 4.26 (brs, 100H), 4.08 (t, 198H), 2.32 (t, 200H), 1.68 (m, 426H), 1.41 (m, 213H) ppm.

**PCL<sub>20</sub>-AlaNH<sub>2</sub> 9.** **PCL<sub>20</sub>-AlaFmoc 8** (95.0 g) was dissolved in DCM (400 mL), and piperidine (5.0 g) was added. The reaction mixture was stirred at room temperature for 1 d and then poured into MeOH (1.5 L).

The precipitate was re-dissolved in DCM and poured again into MeOH. The precipitation procedure was repeated one more time. The precipitate was washed with MeOH and hexane and was dried in high vacuum to yield **PCL<sub>20</sub>-AlaNH<sub>2</sub> 9** as a colorless solid in a yield of 79 g (83%). <sup>1</sup>H NMR (400 MHz, CDCl<sub>3</sub>): δ = 4.09 (t, 1.94H), 3.92 (t, 0.03H), 3.57 (m, 0.02H), 2.33 (t, 2.00H), 1.67 (m, 4.26H), 1.41 (m, 2.16H) ppm.

**PCL<sub>20</sub>-Ala<sub>2</sub>Fmoc 10.** *N*-(9-Fluorenylmethoxycarbonyl)-L-alanine (7.35 g, 47.2 mmol), DIEA (3.78 g, 28.5 mmol), and PyBOP (13.2 g, 25.7 mmol) were added to a solution of **PCL<sub>20</sub>-AlaNH<sub>2</sub> 9** (70 g) in THF (700 mL). The reaction mixture was stirred at room temperature for 3 d and then poured into MeOH (1.2 L). The precipitate was re-dissolved in DCM, and the solution was again precipitated into MeOH. The precipitate was collected, washed with hexane, and dried in high vacuum to yield **PCL<sub>20</sub>-Ala<sub>2</sub>Fmoc 10** as a colorless solid in a yield of 70 g (99 %). <sup>1</sup>H NMR (400 MHz, CDCl<sub>3</sub>): δ = 7.79 (d, 0.03H), 7.61 (d, 0.03H), 7.42 (m, 0.03H), 7.34 (m, 0.04H), 6.46 (brs, 0.01H), 5.45 (brs, 0.01H), 4.58 (t, 0.02H), 4.07 (t, 1.89H), 2.33 (t, 2.00H), 1.67 (m, 4.26H), 1.41 (m, 2.21H) ppm.

**PCL<sub>20</sub>-Ala<sub>2</sub>NH<sub>2</sub> 11.** **PCL<sub>20</sub>-Ala<sub>2</sub>Fmoc 10** (69 g) was dissolved in DCM (400 mL), and piperidine (5.0 g) was added. The reaction mixture was stirred at room temperature for 1 d and then poured into MeOH (1.5 L). The precipitate was re-dissolved in DCM, and the solution was again precipitated into MeOH. The precipitate was washed with MeOH and hexane and dried in high vacuum to yield **PCL<sub>20</sub>-Ala<sub>2</sub>-NH<sub>2</sub> 11** as a colorless solid in a yield of 62 g (90%). <sup>1</sup>H NMR (400 MHz, CDCl<sub>3</sub>): δ = 7.73 (brs, 0.01H), 4.59 (t, 0.01H), 4.09 (t, 2.06H), 2.34 (t, 2.00H), 1.67 (m, 3.98H), 1.41 (m, 2.34H) ppm.

**PCL<sub>20</sub>-Ala<sub>3</sub>Ac 12.** *N*-acetyl-L-alanine **7** (1.76 g, 13.4 mmol), DIEA (2.16 g, 16.7 mmol), and PyBOP (7.56 g, 14.5 mmol) were added to a solution of **PCL<sub>20</sub>-Ala<sub>2</sub>-NH<sub>2</sub> 11** (*M<sub>n</sub>* = 20000) (40 g) in THF (500 mL). The reaction mixture was stirred at room temperature for 5 d, then poured into MeOH (1.5 L). The precipitate was collected, washed with hexane, and dried in high vacuum to yield **PCL<sub>20</sub>-Ala<sub>3</sub>Ac 12** as a white solid in a yield of 39 g (98 %). <sup>1</sup>H-NMR (400 MHz, CDCl<sub>3</sub>): δ = 6.60 (m, 0.02H), 6.13 (m, 0.01H), 4.47 (m, 0.04H), 4.09 (t, 1.90H), 2.33 (t, 2.00H), 2.04 (s, 0.07H), 1.67 (m, 3.94H), 1.41 (m, 2.14H) ppm; GPC: *M<sub>n</sub>* = 22200 g/mol; *M<sub>w</sub>* = 29300 g/mol; *D* = 1.32. TGA: decomposition onset: 387°C. DSC: *T<sub>m</sub>* = 54.3°C, *T<sub>c</sub>* = 24.4°C, *T<sub>d</sub>* = 82°C (determined from first heating curve), *T<sub>a</sub>* = 75°C.

**PCL<sub>80</sub>-AlaFmoc 13.** Hydroxy-telechelic poly(ε-caprolactone) (*M<sub>n</sub>* = 80'000, 30 g) was dissolved in DCM (200 mL). *N*-(9-Fluorenylmethoxycarbonyl)-L-alanine (0.43 g, 1.41 mmol), DPTS (0.27 g, 0.94 mmol), and DCC (0.58 g, 2.82 mmol) were added, and the reaction mixture was stirred at room temperature for 6 d. The mixture was poured into MeOH. The precipitate was dried in high vacuum to yield **PCL<sub>80</sub>-**

**AlaFmoc 13** as a colorless solid in a yield of 29 g (97%).  $^1\text{H NMR}$  (400 MHz,  $\text{CDCl}_3$ ):  $\delta$  = 7.77 (d, 4H), 7.61 (m, 4H), 7.41 (m, 4H), 7.34 (m, 4H), 5.40 (d, 2H), 4.40 (m, 2H), 4.08 (t, 568H), 2.32 (t, 568H), 1.68 (m, 1148H), 1.41 (m, 568H) ppm.

**PCL<sub>80</sub>-AlaNH<sub>2</sub> 14.** **PCL<sub>80</sub>-AlaFmoc 13** (28 g) was dissolved in DCM (200 mL), and piperidine (2.0 g) was added. The reaction mixture was stirred at room temperature for 1 d and then poured into MeOH (1.5 L). The precipitate was re-dissolved in DCM before being poured again into MeOH. The precipitate was washed with MeOH and hexane and dried in high vacuum to yield **PCL<sub>80</sub>-AlaNH<sub>2</sub> 14** as a colorless solid in a yield of 26 g (93%).  $^1\text{H NMR}$  (400 MHz,  $\text{CDCl}_3$ ):  $\delta$  = 8.70 (s, 4H), 4.00 (t, 3725H), 2.23 (t, 3697H), 1.58 (m, 7572H), 1.35 (m, 3687H) ppm.

**PCL-Ala<sub>3</sub>Ac 15.** *N*-acetyl-L-alanyl-L-alanine (0.13 g, 0.66 mmol), DIEA (0.11 g, 0.83 mmol), and PyBOP (0.37 g, 0.72 mmol) were added to a solution of **PCL<sub>80</sub>-AlaNH<sub>2</sub> 14** (22 g) in THF (380 mL). The reaction mixture was stirred at room temperature for 5 d and then precipitated twice into MeOH (1.5 L). The precipitate was collected, washed with hexane, and dried in high vacuum to yield **PCL-Ala<sub>3</sub>Ac 15** as a colorless solid in a yield of 21 g (95%).  $^1\text{H NMR}$  (400 MHz,  $\text{CDCl}_3$ ):  $\delta$  = 6.52 (m, 4H), 6.05 (m, 2H), 4.46 (m, 2H), 4.36 (m, 4H), 3.39 (t, 2273H), 2.24 (t, 2275H), 1.95 (s, 6H), 1.57 (m, 4667H), 1.34 (m, 2319H) ppm. GPC:  $M_n$  = 89'500 g/mol;  $M_w$  = 135'600 g/mol;  $D$  = 1.52. DSC:  $T_m$  = 56.3°C,  $T_c$  = 27.3°C.

**Poly(L-lactide) (PLLA).** L-lactide was purified by recrystallization from ethyl acetate and dried overnight in high vacuum before the polymerization. Toluene was dried over sodium and benzophenone for at least 30 min until a deep blue color of the solution emerged, and then distilled into a flash-dried flask. Diethylene glycol (42.4 mg, 0.4 mmol, 1.0 equiv.) stored over 4 Å molecular sieves and DL-lactide or L-lactide (24.1 g, 166.4 mmol, 416.0 equiv.) were dissolved in toluene (140 mL) under a slight flow of Argon, followed by the addition of tin(II) 2-ethylhexanoate (140 mg, 0.32 mmol, 0.8 equiv.). After 4 h, the solution was cooled to room temperature and precipitated into rapidly stirred cold diethyl ether. The precipitate was filtered off, and washed with cold diethyl ether, dried, and redissolved in dichloromethane. The precipitation procedure was repeated two more times to yield hydroxy-telechelic **PLLA** as a white powder. **PLLA**: yield 19.8 g (82.5 %); GPC (THF, 40 °C):  $M_n$  = 61'200,  $D$  = 1.14.  $^1\text{H NMR}$  ( $\text{CDCl}_3$ , 400 MHz, 400 K):  $\delta$  5.16 (q,  $J$  = 7.1 Hz, 880H), 4.35 (q,  $J$  = 7.1 Hz, 3H), 4.27 (dt,  $J$  = 6.5, 4.7 Hz, 4H), 3.66 (t,  $J$  = 4.8 Hz, 4H), 1.58 (d,  $J$  = 7.1 Hz, 2901H).

**Poly(DL-lactide) (PDLLA).** DL-lactide or were purified by recrystallization from ethyl acetate and dried overnight in high vacuum before the polymerization. Toluene was dried over sodium and benzophenone

for at least 30 min until a deep blue color of the solution emerged and distilled into a flash-dried flask. Diethylene glycol (42.4 mg, 0.4 mmol, 1.0 equiv.) stored over 4 Å molecular sieves and DL-lactide or L-lactide (24.1 g, 166.4 mmol, 416.0 equiv.) were dissolved in toluene (140 mL) under a slight flow of Argon, followed by the addition of tin(II) 2-ethylhexanoate (140 mg, 0.32 mmol, 0.8 equiv.). After 4 h, the solution was cooled to room temperature and precipitated into rapidly stirred cold diethyl ether. The precipitate was filtered off, and washed with cold diethyl ether, dried, and redissolved in dichloromethane. The precipitation procedure was repeated two more times to yield hydroxy-telechelic poly(DL-lactide) **PDLLA** or poly(L-lactide) **PLLA** as white powders in yields of 15.1 (62.7%) and 17.2 g (71.7 %), respectively. GPC (THF, 40 °C):  $M_n = 61'800$ ,  $D = 1.16$ .  $^1\text{H NMR}$  ( $\text{CDCl}_3$ , 400 MHz, 400 K):  $\delta$  5.19 (d,  $J = 21.3$  Hz, 933H), 4.35 (s, 2H), 4.27 (d,  $J = 7.2$  Hz, 4H), 3.66 (t, 4H), 1.56 (d,  $J = 6.9$  Hz, 2952H).

**PLLA-Cbz.** **PLLA** (20.0 g, 0.33 mmol, 1 equiv.) was dissolved in dry dichloromethane (300 mL) at room temperature, followed by the addition of *N*-[(Benzyloxy)carbonyl]-L-alanine (2.31 g, 9.9 mmol, 30 equiv.), *N,N'*-dicyclohexylcarbodiimide (1.1 g, 5.3 mmol, 16 equiv.) and 4-(*N,N*-dimethylamino)pyridine (820 mg, 6.7 mmol, 20 equiv.). The reaction mixture was stirred overnight and then precipitated into rapidly stirred cold diethyl ether. The precipitate was filtered off, and washed with cold diethyl ether, dried, and redissolved in dichloromethane. The precipitation procedure was repeated two more times. **PLLA-Cbz** was obtained as a white powder in a yield of 18.5 g (92.9 %). GPC (THF, 40 °C):  $M_n = 62'300$ ,  $D = 1.16$ .  $^1\text{H NMR}$  ( $\text{CDCl}_3$ , 400 MHz, 400 K):  $\delta$  7.34 (s, 13H), 5.15 (q,  $J = 7.1$  Hz, 869H), 4.45 (q,  $J = 7.1$  Hz, 2H), 4.26 (dt,  $J = 6.5, 4.7$  Hz, 4H), 3.65 (t,  $J = 4.8$  Hz, 4H), 1.57 (d,  $J = 7.1$  Hz, 2851H).

**PDLLA-Cbz.** **PDLLA** (6.0 g, 0.1 mmol, 1 equiv.) was dissolved in dry dichloromethane (100 mL) at room temperature, followed by the addition of *N*-[(Benzyloxy)carbonyl]-L-alanine (450 mg, 1.9 mmol, 19 equiv.), *N,N'*-dicyclohexylcarbodiimide (212 mg, 1.0 mmol, 10 equiv.) and 4-(*N,N*-dimethylamino)pyridine (145 mg, 1.2 mmol, 12 equiv.). The reaction mixture was stirred overnight and then precipitated into rapidly stirred cold diethyl ether. The precipitate was filtered off, and washed with cold diethyl ether, dried, and redissolved in dichloromethane. The precipitation procedure was repeated two more times. **PDLLA-Cbz** was obtained as a white powder in a yield of 4.9 g (81.3 %). GPC (THF, 40 °C):  $M_n = 60'900$ ,  $D = 1.18$ .  $^1\text{H NMR}$  ( $\text{CDCl}_3$ , 400 MHz, 400 K):  $\delta$  7.35 (s, 10H), 5.15 (d,  $J = 7.1$  Hz, 670H), 4.47 (q,  $J = 7.1$  Hz, 2H), 4.26 (dt,  $J = 6.5, 4.7$  Hz, 4H), 3.67 (t,  $J = 4.8$  Hz, 4H), 1.57 (d,  $J = 7.1$  Hz, 2112H).



**PLLA-NH<sub>2</sub>.** PLLA-Cbz (7.0 g, 0.12 mmol, 1 equiv.) was dissolved in dry dichloromethane (110 mL) at room temperature, followed by the addition of trimethylsilyl iodide (1.0 g, 4.9 mmol, 40 equiv.). After 2.5 h, more trimethylsilyl iodide (0.42 g, 2.1 mmol, 18 equiv.) was added, and the reaction mixture was stirred for 0.5 h. The solution was precipitated into rapidly stirred cold diethyl ether. The precipitate was filtered off, washed with cold diethyl ether, dried, and redissolved in dichloromethane. The precipitation procedure was repeated two more times. PLLA-NH<sub>2</sub> was obtained as a white powder in a yield of 5.8 g (82.9 %). GPC (THF, 40 °C):  $M_n = 61'200$ ,  $D = 1.18$ . <sup>1</sup>H NMR (CDCl<sub>3</sub>, 400 MHz, 400 K): δ 7.34 (s, 0.7H), 6.17 (d, 2H), 5.15 (q,  $J = 7.1$  Hz, 809H), 4.26 (dt,  $J = 6.5, 4.7$  Hz, 4H), 3.66f (t,  $J = 4.8$  Hz, 4H), 1.57 (d,  $J = 7.1$  Hz, 2604H).

**PDLLA-NH<sub>2</sub>.** PDLLA-Cbz (6.0 g, 0.1 mmol, 1 equiv.) was dissolved in dry dichloromethane (100 mL) at room temperature, followed by the addition of trimethylsilyl iodide (0.84 g, 4.2 mmol, 42 equiv.). After 2.5 h, more trimethylsilyl iodide (0.28 g, 1.4 mmol, 14 equiv.) was added, and the reaction mixture was stirred for 0.5 h. The solution was precipitated into rapidly stirred cold diethyl ether. The precipitate was filtered off, washed with cold diethyl ether, dried, and redissolved in dichloromethane. The precipitation procedure was repeated two more times. PDLLA-NH<sub>2</sub> was obtained as a white powder in a yield of 4.3 g (71.6 %); GPC (THF, 40 °C):  $M_n = 62'295$ ,  $D = 1.25$ . <sup>1</sup>H NMR (CDCl<sub>3</sub>, 400 MHz, 400 K): δ 5.16 (d,  $J = 7.1$  Hz, 675H), 4.26 (dt,  $J = 6.5, 4.7$  Hz, 4H), 3.66 (t,  $J = 4.8$  Hz, 4H), 1.57 (d,  $J = 7.1$  Hz, 2132zH).

**PLLA-B5.** PLLA-NH<sub>2</sub> (7.0 g, 0.12 mmol, 1 equiv.) and 3,5-bis(3-methylbutylcarbamoyl)benzoic acid (312 mg, 0.89 mmol, 8.9 equiv.) was dissolved in tetrahydrofuran (200 mL), followed by the addition of benzotriazol-1-yloxytripyrrolidinophosphonium hexafluorophosphate (0.8 g, 1.5 mmol, 13 equiv.) and diisopropylethylamine (0.9 g, 6.8 mmol, 34 equiv.). The solution was stirred overnight and then precipitated into rapidly stirred cold methanol. The precipitate was filtered off, washed with cold diethyl ether, dried, and redissolved in tetrahydrofuran. The solution was precipitated into rapidly stirred cold diethyl ether. The precipitate was filtered off, washed with cold diethyl ether, and dried. PLLA-B5 was obtained as a white powder in a yield of 5.9 g (84.3 %). GPC (THF, 40 °C):  $M_n = 67'000$ ,  $D = 1.20$ . <sup>1</sup>H NMR (CDCl<sub>3</sub>, 400 MHz, 400 K): δ 8.33 (s, 6H), 6.84 (d, 2H), 6.31 (s, 5H), 5.16 (q,  $J = 7.1$  Hz, 768H), 4.85 (m, 2H), 4.27 (dt,  $J = 6.5, 4.7$  Hz, 4H), 3.66f (t,  $J = 4.8$  Hz, 4H), 3.50 (q,  $J = 7.1$  Hz, 9H), 1.58 (d,  $J = 7.1$  Hz, 2430H).

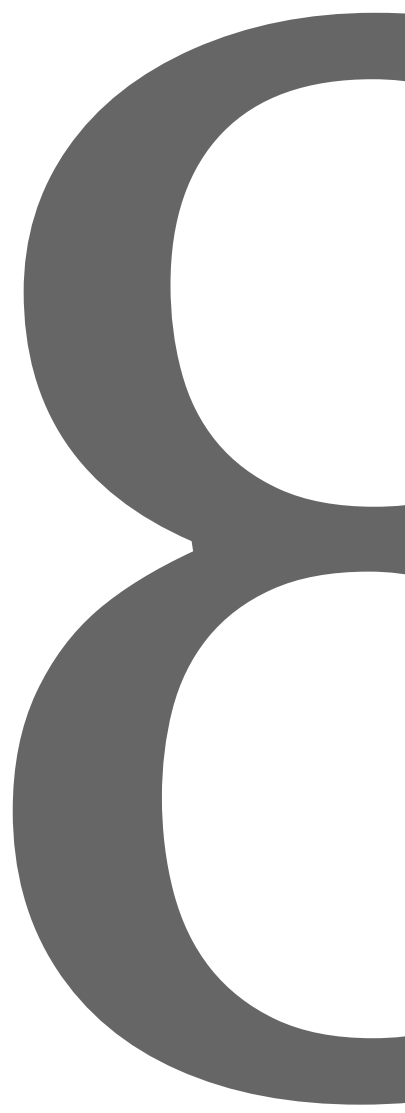
**PDLLA-B5).** PDLLA-NH<sub>2</sub> (3.0 g, 0.05 mmol, 1 equiv.) and 3,5-bis(3-methylbutylcarbamoyl)benzoic acid (150 mg, 0.43 mmol, 8.6 equiv.) was dissolved in tetrahydrofuran (100 mL), followed by the addition of benzotriazol-1-yloxytripyrrolidinophosphonium hexafluorophosphate (420 mg, 0.8 mmol, 16 equiv.)

and diisopropylethylamine (74 mg, 0.6 mmol, 12 equiv.). The solution was stirred overnight and then precipitated into rapidly stirred cold methanol. The precipitate was filtered off, and washed with cold diethyl ether, dried, and redissolved in tetrahydrofuran. The solution was precipitated into rapidly stirred cold diethyl ether, the precipitate was filtered off, washed with cold diethyl ether, and dried. **PDLLA-B5** was obtained as a white powder in a yield of 2.5 g (81.7 %). GPC (THF, 40 °C):  $M_n = 70'500$ ,  $\mathcal{D} = 1.22$ .  $^1\text{H NMR}$  ( $\text{CDCl}_3$ , 400 MHz, 400 K):  $\delta$  8.34z (s, 6H), 6.85 (d, 1fH), 6.33 (s, 3H), 5.16 (q,  $J = 7.1$  Hz, 643H), 4.97 (m, 3H), 4.27 (dt,  $J = 6.5, 4.7$  Hz, 4H), 3.66f (t,  $J = 4.8$  Hz, 4H), 3.50 (q,  $J = 7.1$  Hz, 9H), 1.58 (d,  $J = 7.1$  Hz, 2049H), 0.91 (d,  $J = 6.6$  Hz, 20H).

**PDLLA-A.** **PDLLA-NH<sub>2</sub>** (7.0 g, 0.12 mmol, 1 equiv.) and acetyl-L-alanyl-L-alanine **4** (121.4 mg, 1.79 mmol, 18.8 equiv.) were dissolved in tetrahydrofuran (400 mL), followed by the addition of benzotriazol-1-yloxytripyrrolidinophosphonium hexafluorophosphate (1.6 g, 3.0 mmol, 26 equiv.) and diisopropylethylamine (1.8 g, 13.6 mmol, 68 equiv.). The solution was stirred overnight and then precipitated into rapidly stirred cold diethyl ether. The precipitate was filtered off, washed with cold diethyl ether, dried, and redissolved in tetrahydrofuran. The precipitation was repeated two more times. **PDLLA-A** was obtained as a white powder in a yield of 4.9 g (70.3 %). GPC (THF, 40 °C):  $M_n = 64'400$ ,  $\mathcal{D} = 1.22$ .  $^1\text{H NMR}$  (400 MHz, Chloroform-d)  $\delta$  6.53 (d,  $J = 41.3$  Hz, 1H), 6.16 (s, 0H), 5.18 (d,  $J = 21.4$  Hz, 4508H), 4.60 (s, 4H), 4.43 (d,  $J = 7.7$  Hz, 21H), 4.27 (d,  $J = 7.7$  Hz, 35H), 3.66 (s, 50H), 1.55 (d,  $J = 6.8$  Hz, 47262H).

**PLLA-A.** **PLLA-NH<sub>2</sub>** (7.0 g, 0.12 mmol, 1 equiv.) and acetyl-L-alanyl-L-alanine **4** (121.4 mg, 1.79 mmol, 18.8 equiv.) were dissolved in tetrahydrofuran (400 mL), followed by the addition of benzotriazol-1-yloxytripyrrolidinophosphonium hexafluorophosphate (1.6 g, 3.0 mmol, 26 equiv.) and diisopropylethylamine (1.8 g, 13.6 mmol, 68 equiv.). The solution was stirred overnight and then precipitated into rapidly stirred cold diethyl ether. The precipitate was filtered off, washed with cold diethyl ether, dried, and redissolved in tetrahydrofuran. The precipitation was repeated two more times. **PLLA-A** was obtained as a white powder in a yield of 5.6 g (80.3 %). GPC (THF, 40 °C):  $M_n = 66'889$ ,  $\mathcal{D} = 1.31$ .  $^1\text{H NMR}$  (400 MHz, Chloroform-d)  $\delta$  6.53 (s, 0H), 6.43 (s, 1H), 6.03 (s, 1H), 5.15 (s, 488H), 4.61 (s, 2H), 4.42 (s, 2H), 4.26 (s, 2H), 3.65 (s, 4H), 1.57 (s, 2100H).

# References



1. Geyer, R., Jambeck, J. R. & Law, K. L. Production, use, and fate of all plastics ever made. *Sci. Adv.* **3**, e1700782 (2017).
2. Plastics - the Facts 2022 • Plastics Europe. *Plastics Europe* <https://plasticseurope.org/knowledge-hub/plastics-the-facts-2022/>.
3. World Economic Forum, Ellen MacArthur Foundation & McKinsey & Company. *The New Plastics Economy – Rethinking the Future of Plastics*. (2016).
4. Zheng, J. & Suh, S. Strategies to reduce the global carbon footprint of plastics. *Nat. Clim. Change* **9**, 374–378 (2019).
5. Lebreton, L. *et al.* Evidence that the Great Pacific Garbage Patch is rapidly accumulating plastic. *Sci. Rep.* **8**, 4666 (2018).
6. Chamas, A. *et al.* Degradation Rates of Plastics in the Environment. *ACS Sustain. Chem. Eng.* **8**, 3494–3511 (2020).
7. MacLeod, M., Arp, H. P. H., Tekman, M. B. & Jahnke, A. The global threat from plastic pollution. *Science* **373**, 61–65 (2021).
8. Santos, R. G., Machovsky-Capuska, G. E. & Andrades, R. Plastic ingestion as an evolutionary trap: Toward a holistic understanding. *Science* **373**, 56–60 (2021).
9. Schirmeister, C. G. & Mülhaupt, R. Closing the Carbon Loop in the Circular Plastics Economy. *Macromol. Rapid Commun.* **43**, 2200247 (2022).
10. Castro-Aguirre, E., Iñiguez-Franco, F., Samsudin, H., Fang, X. & Auras, R. Poly(lactic acid)—Mass production, processing, industrial applications, and end of life. *Adv. Drug Deliv. Rev.* **107**, 333–366 (2016).
11. Rahimi, A. & García, J. M. Chemical recycling of waste plastics for new materials production. *Nat. Rev. Chem.* **1**, 0046 (2017).
12. Coates, G. W. & Getzler, Y. D. Y. L. Chemical recycling to monomer for an ideal, circular polymer economy. *Nat. Rev. Mater.* **5**, 501–516 (2020).
13. Garcia, J. M. & Robertson, M. L. The future of plastics recycling. *Science* **358**, 870–872 (2017).
14. The New Plastics Economy: Rethinking the future of plastics. <https://ellenmacarthurfoundation.org/the-new-plastics-economy-rethinking-the-future-of-plastics>.
15. Law, K. L. & Narayan, R. Reducing environmental plastic pollution by designing polymer materials for managed end-of-life. *Nat. Rev. Mater.* **7**, 104–116 (2021).
16. Tang, X. & Chen, E. Y.-X. Toward Infinitely Recyclable Plastics Derived from Renewable Cyclic Esters. *Chem* **5**, 284–312 (2019).
17. Zhu, Y., Romain, C. & Williams, C. K. Sustainable polymers from renewable resources. *Nature* **540**, 354–362 (2016).
18. Haider, T. P., Völker, C., Kramm, J., Landfester, K. & Wurm, F. R. Plastics of the Future? The Impact of Biodegradable Polymers on the Environment and on Society. *Angew. Chem. Int. Ed.* **58**, 50–62 (2019).
19. Min, K., Cuiffi, J. D. & Mathers, R. T. Ranking environmental degradation trends of plastic marine debris based on physical properties and molecular structure. *Nat. Commun.* **11**, 727 (2020).
20. Sivalingam, G. & Madras, G. Thermal degradation of poly ( $\epsilon$ -caprolactone). *Polym. Degrad. Stab.* **80**, 11–16 (2003).
21. Carothers, W. H., Dorough, G. L. & Natta, F. J. van. STUDIES OF POLYMERIZATION AND RING FORMATION. X. THE REVERSIBLE POLYMERIZATION OF SIX-MEMBERED CYCLIC ESTERS. *J. Am. Chem. Soc.* **54**, 761–772 (1932).
22. Lowe, C. E. Preparation of high molecular weight polyhydroxyacetic ester. (1954).
23. EUBIO\_Admin. Market. *European Bioplastics e.V.* <https://www.european-bioplastics.org/market/>.
24. Standau, T., Zhao, C., Murillo Castellón, S., Bonten, C. & Altstädt, V. Chemical Modification and Foam Processing of Polylactide (PLA). *Polymers* **11**, 306 (2019).
25. Hartmann, M. H. High Molecular Weight Polylactic Acid Polymers. in *Biopolymers from Renewable Resources* (ed. Kaplan, D. L.) 367–411 (Springer Berlin Heidelberg, 1998). doi:10.1007/978-3-662-03680-8\_15.
26. Perego, G., Cella, G. D. & Bastioli, C. Effect of molecular weight and crystallinity on poly(lactic acid) mechanical properties. *J. Appl. Polym. Sci.* **59**, 37–43 (1996).
27. Groot, W. J. & Borén, T. Life cycle assessment of the manufacture of lactide and PLA biopolymers from sugarcane in Thailand. *Int. J. Life Cycle Assess.* **15**, 970–984 (2010).

28. Cosate de Andrade, M. F., Souza, P. M. S., Cavalett, O. & Morales, A. R. Life Cycle Assessment of Poly(Lactic Acid) (PLA): Comparison Between Chemical Recycling, Mechanical Recycling and Composting. *J. Polym. Environ.* **24**, 372–384 (2016).
29. McNeill, I. C. & Leiper, H. A. Degradation studies of some polyesters and polycarbonates—2. Polylactide: Degradation under isothermal conditions, thermal degradation mechanism and photolysis of the polymer. *Polym. Degrad. Stab.* **11**, 309–326 (1985).
30. Ikada, E. Relationship between Photodegradability and Biodegradability of Some Aliphatic Polyesters. *J. Photopolym. Sci. Technol.* **12**, 251–256 (1999).
31. Iñiguez-Franco, F. *et al.* Concurrent solvent induced crystallization and hydrolytic degradation of PLA by water-ethanol solutions. *Polymer* **99**, 315–323 (2016).
32. Wasanasuk, K. & Tashiro, K. Crystal structure and disorder in Poly(l-lactic acid)  $\delta$  form ( $\alpha'$  form) and the phase transition mechanism to the ordered  $\alpha$  form. *Polymer* **52**, 6097–6109 (2011).
33. Eling, B., Gogolewski, S. & Pennings, A. J. Biodegradable materials of poly(l-lactic acid): 1. Melt-spun and solution-spun fibres. *Polymer* **23**, 1587–1593 (1982).
34. Wang, H., Zhang, J. & Tashiro, K. Phase Transition Mechanism of Poly(l-lactic acid) among the  $\alpha$ ,  $\delta$ , and  $\beta$  Forms on the Basis of the Reinvestigated Crystal Structure of the  $\beta$  Form. *Macromolecules* **50**, 3285–3300 (2017).
35. Leenslag, J. W. & Pennings, A. J. High-strength poly(l-lactide) fibres by a dry-spinning/hot-drawing process. *Polymer* **28**, 1695–1702 (1987).
36. Ru, J.-F. *et al.* Dominant  $\beta$ -Form of Poly(l-lactic acid) Obtained Directly from Melt under Shear and Pressure Fields. *Macromolecules* **49**, 3826–3837 (2016).
37. Liu, G., Zhang, X. & Wang, D. Tailoring Crystallization: Towards High-Performance Poly(lactic acid). *Adv. Mater.* **26**, 6905–6911 (2014).
38. Cartier, L. *et al.* Epitaxial crystallization and crystalline polymorphism of polylactides. *Polymer* **41**, 8909–8919 (2000).
39. Saeidlou, S., Huneault, M. A., Li, H. & Park, C. B. Poly(lactic acid) crystallization. *Prog. Polym. Sci.* **37**, 1657–1677 (2012).
40. Yin, H.-Y. *et al.* High-melting-point crystals of poly(L-lactic acid) (PLLA): the most efficient nucleating agent to enhance the crystallization of PLLA. *CrystEngComm* **17**, 2310–2320 (2015).
41. Dargent, E., Arnoult, M. & Mano, J. F. Mobile amorphous phase fragility in semi-crystalline polymers: Comparison of PET and PLLA. *Polymer* **48**, 1012–1019 (2007).
42. Razavi, M. & Wang, S.-Q. Why Is Crystalline Poly(lactic acid) Brittle at Room Temperature? *Macromolecules* **52**, 5429–5441 (2019).
43. Lizundia, E., Petisco, S. & Sarasua, J.-R. Phase-structure and mechanical properties of isothermally melt- and cold-crystallized poly(L-lactide). *J. Mech. Behav. Biomed. Mater.* **17**, 242–251 (2013).
44. Gao, X.-R. *et al.* Extensional Stress-Induced Orientation and Crystallization can Regulate the Balance of Toughness and Stiffness of Polylactide Films: Interplay of Oriented Amorphous Chains and Crystallites. *Macromolecules* **52**, 5278–5288 (2019).
45. Huang, Z.-X., Wang, M.-M., Feng, Y.-H. & Qu, J.-P. Supertough, Ultrastrong, and Transparent Poly(lactic acid) via Directly Hot Pressing under Cyclic Compressing–Releasing. *Macromolecules* **54**, 4847–4853 (2021).
46. Huang, T., Miura, M., Nobukawa, S. & Yamaguchi, M. Chain Packing and Its Anomalous Effect on Mechanical Toughness for Poly(lactic acid). *Biomacromolecules* **16**, 1660–1666 (2015).
47. Zhang, X. *et al.* Structure variation of tensile-deformed amorphous poly(l-lactic acid): Effects of deformation rate and strain. *Polymer* **52**, 4141–4149 (2011).
48. Wietzke, S. *et al.* Thermomorphological study of the terahertz lattice modes in polyvinylidene fluoride and high-density polyethylene. *Appl. Phys. Lett.* **97**, 022901 (2010).
49. Anderson, K., Schreck, K. & Hillmyer, M. Toughening Polylactide. *Polym. Rev.* **48**, 85–108 (2008).
50. Shao, J. *et al.* Modified PLA Homochiral Crystallites Facilitated by the Confinement of PLA Stereocomplexes. *Macromolecules* **46**, 6963–6971 (2013).
51. Tsuji, H. & Ikada, Y. Crystallization from the melt of poly(lactide)s with different optical purities and their blends. *Macromol. Chem. Phys.* **197**, 3483–3499 (1996).
52. Ikada, Y., Jamshidi, K., Tsuji, H. & Hyon, S. H. Stereocomplex formation between enantiomeric poly(lactides). *Macromolecules* **20**, 904–906 (1987).
53. Nofar, M., Sacligil, D., Carreau, P. J., Kamal, M. R. & Heuzey, M.-C. Poly(lactic acid) blends: Processing, properties and applications. *Int. J. Biol. Macromol.* **125**, 307–360 (2019).

54. Maillard, D. & Prud'homme, R. E. Differences Between Crystals Obtained in PLLA-Rich or PDLA-Rich Stereocomplex Mixtures. *Macromolecules* **43**, 4006–4010 (2010).
55. Tsuji, H. Poly(lactide) stereocomplexes: formation, structure, properties, degradation, and applications. *Macromol. Biosci.* **5**, 569–597 (2005).
56. Anderson, K. S. & Hillmyer, M. A. Melt preparation and nucleation efficiency of polylactide stereocomplex crystallites. *Polymer* **47**, 2030–2035 (2006).
57. Tsuji, H. Poly(lactic acid) stereocomplexes: A decade of progress. *Adv. Drug Deliv. Rev.* **107**, 97–135 (2016).
58. Nofar, M., Mohammadi, M. & Carreau, P. J. Super enhancement of rheological properties of amorphous PLA through generation of a fiberlike oriented crystal network. *J. Rheol.* **65**, 493–505 (2021).
59. Saeidlou, S., Huneault, M. A., Li, H. & Park, C. B. Poly(lactic acid) stereocomplex formation: Application to PLA rheological property modification. *J. Appl. Polym. Sci.* **131**, (2014).
60. Yamane, H., Sasai, K., Takano, M. & Takahashi, M. Poly(D-lactic acid) as a rheological modifier of poly(L-lactic acid): Shear and biaxial extensional flow behavior. *J. Rheol.* **48**, 599–609 (2004).
61. Södergård, A. & Stolt, M. Properties of lactic acid based polymers and their correlation with composition. *Prog. Polym. Sci.* **27**, 1123–1163 (2002).
62. Takasaki, M., Ito, H. & Kikutani, T. Development of Stereocomplex Crystal of Polylactide in High-Speed Melt Spinning and Subsequent Drawing and Annealing Processes. *J. Macromol. Sci. Part B* **42**, 403–420 (2003).
63. Van Wouwe, P., Dusselier, M., Vanleeuw, E. & Sels, B. Lactide Synthesis and Chirality Control for Poly(lactic acid) Production. *ChemSusChem* **9**, 907–921 (2016).
64. Woodruff, M. A. & Hutmacher, D. W. The return of a forgotten polymer—Polycaprolactone in the 21st century. *Prog. Polym. Sci.* **35**, 1217–1256 (2010).
65. Labet, M. & Thielemans, W. Synthesis of polycaprolactone: a review. *Chem. Soc. Rev.* **38**, 3484 (2009).
66. STOREY, R. F. & TAYLOR, A. E. Effect of Stannous Octoate on the Composition, Molecular Weight, and Molecular Weight Distribution of Ethylene Glycol-Initiated Poly( $\epsilon$ -Caprolactone). *J. Macromol. Sci. Part A* **35**, 723–750 (1998).
67. Buntara, T. *et al.* Caprolactam from Renewable Resources: Catalytic Conversion of 5-Hydroxymethylfurfural into Caprolactone. *Angew. Chem. Int. Ed.* **50**, 7083–7087 (2011).
68. Lundberg, D. J., Lundberg, D. J., Hillmyer, M. A. & Dauenhauer, P. J. Techno-economic Analysis of a Chemical Process To Manufacture Methyl- $\epsilon$ -caprolactone from Cresols. *ACS Sustain. Chem. Eng.* **6**, 15316–15324 (2018).
69. Gross, R. A. & Kalra, B. Biodegradable Polymers for the Environment. *Science* **297**, 803–807 (2002).
70. Peña, J., Corrales, T., Izquierdo-Barba, I., Doadrio, A. L. & Vallet-Regí, M. Long term degradation of poly( $\epsilon$ -caprolactone) films in biologically related fluids. *Polym. Degrad. Stab.* **91**, 1424–1432 (2006).
71. Sinha, V. R., Bansal, K., Kaushik, R., Kumria, R. & Trehan, A. Poly-epsilon-caprolactone microspheres and nanospheres: an overview. *Int. J. Pharm.* **278**, 1–23 (2004).
72. Chen, D. R., Bei, J. Z. & Wang, S. G. Polycaprolactone microparticles and their biodegradation. *Polym. Degrad. Stab.* **67**, 455–459 (2000).
73. Iwabuchi, S., Jaacks, V., & Kern, W. The thermal degradation of poly-epsilon-caprolactone. *Makromol Chem* 2675–2679 (1976).
74. Effects of Residual Zinc Compounds and Chain-End Structure on Thermal Degradation of Poly( $\epsilon$ -caprolactone) | Biomacromolecules. <https://pubs.acs.org/doi/10.1021/bm049945p>.
75. Bittiger, H., Marchessault, R. H. & Niegisch, W. D. Crystal structure of poly- $\epsilon$ -caprolactone. *Acta Crystallogr. B* **26**, 1923–1927 (1970).
76. Agostinho, B., Silvestre, A. J. D., Coutinho, J. A. P. & Sousa, A. F. Synthetic (bio)degradable polymers – when does recycling fail? *Green Chem.* **25**, 13–31 (2023).
77. Azimi, B., Nourpanah, P., Rabiee, M. & Arbab, S. Poly ( $\epsilon$ -caprolactone) Fiber: An Overview. *J. Eng. Fibers Fabr.* **9**, 17 (2014).
78. Hutmacher, D. W. *et al.* Mechanical properties and cell cultural response of polycaprolactone scaffolds designed and fabricated via fused deposition modeling. *J. Biomed. Mater. Res.* **55**, 203–216 (2001).
79. Jenkins, M. J. *et al.* Characterisation of microcellular foams produced from semi-crystalline PCL using supercritical carbon dioxide. *Eur. Polym. J.* **42**, 3145–3151 (2006).
80. Polymer Data Handbook. 1102.
81. Selli, F., Erdoğan, U. H., Hufenus, R. & Perret, E. Mesophase in melt-spun poly( $\epsilon$ -caprolactone) filaments: Structure–mechanical property relationship. *Polymer* **206**, 122870 (2020).

82. Wang, K., Chen, F., Li, Z. & Fu, Q. Control of the hierarchical structure of polymer articles via “structuring” processing. *Prog. Polym. Sci.* **39**, 891–920 (2014).
83. Ariffin, H., Nishida, H., Shirai, Y. & Hassan, M. A. Determination of multiple thermal degradation mechanisms of poly(3-hydroxybutyrate). *Polym. Degrad. Stab.* **93**, 1433–1439 (2008).
84. Nishida, H. Thermal Degradation. in *Poly(Lactic Acid)* 401–412 (John Wiley & Sons, Ltd, 2010). doi:10.1002/9780470649848.ch23.
85. Barletta, M. *et al.* Poly(butylene succinate) (PBS): Materials, processing, and industrial applications. *Prog. Polym. Sci.* **132**, 101579 (2022).
86. Jamshidi, K., Hyon, S.-H. & Ikada, Y. Thermal characterization of polylactides. *Polymer* **29**, 2229–2234 (1988).
87. Hydrolytic degradation of branched PLA produced by reactive extrusion | Elsevier Enhanced Reader..
88. Turco, R., Santagata, G., Corrado, I., Pezzella, C. & Di Serio, M. In vivo and Post-synthesis Strategies to Enhance the Properties of PHB-Based Materials: A Review. *Front. Bioeng. Biotechnol.* **8**, (2021).
89. Lim, L.-T., Cink, K. & Vanyo, T. Processing of Poly(Lactic Acid). in *Poly(Lactic Acid)* 189–215 (John Wiley & Sons, Ltd, 2010). doi:10.1002/9780470649848.ch14.
90. Castilla-Cortázar, I., Vidaurre, A., Marí, B. & Campillo-Fernández, A. J. Morphology, Crystallinity, and Molecular Weight of Poly( $\epsilon$ -caprolactone)/Graphene Oxide Hybrids. *Polymers* **11**, 1099 (2019).
91. Morphology and crystallization behaviour of polyhydroxyalkanoates-based blends and composites: A review | Elsevier Enhanced Reader.
92. Huneault, M. A. & Li, H. Effect of nucleation and plasticization on the crystallization of poly(lactic acid). *Polymer* **48**, 6855–6866 (2007).
93. Münstedt, H. Rheological properties and molecular structure of polymer melts. *Soft Matter* **7**, 2273–2283 (2011).
94. Gahleitner, M. Melt rheology of polyolefins. *Prog Polym Sci* **50** (2001).
95. Gahleitner, M., Wolfschwenger, J., Bachner, C., Bernreitner, K. & Neißl, W. Crystallinity and mechanical properties of PP-homopolymers as influenced by molecular structure and nucleation. *J. Appl. Polym. Sci.* **61**, 649–657 (1996).
96. Gahleitner, M., Bachner, C., Ratajski, E., Rohaczek, G. & Neißl, W. Effects of the catalyst system on the crystallization of polypropylene\*. *J. Appl. Polym. Sci.* **73**, 2507–2515 (1999).
97. Easy access to ultra-high molecular weight polylactones using a bismuth catalyst |.
98. Nofar, M., Salehiyan, R. & Sinha Ray, S. Rheology of poly (lactic acid)-based systems. *Polym. Rev.* **59**, 465–509 (2019).
99. Recent progress of preparation of branched poly(lactic acid) and its application in the modification of polylactic acid materials |
100. Lusignan, C. P., Mourey, T. H., Wilson, J. C. & Colby, R. H. Viscoelasticity of randomly branched polymers in the vulcanization class. *Phys. Rev. E Stat. Phys. Plasmas Fluids Relat. Interdiscip. Top.* **60**, 5657–5669 (1999).
101. Branched polyesters: recent advances in synthesis and performance.
102. Tiwary, P., Najafi, N. & Kontopoulou, M. Advances in peroxide-initiated graft modification of thermoplastic biopolyesters by reactive extrusion. *Can. J. Chem. Eng.* **99**, 1870–1884 (2021).
103. Nerkar, M., Ramsay, J. A., Ramsay, B. A. & Kontopoulou, M. Dramatic Improvements in Strain Hardening and Crystallization Kinetics of PLA by Simple Reactive Modification in the Melt State. *Macromol. Mater. Eng.* **299**, 1419–1424 (2014).
104. Star-shaped and branched polylactides: Synthesis, characterization, and properties |
105. Darwis, D., Nishimura, K., Mitomo, H. & Yoshii, F. Improvement of processability of poly( $\epsilon$ -caprolactone) by radiation techniques. *J. Appl. Polym. Sci.* **74**, 1815–1820 (1999).
106. Avella, A., Mincheva, R., Raquez, J.-M. & Lo Re, G. Substantial Effect of Water on Radical Melt Crosslinking and Rheological Properties of Poly( $\epsilon$ -Caprolactone). *Polymers* **13**, 491 (2021).
107. Navarro, R., Burillo, G., Adem, E. & Marcos-Fernández, A. Effect of Ionizing Radiation on the Chemical Structure and the Physical Properties of Polycaprolactones of Different Molecular Weight. *Polymers* **10**, 397 (2018).
108. Chae, D. W. *et al.* Effects of molecular architecture on the rheological and physical properties of polycaprolactone. *Korea-Aust. Rheol. J.* **29**, 129–135 (2017).
109. Weinmann, S. & Bonten, C. Thermal and rheological properties of modified polyhydroxybutyrate (PHB). *Polym. Eng. Sci.* **59**, 1057–1064 (2019).

110. Gopi, S., Kontopoulou, M., Ramsay, B. A. & Ramsay, J. A. Manipulating the structure of medium-chain-length polyhydroxyalkanoate (MCL-PHA) to enhance thermal properties and crystallization kinetics. *Int. J. Biol. Macromol.* **119**, 1248–1255 (2018).
111. Zhu, X., Zhou, Y. & Yan, D. Influence of branching architecture on polymer properties. *J. Polym. Sci. Part B Polym. Phys.* **49**, 1277–1286 (2011).
112. Flory, P. J. Thermodynamics of High Polymer Solutions. *J. Chem. Phys.* **9**, 660–660 (1941).
113. Huggins, M. L. Solutions of Long Chain Compounds. *J. Chem. Phys.* **9**, 440–440 (1941).
114. Young, R. J. & Lovell, P. A. *Introduction to Polymers, Second Edition*. (Taylor & Francis, 1991).
115. Lin, D. & Huang, Y. A thermal analysis method to predict the complete phase diagram of drug–polymer solid dispersions. *Int. J. Pharm.* **399**, 109–115 (2010).
116. Flory, P. J. *Principles of Polymer Chemistry*. (Cornell University Press, 1953).
117. Leibler, L. Theory of Microphase Separation in Block Copolymers. *Macromolecules* **13**, 1602–1617 (1980).
118. Fredrickson, G. H., Liu, A. J. & Bates, F. S. Entropic Corrections to the Flory-Huggins Theory of Polymer Blends: Architectural and Conformational Effects. *Macromolecules* **27**, 2503–2511 (1994).
119. Painter, P. C., Park, Y. & Coleman, M. M. Hydrogen bonding in polymer blends. 2. Theory. *Macromolecules* **21**, 66–72 (1988).
120. Vilgis, T. A. & Noolandi, J. On the compatibilization of polymer blends. *Makromol. Chem. Macromol. Symp.* **16**, 225–234 (1988).
121. Lee, J. Y., Painter, P. C. & Coleman, M. M. Hydrogen bonding in polymer blends. 4. Blends involving polymers containing methacrylic acid and vinylpyridine groups. *Macromolecules* **21**, 954–960 (1988).
122. Cor, K., Martin, V. D., Christophe, P. & Robert, J. STRATEGIES FOR COMPATIBILIZATION OF POLYMER BLENDS. *Prog. Polym. Sci.* **23**, 44 (1998).
123. Sundararajan, P. R. Small molecule self-assembly in polymer matrices. *J. Polym. Sci. Part B Polym. Phys.* **56**, 451–478 (2018).
124. Sears, J. K. & Darby, J. R. *The technology of plasticizers*. (Wiley, 1982).
125. *Handbook of Plasticizers*. (Elsevier, 2012). doi:10.1016/C2011-0-07408-2.
126. Thakore, S. D., Akhtar, J., Jain, R., Paudel, A. & Bansal, A. K. Analytical and Computational Methods for the Determination of Drug-Polymer Solubility and Miscibility. *Mol. Pharm.* **18**, 2835–2866 (2021).
127. Marsac, P. J., Shamblin, S. L. & Taylor, L. S. Theoretical and Practical Approaches for Prediction of Drug–Polymer Miscibility and Solubility. *Pharm. Res.* **23**, 2417–2426 (2006).
128. Coiai, S., Di Lorenzo, M. L., Cinelli, P., Righetti, M. C. & Passaglia, E. Binary Green Blends of Poly(lactic acid) with Poly(butylene adipate-co-butylene terephthalate) and Poly(butylene succinate-co-butylene adipate) and Their Nanocomposites. *Polymers* **13**, 2489 (2021).
129. PLA-PBAT-PLA tri-block copolymers\_ Effective compatibilizers for promotion of the mechanical and rheological properties of PLA/PBAT blends |
130. Maglio, G., Malinconico, M., Migliozi, A. & Groeninckx, G. Immiscible poly(L-lactide)/poly( $\epsilon$ -caprolactone) blends: Influence of the addition of a poly(L-lactide)-poly(oxyethylene) block copolymer on thermal behavior and morphology. *Macromol. Chem. Phys.* **205**, 946–950 (2004).
131. PLA-PEG-PLA tri-block copolymers: Effective compatibilizers for promotion of the interfacial structure and mechanical properties of PLA/PBAT blends |
132. Compatibilization of immiscible PLA-based biodegradable polymer blends using amphiphilic di-block copolymers |
133. Mechanical properties, rheological behaviors, and phase morphologies of high-toughness PLA/PBAT blends by in-situ reactive compatibilization |
134. Jiang, L. *et al.* Crystallization modification of poly(lactide) by using nucleating agents and stereocomplexation. *E-Polym.* **16**, 1–13 (2016).
135. Haubruge, H. G. *et al.* Epitaxial Nucleation of Poly(ethylene terephthalate) by Talc: Structure at the Lattice and Lamellar Scales. *Macromolecules* **36**, 4452–4456 (2003).
136. Jiang, L., Zhang, J. & Wolcott, M. P. Comparison of polylactide/nano-sized calcium carbonate and polylactide/montmorillonite composites: Reinforcing effects and toughening mechanisms. *Polymer* **48**, 7632–7644 (2007).
137. Gu, S.-Y., Zou, C.-Y., Zhou, K. & Ren, J. Structure-rheology responses of polylactide/calcium carbonate composites. *J. Appl. Polym. Sci.* **114**, 1648–1655 (2009).



138. Xu, H.-S., Dai, X. J., Lamb, P. R. & Li, Z.-M. Poly(L-lactide) crystallization induced by multiwall carbon nanotubes at very low loading. *J. Polym. Sci. Part B Polym. Phys.* **47**, 2341–2352 (2009).
139. Barrau, S. *et al.* Crystallization Behavior of Carbon Nanotube–Polylactide Nanocomposites. *Macromolecules* **44**, 6496–6502 (2011).
140. Wu, D., Wu, L., Zhou, W., Sun, Y. & Zhang, M. Relations between the aspect ratio of carbon nanotubes and the formation of percolation networks in biodegradable polylactide/carbon nanotube composites. *J. Polym. Sci. Part B Polym. Phys.* **48**, 479–489 (2010).
141. Wu, D., Wu, L., Zhang, M. & Zhao, Y. Viscoelasticity and thermal stability of polylactide composites with various functionalized carbon nanotubes. *Polym. Degrad. Stab.* **93**, 1577–1584 (2008).
142. PLA nanocomposites: Effect of filler type on non-isothermal crystallization |
143. Xu, H.-S., Dai, X. J., Lamb, P. R. & Li, Z.-M. Poly(L-lactide) crystallization induced by multiwall carbon nanotubes at very low loading: Poly(L-Lactide) Crystallization. *J. Polym. Sci. Part B Polym. Phys.* **47**, 2341–2352 (2009).
144. Qiu, Z. & Li, Z. Effect of Orotic Acid on the Crystallization Kinetics and Morphology of Biodegradable Poly(L-lactide) as an Efficient Nucleating Agent. *Ind. Eng. Chem. Res.* **50**, 12299–12303 (2011).
145. Ma, P., Xu, Y., Wang, D., Dong, W. & Chen, M. Rapid Crystallization of Poly(lactic acid) by Using Tailor-Made Oxalamide Derivatives as Novel Soluble-Type Nucleating Agents. *Ind. Eng. Chem. Res.* **53**, 12888–12892 (2014).
146. Kawamoto, N., Sakai, A., Horikoshi, T., Urushihara, T. & Tobita, E. Nucleating agent for poly(L-lactic acid)—An optimization of chemical structure of hydrazide compound for advanced nucleation ability. *J. Appl. Polym. Sci.* **103**, 198–203 (2007).
147. Nonisothermal crystallization kinetics of poly(lactic acid) formulations comprising talc with poly(ethylene glycol) - Li - 2010 - Polymer Engineering & Science - Wiley Online Library. <https://4spublicationsonlinelibrary.wiley.com/doi/10.1002/pen.21755>.
148. Ogata, N., Jimenez, G., Kawai, H. & Ogiwara, T. Structure and thermal/mechanical properties of poly(l-lactide)-clay blend. *J. Polym. Sci. Part B Polym. Phys.* **35**, 389–396 (1997).
149. Trifol, J. *et al.* Impact of thermal processing or solvent casting upon crystallization of PLA nanocellulose and/or nanoclay composites. *J. Appl. Polym. Sci.* **136**, 47486 (2019).
150. Nakajima, H., Takahashi, M. & Kimura, Y. Induced Crystallization of PLLA in the Presence of 1,3,5-Benzenetricarboxylamide Derivatives as Nucleators: Preparation of Haze-Free Crystalline PLLA Materials. *Macromol. Mater. Eng.* **295**, 460–468 (2010).
151. Wang, W. *et al.* Crystallization of a Self-Assembling Nucleator in Poly(l-lactide) Melt. *Cryst. Growth Des.* **21**, 5880–5888 (2021).
152. Wang, T. *et al.* Effect of 1,3,5-trialkyl-benzenetricarboxylamide on the crystallization of poly(lactic acid). *J. Appl. Polym. Sci.* **130**, 1328–1336 (2013).
153. Smulders, M. M. J. *et al.* Cooperative Two-Component Self-Assembly of Mono- and Ditopic Monomers. *Macromolecules* **44**, 6581–6587 (2011).
154. Kulkarni, C., Meijer, E. W. & Palmans, A. R. A. Cooperativity Scale: A Structure–Mechanism Correlation in the Self-Assembly of Benzene-1,3,5-tricarboxamides. *Acc. Chem. Res.* **50**, 1928–1936 (2017).
155. Blomenhofer, M. *et al.* “Designer” Nucleating Agents for Polypropylene. *Macromolecules* **38**, 3688–3695 (2005).
156. Abraham, F., Kress, R., Smith, P. & Schmidt, H.-W. A New Class of Ultra-Efficient Supramolecular Nucleating Agents for Isotactic Polypropylene. *Macromol. Chem. Phys.* **214**, 17–24 (2013).
157. Bai, H., Zhang, W., Deng, H., Zhang, Q. & Fu, Q. Control of Crystal Morphology in Poly(l-lactide) by Adding Nucleating Agent. *Macromolecules* **44**, 1233–1237 (2011).
158. Stumpf, M., Spörrer, A., Schmidt, H.-W. & Altstädt, V. Influence of supramolecular additives on foam morphology of injection-molded i-PP. *J. Cell. Plast.* **47**, 519–534 (2011).
159. Aida, T., Meijer, E. W. & Stupp, S. I. Functional Supramolecular Polymers. *Science* **335**, 813–817 (2012).
160. Cordier, P., Tournilhac, F., Soulié-Ziakovic, C. & Leibler, L. Self-healing and thermoreversible rubber from supramolecular assembly. *Nature* **451**, 977–980 (2008).
161. Yanagisawa, Y., Nan, Y., Okuro, K. & Aida, T. Mechanically robust, readily repairable polymers via tailored noncovalent cross-linking. *Science* **359**, 72–76 (2018).
162. Sautaux, J., Marx, F., Gunkel, I., Weder, C. & Schrettl, S. Mechanically robust supramolecular polymer co-assemblies. *Nat. Commun.* **13**, 356 (2022).

163. Sijbesma, R. P. *et al.* Reversible Polymers Formed from Self-Complementary Monomers Using Quadruple Hydrogen Bonding. *Science* **278**, 1601–1604 (1997).
164. Lutz, J.-F., Lehn, J.-M., Meijer, E. W. & Matyjaszewski, K. From precision polymers to complex materials and systems. *Nat. Rev. Mater.* **1**, 16024 (2016).
165. Kim, J., Jung, H. Y. & Park, M. J. End-Group Chemistry and Junction Chemistry in Polymer Science: Past, Present, and Future. *Macromolecules* **53**, 746–763 (2020).
166. Wojtecki, R. J. & Nelson, A. Small changes with big effects: Tuning polymer properties with supramolecular interactions. *J. Polym. Sci. Part Polym. Chem.* **54**, 457–472 (2016).
167. Khare, E., Holten-Andersen, N. & Buehler, M. J. Transition-metal coordinate bonds for bioinspired macromolecules with tunable mechanical properties. *Nat. Rev. Mater.* **6**, 421–436 (2021).
168. Voorhaar, L. & Hoogenboom, R. Supramolecular polymer networks: hydrogels and bulk materials. *Chem. Soc. Rev.* **45**, 4013–4031 (2016).
169. Peng, H.-Q. *et al.* Supramolecular polymers: Recent advances based on the types of underlying interactions. *Prog. Polym. Sci.* **137**, 101635 (2023).
170. Sangeetha, N. M. & Maitra, U. Supramolecular gels: Functions and uses. *Chem. Soc. Rev.* **34**, 821 (2005).
171. Ji, X. *et al.* Supramolecular Construction of Multifluorescent Gels: Interfacial Assembly of Discrete Fluorescent Gels through Multiple Hydrogen Bonding. *Adv. Mater.* **27**, 8062–8066 (2015).
172. Chen, S. *et al.* Hydrogen-Bonded Supramolecular Polymer Adhesives: Straightforward Synthesis and Strong Substrate Interaction. *Angew. Chem. Int. Ed.* **61**, e202203876 (2022).
173. Yang, S. K., Ambade, A. V. & Weck, M. Main-chain supramolecular block copolymers. *Chem Soc Rev* **40**, 129–137 (2011).
174. Balkenende, D. W. R., Monnier, C. A., Fiore, G. L. & Weder, C. Optically responsive supramolecular polymer glasses. *Nat. Commun.* **7**, 10995 (2016).
175. Croisier, E. *et al.* A toolbox of oligopeptide-modified polymers for tailored elastomers. *Nat. Commun.* **5**, 4728 (2014).
176. Wojtecki, R. J., Meador, M. A. & Rowan, S. J. Using the dynamic bond to access macroscopically responsive structurally dynamic polymers. *Nat. Mater.* **10**, 14–27 (2011).
177. Wang, S. & Urban, M. W. Self-healing polymers. *Nat. Rev. Mater.* **5**, 562–583 (2020).
178. Campanella, A., Döhler, D. & Binder, W. H. Self-Healing in Supramolecular Polymers. *Macromol. Rapid Commun.* **39**, 1700739 (2018).
179. Habault, D., Zhang, H. & Zhao, Y. Light-triggered self-healing and shape-memory polymers. *Chem. Soc. Rev.* **42**, 7244–7256 (2013).
180. Qin, B. *et al.* Tough and Multi-Recyclable Cross-Linked Supramolecular Polyureas via Incorporating Noncovalent Bonds into Main-Chains. *Adv. Mater.* **32**, 2000096 (2020).
181. Aida, T. & Meijer, E. W. Supramolecular Polymers – we’ve Come Full Circle. *Isr. J. Chem.* **60**, 33–47 (2020).
182. Song, P. & Wang, H. High-Performance Polymeric Materials through Hydrogen-Bond Cross-Linking. *Adv. Mater.* **32**, 1901244 (2020).
183. Folmer, B. J. B., Sijbesma, R. P., Versteegen, R. M., Rijt, J. A. J. van der & Meijer, E. W. Supramolecular Polymer Materials: Chain Extension of Telechelic Polymers Using a Reactive Hydrogen-Bonding Synthron. *Adv. Mater.* **12**, 874–878 (2000).
184. Hohl, D. K., Ferahian, A.-C., Montero de Espinosa, L. & Weder, C. Toughening of Glassy Supramolecular Polymer Networks. *ACS Macro Lett.* **8**, 1484–1490 (2019).
185. van Beek, D. J. M., Spiering, A. J. H., Peters, G. W. M., te Nijenhuis, K. & Sijbesma, R. P. Unidirectional Dimerization and Stacking of Ureidopyrimidinone End Groups in Polycaprolactone Supramolecular Polymers. *Macromolecules* **40**, 8464–8475 (2007).
186. Watts, A. & Hillmyer, M. A. Aliphatic Polyester Thermoplastic Elastomers Containing Hydrogen-Bonding Ureidopyrimidinone Endgroups. *Biomacromolecules* **20**, 2598–2609 (2019).
187. Houston, K. R., Jackson, A.-M. S., Yost, R. W., Carman, H. S. & Ashby, V. S. Supramolecular engineering polyesters: endgroup functionalization of glycol modified PET with ureidopyrimidinone. *Polym. Chem.* **7**, 6744–6751 (2016).
188. Yamauchi, K., Lizotte, J. R., Hercules, D. M., Vergne, M. J. & Long, T. E. Combinations of Microphase Separation and Terminal Multiple Hydrogen Bonding in Novel Macromolecules. *J. Am. Chem. Soc.* **124**, 8599–8604 (2002).
189. van Beek, D. J. M., Gillissen, M. A. J., van As, B. A. C., Palmans, A. R. A. & Sijbesma, R. P. Supramolecular Copolyesters with Tunable Properties. *Macromolecules* **40**, 6340–6348 (2007).

190. Bao, J. *et al.* Preferential Formation of  $\beta$ -Form Crystals and Temperature-Dependent Polymorphic Structure in Supramolecular Poly(L-lactic acid) Bonded by Multiple Hydrogen Bonds. *Macromolecules* **50**, 8619–8630 (2017).
191. Hohl, D. K., Balog, S., Cappelletti, C., Karasu, F. & Weder, C. Crystallizable Supramolecular Polymers: Binding Motif and Processing Matter. *Macromolecules* **53**, 9086–9096 (2020).
192. Yamauchi, K., Kanomata, A., Inoue, T. & Long, T. E. Thermoreversible Polyesters Consisting of Multiple Hydrogen Bonding (MHB). *Macromolecules* **37**, 3519–3522 (2004).
193. Botterhuis, N. E., van Beek, D. J. M., van Gemert, G. M. L., Bosman, A. W. & Sijbesma, R. P. Self-assembly and morphology of polydimethylsiloxane supramolecular thermoplastic elastomers. *J. Polym. Sci. Part Polym. Chem.* **46**, 3877–3885 (2008).
194. Appel, W. P. J., Portale, G., Wisse, E., Dankers, P. Y. W. & Meijer, E. W. Aggregation of Ureido-Pyrimidinone Supramolecular Thermoplastic Elastomers into Nanofibers: A Kinetic Analysis. *Macromolecules* **44**, 6776–6784 (2011).
195. Cornwell, D. J. & Smith, D. K. Expanding the scope of gels – combining polymers with low-molecular-weight gelators to yield modified self-assembling smart materials with high-tech applications. *Mater. Horiz.* **2**, 279–293 (2015).
196. Isare, B., Pensec, S., Raynal, M. & Bouteiller, L. Bisurea-based supramolecular polymers: From structure to properties. Dedicated to Professor Jean-Pierre Vairon on the occasion of his 78th birthday. *Comptes Rendus Chim.* **19**, 148–156 (2016).
197. Colombani, O. *et al.* Attempt toward 1D Cross-Linked Thermoplastic Elastomers: Structure and Mechanical Properties of a New System. *Macromolecules* **38**, 1752–1759 (2005).
198. Callies, X. *et al.* Effects of multifunctional cross-linkers on rheology and adhesion of soft nanostructured materials. *Soft Matter* **13**, 7979–7990 (2017).
199. Jangizehi, A., Ahmadi, M. & Seiffert, S. Emergence, evidence, and effect of junction clustering in supramolecular polymer materials. *Mater. Adv.* **2**, 1425–1453 (2021).
200. Cantekin, S., de Greef, T. F. A. & Palmans, A. R. A. Benzene-1,3,5-tricarboxamide: a versatile ordering moiety for supramolecular chemistry. *Chem. Soc. Rev.* **41**, 6125 (2012).
201. Stals, P. J. M., Smulders, M. M. J., Martín-Rapún, R., Palmans, A. R. A. & Meijer, E. W. Asymmetrically Substituted Benzene-1,3,5-tricarboxamides: Self-Assembly and Odd–Even Effects in the Solid State and in Dilute Solution. *Chem. – Eur. J.* **15**, 2071–2080 (2009).
202. Albertazzi, L. *et al.* Probing Exchange Pathways in One-Dimensional Aggregates with Super-Resolution Microscopy. *Science* **344**, 491–495 (2014).
203. Gasparotto, P., Bochicchio, D., Ceriotti, M. & Pavan, G. M. Identifying and Tracking Defects in Dynamic Supramolecular Polymers. *J. Phys. Chem. B* **124**, 589–599 (2020).
204. Mes, T., Smulders, M. M. J., Palmans, A. R. A. & Meijer, E. W. Hydrogen-Bond Engineering in Supramolecular Polymers: Polarity Influence on the Self-Assembly of Benzene-1,3,5-tricarboxamides. *Macromolecules* **43**, 1981–1991 (2010).
205. Roosma, J., Mes, T., Leclère, P., Palmans, A. R. A. & Meijer, E. W. Supramolecular Materials from Benzene-1,3,5-tricarboxamide-Based Nanorods. *J. Am. Chem. Soc.* **130**, 1120–1121 (2008).
206. Scavuzzo, J. *et al.* Supramolecular Elastomers: Self-Assembling Star–Blocks of Soft Polyisobutylene and Hard Oligo( $\beta$ -alanine) Segments. *Macromolecules* **48**, 1077–1086 (2015).
207. Scavuzzo, J. J. *et al.* Supramolecular Elastomers. Particulate  $\beta$ -Sheet Nanocrystal-Reinforced Synthetic Elastic Networks. *Macromolecules* **49**, 2688–2697 (2016).
208. Srivastava, A., Zhao, Y., Meyerhofer, J., Jia, L. & Foster, M. D. Design of Interfacial Crowding for Elastomeric Reinforcement with Nanocrystals. *ACS Appl. Mater. Interfaces* **13**, 10349–10358 (2021).
209. Tang, M. *et al.* Towards a Supertough Thermoplastic Polyisoprene Elastomer Based on a Biomimic Strategy. *Angew. Chem. Int. Ed.* **57**, 15836–15840 (2018).
210. He, Y. *et al.* Promoted Comprehensive Properties of Polyisoprene Rubber with Extremely High Fatigue Resistance Enabled by Oligopeptide Aggregates. *Chin. J. Polym. Sci.* (2023) doi:10.1007/s10118-023-2933-3.
211. Tang, M. *et al.* Oligopeptide binding guided by spacer length lead to remarkably strong and stable network of polyisoprene elastomers. *Polymer* **233**, 124185 (2021).
212. Wang, C.-C. *et al.* Influence of Oligopeptide Length and Distribution on Polyisoprene Properties. *Polymers* **13**, 4408 (2021).

213. Hirschberg, J. H. K. K. *et al.* Supramolecular Polymers from Linear Telechelic Siloxanes with Quadruple-Hydrogen-Bonded Units. *Macromolecules* **32**, 2696–2705 (1999).
214. Véchambre, C. *et al.* Microstructure and Self-Assembly of Supramolecular Polymers Center-Functionalized with Strong Stickers. *Macromolecules* **48**, 8232–8239 (2015).
215. Boothroyd, S. C. *et al.* Association and relaxation of supra-macromolecular polymers. *Soft Matter* **15**, 5296–5307 (2019).
216. de Gennes, P. G. Reptation of a Polymer Chain in the Presence of Fixed Obstacles. *J. Chem. Phys.* **55**, 572–579 (1971).
217. Wool, R. P. Polymer entanglements. *Macromolecules* **26**, 1564–1569 (1993).
218. Porter, R. S. & Johnson, J. F. The Entanglement Concept in Polymer Systems. *Chem. Rev.* **66**, 1–27 (1966).
219. Hallam, M. A., Cansfield, D. L. M., Ward, I. M. & Pollard, G. A study of the effect of molecular weight on the tensile strength of ultra-high modulus polyethylenes. *J. Mater. Sci.* **21**, 4199–4205 (1986).
220. Ippel, B. D., Van Haften, E. E., Bouten, C. V. C. & Dankers, P. Y. W. Impact of Additives on Mechanical Properties of Supramolecular Electrospun Scaffolds. *ACS Appl. Polym. Mater.* **2**, 3742–3748 (2020).
221. Versteegen, R. M., Kleppinger, R., Sijbesma, R. P. & Meijer, E. W. Properties and Morphology of Segmented Copoly(ether urea)s with Uniform Hard Segments. *Macromolecules* **39**, 772–783 (2006).
222. Koevoets, R. A. *et al.* Molecular Recognition in a Thermoplastic Elastomer. *J. Am. Chem. Soc.* **127**, 2999–3003 (2005).
223. Wisse, E., Govaert, L. E., Meijer, H. E. H. & Meijer, E. W. Unusual Tuning of Mechanical Properties of Thermoplastic Elastomers Using Supramolecular Fillers. *Macromolecules* **39**, 7425–7432 (2006).
224. Wisse, E. *et al.* Segmental Orientation in Well-Defined Thermoplastic Elastomers Containing Supramolecular Fillers. *Macromolecules* **42**, 524–530 (2009).
225. Tan, X., Zhao, Y., Qian, M., Hamed, G. R. & Jia, L. Reactive supramolecular filler for elastomer reinforcement. *Polymer* **129**, 12–20 (2017).
226. World Economic Forum, Ellen MacArthur Foundation & McKinsey & Company. *The New Plastics Economy – Rethinking the Future of Plastics*. (2016).
227. Stubbins, A., Law, K. L., Muñoz, S. E., Bianchi, T. S. & Zhu, L. Plastics in the Earth system. *Science* **373**, 51–55 (2021).
228. MacLeod, M., Arp, H. P. H., Tekman, M. B. & Jahnke, A. The global threat from plastic pollution. *Science* **373**, 61–65 (2021).
229. The New Plastics Economy: Rethinking the future of plastics. <https://www.ellenmacarthurfoundation.org/publications/the-new-plastics-economy-rethinking-the-future-of-plastics>.
230. Stempfle, F., Ortmann, P. & Mecking, S. Long-Chain Aliphatic Polymers To Bridge the Gap between Semicrystalline Polyolefins and Traditional Polycondensates. *Chem. Rev.* **116**, 4597–4641 (2016).
231. Zhu, J.-B., Watson, E. M., Tang, J. & Chen, E. Y.-X. A synthetic polymer system with repeatable chemical recyclability. *Science* **360**, 398–403 (2018).
232. Häußler, M., Eck, M., Rothauer, D. & Mecking, S. Closed-loop recycling of polyethylene-like materials. *Nature* **590**, 423–427 (2021).
233. Manker, L. P. *et al.* Sustainable polyesters via direct functionalization of lignocellulosic sugars. *Nat. Chem.* **14**, 976–984 (2022).
234. Albertsson, A.-C. & Hakkarainen, M. Designed to degrade. *Science* **358**, 872–873 (2017).
235. Eck, M. *et al.* Biodegradable High-Density Polyethylene-like Material. *Angew. Chem. Int. Ed.* **62**, (2023).
236. Klemm, D. *et al.* Nanocelluloses: A New Family of Nature-Based Materials. *Angew. Chem. Int. Ed.* **50**, 5438–5466 (2011).
237. Blumenhofer, M. *et al.* “Designer” Nucleating Agents for Polypropylene. *Macromolecules* **38**, 3688–3695 (2005).
238. Montarnal, D., Capelot, M., Tournilhac, F. & Leibler, L. Silica-Like Malleable Materials from Permanent Organic Networks. *Science* **334**, 965–968 (2011).
239. Denissen, W., Winne, J. M. & Du Prez, F. E. Vitrimers: permanent organic networks with glass-like fluidity. *Chem. Sci.* **7**, 30–38 (2016).
240. Röttger, M. *et al.* High-performance vitrimers from commodity thermoplastics through dioxaborolane metathesis. *Science* **356**, 62–65 (2017).

241. Khare, E., Holten-Andersen, N. & Buehler, M. J. Transition-metal coordinate bonds for bioinspired macromolecules with tunable mechanical properties. *Nat. Rev. Mater.* **6**, 421–436 (2021).
242. Voorhaar, L. & Hoogenboom, R. Supramolecular polymer networks: hydrogels and bulk materials. *Chem. Soc. Rev.* **45**, 4013–4031 (2016).
243. Peng, H.-Q. *et al.* Supramolecular polymers: Recent advances based on the types of underlying interactions. *Prog. Polym. Sci.* **137**, 101635 (2023).
244. Seiffert, S. & Sprakel, J. Physical chemistry of supramolecular polymer networks. *Chem. Soc. Rev.* **41**, 909–930 (2012).
245. Folmer, B. J. B., Sijbesma, R. P., Versteegen, R. M., van der Rijt, J. a. J. & Meijer, E. W. Supramolecular Polymer Materials: Chain Extension of Telechelic Polymers Using a Reactive Hydrogen-Bonding Synthron. *Adv. Mater.* **12**, 874–878 (2000).
246. Aida, T. & Meijer, E. W. Supramolecular Polymers – we’ve Come Full Circle. *Isr. J. Chem.* **60**, 33–47 (2020).
247. Hong, M. & Chen, E. Y.-X. Future Directions for Sustainable Polymers. *Trends Chem.* **1**, 148–151 (2019).
248. Cordier, P., Tournilhac, F., Soulié-Ziakovic, C. & Leibler, L. Self-healing and thermoreversible rubber from supramolecular assembly. *Nature* **451**, 977–980 (2008).
249. Yanagisawa, Y., Nan, Y., Okuro, K. & Aida, T. Mechanically robust, readily repairable polymers via tailored noncovalent cross-linking. *Science* **359**, 72–76 (2018).
250. Montero de Espinosa, L., Meesorn, W., Moatsou, D. & Weder, C. Bioinspired Polymer Systems with Stimuli-Responsive Mechanical Properties. *Chem. Rev.* **117**, 12851–12892 (2017).
251. Yan, X., Wang, F., Zheng, B. & Huang, F. Stimuli-responsive supramolecular polymeric materials. *Chem. Soc. Rev.* **41**, 6042 (2012).
252. Jiang, Z.-C. *et al.* Shape Memory Polymers Based on Supramolecular Interactions. *ACS Appl. Mater. Interfaces* **9**, 20276–20293 (2017).
253. Roosma, J., Mes, T., Leclère, P., Palmans, A. R. A. & Meijer, E. W. Supramolecular Materials from Benzene-1,3,5-tricarboxamide-Based Nanorods. *J. Am. Chem. Soc.* **130**, 1120–1121 (2008).
254. Hosono, N., Pitet, L. M., Palmans, A. R. A. & Meijer, E. W. The effect of pendant benzene-1,3,5-tricarboxamides in the middle block of ABA triblock copolymers: synthesis and mechanical properties. *Polym. Chem.* **5**, 1463–1470 (2014).
255. Hosono, N. *et al.* Orthogonal Self-Assembly in Folding Block Copolymers. *J. Am. Chem. Soc.* **135**, 501–510 (2013).
256. Cantekin, S., Greef, T. F. A. de & Palmans, A. R. A. Benzene-1,3,5-tricarboxamide: a versatile ordering moiety for supramolecular chemistry. *Chem. Soc. Rev.* **41**, 6125–6137 (2012).
257. Tian, L. *et al.* Development of a robust supramolecular method to prepare well-defined nanofibrils from conjugated molecules. *Chem. Sci.* **3**, 1512–1521 (2012).
258. Aggeli, A. *et al.* Hierarchical self-assembly of chiral rod-like molecules as a model for peptide  $\beta$ -sheet tapes, ribbons, fibrils, and fibers. *Proc. Natl. Acad. Sci.* **98**, 11857–11862 (2001).
259. Levin, A. *et al.* Biomimetic peptide self-assembly for functional materials. *Nat. Rev. Chem.* **4**, 615–634 (2020).
260. Frauenrath, H. & Jahnke, E. A general concept for the preparation of hierarchically structured  $\pi$ -conjugated polymers. *Chem. - Eur. J.* **14**, 2942–2955 (2008).
261. Croisier, E. *et al.* A toolbox of oligopeptide-modified polymers for tailored elastomers. *Nat. Commun.* **5**, 4728 (2014).
262. Tang, M. *et al.* Towards a Supertough Thermoplastic Polyisoprene Elastomer Based on a Biomimic Strategy. *Angew. Chem. Int. Ed.* **57**, 15836–15840 (2018).
263. Jahnke, E., Lieberwirth, I., Severin, N., Rabe, J. P. & Frauenrath, Holger. Topochemical polymerization in supramolecular polymers of oligopeptide-functionalized diacetylenes. *Angew. Chem. Int. Ed.* **45**, 5383–5386 (2006).
264. Jahnke, E., Severin, N., Kreutzkamp, P., Rabe, J. P. & Frauenrath, Holger. Molecular level control over hierarchical structure formation and polymerization of oligopeptide-polymer conjugates. *Adv. Mater.* **20**, 409–414 (2008).
265. Marty, R. *et al.* Hierarchically Structured Microfibers of ‘Single Stack’ Perylene Bisimide and Quaterthiophene Nanowires. *ACS Nano* **7**, 8498–8508 (2013).
266. Hafner, R. J. *et al.* Unusually Long-Lived Photocharges in Helical Organic Semiconductor Nanostructures. *ACS Nano* **12**, 9116–9125 (2018).
267. Spitzner, E.-C. *et al.* Multi-Set Point Intermittent Contact (MUSIC) Mode Atomic Force Microscopy of Oligothiophene Fibrils. *ACS Macro Lett.* **1**, 380–383 (2012).

268. Diegelmann, S. R., Gorham, J. M. & Tovar, J. D. One-Dimensional Optoelectronic Nanostructures Derived from the Aqueous Self-Assembly of  $\pi$ -Conjugated Oligopeptides. *J. Am. Chem. Soc.* **130**, 13840–13841 (2008).
269. Herbst, F., Seiffert, S. & H. Binder, W. Dynamic supramolecular poly(isobutylene)s for self-healing materials. *Polym. Chem.* **3**, 3084–3092 (2012).
270. Boothroyd, S. C. *et al.* Association and relaxation of supra-macromolecular polymers. *Soft Matter* **15**, 5296–5307 (2019).
271. Bouteiller, L. *et al.* Attempt toward 1D Cross-Linked Thermoplastic Elastomers: Structure and Mechanical Properties of a New System. *Macromolecules* **38**, 1752–1759 (2005).
272. Creton, C. *et al.* Microstructure and Self-Assembly of Supramolecular Polymers Center-Functionalized with Strong Stickers. *Macromolecules* **48**, 8232–8239 (2015).
273. Ippel, B. D., Van Haafte, E. E., Bouten, C. V. C. & Dankers, P. Y. W. Impact of Additives on Mechanical Properties of Supramolecular Electrospun Scaffolds. *ACS Appl. Polym. Mater.* **2**, 3742–3748 (2020).
274. Huang, G. *et al.* Towards a Supertough Thermoplastic Polyisoprene Elastomer Based on a Biomimic Strategy. *Angew. Chem. Int. Ed.* **57**, 15836–15840 (2018).
275. Meijer, E. W. *et al.* Segmental Orientation in Well-Defined Thermoplastic Elastomers Containing Supramolecular Fillers. *Macromolecules* **42**, 524–530 (2009).
276. Meijer, E. W., Wisse, E., Govaert, L. E. & Meijer, H. E. H. Unusual Tuning of Mechanical Properties of Thermoplastic Elastomers Using Supramolecular Fillers. *Macromolecules* **39**, 7425–7432 (2006).
277. Brzeziński, M. & Biela, T. Supramolecular Poly lactides by the Cooperative Interaction of the End Groups and Stereocomplexation. *Macromolecules* **48**, 2994–3004 (2015).
278. German, I., D'Agosto, F., Boisson, C., Tencé-Girault, S. & Soulié-Ziakovic, C. Microphase Separation and Crystallization in H-Bonding End-Functionalized Polyethylenes. *Macromolecules* **48**, 3257–3268 (2015).
279. van Beek, D. J. M., Spiering, A. J. H., Peters, G. W. M., te Nijenhuis, K. & Sijbesma, R. P. Unidirectional Dimerization and Stacking of Ureidopyrimidinone End Groups in Polycaprolactone Supramolecular Polymers. *Macromolecules* **40**, 8464–8475 (2007).
280. van Beek, D. J. M., Gillissen, M. A. J., van As, B. A. C., Palmans, A. R. A. & Sijbesma, R. P. Supramolecular Copolyesters with Tunable Properties. *Macromolecules* **40**, 6340–6348 (2007).
281. Houston, K. R., Jackson, A.-M. S., Yost, R. W., Carman, H. S. & Ashby, V. S. Supramolecular engineering polyesters: endgroup functionalization of glycol modified PET with ureidopyrimidinone. *Polym. Chem.* **7**, 6744–6751 (2016).
282. Yamauchi, K., Lizotte, J. R., Hercules, D. M., Vergne, M. J. & Long, T. E. Combinations of Microphase Separation and Terminal Multiple Hydrogen Bonding in Novel Macromolecules. *J. Am. Chem. Soc.* **124**, 8599–8604 (2002).
283. Yamauchi, K., Kanomata, A., Inoue, T. & Long, T. E. Thermoreversible polyesters consisting of multiple hydrogen bonding (MHB). *Macromolecules* **37**, 3519–3522 (2004).
284. Gross, R. A. & Kalra, B. Biodegradable Polymers for the Environment. *Science* **297**, 803–807 (2002).
285. Izuka, A., Winter, H. H. & Hashimoto, T. Molecular weight dependence of viscoelasticity of polycaprolactone critical gels. *Macromolecules* **25**, 2422–2428 (1992).
286. Takahashi, Y. *et al.* Effect of Loop/Bridge Conformation Ratio on Elastic Properties of the Sphere-Forming ABA Triblock Copolymers under Uniaxial Elongation. *Macromolecules* **38**, 9724–9729 (2005).
287. Matsen, M. W. & Thompson, R. B. Equilibrium behavior of symmetric ABA triblock copolymer melts. *J. Chem. Phys.* **111**, 7139–7146 (1999).
288. Matsen, M. W. & Schick, M. Lamellar phase of a symmetric triblock copolymer. *Macromolecules* **27**, 187–192 (1994).
289. Watanabe, H. Slow Dielectric Relaxation of a Styrene-Isoprene-Styrene Triblock Copolymer with Dipole Inversion in the Middle Block: A Challenge to a Loop/Bridge Problem. *Macromolecules* **28**, 5006–5011 (1995).
290. Crescenzi, V., Manzini, G., Calzolari, G. & Borri, C. Thermodynamics of fusion of poly- $\beta$ -propiolactone and poly- $\epsilon$ -caprolactone. comparative analysis of the melting of aliphatic polylactone and polyester chains. *Eur. Polym. J.* **8**, 449–463 (1972).
291. Pham, X.-T., Thibault, F. & Lim, L.-T. Modeling and simulation of stretch blow molding of polyethylene terephthalate. *Polym. Eng. Sci.* **44**, 1460–1472 (2004).
292. Koziol, P., Liberda, D., Kwiatek, W. M. & Wrobel, T. P. Macromolecular Orientation in Biological Tissues Using a Four-Polarization Method in FT-IR Imaging. *Anal. Chem.* **92**, 13313–13318 (2020).

293. Jiang, Z. *et al.* Tensile Deformation of Oriented Poly( $\epsilon$ -caprolactone) and Its Miscible Blends with Poly(vinyl methyl ether). *Macromolecules* **46**, 6981–6990 (2013).
294. Chen, X., Dong, B., Wang, B., Shah, R. & Li, C. Y. Crystalline Block Copolymer Decorated, Hierarchically Ordered Polymer Nanofibers. *Macromolecules* **43**, 9918–9927 (2010).
295. Wang, X. *et al.* Poly( $\epsilon$ -caprolactone) Nanofibers with a Self-Induced Nanohybrid Shish-Kebab Structure Mimicking Collagen Fibrils. *Biomacromolecules* **14**, 3557–3569 (2013).
296. Formation and morphology of “shish-like” fibril crystals of aliphatic polyesters from the sheared melt |.
297. Jiang, Z., Fu, L., Sun, Y., Li, X. & Men, Y. Deformation-Induced Phase Separation in Blends of Poly( $\epsilon$ -caprolactone) with Poly(vinyl methyl ether). *Macromolecules* **44**, 7062–7065 (2011).
298. Haque, F. M. *et al.* Defining the Macromolecules of Tomorrow through Synergistic Sustainable Polymer Research. *Chem. Rev.* **122**, 6322–6373 (2022).
299. Garcia, J. M. & Robertson, M. L. The future of plastics recycling. *Science* **358**, 870–872 (2017).
300. Yu, Y. J., Kim, H., Chung, C.-M. & Chung, J. W. Damage-Detectable and Self-Healable Photoluminescent Dual Dynamic Supramolecular Networks. *ACS Appl. Polym. Mater.* **4**, 9103–9115 (2022).
301. Daniel Görl, Yevhen Hryshunin, Shuichi Haraguchi, Matthieu Wendling,<sup>1</sup> Sophia Thiele,<sup>1</sup> Giorgia Scetta,<sup>1</sup> Alexandre Simula,<sup>1</sup> Nicolas Candau,<sup>1,2</sup> Torne Tänzer,<sup>3</sup> Marianne Liebi,<sup>3</sup> & Christopher Plummer,<sup>1</sup> Holger Frauenrath<sup>1\*</sup>. Supramolecular Modification for High Performance Sustainable Polyesters.
302. Wong, S.-C., Baji, A. & Leng, S. Effect of fiber diameter on tensile properties of electrospun poly( $\epsilon$ -caprolactone). *Polymer* **49**, 4713–4722 (2008).
303. Koerner, H., Kelley, J. J. & Vaia, R. A. Transient Microstructure of Low Hard Segment Thermoplastic Polyurethane under Uniaxial Deformation. *Macromolecules* **41**, 4709–4716 (2008).
304. Selli, F., Erdoğan, U. H., Hufenus, R. & Perret, E. Mesophase in melt-spun poly( $\epsilon$ -caprolactone) filaments: Structure–mechanical property relationship. *Polymer* **206**, 122870 (2020).
305. Santos, R. G., Machovsky-Capuska, G. E. & Andrades, R. Plastic ingestion as an evolutionary trap: Toward a holistic understanding. *Science* **373**, 56–60 (2021).
306. Ncube, L. K., Ude, A. U., Ogunmuyiwa, E. N., Zulkifli, R. & Beas, I. N. Environmental Impact of Food Packaging Materials: A Review of Contemporary Development from Conventional Plastics to Polylactic Acid Based Materials. *Materials* **13**, 4994 (2020).
307. Buchholz, O. Global bioplastics production will more than triple within the next five years. *European Bioplastics e.V.* <https://www.european-bioplastics.org/global-bioplastics-production-will-more-than-triple-within-the-next-five-years/>.
308. Corneillie, S. & Smet, M. PLA architectures: the role of branching. *Polym. Chem.* **6**, 850–867 (2015).
309. Fetters, L., Lohse, D., Richter, D., Witten, T. & Zirkel, A. Connection Between Polymer Molecular-Weight, Density, Chain Dimensions, and Melt Viscoelastic Properties. *Macromolecules* **27**, 4639–4647 (1994).
310. Kim, J., Zhang, G., Shi, M. & Suo, Z. Fracture, fatigue, and friction of polymers in which entanglements greatly outnumber cross-links. *Science* **374**, 212–216 (2021).
311. Sogah, D. Y. & Rathore, O. Nanostructure Formation through  $\beta$ -Sheet Self-Assembly in Silk-Based Materials. *Macromolecules* **34**, 1477–1486 (2001).
312. Davies, R. P. W. *et al.* Self-assembling  $\beta$ -Sheet Tape Forming Peptides. *Supramol. Chem.* **18**, 435–443 (2006).
313. Auras, R., Harte, B. & Selke, S. An overview of polylactides as packaging materials. *Macromol. Biosci.* **4**, 835–864 (2004).
314. Lim, L.-T., Auras, R. & Rubino, M. Processing technologies for poly(lactic acid). *Prog. Polym. Sci.* **33**, 820–852 (2008).
315. Ma, B. *et al.* Effect of poly(lactic acid) crystallization on its mechanical and heat resistance performances. *Polymer* **212**, 123280 (2021).
316. Mehrabi Mazidi, M., Edalat, A., Berahman, R. & Hosseini, F. S. Highly-Toughened Polylactide- (PLA-) Based Ternary Blends with Significantly Enhanced Glass Transition and Melt Strength: Tailoring the Interfacial Interactions, Phase Morphology, and Performance. *Macromolecules* **51**, 4298–4314 (2018).
317. Narmon, A. S. *et al.* Boosting PLA melt strength by controlling the chirality of co-monomer incorporation. *Chem. Sci.* **12**, 5672–5681 (2021).
318. Watts, A. & Hillmyer, M. A. Aliphatic Polyester Thermoplastic Elastomers Containing Hydrogen-Bonding Ureidopyrimidinone Endgroups. *Biomacromolecules* **20**, 2598–2609 (2019).
319. Delgado, P. A. & Hillmyer, M. A. Combining block copolymers and hydrogen bonding for poly(lactide) toughening. *RSC Adv.* **4**, 13266–13273 (2014).

320. Roosma, J., Mes, T., Leclère, P., Palmans, A. R. A. & Meijer, E. W. Supramolecular Materials from Benzene-1,3,5-tricarboxamide-Based Nanorods. *J. Am. Chem. Soc.* **130**, 1120–1121 (2008).
321. Michael Giffin, Christopher Plummer Michael Giffin, Yevhen Hryshunin, Daniel Görl, & Holger Frauenrath. Additive Design for Polyethylene-Based Supramolecular Materials.
322. Farah, S., Anderson, D. G. & Langer, R. Physical and mechanical properties of PLA, and their functions in widespread applications - A comprehensive review. *Adv. Drug Deliv. Rev.* **107**, 367–392 (2016).



# 9. Appendix

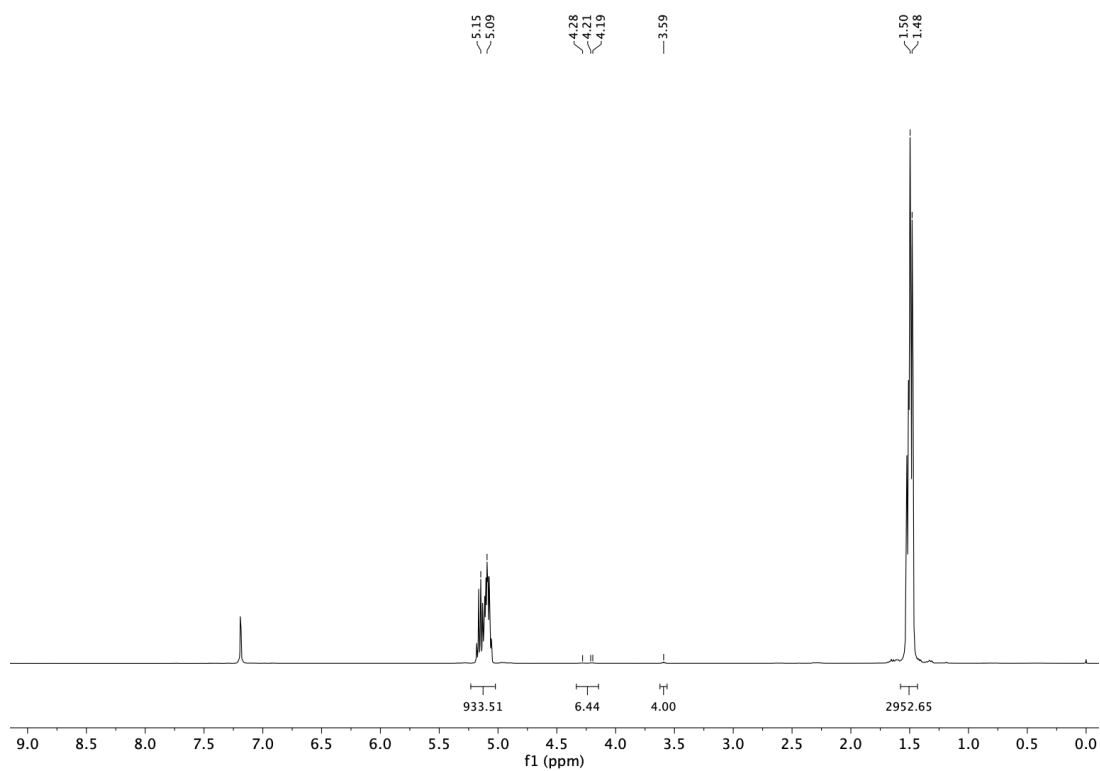


Figure 73.  $^1\text{H}$  NMR spectrum ( $\text{CDCl}_3$ , 400 MHz) of PDLLA

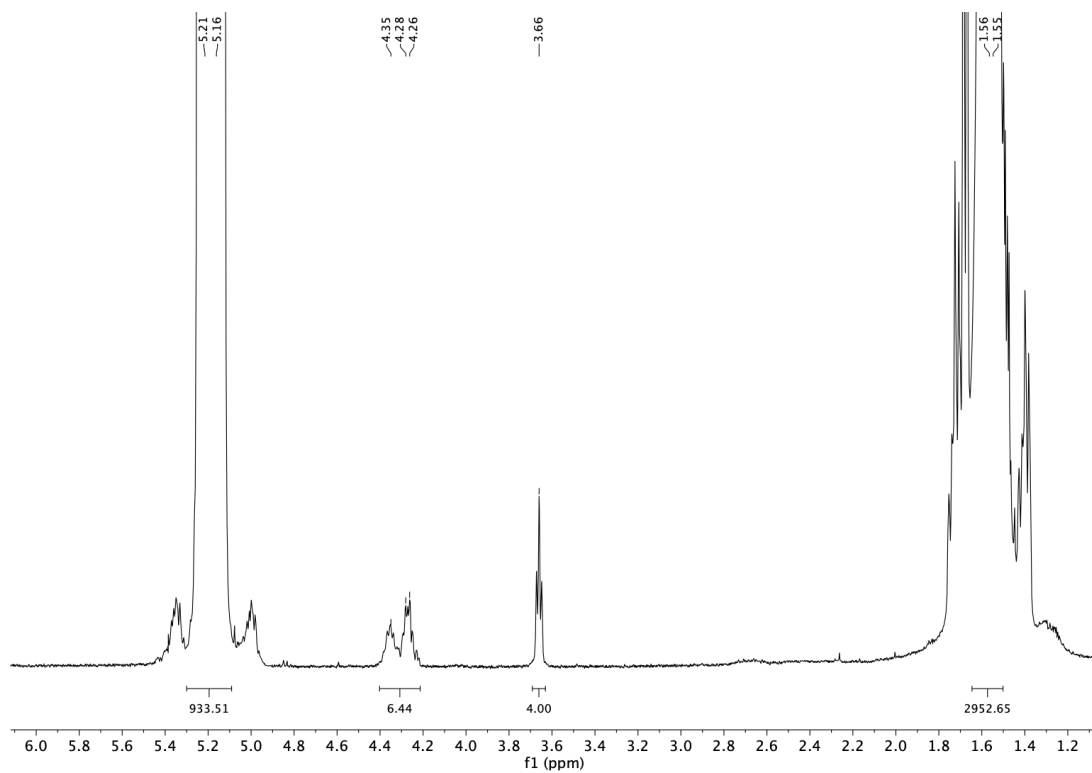
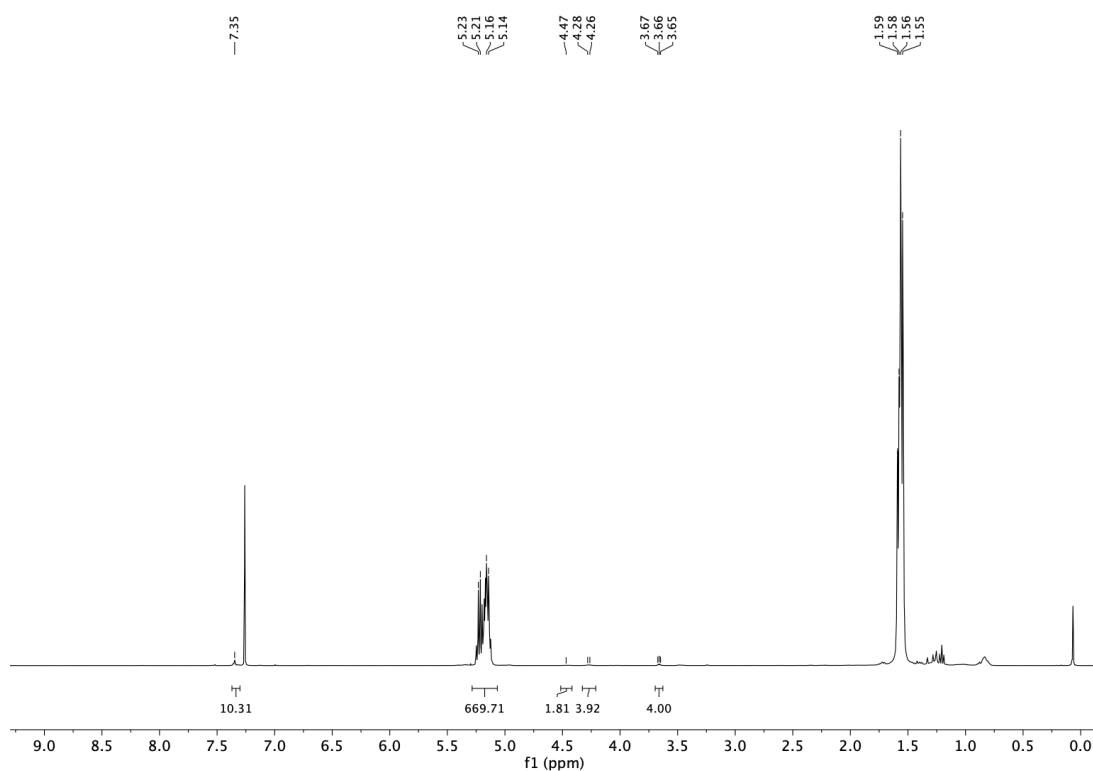
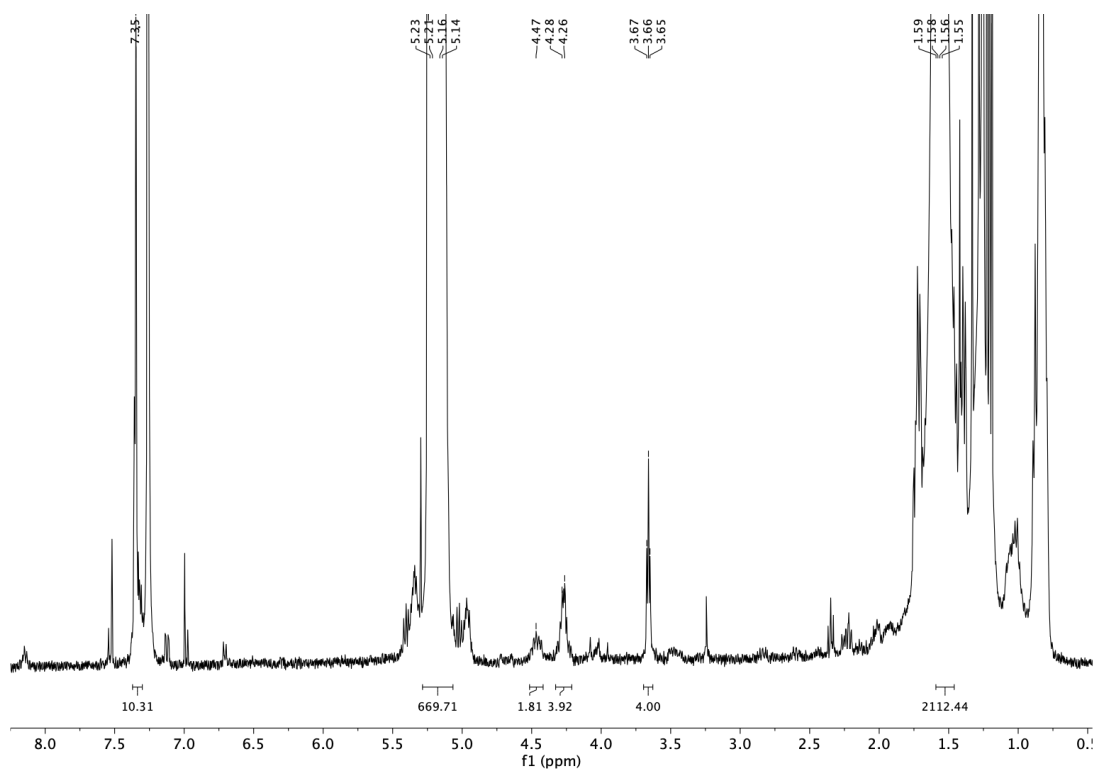


Figure 74.  $^1\text{H}$  NMR spectrum ( $\text{CDCl}_3$ , 400 MHz) of PDLLA, zoomed in



**Figure 75.**  $^1\text{H}$  NMR spectrum ( $\text{CDCl}_3$ , 400 MHz) of **PDLLA-Cbz**



$^1\text{H}$  NMR spectrum ( $\text{CDCl}_3$ , 400 MHz) of **PDLLA-Cbz**, zoomed in

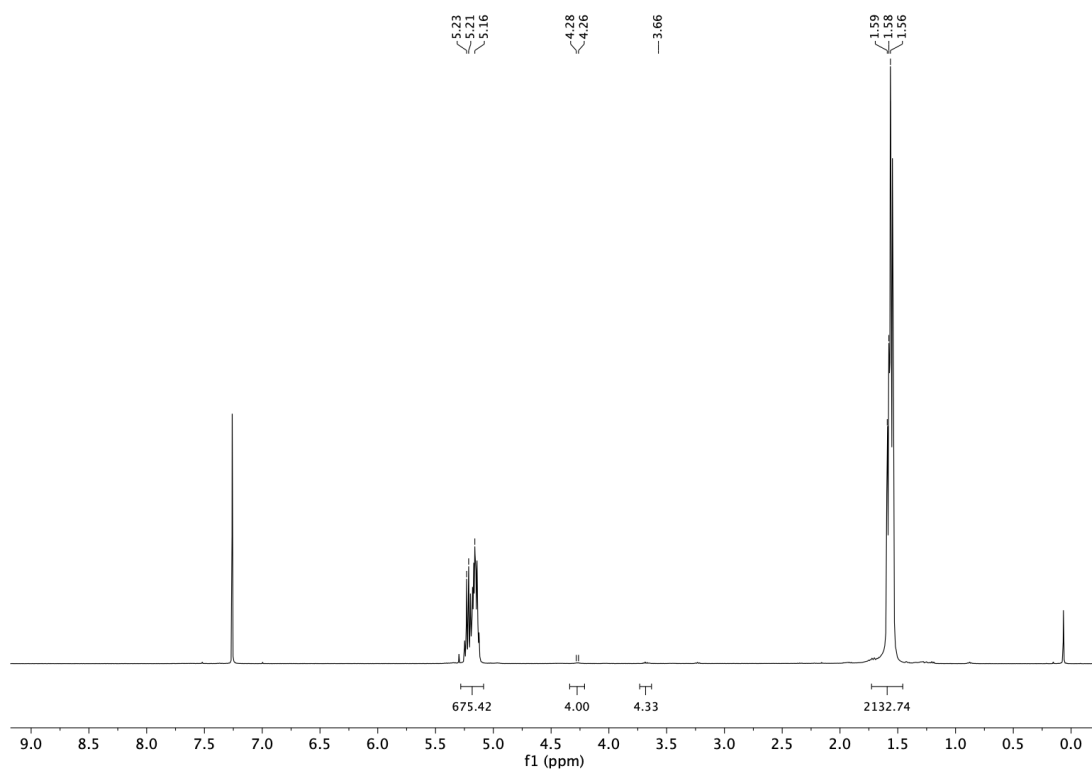


**Figure 76.**  $^1\text{H}$  NMR spectrum ( $\text{CDCl}_3$ , 400 MHz) of **PDLLA-NH<sub>2</sub>**

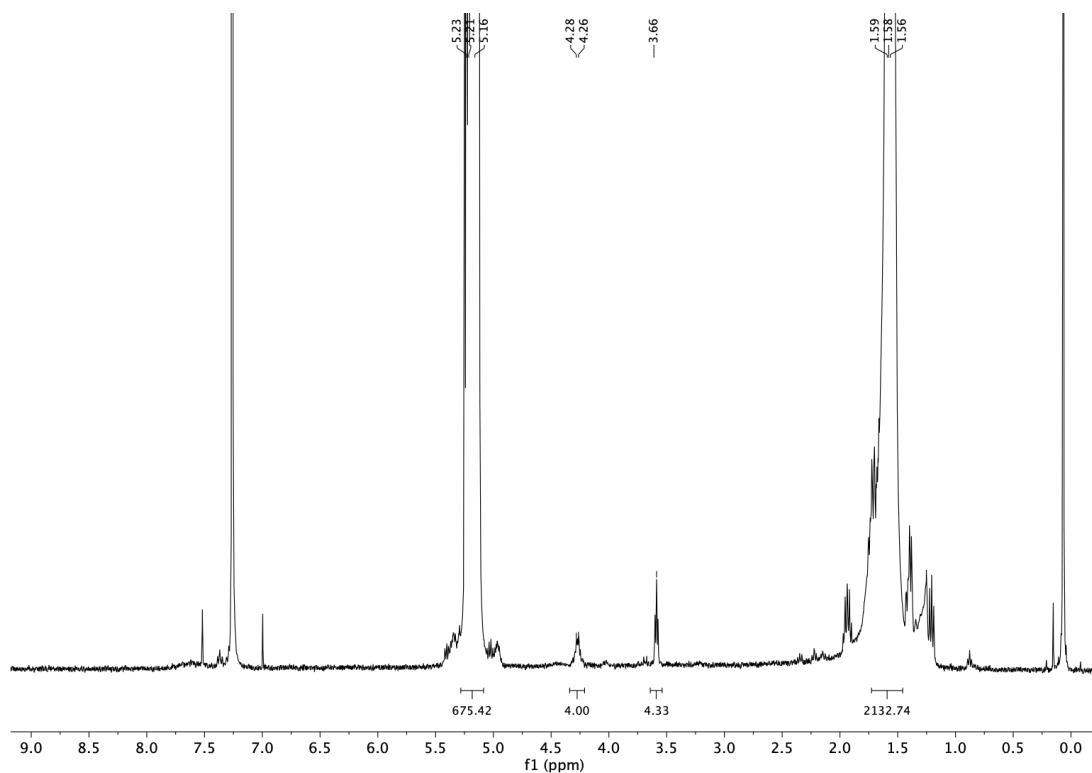


**Figure 77.**  $^1\text{H}$  NMR spectrum ( $\text{CDCl}_3$ , 400 MHz) of **PDLLA-NH<sub>2</sub>**, zoomed in

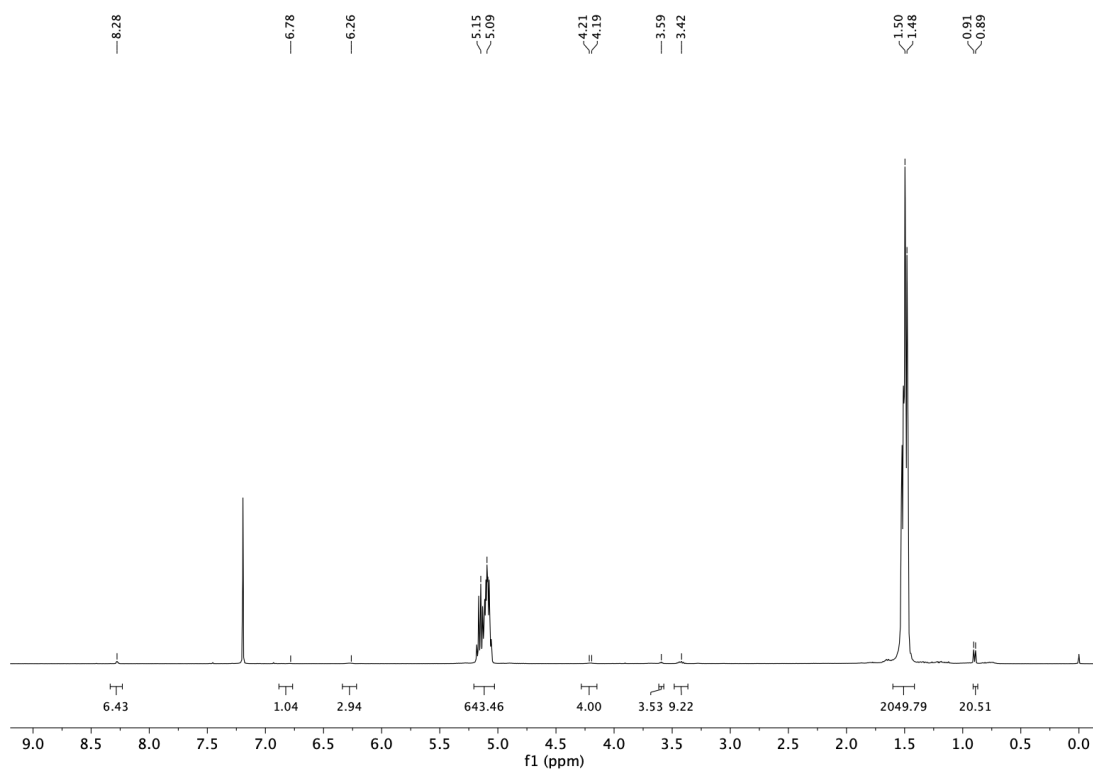


**Figure 78.**  $^1\text{H}$  NMR spectrum ( $\text{CDCl}_3$ , 400 MHz) of PDLLA-B5:

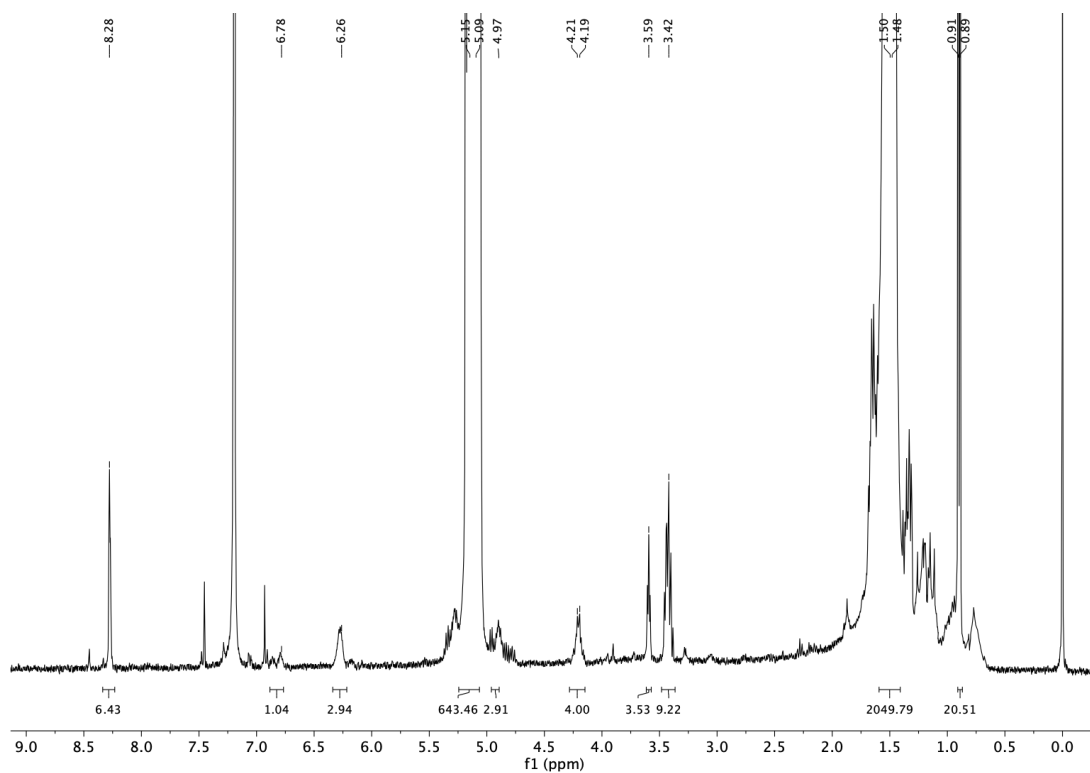


**Figure 79.**  $^1\text{H}$  NMR spectrum ( $\text{CDCl}_3$ , 400 MHz) of PDLLA-B5 zoomed in

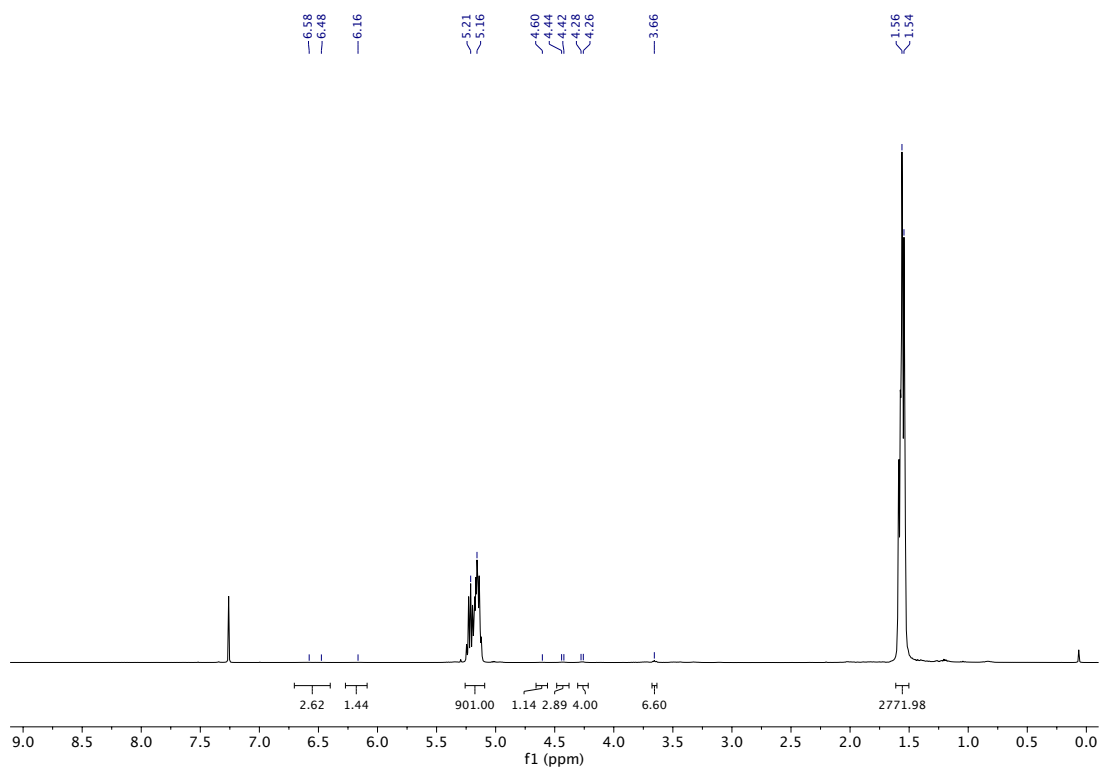


**Figure 80.**  $^1\text{H}$  NMR spectrum ( $\text{CDCl}_3$ , 400 MHz) of PDLLA-A

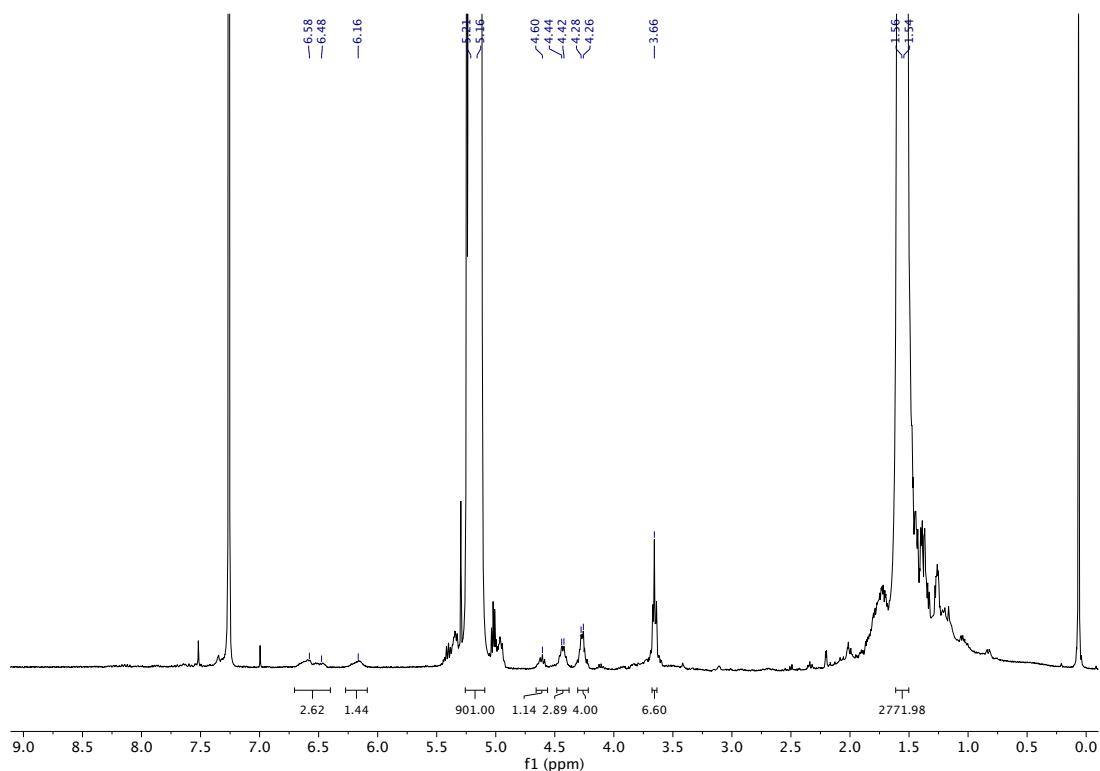


**Figure 81.**  $^1\text{H}$  NMR spectrum ( $\text{CDCl}_3$ , 400 MHz) of PDLLA-A zoomed in

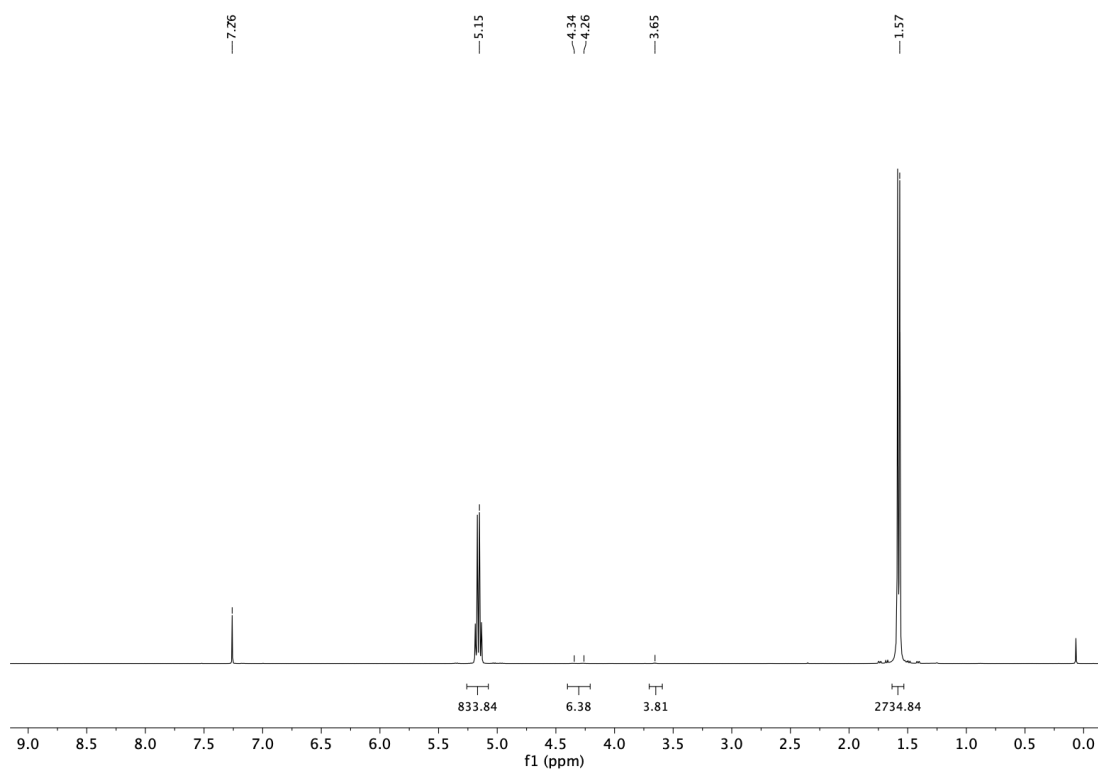


**Figure 82.**  $^1\text{H}$  NMR spectrum ( $\text{CDCl}_3$ , 400 MHz) of **PLLA**

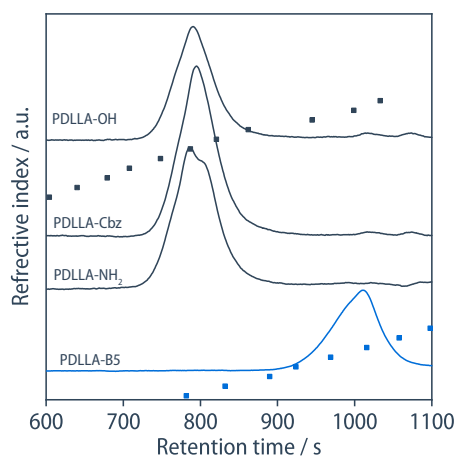


**Figure 83.** GPC (THF, 40 °C) of **PDLLA**, **PDLLA-Cbz**, **PDLLA-NH<sub>2</sub>** and **PDLLA-B5** with corresponding calibration data (black: 2 columns PLgel 5  $\mu\text{m}$  MIXED-C Analytical; blue: 2 columns PSS SDV analytical linear XL)

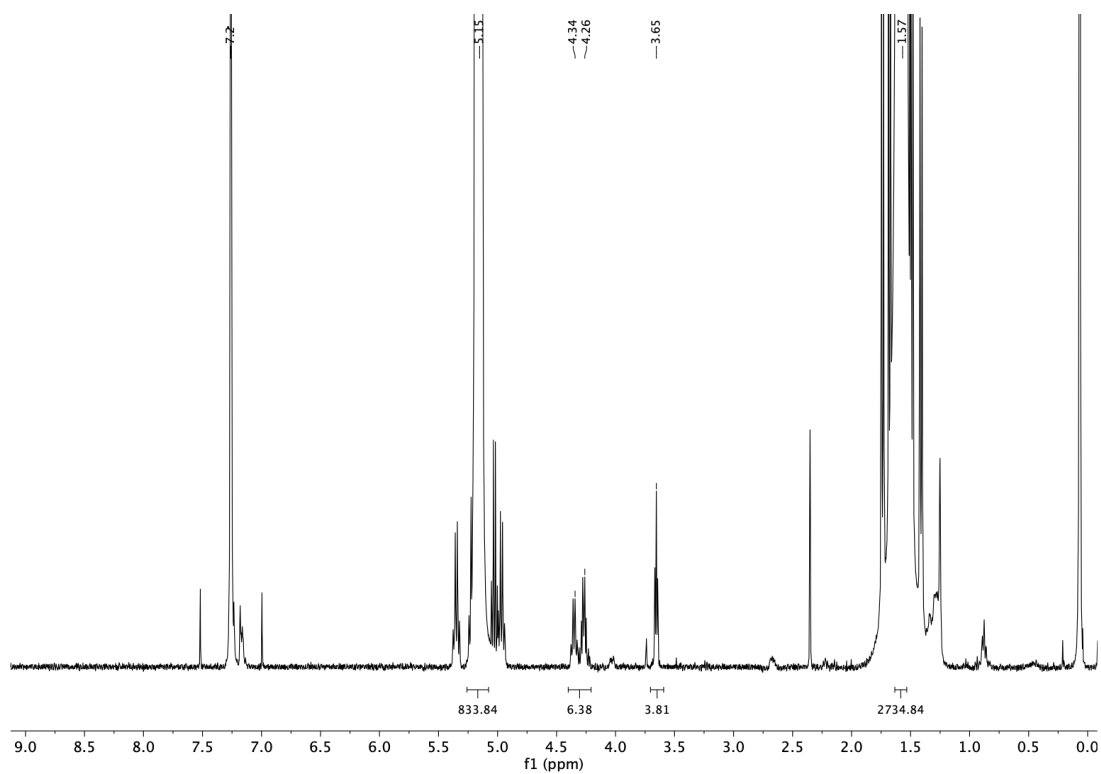


**Figure 84.**  $^1\text{H}$  NMR spectrum ( $\text{CDCl}_3$ , 400 MHz) of PLLA zoomed in

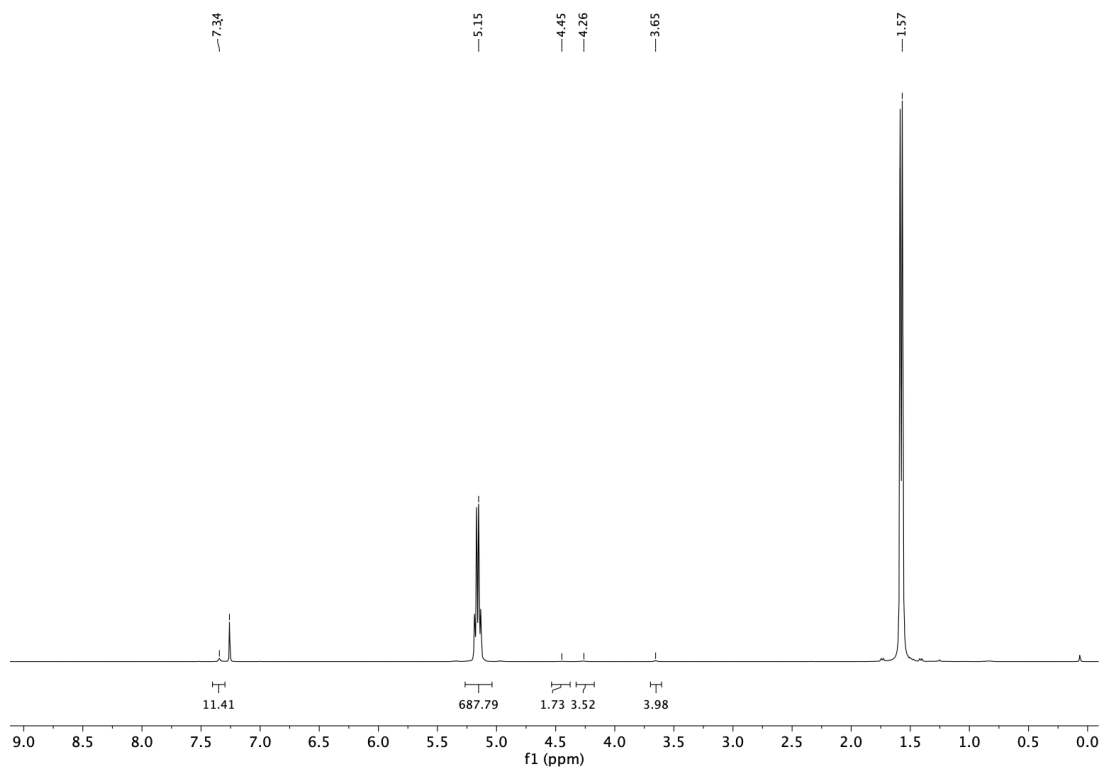


**Figure 85.**  $^1\text{H}$  NMR spectrum ( $\text{CDCl}_3$ , 400 MHz) of PLLA-Cbz

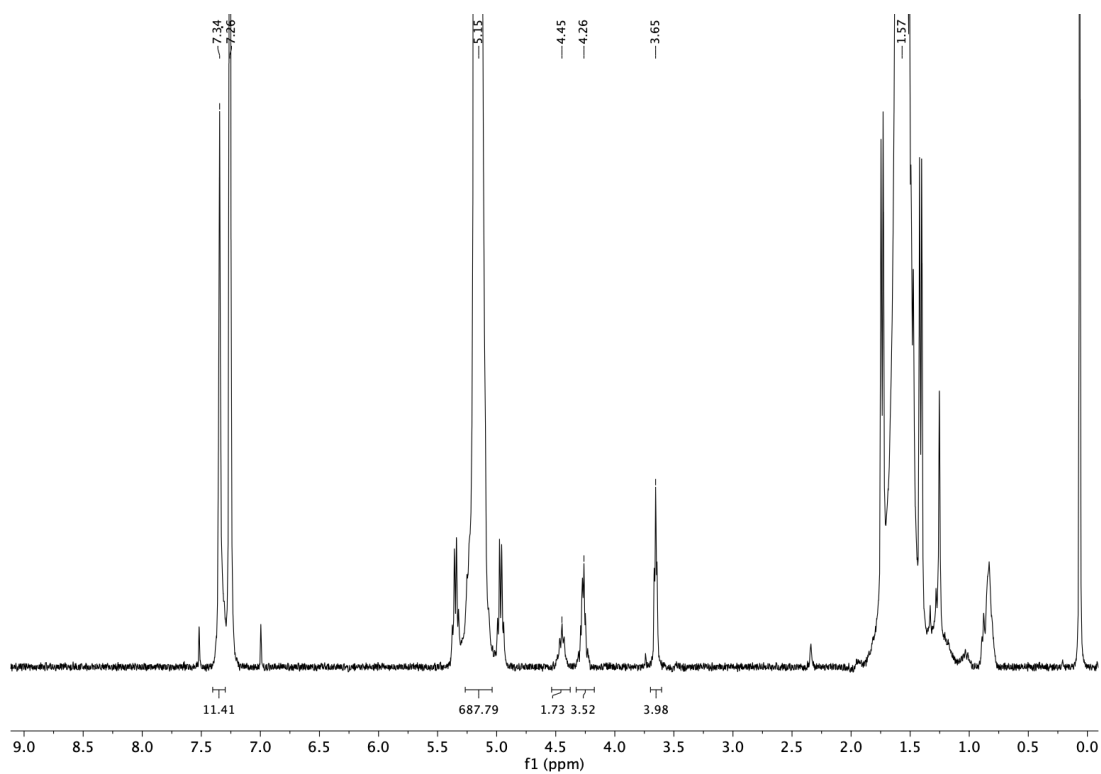


**Figure 86.**  $^1\text{H}$  NMR spectrum ( $\text{CDCl}_3$ , 400 MHz) of **PLLA-Cbz** zoomed in

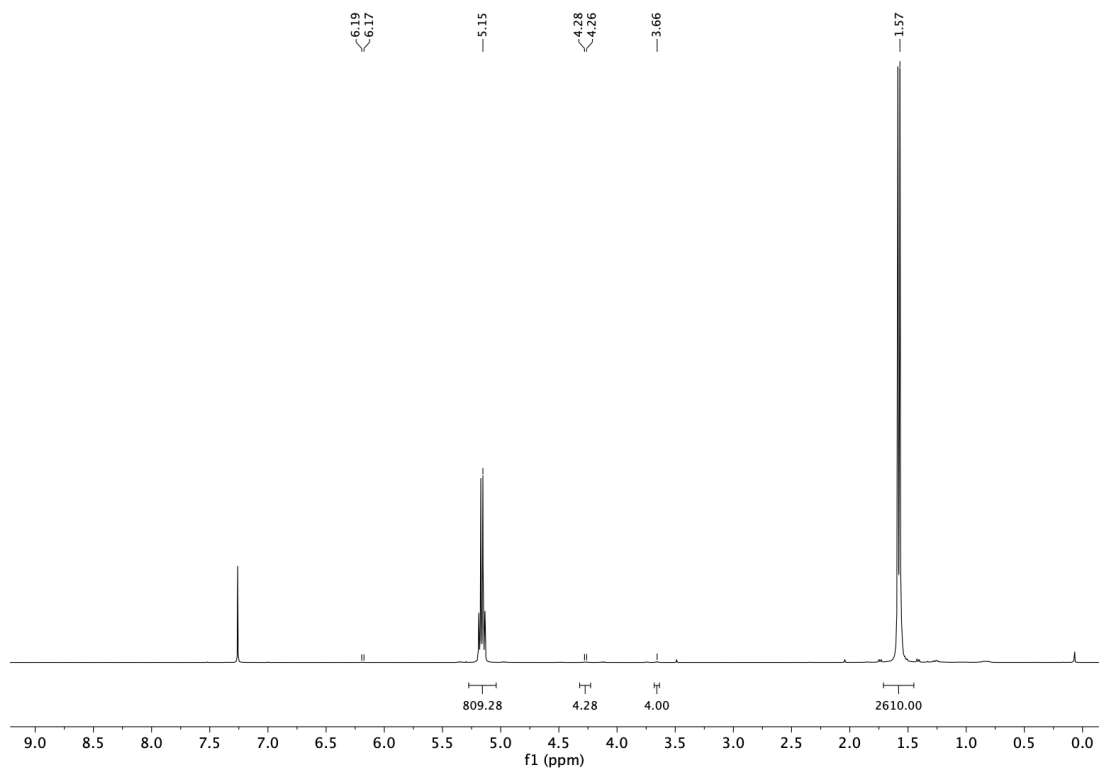


**Figure 87.**  $^1\text{H}$  NMR spectrum ( $\text{CDCl}_3$ , 400 MHz) of **PLLA-NH<sub>2</sub>**



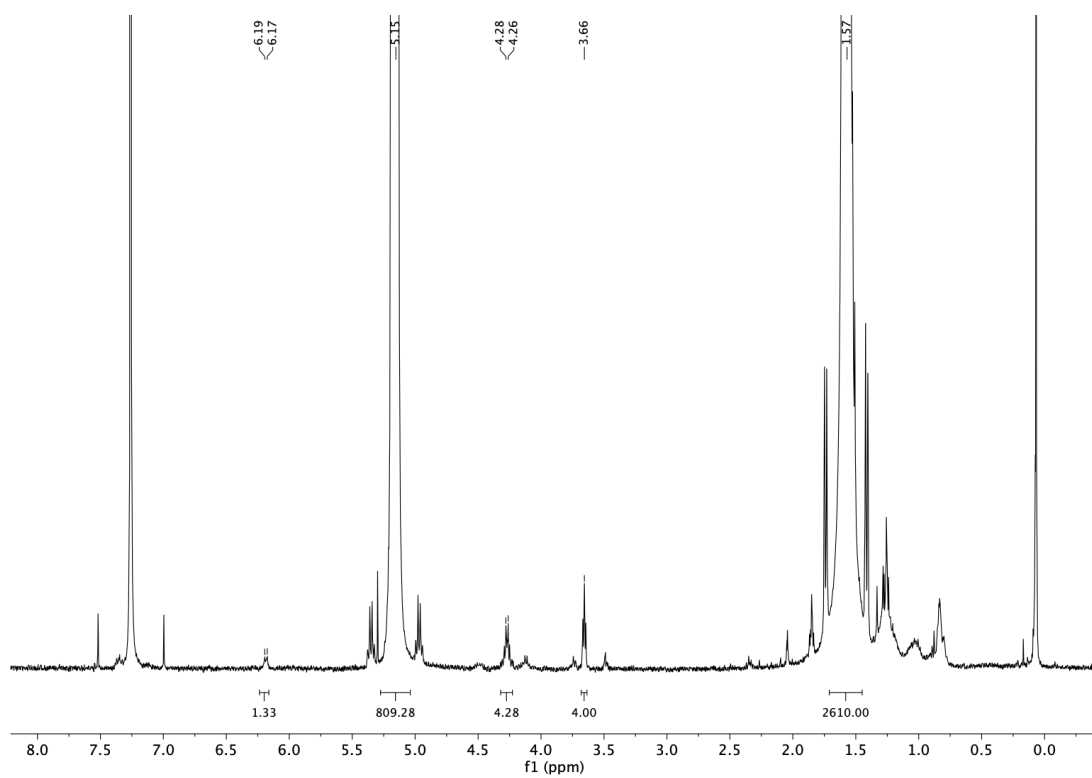


**Figure 88.**  $^1\text{H}$  NMR spectrum ( $\text{CDCl}_3$ , 400 MHz) of PLLA- $\text{NH}_2$  zoomed in

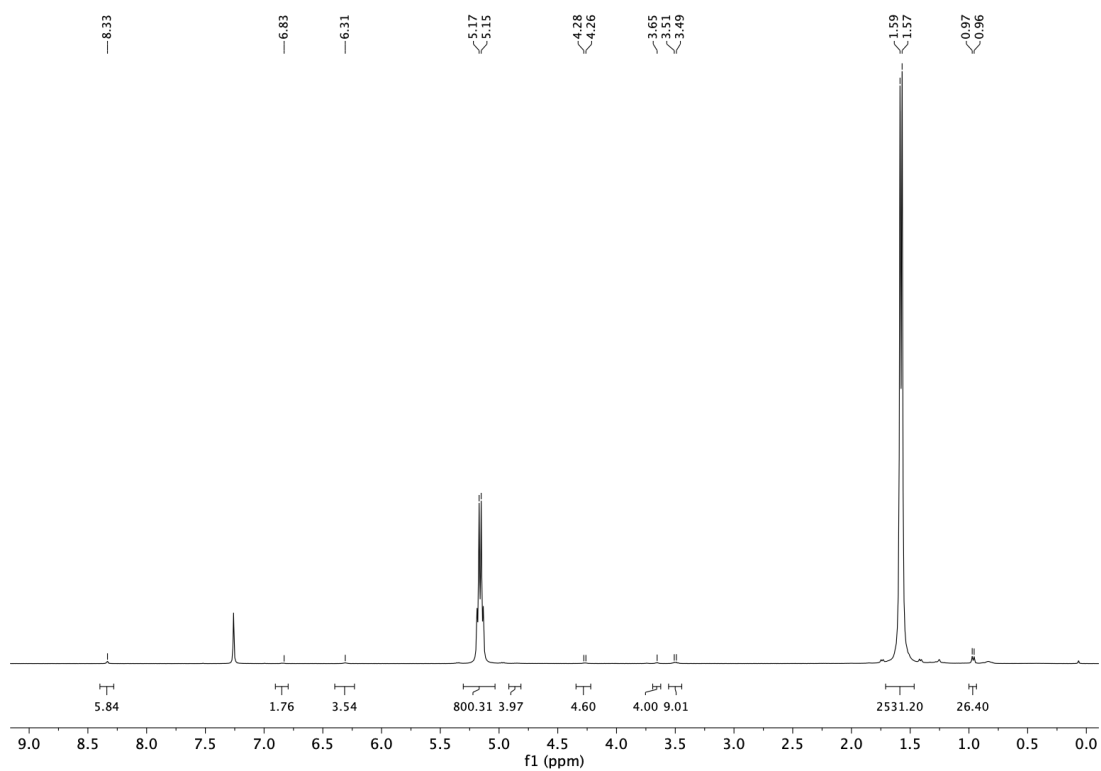


**Figure 89.**  $^1\text{H}$  NMR spectrum ( $\text{CDCl}_3$ , 400 MHz) of PLLA-B5

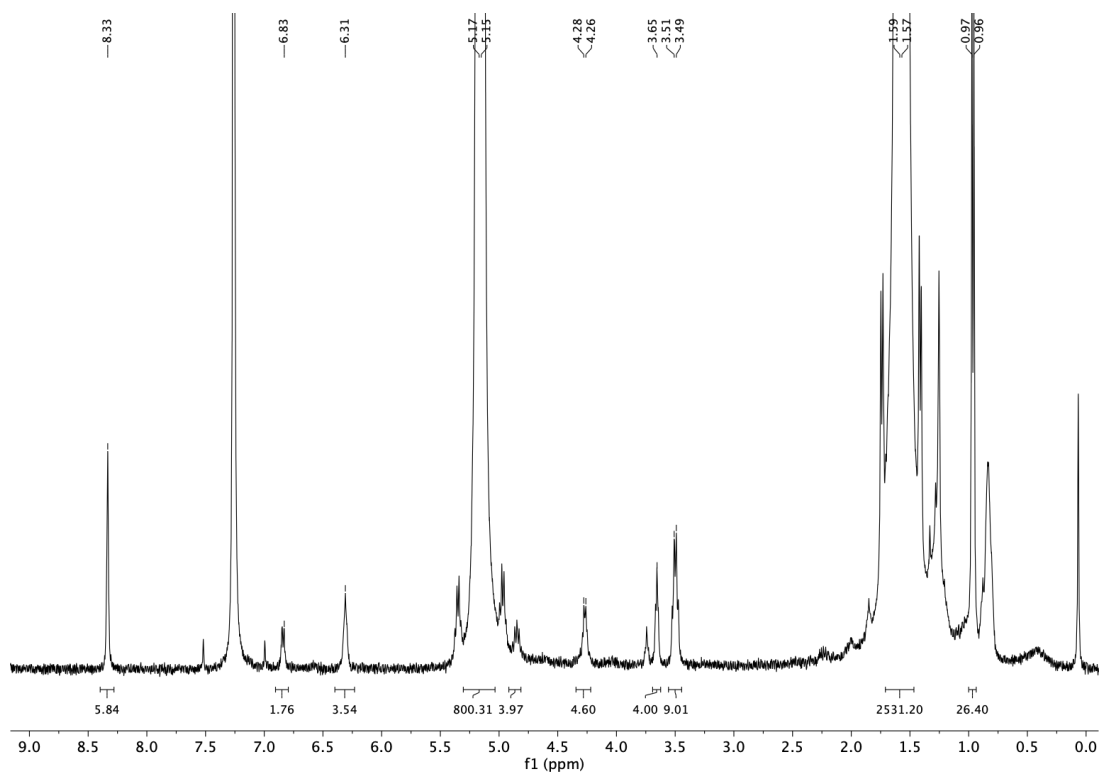


**Figure 90.**  $^1\text{H}$  NMR spectrum ( $\text{CDCl}_3$ , 400 MHz) of PLLA-B5 zoomed in

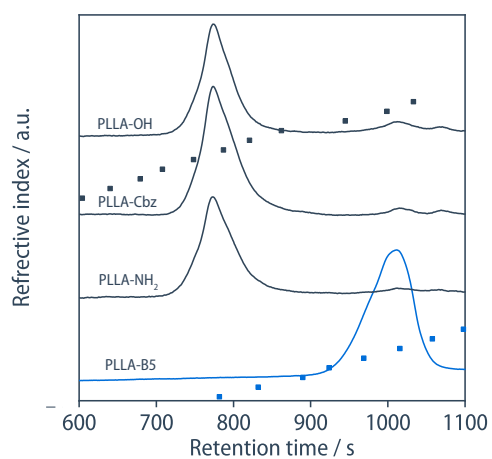


**Figure 91.** GPC (THF, 40 °C) of **PLLA**, **PLLA-Cbz**, **PLLA-NH<sub>2</sub>** and **PLLA-B5** with corresponding calibration data (black: 2 columns PLgel 5 μm MIXED-C Analytical; blue: 2 columns PSS SDV analytical linear XL)

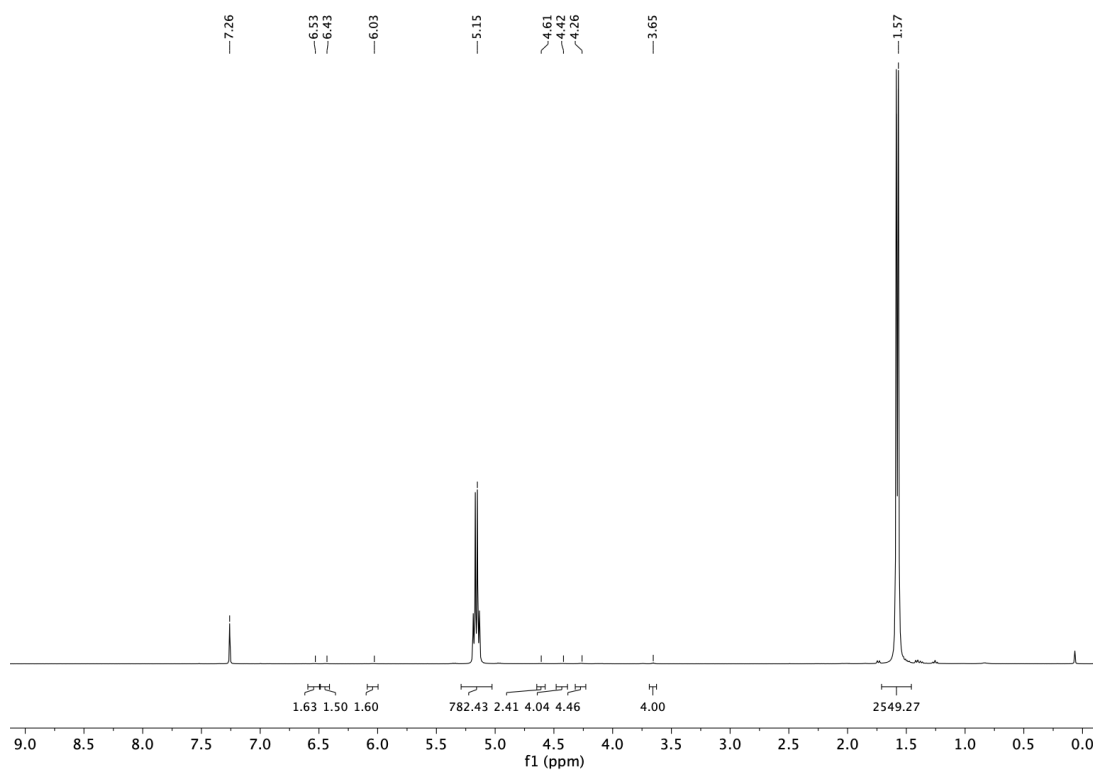


**Figure 92.** <sup>1</sup>H NMR spectrum (CDCl<sub>3</sub>, 400 MHz) of **PLLA-A**

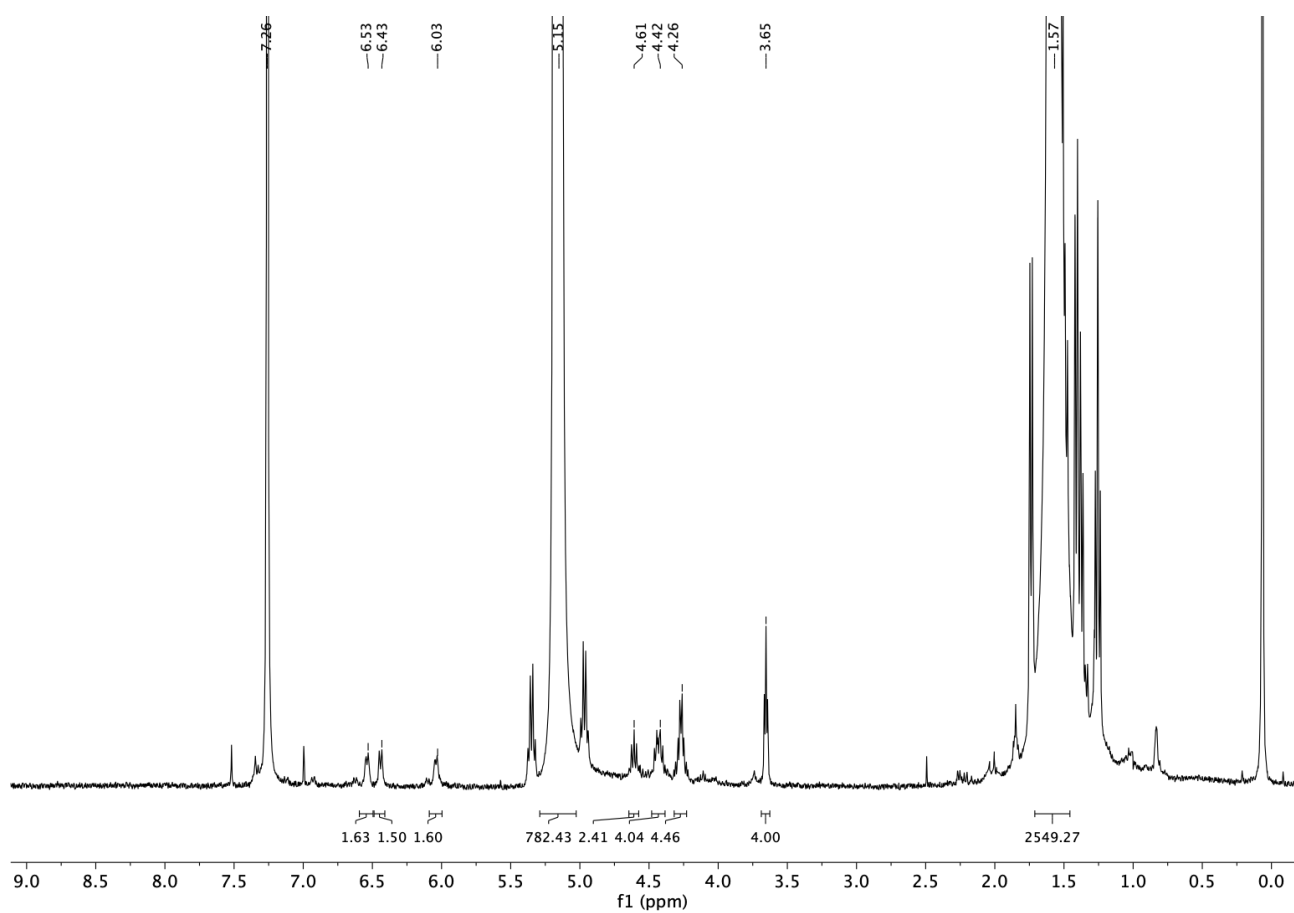


**Figure 93.**  $^1\text{H}$  NMR spectrum ( $\text{CDCl}_3$ , 400 MHz) of PLLA-A zoomed in

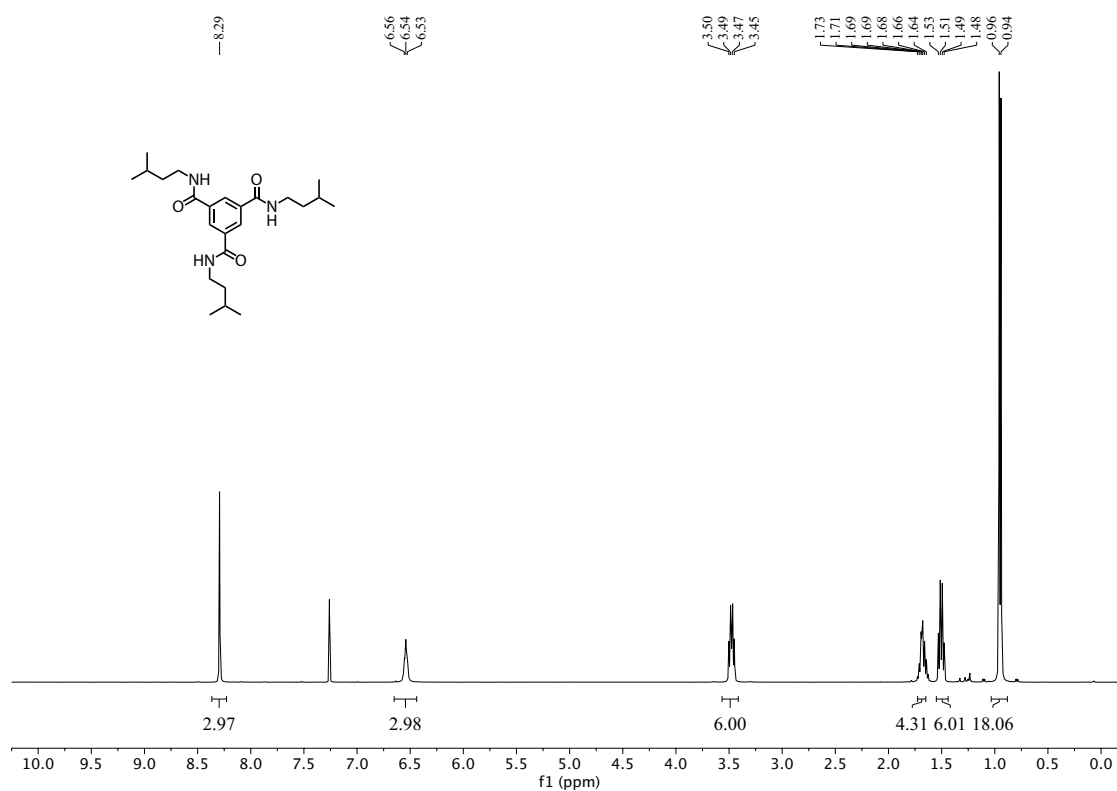


**Figure 94.**  $^1\text{H}$  NMR spectrum ( $\text{CDCl}_3$ , 400 MHz) of N,N,N-Tri(3-methylbutyl) benzene-1,3,5-tricarboxamide (B5)

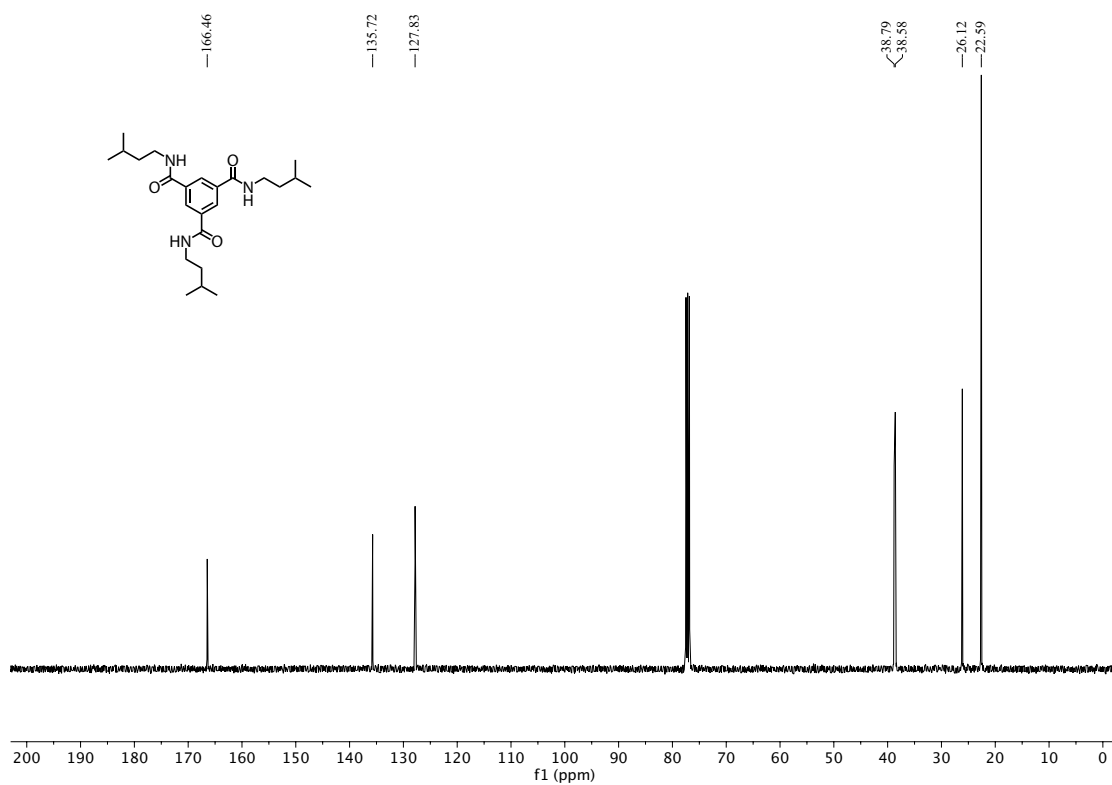


**Figure 95.**  $^{13}\text{C}$  NMR spectrum ( $\text{CDCl}_3$ , 100 MHz) of *N,N,N*-Tri(3-methylbutyl) benzene-1,3,5-tricarboxamide (**B5**)

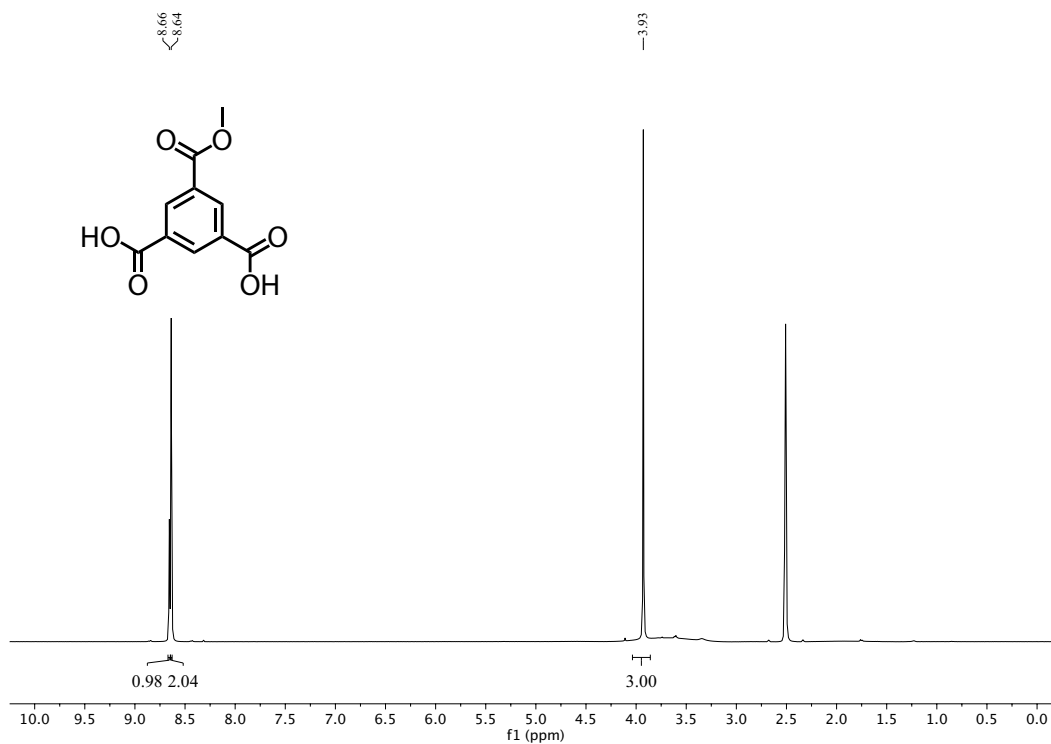


**Figure 96.**  $^1\text{H}$  NMR spectrum ( $\text{DMSO}-d_6$ , 400 MHz) of 5-methoxycarbonylbenzene-1,3-dicarboxylic acid (**1**)

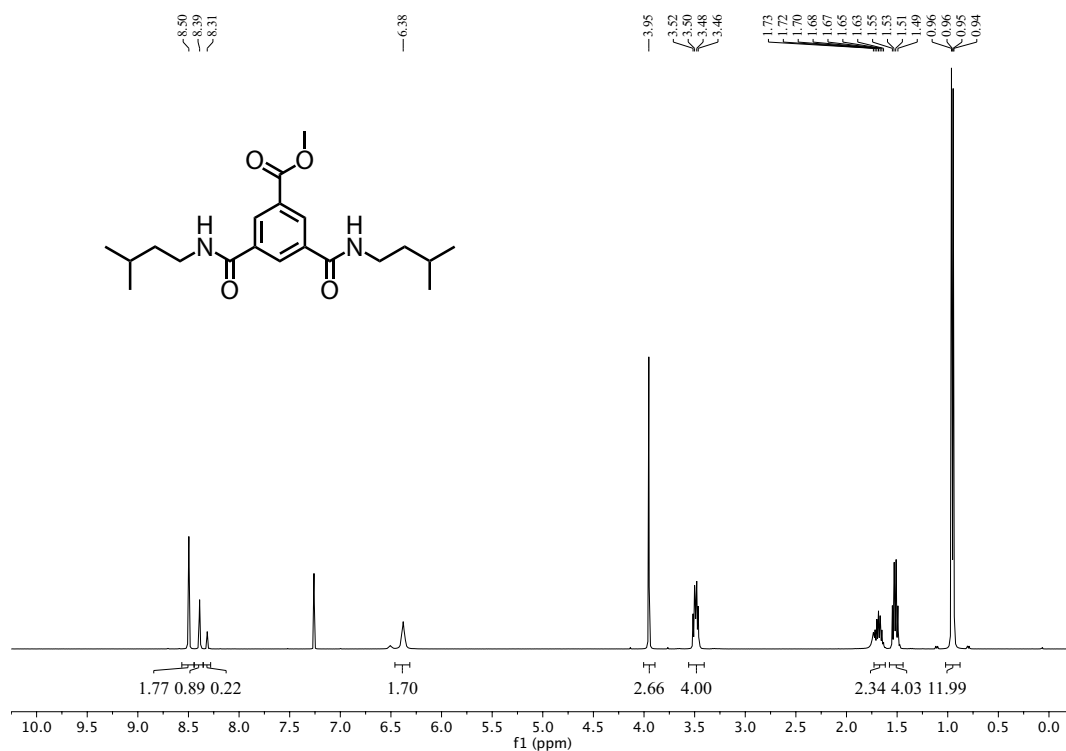


Figure 97. <sup>1</sup>H NMR spectrum (CDCl<sub>3</sub>, 400 MHz) of methyl 3,5-bis(3-methylbutylcarbamoyl)benzoate (2)

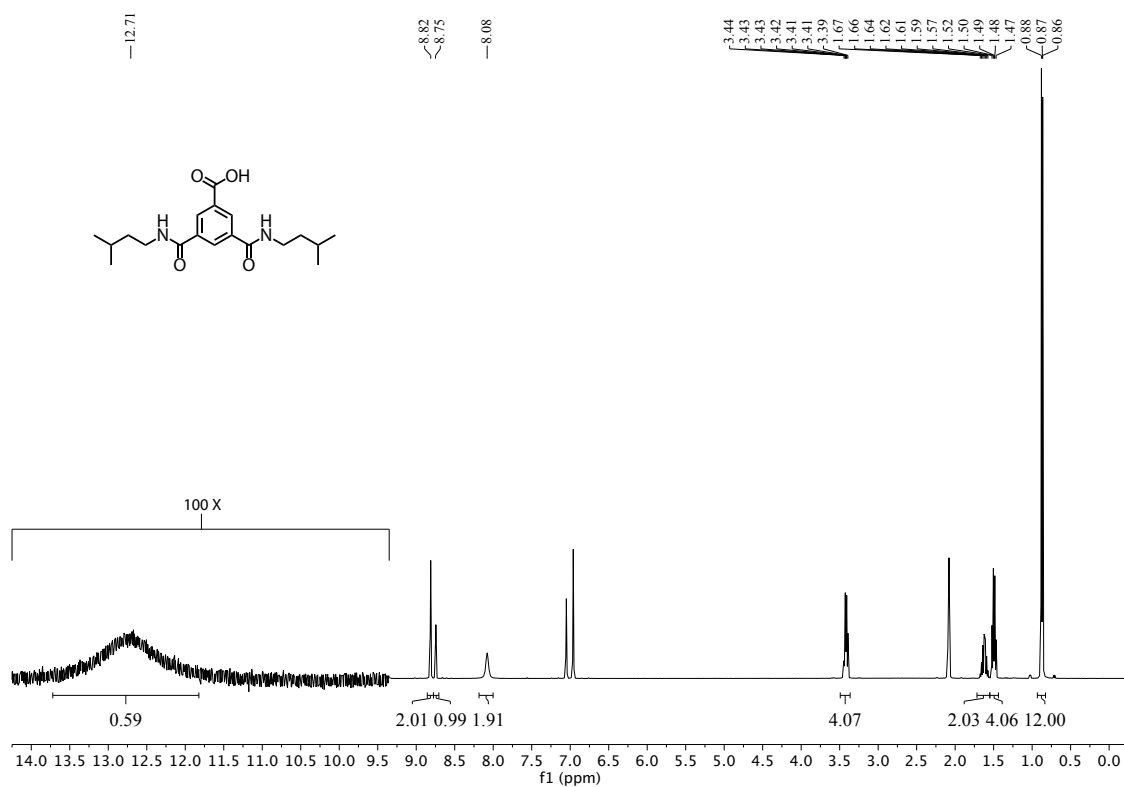
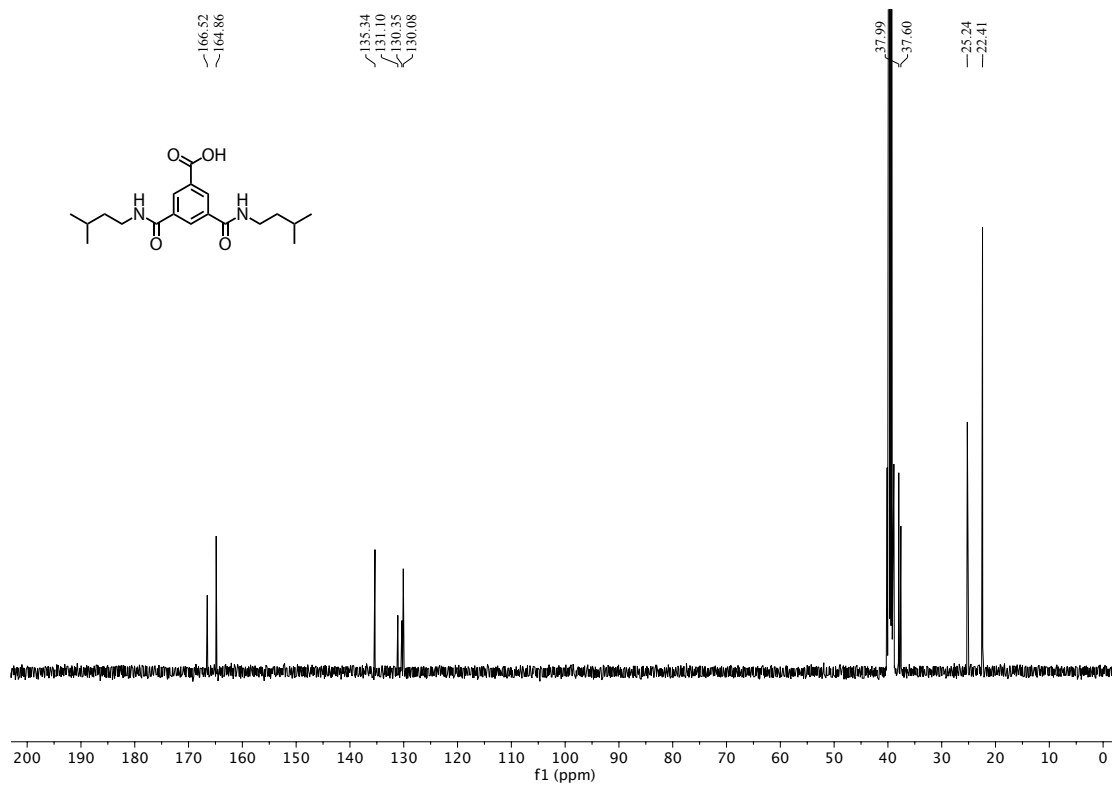
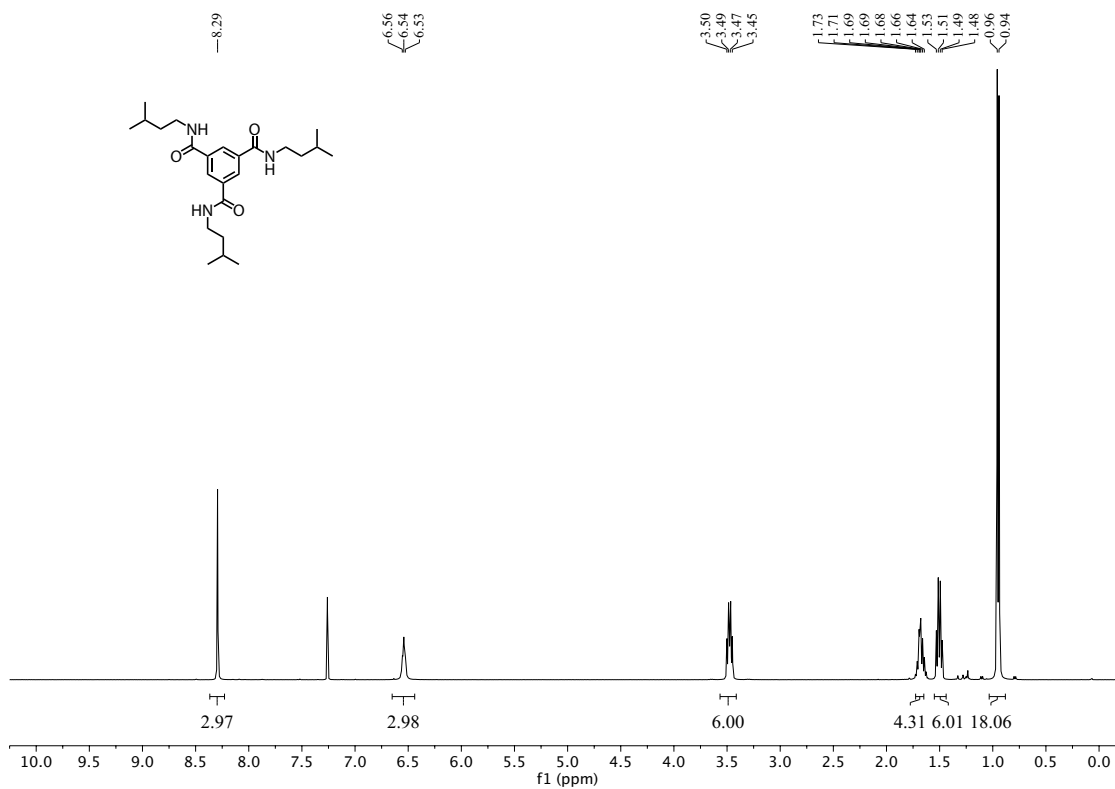


Figure 98. <sup>1</sup>H NMR spectrum (Tol-*d*<sub>8</sub>, 400 MHz, 375 K) of 3,5-bis(3-methylbutylcarbamoyl)benzoic acid (3)



**Figure 99.**  $^{13}\text{C}$  NMR spectrum ( $\text{DMSO-}d_6$ , 100 MHz) of 3,5-bis(3-methylbutylcarbamoyl)benzoic acid (3)



**Figure 100.**  $^1\text{H}$  NMR spectrum ( $\text{CDCl}_3$ , 400 MHz) of N,N,N-Tri(3-methylbutyl) benzene-1,3,5-tricarboxamide (B5)

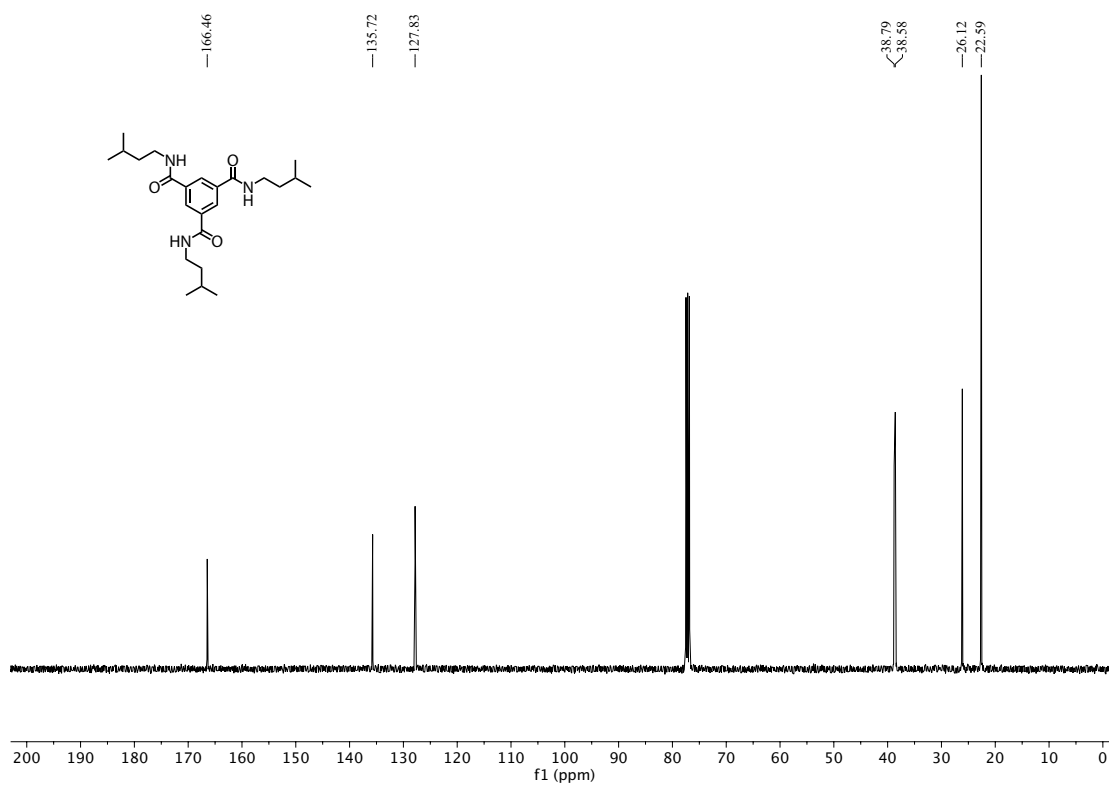


**Figure 101.**  $^{13}\text{C}$  NMR spectrum (CDCl<sub>3</sub>, 100 MHz) of *N,N*-Tri(3-methylbutyl) benzene-1,3,5-tricarboxamide (B5)

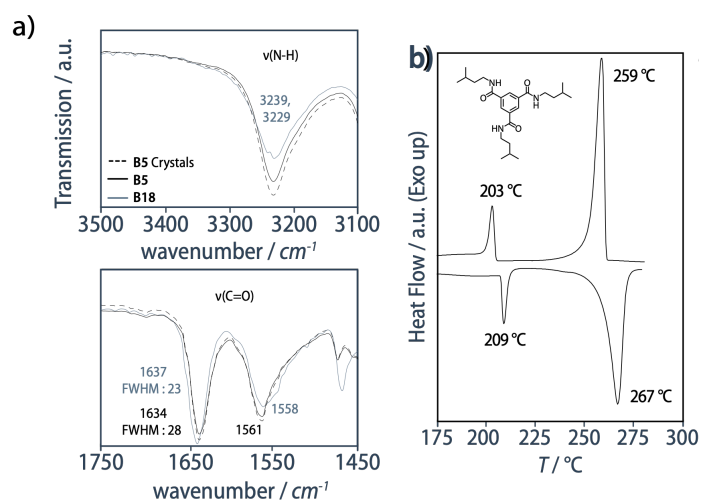


**Figure 102.** a) FT-IR spectroscopy and b) DSC scan of B5



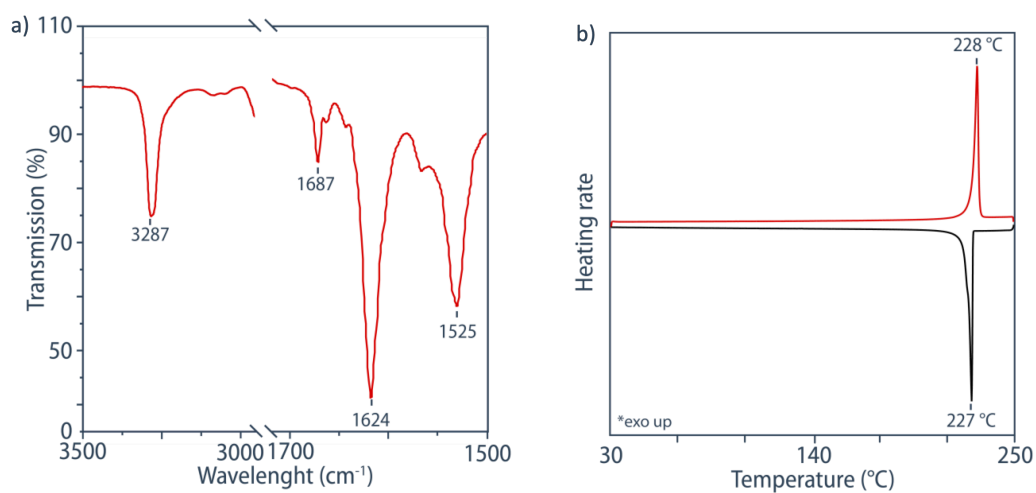


**Figure 103.** a) Infrared spectrum of **A8** showing the characteristic bands of antiparallel  $\beta$ -sheets; b) first cooling and second heating DSC scans of **A8** performed at 10 °C/min between 30 °C and 250 °C.

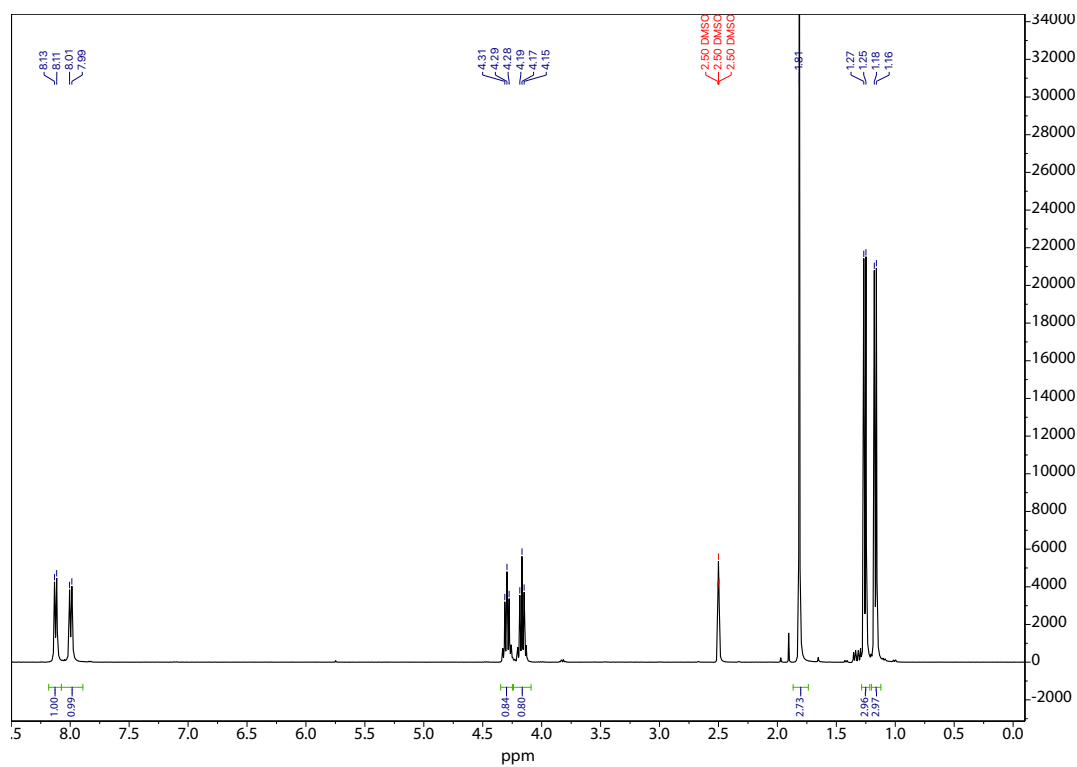


**Figure 104.**  $^1\text{H}$  NMR (400 MHz,  $\text{DMSO-d}_6$ ) of **7**.

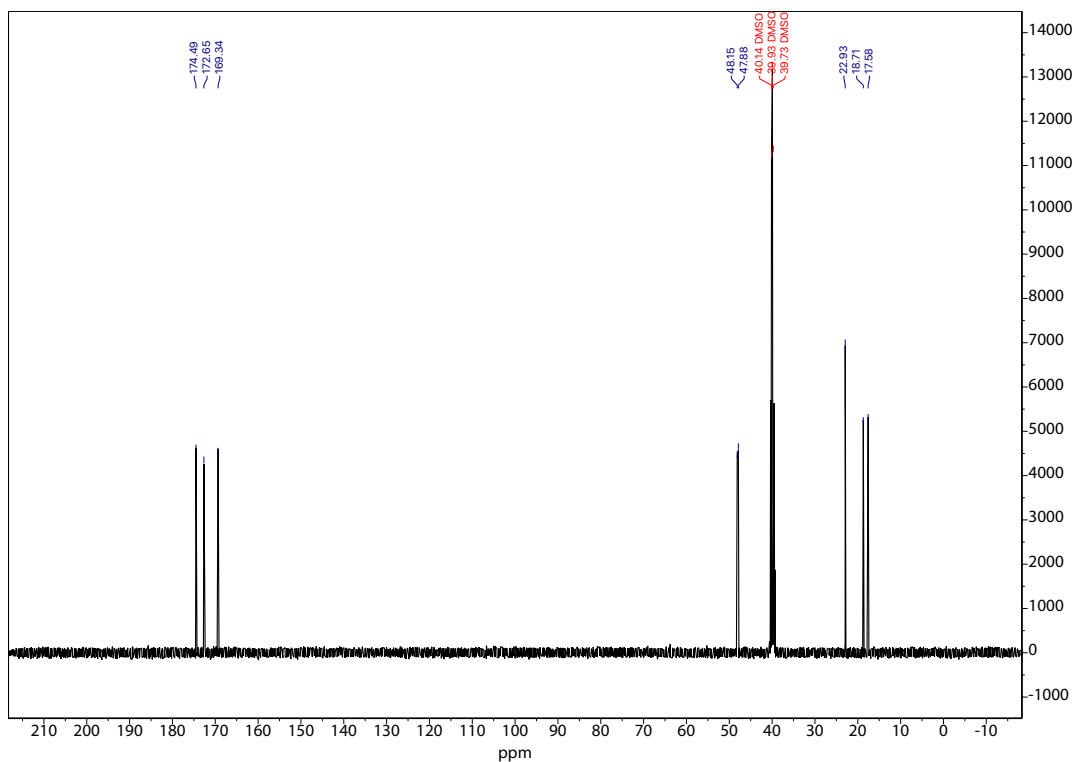


Figure 105.  $^{13}\text{C}$  NMR (400 MHz,  $\text{DMSO-d}_6$ ) of 7.

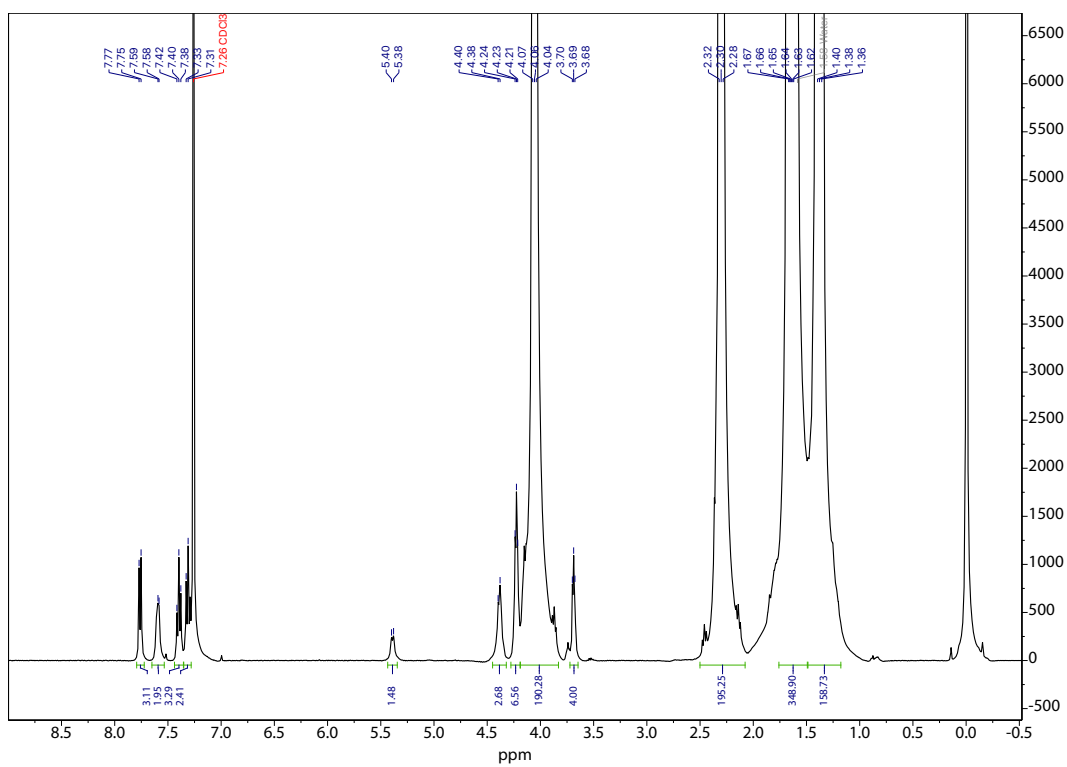


Figure 106.  $^1\text{H}$  NMR (400 MHz,  $\text{DMSO-d}_6$ ) of 8

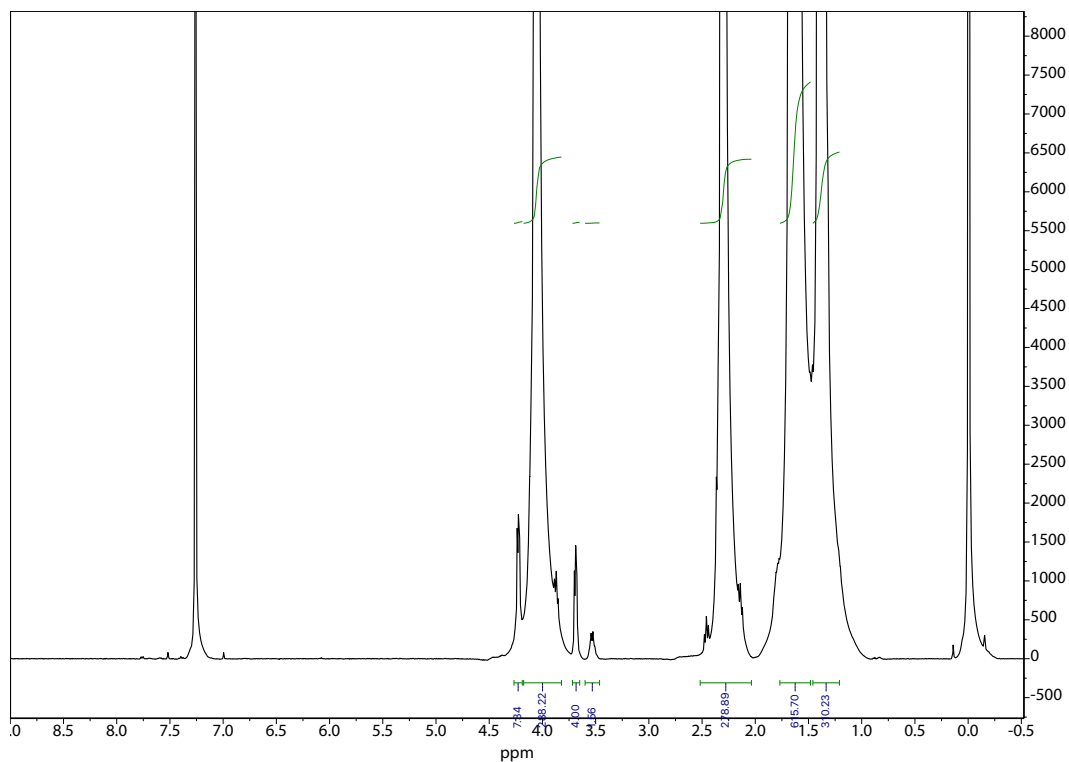


Figure 107. <sup>1</sup>H NMR (400 MHz, DMSO-d<sub>6</sub>) of **9**

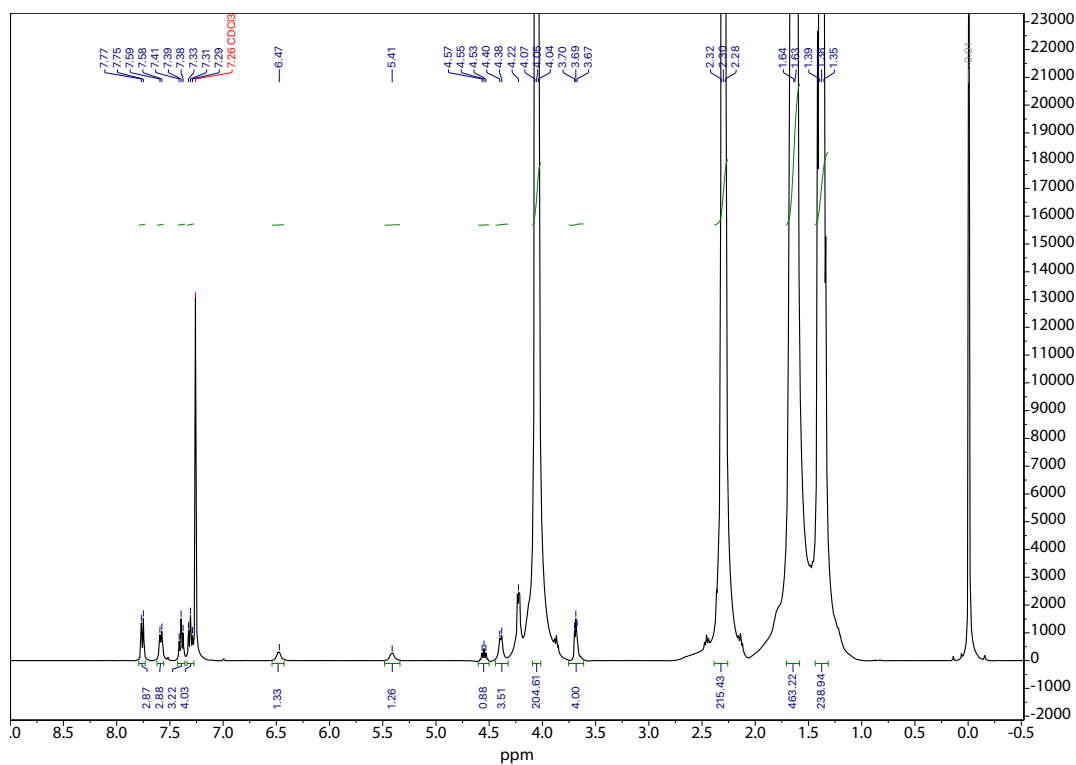
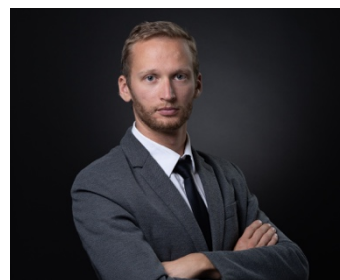


Figure 108. <sup>1</sup>H NMR (400 MHz, DMSO-d<sub>6</sub>) of **8**

# Curriculum Vitae

## Yevhen Hryshunin

yevhen.hryshunin@gmail.com  
St Sulpice 1025, Switzerland  
+41 79 818 57 64



### Profile

High-performing polymer scientist and engineer who strives for research and development excellence with a strong focus on novel sustainable packaging solutions with relation to the new sustainable plastics, polymer processing, thermomechanical characterization and final performance.

### Experience

03.2018 – present	<p><b>PhD candidate under supervision of Prof. Holger Fruenrath at the École polytechnique fédérale de Lausanne (EPFL)</b></p> <ul style="list-style-type: none"><li>• Title: New Processing Avenues for of PLA and PCL Based Materials for Novel Sustainable Packaging</li><li>• <i>Key Achievement:</i> PLA and PCL of 80'000 molecular weight were modified to yield materials with <b>higher crystallization speed and improved melt strength</b>. Both properties were then effectively utilized to process the polymers in the melt into films and fibers with consecutive <b>significant improvement in mechanical properties</b> at room temperature. The production of polymers was then <b>scaled-up to 1 kg scale</b> by reactive extrusion. Packaging articles like <b>liners and yogurt cups</b> were obtained to showcase improved mechanical properties, thermal stability and processability of the obtained materials.</li></ul>
01.2017 – 06.2017	<p><b>Master thesis under supervision of Prof. De Cola at the Institute of Supramolecular Chemistry and Engineering, Strasbourg University</b></p> <ul style="list-style-type: none"><li>• Title: Novel Nanocomposite pH Responsive Hydrogels</li><li>• <i>Key Achievement:</i> It was demonstrated that, in a nanocomposite based on a pH-responsive hydrogel, <b>the pH-dependent degradation of the hydrogel is a viable approach to trigger the release of encapsulated bioactive molecules</b>. A patent on this finding is currently in preparation.</li></ul>
09.2016 – 12.2016	<p><b>Internship under supervision of Prof. De Cola at the Institute of Supramolecular Chemistry and Engineering, Strasbourg University</b></p> <ul style="list-style-type: none"><li>• Title: A Hybrid, Emission-Switchable Hydrogel for <i>in Vitro</i> Cell Studies</li><li>• <i>Key Achievement:</i> In hydrogels with covalently attached iridium complexes loaded with cells, the interaction between the complex and the lipid bilayer cell membrane led to a fluorescence switch-on due to the suppression of the fluorescence quenching by molecular oxygen. <b>Fluorescent complexes sensitive to molecular oxygen hence allow for a real-time analysis of the 3D movement of cells and can be used as a substitute to conventional cell staining agents.</b></li></ul>
09.2016 – 06.2017	<p><b>Assistant Technician in the group of Prof. De Cola at Institute of Supramolecular Chemistry and Engineering, and at the National Center for Scientific Research, Strasbourg University</b></p> <ul style="list-style-type: none"><li>• Large-scale synthesis of polyamidoamine gels as bulk materials and surface modification of nanoparticles as well as silica particles for <i>in vivo</i> testing.</li></ul>

	<ul style="list-style-type: none"> <li>• Loading of polyamidoamine gel particles and silica particles with drugs, proteins, and contrast agents.</li> </ul>
<b>09.2015 – 06.2017</b>	<p><b>Double international Master's Degree in Polymer Engineering and Sustainable Materials at the Strasbourg and Freiburg Universities.</b></p> <ul style="list-style-type: none"> <li>• Grade: 16.3/20; Final class ranking 1/25</li> </ul>

## Skills

---

<b>Chemistry</b>	Synthesis, characterization and scale-up of discrete organic compounds and polymers: PLA, PCL, PDMS, PP, PS. Conversant with Schlenk techniques. Preparation and functionalization of silica and hydrogel particles;
<b>Analytcs</b>	<p>Polymer processing: thermoforming, hot pressing, fiber and film drawing, extrusion molding.</p> <p>Mechanical and thermal characterization: differential scanning calorimetry (DSC), oscillatory and elongational rheology, dynamic mechanical analysis (DMA) and tensile testing (UTM).</p> <p>Structural characterization: X-ray diffraction (SAXS and WAXS), scanning electron microscopy (SEM), atomic force microscopy (AFM), mass distribution and branching analysis by size exclusion chromatography (SEC) and MALDI-TOF mass spectrometry.</p> <p>Other: cell visualization by confocal laser microscopy, colloid characterization by dynamic light scattering and zeta-potential analysis, Nuclear Magnetic Resonance (NMR) spectroscopy, UV-vis absorption, and fluorescence spect</p>
<b>IT</b>	Conversant with Origin, Adobe Illustrator, Adobe Photoshop, Image J, Microsoft Office, ChemDraw, TOPSPIN, HTML and web-design.
<b>Business</b>	<p>2018-2022 EPFL innovators scholar with direction towards innovation, entrepreneurship and business management</p> <p>2016-2017 status of student-entrepreneur, conversant with preparation of a business plan, tax liability and launching a company.</p>

## Awards

---

<b>03.2018</b>	Innoswiss Business Scholarship, EPFL innovators
<b>11.2017</b>	Swiss Government Excellence Scholarship
<b>09.2016</b>	French Government Scholarship from Campus France for foreign students
<b>05.2016</b>	Boussole Mobility Scholarship from Region Alsace Champagne-Ardenne Lorraine
<b>02.2016</b>	Mobility Aid Scholarship from the Franco-German University (DFH-UFA)
<b>09.2015</b>	French Government Scholarship from Campus France for foreign students

## Languages

---

- Ukrainian, Russian – native
- English – C1
- French – B2
- German – A1